ODESSA ASTRONOMICAL PUBLICATIONS

Volume 35
(2022)

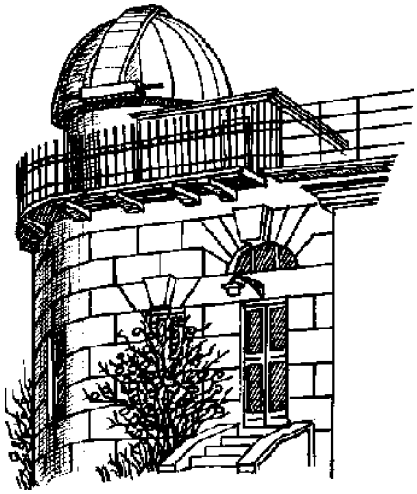

Astronomical Observatory
of I. I. Mechnikov Odesa National
University

ODESSA ASTRONOMICAL PUBLICATIONS

Volume 35
(2022)

Address:
Astronomical Observatory, Odesa National University,
T. G. Shevchenko Park, Odesa, 65014, UKRAINE
Tel.: + 38 048 722-84-42

E-mail: astronomical_observatory@onu.edu.ua
http://www.astro-observ-odessa0.1gb.ua

The electronic version of the journal is on the web page: http://oap.onu.edu.ua

Одеські Астрономічні Публікації
Видається з 1946 року (видання відновлено в 1993 р., №6)

Свідоцтво про державну реєстрацію друкованого засобу масової інформації:
серія КВ № 14722-3693Р від 30.10.2008 р.
Журнал включено до списку МОН України наказом МОНУ № 1643 від 28.12.2019 р.

Друкується за рішенням Вченої ради НДІ "Астрономічна обсерваторія" Одеського національного університету імені І.І.Мечникова від 27 вересня 2022 р., протокол №4

Printed in UKRAINE
"ONU" PUBLISHING COMPANY

ISSN 1810-4215

CONTENTS

COSMOLOGY, GRAVITATION, ASTROPARTICLE PHYSICS, HIGH ENERGY PHYSICS

DOI 10.18524/1810-4215.2022.35.268190

SPHERICALLY SYMMETRIC SYSTEM OF GRAVITATIONAL AND ELECTROMAGNETIC FIELDS AND THE STRUCTURE OF ITS CONFIGURATION SPACE

V.D. Gladush

Oles Honchar Dnipro National University,
Dnipro, Ukraine, *vgladush@gmail.com*

ABSTRACT. Geometrodynamics of charged black holes (BH) described by the system of Maxwell-Einstein equations is considered. We start from a spherically symmetric metric, a reduced action, and a Lagrangian written in characteristic variables. The configuration space (CS) metric, Hamiltonian, momentum and electromagnetic constraints are constructed. The system has conservation laws of charge q and mass m. The action functional is transformed into a Jacobi-type functional in CS with a metric conformal to the CS metric. A transformation of field variables is introduced which brings the CS metric to the "Lorentzian"form. The resulting CS metric is the metric of a flat nonholonomic section of a 4-dimensional space. In the new variables, the squared momenta of the system has the Lorentz form. On this basis, quantization is considered. Thanks to the structure of the CS, the momentum operators, the DeWitt equations, and the mass and charge operators are constructed. The equations system of CBH quantum states with certain q and m is constructed. For comparison, we consider the CBH reduced model limited in the T-region. In such the simplified formulation, the T-model equations are integrated and lead to the CBH with continuous spectrum of m and q.

Keywords: spherically symmetric configurations, configuration space, Hamiltonian constraint, DeWitt operators, mass and charge, quantization, charged black holes.

АНОТАЦІЯ. Розглядається загальний підхід до геометродинаміки заряджених чорних дірок (ЗЧД), що описуються сферично-симетричними конфігураціями гравітаційного та електромагнітного полів. Ми виходимо з метрики, редукованої дії та лагранжіана, записаних у характеристичних змінних. Вводяться узагальнені швидкості та метрика конфігураційного простору (КП). Будуються гамільтонова, імпульсна та електромагнітна в'язі. Система має закони збереження заряду q та маси m. Використовуючи гамільтонову в'язь та закони збереження, знаходяться вирази для імпульсів через конфігураційні змінні та q і m. З рівнянь для імпульсів у функціональних похідних від дії будується функціонал дії. Похідні дії по q і m призводять до рівнянь траєкторій в КП. Далі функціонал дії перетворюється на функціонал дії типу Якобі в КП з метрикою, конформної до метрики КП. Вводиться перетворення польових змінних, які зводять метрику КП до "лоренцевого"виду. Це приводе нелінійну систему рівнянь ЗЧД до лінійної, де всі компоненти поля поділяються. Одержана метрика КП може розглядатися як метрика плоского неголономного перерізу 4-вимірного простору. В нових змінних квадрат імпульсів системи має теж Лоренців вигляд. На цій основі розглядається квантування системи. Завдяки структурі КП вдається побудувати коректні оператори імпульсів, рівняння Девітта та оператори маси та заряду. Будується система рівнянь у функціональних похідних для квантових станів ЗЧД із певними q і m. Для порівняння розглядається редукована модель ЗЧД, обмеженої в Т-області. У такій спрощеній постановці рівняння Т-моделі інтегруються і призводять до моделі ЗЧД із безперервними спектрами m і q. Побудова редукована Т-модель намічає шляхи подальшого дослідження загальної системи рівнянь квантової геометродинаміки ЗЧД.

Ключові слова: сферично-симетричні конфігурації, конфігураційний простір, Гамільтонова в'язь, оператори Девітта, маси і заряду, квантування, заряджені чорні діри.

1. Introduction

The paper is devoted to the study of the classical and quantum aspects of the geometrodynamics of charged black holes (CBH), the research on the structure of their configuration space (CS) and the construction of a

system of quantum equations in functional derivatives that describe the model of CBH.

Geometrodynamics of CBH is described by the Einstein equations system for a spherically symmetric configuration of the gravitational and electromagnetic fields in GR. As is known, the space-time metric $g_{\mu\nu}$ of such a configuration of fields admits the Killing vector. The region $R \subset \mathbf{M}^{(4)}$, where this vector is timelike, is called the R-region, while the region $T \subset \mathbf{M}^{(4)}$, where this vector is spacelike, is called the T-region [Gladush 21].

First, consider the configuration of fields in the whole $\mathbf{M}^{(4)} = T \bigcup R$. We proceed from the following standard general action for the system of gravitational and electromagnetic fields in GR [Louko 1996, Mäkelä 1998]

$$S_{tot} = -\frac{1}{16\pi c}\int\left(\frac{c^4}{\kappa}\ {}^{(4)}R + F^{\mu\nu}F_{\mu\nu}\right)\sqrt{-g}d^4x\,, \quad (1)$$

where ${}^{(4)}R$ is the scalar curvature, κ is the gravitational constant, $F_{\mu\nu} = A_{\nu,\mu} - A_{\mu,\nu}$ is the electromagnetic field tensor, $d^4x = dx^0dx^1dx^2dx^3$, $g = \det|g_{\mu\nu}|$.

2. Classical geometrodynamics of charged BH

For non-rotating spherically symmetric configurations, we consider the space-time metric $\mathbf{M}^{(4)}$ and the electromagnetic field of the type [Gladush 19]

$$ds^2 = \frac{R}{\xi}\left(Ndx^0\right)^2 - \frac{\xi}{R}\left(dr + N^r dx^0\right)^2 - R^2 d\sigma^2, \quad (2)$$

$$E = F_{01} = A_{r,0} - A_{0,r} = \phi_{,0} - \varphi_{,r}, \quad (3)$$

where $d\sigma^2 = d\theta^2 + \sin^2\theta d\alpha^2$. Field configuration variables

$$q^A = \left\{q^1 = q^R = R,\ q^2 = q^\xi = \xi,\ q^3 = q^\phi = \phi\right\} \quad (4)$$

are generalized coordinates that depend on space-time coordinates x^0, r, besides $A, B = \{1, 2, 3\}$.

The action S_{tot} after dimensional reduction, can be written as [Gladush 19]:

$$S_{tot} = \int dx^0 \int dr\mathcal{L}\,, \qquad \mathcal{L} = \frac{V^2}{2N} + N\mathcal{U} \quad (5)$$

where

$$V^2 = \Gamma_{AB}V^AV^B = -\frac{c^3}{\kappa}V^RV^\xi + \frac{1}{c}R^2\left(V^\phi\right)^2 \quad (6)$$

is the velocity square of the kinetic part of the Lagrangian. Here Γ_{AB} are the covariant components of the CS metric, and $\Gamma = \det\|\Gamma_{AB}\| = -(c^5/4\kappa^2)R^2$, $V^A = q^A_{,0} + K^A$ – are the generalized velocity components

$$V^R = R_{,0} + K^R,\ V^\xi = \xi_{,0} + K^\xi,\ V^\phi = \phi_{,0} + K^\phi \quad (7)$$

where

$$K^R = -N^rR_{,r}, K^\xi = -\xi_{,r}N^r - 2\xi N^r_{,r}, K^\phi = -\varphi_{,r} \quad (8)$$

$\mathcal{U}$ is the potential part of the Lagrangian

$$\mathcal{U} = \frac{c^3}{2\kappa}\left(1 + \frac{R^2}{\xi^2}R_{,r}\xi_{,r} - \frac{2R}{\xi}R^2_{,r} - \frac{2R^2}{\xi}R_{,rr}\right) \quad (9)$$

Let us introduce the CS metric of the by the formula

$$d\Omega^2 = \Gamma_{AB}V^AV^B\left(dx^0\right)^2 = \Gamma_{AB}Dq^ADq^B \quad (10)$$

Here $Dq^a = dq^A + K^Adx^0$ are the Lie differentials

$$DR = dR + K^Rdx^0, D\xi = d\xi + K^\xi dx^0, D\phi = d\phi + K^\phi dx^0$$

At that, the Γ_{AB} components are defined in (6). Then

$$d\Omega^2 = -\frac{c^3}{\kappa}D\xi DR + \frac{1}{c}R^2\,D\phi^2 \quad (11)$$

The Legendre transformation of the system leads to the Hamiltonian action [Louko 1996]

$$\begin{aligned} S \ = \ & \int dx^0\int_0^\infty dr\ \{\mathcal{P}_\xi\xi_0 + \mathcal{P}_RR_{,0} + \mathcal{P}_\phi\phi_{,0} \\ & -N\mathcal{H} - N^r\mathcal{H}_r - \varphi\mathcal{H}_\phi\} \end{aligned} \quad (12)$$

where

$$\mathcal{H} = -\frac{2\kappa}{c^3}\mathcal{P}_R\mathcal{P}_\xi + \frac{c}{2R^2}\mathcal{P}_\phi^2 - \mathcal{U} \sim 0\,, \quad (13)$$

$$\mathcal{H}_r = -\xi_{,r}\mathcal{P}_\xi - 2\xi\mathcal{P}_{\xi,r} + R_{,r}\mathcal{P}_R \sim 0\,, \quad (14)$$

$$\mathcal{H}_\phi = -\mathcal{P}_{\phi,r} \sim 0\,. \quad (15)$$

so that $\mathcal{H}$ is Hamiltonian, $\mathcal{H}_r$ is momentum, and $\mathcal{H}_\phi$ is electromagnetic constraints expressed in terms of momenta. For convenience, we represent the Hamiltonian constraint in the form

$$H = \frac{1}{2}\mathcal{P}^2 - \mathcal{U} \quad (16)$$

where

$$\mathcal{P}^2 = \Gamma^{AB}\mathcal{P}_A\mathcal{P}_B = -\frac{4\kappa}{c^3}\mathcal{P}_R\mathcal{P}_\xi + \frac{c}{R^2}\mathcal{P}_\phi^2 \quad (17)$$

is the momentum square. Note that Γ^{AB} are the contravariant components of the metric in the CS introduced earlier in (6) so that $\Gamma_{AB}\Gamma^{AD} = \delta^D_B$.

Electromagnetic constraint (15) determines the electric field E generated by the charge Q according to the formula

$$\mathcal{P}_\phi = \frac{R^2}{cN}E = \frac{Q}{c} = const \Rightarrow E = N\frac{Q}{R^2} \quad (18)$$

The system admits the motion integrals: the total mass M_{tot} and the charge $Q = c\mathcal{P}_\phi$ of configuration. The

mass is determined by the mass function, which in terms of momenta has the form (Gladush 2012, 2018)

$$M_{tot} = \frac{c^2}{2\kappa}\left(R + \frac{4\kappa^2}{c^6}\xi\mathcal{P}_\xi^2 - \frac{R^2}{\xi}R_r^2\right) + \frac{\mathcal{P}_\phi^2}{2R} \qquad (19)$$

Using the Hamiltonian constraint and conservation laws, one can find analytical expressions for momenta as functions of configuration variables and parameters m and q. Indeed, using the relations (18), (19) and (13), we obtain

$$\mathcal{P}_\xi = \frac{c^3}{2\kappa}\sqrt{\frac{R}{\xi}F_{tot}}\,, \qquad (20)$$

$$\mathcal{P}_R = \sqrt{\frac{\xi}{RF_{tot}}}\left(\frac{q^2}{2cR^2} - \mathcal{U}\right). \qquad (21)$$

where

$$F_{tot} = \frac{R}{\xi}\left(R_r\right)^2 - 1 + \frac{2\kappa m}{Rc^2} - \frac{\kappa q^2}{c^4R^2} \qquad (22)$$

The momenta obtained in this way identically satisfy the invariance condition of the action functional, i.e. momentum constraint (14).

Using implicitly the integrability conditions of functional equations

$$\mathcal{P}_R = \frac{\delta S}{\delta R}, \quad \mathcal{P}_\xi = \frac{\delta S}{\delta \xi}, \quad \mathcal{P}_\phi = \frac{\delta S}{\delta \phi} = \frac{q}{c}\,, \qquad (23)$$

we find the action functional S as a solution of the Einstein-Hamilton-Jacobi equation in functional derivatives depending on the variables R, ξ and parameters$m$ and q [Gladush 19]:

$$S = \int dr\left\{g\left(m,q;r\right) + \frac{Q}{c}\phi + \right. \qquad (24)$$
$$\left.\frac{c^3}{\kappa}\left(\sqrt{\xi RF_{tot}} - \frac{1}{2}RR_r\ln\left|\frac{RR_r + \sqrt{\xi RF_{tot}}}{RR_r - \sqrt{\xi RF_{tot}}}\right|\right)\right\}$$

Variations of S with respect to mass m and charge q lead to motion trajectories in the CS

$$\frac{\delta S}{\delta m} = -c\frac{\sqrt{R\xi F_{tot}}}{FR} + \frac{\partial g}{\partial m} = 0, \qquad (25)$$

$$\frac{\delta S}{\delta q} = \frac{\sqrt{R\xi F_{tot}}}{cFR}\frac{q}{R} + \frac{\phi}{c} + \frac{\partial g}{\partial q} = 0\,. \qquad (26)$$

From this, follows the expressions for ξ/R and electric potential

$$\frac{\xi}{R} = F_0 f^2 - \frac{R_r^2}{F}, \qquad \phi = \phi_0 - f\frac{q}{R}\,, \qquad (27)$$

where the designations are introduced

$$f = \frac{1}{c}\frac{\partial g}{\partial m}, \quad \phi_0 = -c\frac{\partial g}{\partial q}\,, \quad F = -1 + \frac{2\kappa m}{c^2R} - \frac{\kappa Q^2}{c^4R^2}\,. \qquad (28)$$

The resulting solution leads to the metric $\mathbf{M}^{(4)}$:

$$ds^2 = \frac{N^2\left(dx^0\right)^2}{Ff^2 - R_r^2F^{-1}} - \qquad (29)$$
$$- \left(Ff^2 - R_r^2F^{-1}\right)\left(dr + N^r dx^0\right)^2 - R^2 d\sigma^2\,.$$

Since time is nowhere explicitly included in the system, we can transform the (5) action from a space-time representation into a configuration one, writing it in a form similar to the Jacobi action [Landau 88]. To do this, from the Lagrangian (5) we get

$$\frac{\partial \mathcal{L}}{\partial N} = -\frac{V^2}{2N^2} + \mathcal{U} = 0 \qquad (30)$$

From here we find the multiplier $N = \sqrt{V^2/2\mathcal{U}}$. Excluding N from the action (5), we rewrite it as follows [Barbour 2002, Kiefer 2007, Anderson 2013]

$$S_{tot} = \int dr\int\sqrt{2\mathcal{U}V^2\left(dx^0\right)^2} = \int dr\int\sqrt{D\Omega_{tot}^2} \qquad (31)$$

where

$$D\Omega_{tot}^2 = 2\mathcal{U}D\Omega^2 = 2\mathcal{U}\Gamma_{AB}Dq^ADq^B \qquad (32)$$

is the supermetric, conformal to the metric of the original CS $D\Omega^2$ (10)-(11).

Note that by transforming [Gladush 21]. the field variables

$$\xi = c\tau - x - \frac{y^2}{R}\,, \quad \varphi = \frac{c^2}{\sqrt{\kappa}}\frac{y}{R}\,, \quad R = c\tau + x \qquad (33)$$

the metric $D\Omega^2$ is reduced to the Lorentzian form

$$d\Omega^2 = -c^2D\tau^2 + Dx^2 + Dy^2 = -c^2(d\tau + B^\tau dx^0)^2$$
$$+(dx + B^x dx^0)^2 + (dy + B^y dx^0)^2 \qquad (34)$$

Thus, the metric $d\Omega^2$ in CS can be considered as the metric of a flat nonholonomic section of a 4-dimensional space. So the structure of the CS is similar to the family of flat nonholonomic sections $\mathbf{M}^{(4)}$. It can be shown that the squared momenta (17) under the transformation (33) also takes the Lorentian form

$$P^2 = -\frac{4\kappa}{c^3}P_RP_\xi + \frac{c}{R^2}P_\phi^2 = -\frac{1}{c^2}P_{\acute{\tau}}^2 + P_{\acute{x}}^2 + \left(P_{\acute{y}}\right)^2 \qquad (35)$$

3. On the quantum geometrodynamics of CBH

The quantum states of the field configuration are determined by the wave functional $\Psi(R,\xi,\phi)$ in the CS. At the same time, the momenta P_A are associated with

the momentum operators $\hat{P}_A$, which in the coordinate representation have the form of functional derivatives:

$$\hat{\mathcal{P}}_R = -i\hbar\frac{\delta}{\partial R}, \quad \hat{\mathcal{P}}_\xi = -i\hbar\frac{\delta}{\partial \xi}, \quad \hat{\mathcal{P}}_\phi = -i\hbar\frac{\delta}{\partial \phi} \quad (36)$$

In the case of charge $Q = cP_\phi$ from here we immediately obtain

$$Q \longrightarrow \hat{Q} = c\hat{\mathcal{P}}_\phi = -ic\hbar\frac{\delta}{\partial\phi} \quad (37)$$

Similarly, (14) yields the operator momentum constraint equation

$$R_{,\,r}\frac{\delta\Psi}{\delta R} - \xi_{,\,r}\frac{\delta\Psi}{\delta\xi} - 2\xi\frac{\partial}{\partial r}\frac{\delta\Psi}{\delta\xi} = 0 \quad (38)$$

and (15) implies the operator electromagnetic constraint equation

$$\frac{\partial}{\partial r}\left(\frac{\delta\Psi}{\delta\varphi}\right) = 0\,. \quad (39)$$

With the mass function M_{tot} (19) is related to the problem of ordering momentum operators. For the hermiticity of the total mass operator, in the CS with the volume element $dV = (c^{5/2}/2\kappa)Rd\xi dRd\phi$, the following ordering is used $\xi P_\xi \to \hat{P}_\xi\xi\hat{P}_\xi$. Therefore, the mass function M_{tot} (19) corresponds with the operator

$$\begin{aligned}\hat{M} &= \frac{c^2}{2\kappa}\left(R - \frac{4\kappa^2\hbar^2}{c^6}\frac{\delta}{\delta\xi}\xi\frac{\delta}{\delta\xi} - \right.\\ &\left. - \frac{\kappa\hbar^2}{c^2R}\frac{\delta^2}{\delta\phi^2} - \frac{R^2}{\xi}\left(R_r\right)^2\right) \end{aligned} \quad (40)$$

When the Hamiltonian constraint $H = 0$ (16) is quantized, it is associated with its quantum counterpart $\hat{H}\Psi = 0$, the DeWitt equation. We note that the squared momentum P^2 in (17), as well as the CS metric $d\Omega^2$ can be reduced to the "Lorentzian"form using the transformation (33) . Therefore, in the coordinates $\{\tau, x, y\}$, when quantizing the constraint $H = 0$, you can use the usual quantization recipe in the form (36).

To construct a quantum Hermitian operator in the original curvilinear coordinates $\{R, \xi, \phi\}$, it is necessary to perform an inverse transformation of coordinates and operators, which is equivalent to passing to covariant derivatives $P_A \to \hat{P}_A = -i\hbar\bigtriangledown_A$ with respect to the metric Γ_{AB} defined in (6). However, in the case under consideration, one should pass to covariant functional derivatives according to the formulas

$$P_A \to \hat{P}_A = -i\hbar\frac{D}{\delta q_A}\,. \quad (41)$$

Here the covariant functional derivatives are defined as follows

$$\frac{DU_B}{\delta q_A} = \frac{\delta U_B}{\delta q_A} - \Gamma^C_{AB}U_C\,, \quad (42)$$

at that $D\Psi/\delta q_A = \delta\Psi/\delta q_A$. Then, for the momentum squared P^2 (17) in the Hamiltonian constraint (16) after the replacement (41) we have

$$P^2 \longrightarrow \hat{P}^2 = -\hbar^2\Delta \quad (43)$$

Here

$$\begin{aligned}\Delta &= \Gamma^{AB}\frac{D}{\delta q_A}\frac{D}{\delta q_B} = \frac{1}{\sqrt{-\Gamma}}\frac{D}{\delta q_A}\sqrt{-\Gamma}\;\Gamma^{AB}\frac{D}{\delta q_B} = \\ &= -\frac{2\kappa}{c^4}\frac{\delta^2}{\delta\xi\delta R} - \frac{2\kappa}{c^4}\frac{1}{R}\frac{\delta}{\delta R}R\frac{\delta}{\delta\xi} + \frac{1}{R^2}\frac{\delta^2}{\delta\varphi^2}\end{aligned} \quad (44)$$

is the Laplace-Beltrami operator, which is Hermitian in natural measure. Note that the formula $\bigtriangledown_\xi = \partial/\partial\xi$ takes place, so in the mass operator (2.3) for the momentum operator $\hat{P}_\xi$ it suffices to restrict ourselves to the functional derivative $P_\xi = -i\hbar\delta/\delta\xi$.

As a result, the Hamiltonian constraint (16) leads to the following DeWitt operator

$$\hat{H} = -\frac{c}{2}\hbar^2\Delta - \mathcal{U} \quad (45)$$

or to the DeWitt equation

$$\frac{c}{2}\hbar^2\left(\frac{2\kappa}{c^4}\frac{\delta^2\Psi}{\delta\xi\delta R} + \frac{2\kappa}{c^4}\frac{1}{R}\frac{\delta}{\delta R}R\frac{\delta\Psi}{\delta\xi} - \frac{1}{R^2}\frac{\delta^2\Psi}{\delta\varphi^2}\right) - \mathcal{U}\Psi = 0\,. \quad (46)$$

States with a certain charge q and mass m are found by solving problems on eigenvalues and eigenfunctions of operators charge Q and mass M

$$\hat{Q}\Psi_q = q\Psi, \quad \hat{M}\Psi_m = m\Psi \quad (47)$$

These equations, taking into account (37) and (40), can be rewritten as follows

$$-ic\hbar\frac{\delta\Psi}{\delta\phi} = q\Psi \quad (48)$$

$$\left(R - \frac{4\kappa^2\hbar^2}{c^6}\frac{\delta}{\delta\xi}\xi\frac{\delta}{\delta\xi} - \frac{\kappa\hbar^2}{c^2R}\frac{\delta^2}{\delta\phi^2} - \frac{R^2}{\xi}R_r^2\right)\Psi = \frac{2\kappa m}{c^2}\Psi. \quad (49)$$

By virtue of the relation (48), it follows from the constraint (39) that Ψ does not depend on r. Moreover, (48) implies

$$\Psi\left[R, \xi, \phi; m, q\right] = \psi\left[R, \xi; m, q\right]e^{iq/c\hbar\int\phi(r')dr'}\,. \quad (50)$$

Then, the DeWitt equation (46) becomes

$$\frac{\kappa\hbar^2}{c^3}\frac{\delta^2\Psi}{\delta\xi\delta R} + \frac{\kappa\hbar^2}{c^3}\frac{1}{R}\frac{\delta}{\delta R}R\frac{\delta\Psi}{\delta\xi} - \frac{c\hbar^2}{2R^2}\frac{\delta^2\Psi}{\delta\varphi^2} - \mathcal{U}\Psi = 0\,. \quad (51)$$

The equation for the eigenvalues of the mass operator (49) can be rewritten as follows

$$\frac{\delta}{\delta\xi}\xi\frac{\delta}{\delta\xi}\psi + \frac{c^6}{4\kappa^2\hbar^2}RF_{tot}\psi = 0\,. \quad (52)$$

The joint solution of the (51) and (52) equations, together with the momentum constraint (38), describes the quantum state of the considered CBH model with fixed charge q and mass m.

4. Geometrodynamics of CBH in the T-region

The T-domain $\mathbf{M}^{(4)}$ CBH is bounded, where the vector Keeling ξ^μ is spatially similar and can be convert to form $\xi^\mu = \delta^\mu_1$. Then the metric (2) can be written as follows

$$ds^2 = \frac{R}{\xi}\left(Ndx^0\right)^2 - \frac{\xi}{R}dr^2 - R^2 d\sigma^2 \qquad (53)$$

In this case, $N^r = 0$, the coordinate system becomes orthogonal and all fields depend only on time. Integration over the coordinate r is replaced by multiplication by the constant $\int dr \to l < \infty$. As a result, the action S_{tot} and the Lagrangian $\mathcal{L}$ (5) take the form

$$S_{tot} \to S = \int L dx^0\,,\ \mathcal{L} \to L = \left(\frac{V^2}{N2} + NU\right). \quad (54)$$

While, $\mathcal{U} \to U = c^3/2\kappa$ is the potential part of the Lagrangian, $V^2$is the square of the velocity

$$V^2 = \Gamma_{AB}V^A V^B = -\frac{c^3}{\kappa}\xi_{,0}R_{,0} + \frac{1}{c}R^2\,\phi^2_{,0} \qquad (55)$$

Here $V^A = \{V^R = R_{,0},\ V^\xi = \xi_{,0},\ V^\phi = \phi_{,0}\}$ are generalized velocities.

The CS metric is defined similarly to the general case (10):

$$d\Omega^2 = \Gamma_{AB}V^A V^B \left(dx^0\right)^2 = \Gamma_{AB}dq^A dq^B\,, \qquad (56)$$

where the components Γ_{AB} are defined by (6). Then

$$d\Omega^2 = -\frac{c^3}{\kappa}d\xi dR + \frac{1}{c}R^2\,d\phi^2 \qquad (57)$$

Legendre transformation of the system leads to the Hamiltonian action

$$dS = \int (P_\xi d\xi + P_R dR + P_\phi d\phi - NH_0 dx^0) \qquad (58)$$

$$H_0 = \frac{1}{2l}P^2 - lU \ = \frac{c}{2l}\left(-\frac{4\kappa}{c^4}P_R P_\xi + \frac{1}{R^2}\,P^2_\phi + \mu^2\right) \qquad (59)$$

where $H_0 \sim 0$ is the Hamiltonian constraint, $P^2 = \Gamma^{AB}P_A P_B$, $\mu = cl/\sqrt{\kappa}$.

The integrals of system motion are the charge $Q = (c/l)P_\phi$ and mass function

$$M = \frac{1}{2}\left[\frac{c^2}{\kappa}R + \frac{1}{l^2}\left(\frac{4\kappa}{c^4}\xi P^2_\xi + \frac{1}{R}\,P^2_\phi\right)\right], \qquad (60)$$

Together with the Hamiltonian constraint, they, similarly to (21) and (20), lead to momenta

$$P_\xi = \frac{lc^3}{2\kappa}\sqrt{\frac{R}{\xi}F}\,, \qquad (61)$$

$$P_R = \frac{lc^3}{2\kappa}\sqrt{\frac{\xi}{RF}}\left(\frac{\kappa Q^2}{c^4R^2} - 1\right) \qquad (62)$$

where F is defined in (28). Using the integrability conditions for the equations

$$P_R = \frac{\partial S}{\partial R},\ \ P_\xi = \frac{\partial S}{\partial \xi},\ \ P_\phi = \frac{\partial S}{\partial \phi} = \frac{q}{}\,, \qquad (63)$$

we find the action of S,

$$S = \frac{lc^3}{\kappa}\sqrt{\xi RF} + \frac{lq}{c}\phi + lg(m,q)\,, \qquad (64)$$

which depends on the variables R, ξ and the parameters m, q. From here, and from the relations $\partial S/\partial m = 0$ and $\partial S/\partial q = 0$, we arrive at the motion trajectories in the CS

$$\phi = \phi_0 - f\frac{q}{R}\,, \quad \frac{\xi}{R} = f^2 F\,, \qquad (65)$$

where $\phi_0 = -c\partial g/\partial q,\ f = \partial g/c\partial m$. The metric (53) now takes the form

$$ds^2 = \frac{\left(Ndx^0\right)^2}{f^2 F} - f^2 F dr^2 - R^2 d\sigma^2, \qquad (66)$$

As well as in the general case, we can transform the action (54) from a space-time representation into a CS representation To do this, from the Lagrangian L in (54), we obtain

$$\frac{\partial L}{\partial N} = l\left(-\frac{V^2}{2N^2} + U\right) = 0\,, \qquad (67)$$

which implies $N = V^2/2U$. Substituting N into action (54) we get

$$S = \int l\sqrt{2UV^2}dx^0 = \mu\int\sqrt{cd\Omega^2} \qquad (68)$$

where $d\Omega^2$ received in (57).

Using the transformation (33) of field variables, the metric $d\Omega^2$ CS is reduced to a flat form

$$cd\Omega^2 = -c^2 d\tau^2 + dx^2 + dy^2\,. \qquad (69)$$

it that the squared momentum $P^2 = \Gamma^{AB}P_A P_B$ takes the Lorentzian form

$$P^2 = -\frac{4\kappa}{c^3}P_R P_\xi + \frac{c}{R^2}P^2_\phi = -\frac{1}{c^2}P^2_{\dot\tau} + P^2_{\dot x} + (P_{\dot y})^2\ . \quad (70)$$

As we can see, the corresponding equations of geometrodynamics of the CBH in the T-region are greatly simplified. This is especially important in the

case of quantization of the BH. So, the equations system of the quantum theory of BH in functional derivatives for the wave functional $\Psi\left[R,\xi,\phi;m,q\right]$ goes over into the equations system in partial derivatives for the wave function $\Psi(R,\xi,\phi;m,q)$. As a result, we have the DeWitt equation and equations for the eigenvalues ??of mass and charge. The equation for the charge eigenvalue leads to the wave function

$$\Psi[(R,\xi,\phi;m,q)=\psi\left(R,\xi;m,q\right)e^{(iql/c\hbar)\phi} \tag{71}$$

where the function $\psi(R,\xi;m,q)$ obeys the reduced equations DeWitt and the mass eigenvalue

$$\left[\frac{\delta^2}{\delta\xi\delta R}+\frac{1}{R}\frac{\delta}{\delta R}R\frac{\delta}{\delta\xi}+\frac{c^4}{2\kappa\hbar^2}\left(\frac{l^2q^2}{c^2R^2}+\frac{c^2l^2}{\kappa}\right)\right]\Psi=0 \tag{72}$$

$$\frac{\delta}{\delta\xi}\xi\frac{\delta}{\delta\xi}\psi+\frac{c^6}{4\kappa^2\hbar^2}RF\psi=0\,. \tag{73}$$

The joint solution of the system of equations (72) and (73) leads to the following wave function [Gladush 21]

$$\Psi=C\sqrt{\frac{l_{pl}}{R}}J_0\left(\frac{l}{l_{pl}^2}\sqrt{\xi RF_T}\right)e^{\frac{ilq}{\hbar c}\phi}\,, \tag{74}$$

where J_0 is the Bessel function of the first kind of order zero.

We see that in this simplified formulation, the constructed model describes the CBH in the T-region with a continuous spectrum of mass m and charge q.

5. Conclusions

Comparison of the general approach to the geometrodynamics of CBH and the particular approach associated with the reduced model of CBH limited in the T-region of space-time led to the interesting results. The discovered possibility to reduce a nonlinear dynamical system to a linear one, in which all field components are separated, led to the establishment of the configuration space structure as a family of flat non-homogeneous sections of some 4-dimensional space. At the same time, the found transformation led to the construction of the Lorentz form of the momentum square and the subsequent construction of the DeWitt operator containing the Laplace-Beltrami operator in the metric of the configuration space. The construction of this operator and the existence of a solution for the reduced T-model outlines the way to solve the quantum CBH geometrodynamics equations in the general case.

References

Anderson E.: 2013, arXiv:1111.1472 [gr-qc].

Barbour J. et al: 2002, *Clas. and Quant. Grav.,* **19**, 3217.

Gladush V.D. et al: 2012, *Space, time and fund. interect.,* **1**, 48.

Gladush V.D. et al: 2018, *Space, time and fund. interect.,* **2**, 28.

Gladush V.D.: 2019, *J. Phys and Electron.,* **27(1)**, 3.

Gladush V.D.: 2021, *Odessa Astron. Publ.,* **34**, 11.

Gladush V.D.: 2021, *J. Phys and Electronl.,* **29(2)**, 21.

Kiefer C. Quantum Gravity. New York: Oxford University Press, 2007. 375 p.

Landau L.D., Lifshic E.M. Teoreticheskaya fizika. M.: Nauka, 1988. T.1. 216 p.

Louko, J. et al: 1996, *Phys. Rev. D.,* **54**, 2647.

Mäkelä, J. et al: 1998, *Phys. Rev. D.,* **57**, 4899.

ASTROPHYSICS
(stellar atmospheres, interacting binary systems, variable stars)

DOI 10.18524/1810-4215.2022.35.267997

DISCOVERY OF A NEW [WR] STAR

A. F. Abdulkarimova[1], O. V. Maryeva[2], S. V. Karpov[3]

[1] Shamakhy Astrophysical Observatory,
Y.Mammadaliyev, AZ5626, Azerbaijan *wolfraye@gmail.com*
[2] Astronomical Institute of the Czech Academy of Sciences, Ondřejov, Czech Republic
[3] Institute of Physics of the Czech Academy of Sciences, Prague, Czech Republic

ABSTRACT. Wolf–Rayet (WR) stars are evolved massive objects, famous for their spectra rich with emission lines. For the first time WR stars were described more than 150 years ago, and now in our Galaxy we know around 667 objects of this type. However, the discovery of a new WR star, especially based on spectral observations, is still a rare event. The paper is devoted to J040901.83+323955.6 star, discovered a few years ago as WR star in LAMOST spectral survey by machine learning methods. We were interested that different researchers based on different methods classify this object in different ways – ranging from RR Lyr variable to nitrogen rich WR – and so we began our study. We combined spectral and archival photometric data, analysed the spatial location of the star in the Galaxy and concluded what J040901 is [WR] – central star of a planetary nebula.

Keywords: stars: Wolf–Rayet; stars: low-mass; stars: variables: general

АНОТАЦІЯ. Зорі Вольфа-Райє (WR) – це масивні об'єкти, що проеволюціонували, спектри яких багаті емісійними лініями, що свідчать про високий темп втрати маси. Хоча вперше зорі WR були описані понад 150 років тому, зараз у нашій Галактиці відомо лише 667 об'єктів цього типу. Тому відкриття кожної нової зорі WR, особливо з урахуванням спектральних спостережень, є рідкісною подією. Стаття присвячена зорі J040901.83+323955.6, виявленій кілька років тому у спектральному огляді телескопа LAMOST методами машинного навчання та класифікованою як WR зоря. Нас зацікавило, що різні дослідники на основі різних методів класифікують цей об'єкт по-різному – від змінної RR Lyr до багатої на азот WR – і ми почали наше дослідження. Ми визначили положення зорі на діаграмі колір-величина і виявили, що J040901.83+323955.6 знаходиться в області маломасивних зір. На підставі цього робимо висновок, що J040901.83+323955.6 є [WR] – центральною зорею планетарної туманності. Для вивчення її фотометричної змінності ми поєднали дані з різних оглядів неба. Побудовані криві блиску явно показують, що зоря дуже змінна, амплітуда змінності досягає 0.5 зор. величини.

Ключові слова: Вольф-Райє , низькі маси, змінні, загальний

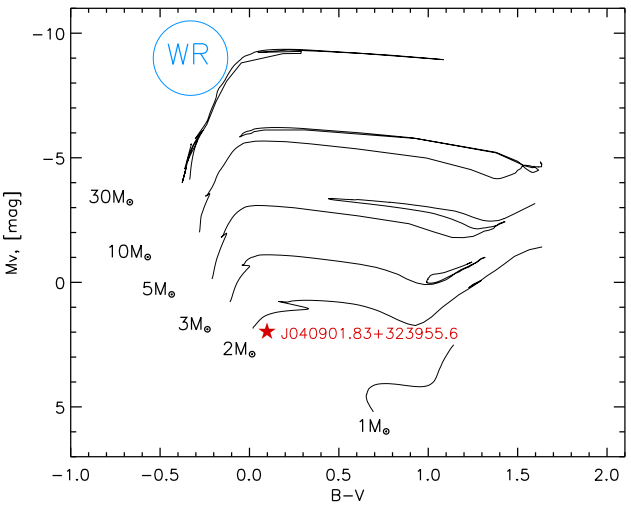

Figure 1: Position of J040901.83+323955.6 in the color–magnitude diagram

1. Introduction

Wolf–Rayet (WR) stars are final point in evolution of massive stars. Location of WR in the Galaxy coincides with spiral arms and star formation regions. Therefore, the discovery of new WR stars in the Galaxy via optical observations has been severely limited by dust extinction. Due to that, most of discoveries of new WR stars nowadays happen in infrared (IR) range. Although the probability of finding a WR star during an optical spectroscopic survey still remains.

Star J040901.83+323955.6 was discovered by Škoda et al (2020) during large spectroscopic survey based on LAMOST archive and classified as WN star. Independently Sun et al. (2021) found J040901 in the

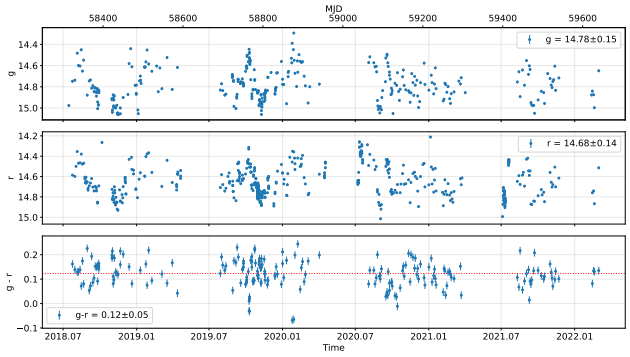

Figure 2: The light curve of J040901.83+323955.6 based on the data from ZTF DR12

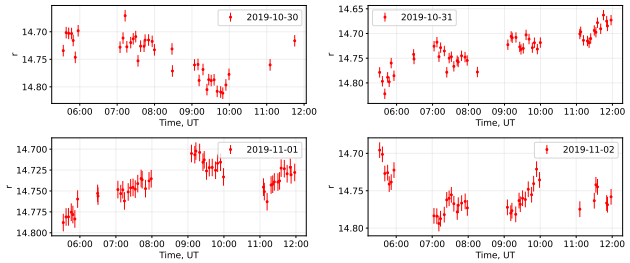

Figure 3: Intra-night variability of J040901 for the four nights based on ZTF DR12

frame of a search for new cataclysmic variables (CVs) in LAMOST data and classified it as Nova-like subtype of CVs. Sun et al. (2021) suggested that J040901.83+323955.6 is surrounded by a disk, because Hα line in its spectrum shows double-peaked profile. Photometric studies of J040901 are also known: Sesar et al. (2017) added J040901 to the list of RR Lyrae stars using machine-learning methods and multi-epoch, asynchronous multi-band photometric data from Pan-STARRS for identification. They found a period P=0.2847 d for the object. Moreover, J040901 was included in the first catalog of variable stars of the All-Sky Automated Survey for Supernovae (ASAS-SN) survey as a variable (Jayasinghe et al. 2018). In the catalog the star is mentioned as a non-periodic object with V=14.48 mean magnitude and amplitude of 0.39 mag.

2. J040901.83+323955.6 in color-magnitude diagram

We started our study of J040901 with the analysis of location of the star in color-magnitude diagram (Figure 1). We recalcultated visible V magnitude of the star to absolute M_V magnitude using distance estimations according to *Gaia* third Data Releases (DR3; Bailer-Jones et al. 2021). Figure 1 clearly shows that J040901 lies in the region of low mass stars and the object significantly differs from WR stars in magnitude.

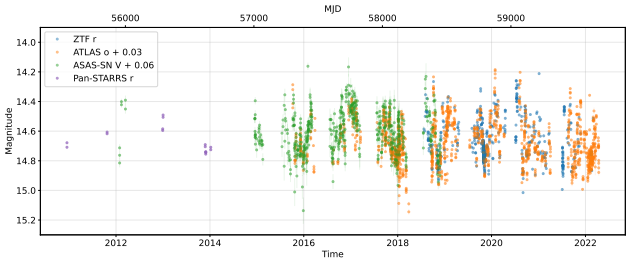

Figure 4: The light curve of J040901.83+323955.6 over last 10 years using the data from ZTF, ATLAS, ASAS-SN and Pan-STARRS sky surveys.

Ii is possible to explain low mass of J040901 and its WR type spectrum if one suggests that the object is a [WR] star. [WR] stars or Wolf-Rayet central stars of planetary nebula (WR CSPN) are objects with *WR phenomenon*. *WR phenomenon* is a fast-moving, hot plasma, normally expanding around a hot star.

3. Photometry and variability

In order to assess the photometric variability of the star we utilized the data from several large-scale sky surveys and public data archives.

The position of J040901 has been repeatedly observed during Zwicky Transient Facility (ZTF, Bellm et al. 2019) survey. The light curve of the object contains 1026 measurements in ZTF g and r filters. We converted them to Pan-STARRS photometric system by using the color terms from the data table, and mean object color $g - r = 0.12$. We then grouped together the measurements in g and r filters separated by no more than 0.3 days (0.05 days on average) to get the color as a function of time. Figure 2 shows the light curves in two bands based on ZTF data, as well as the color. Both the color and magnitudes vary on quite short, most probably intra-night time scale, as illustrated by Figure 3 that shows the light curves of four nights when the field of the object was observed repeatedly in r band.

We also found the data from the archive of Asteroid Terrestrial-impact Last Alert System (ATLAS) (Heinze et al. 2018, Smith et al. 2020, Tonry et al. 2018). We used only o band data (1395 points) with S/N > 10, which we converted to Pan-STARRS photometric system using $r = o + 0.26 \cdot (g - r) = o + 0.03$ equation from Tonry et al. (2018) and $g - r = 0.12$ mean object color.

The ASAS-SN (Shappee et al. 2014) routinely monitors the whole sky. We downloaded from its Light Curve Server (Kochanek et al. 2017) the forced aperture photometry ($16''$ radius) light curve with zero point calibrated to APASS DR9 catalogue zero

point for all epochs available in the service. We then kept only 607 V band measurements with S/N > 10. All these data, converted to Pan-STARRS r band, are shown in Figure 4.

4. Conclusions

J040901 is an evolved low mass star showing WR phenomenon, but not a massive WR star. J040901 shows strong short timescale photometric variability ($\sim$0.5 mag). We are going to continue the study based on new spectral data and numerical modeling.

Acknowledgements. The work is funded from the European Union's Framework Programme for Research and Innovation Horizon 2020 (2014-2020) under the Marie Skłodowska-Curie Grant Agreement No. 823734.

References

Bailer-Jones C. A. L. et al.: 2021, *AJ*, **161**, 147.
Bellm E. C. et al.: 2019, *PASP*, **131**, 018002.
Heinze A. N. et al.: 2018, *AJ*, **156**, 241.
Jayasinghe T. et al.: 2018,*MNRAS*, **477**, 3145.
Kochanek C. S. et al.: 2017, *PASP*, **129**, 104502.
Rosslowe C.K., Crowther P.A.: 2015, *MNRAS* , **447**, 2322.
Sesar B., et al.: 2017, *AJ* , **153**, 204.
Shappee B.J., et al.: 2014,*ApJ*, **788**, 48.
Shara M.M. et al.: 2012, *AJ* , **143**, 149.
Škoda et al.: 2020, *A&A*, **643**, A122.
Sun Y., et al.: 2021, *ApJS* , **257**, 65.
Tonry J.L., et al.: 2018, *PASP*, **130**, 064505.
Tsuboi M. et al.: 2022, *PASJ* , **74**, 738.

10.18524/1810-4215.2022.35.268673

AN ENIGMA OF THE PRZYBYLSKI STAR

S.M. Andrievsky[1,2,3]

[1] Astronomical Observatory, Odessa National University of the Ministry of Education and Science of Ukraine, Shevchenko Park, 65014, Odessa, Ukraine, *andrievskii@ukr.net*
[2] Institut für Astronomie und Astrophysik, Kepler Center for Astro and Particle Physics, Universität Tübingen, Sand 1, 72076 Tübingen, Germany,
[3] GEPI, Observatoire de Paris, Université PSL, CNRS, 5 Place Jules Janssen, F-92190 Meudon, France

ABSTRACT. A new scenario to explain the Przybylski star phenomenon is proposed. It is based on the supposition that this star is a component of a binary system with a neutron star (similar to the hypothesis proposed earlier by Gopka, Ul'yanov & Andrievskii). The main difference with previous scenario is as follows. The orbits of the stars of this system lie in the plane of the sky (or very close to this plane). Thus, we see this star (and its companion) nearly polar-on, and therefore we cannot detect the orbital motion (spectral line based) from the Przybylski's star spectrum. In relation to the Przybylski star, the neutron star is a *γ-ray pulsar* for it. A neutron star is a source of relativistic particles and radiation emitted from the certain parts of its surface. The topology of this radiation strongly depends on the the magnetic field configuration of the neutron star. Existing models suppose that 1) high-energy electron-positron pairs and hard radiation are produced in the (magnetic) polar zones. Accelerated charge particles that move along magnetic lines emit electromagnetic quanta. In this model the radio-emission is genetically linked with the emission of the γ-quanta. 2) Another model of the outer gap is based on the assumption that there is a vacuum gap in the outer magnetosphere of the neutron star, which arises due to the constant escape of charged particles through the light cylinder along the open magnetic field lines. The direction of such escape may be roughly orthogonal to the rotation axis. If the rotation axes of the Przybylski star and the neutron star are close in direction (or even aligned), charged particles and hard radiation ejected in the approximately orthogonal direction at a large solid angle can enter the Przybylski's star atmosphere, causing there different physical processes. As a possible source of the free neutrons could be the nuclear reactions between high-energy γ-quanta and nuclei of some atoms in the Przybylski's star atmosphere gas. As a result, photoneutrons can be generated. Large enough neutron flux can be produced in the reactions with quite abundant element of the atmosphere gas (for example, helium). The photoneutrons produced in these reactions are rapidly thermalized and, as resonant neutrons, react with seed nuclei in the *s*-process. It should be also noted that together with *s*-process elements, the deuterium nuclei could be formed as a result of the interactions of the free resonant neutrons with the hydrogen atoms, but this issue has not yet been worked out.

Keywords: Stars: chemically peculiar

АНОТАЦІЯ. Запропоновано новий сценарій пояснення феномену зорі Пшибильського. Він ґрунтується на припущенні, що ця зоря є компонентом подвійної системи з нейтронною зорею (подібно до гіпотези, запропонованої раніше Гопкою, Ульяновим та Андрієвським). Основна відмінність від попереднього сценарію полягає в наступному. Орбіти зір цієї системи лежать у картинній площині (або дуже близько до цієї площини). Таким чином, ми бачимо цю зорю (і її супутника) майже в полярному положенні, і тому ми не можемо виявити орбітальний рух за спектром зорі Пшибильського. По відношенню до зорі Пшибильського нейтронна зоря є гамма-пульсаром. Нейтронна зоря є джерелом релятивістських частинок і випромінювання, що випускається певними ділянками її поверхні. Топологія цього випромінювання сильно залежить від конфігурації магнітного поля нейтронної зорі. Існуючі моделі припускають, що високоенергетичні електрон-позитронні пари і жорстке випромінювання утворюються в (магнітних) полярних зонах. Прискорені заряджені частинки, які рухаються вздовж магнітних ліній, випромінюють електромагнітні кванти. У цій моделі радіовипромінювання генетично пов'язане з випромінюванням гамма-квантів. Інша модель базується на припущенні, що в зовнішній магнітосфері нейтронної зорі є вакуумний проміжок, який виникає внаслідок постійного витікання заряджених частинок через світловий

циліндр вздовж відкритих силових ліній магнітного поля. Напрямок такої міграції може бути приблизно ортогональним до осі обертання зорі. Якщо осі обертання зорі Пшибильського і нейтронної зорі близькі за напрямком (або навіть співпадають), заряджені частинки і жорстке випромінювання, що викидаються в приблизно ортогональному напрямку у великому тілесному куті, можуть входити в атмосферу зорі Пшибильського, викликаючи там різні фізичні процеси. Можливим джерелом вільних нейтронів можуть бути ядерні реакції між високоенергетичними гамма-квантами і ядрами деяких атомів у газі атмосфери зорі Пшибильського. Як наслідок, можуть генеруватися фотонейтрони. Досить великий потік нейтронів може бути отриманий в реакціях з досить поширеним елементом газу атмосфери (наприклад, Гелієм). Фотонейтрони що утворюються в цих реакціях, швидко втрачають енергію і, вже як резонансні нейтрони, реагують із зародковими ядрами ядрами в s-процесі. Слід також зазначити, що разом з елементами s-процесу ядра Дейтерію могли б утворитися в результаті взаємодії вільних резонансних нейтронів з атомами Гідрогену, але це питання ще не опрацьоване.

Ключові слова: Зорі: хімічно пекулярні

1. Introduction

The Przybylski star (HD 101065) is probably one of the most mysterious objects in our Galaxy. Its spectrum is crowded with lines of various elements. Some of them are identified as lines of rare-earth elements (even at higher ionization stages than expected from the value of the star effective temperature), and others are not identified.

Since the first spectroscopic observation of this star and the first published papers, noting the enormously strong line blanketing in its spectrum (Przybylski 1961, Kron & Gordon 1961), more than sixsty years have already passed, and no acceptable explanation for this phenomenon has yet been given (see, nevertheless, Gopka, Ul'yanov & Andrievskii 2008).

One of the first attempts to identify the lines of chemical elements in the spectrum of this star was made by Cowley et al. (1977). The authors were able to identify many lanthanide lines, but the identification of the lines of the iron-peak elements proved to be uncertain.

However, earlier Wegner & Petford (1974) derived the abundances in the Przybylski star from red spectra. They identified the lines of the iron-peak elements and found that the abundances of these elements are close to solar values, while the abundances of the rare-earth elements are increased by about five orders of magnitude.

A later detailed examination of the high-resolution *IUE* spectrum of this star in the 1900–3200 Å range confirmed the presence of the lines of the iron-peak ions: Ti, Cr, Mn, Fe (Wegner et al. 1983).

Cowley & Mathys (1998) analyzed CASPEC spectra in the visual range and confirmed the presence of the iron lines (mildly deficient iron abundance, of about – 1 dex compared to the solar value). They also found that the rare-earth elements are enhanced by about four orders of magnitude. This finding was confirmed later by Cowley et al. (2000). Cowley et al. (2004) also suggested the presence of radioactive Pm I, Pm II, Tc I, and possibly Tc II lines in the spectrum of this star.

Goriely (2007) attempted to explain the existence of radioactive elements such as Tc and Pm in the Przybylski's star atmosphere. This author proposed spallation mechanism of nucleosynthesis as a possible origin of the discussed chemical anomalies, but he does not specify the nature of the particles that could cause such nucleosynthesis.

Mkrtichian et al. (2008) found the following parameters of this star: M = 1.52 $M_\odot$, $T_{\rm eff}$ = 6622 K, L = 6.31 $L_\odot$. According to Mkrtichian et al. (2008), HD 101065 appears to be a prime candidate to possess a very long rotation period. Using the same effective temperature, Shulyak et al. (2010) derived the abundances of 52 chemical elements in this star. These authors found that the abundances of rare-earth elements are increased by about 3–4 orders of magnitude.

The original idea, which was aimed to explain the phenomenon of the Przybylski star, was first proposed by Gopka, Ul'yanov & Andrievsky (2008). (It should be noted that Martinez & Kurt 1990 having analyzed the photometric observations, concluded that the Przybylski star could be a binary system, but these authors suggested a brown dwarf as a companion). Gopka, Ul'yanov & Andrievsky (2008) supposed that this unique star is a binary star, whose companion is a neutron star. The high-energy processes occuring on the surface of the neutron star surface, may be responsible for the significantly increased abundance of heavy elements in the Przybylski star. For example, according to the authors' qualitative statement, a neutron star emits electron-positron pairs, and if they reach the Przybylski's star atmosphere, reactions occur at the stellar surface producing free neutrons and protons (a weak process). On the other hand, γ-quanta can produce some nuclear transformations. The authors considered the deceleration of the particles ejected by a neutron star in the electric field of the atomic nuclei in the gas of the stellar atmosphere. At the time, this very interesting idea was not properly elaborated, and unfortunately, it was not also properly considered and cited in the literature by specialist who have dealt with this problem.

This paper considers a modification of the above scenario, first proposed by Gopka, Ul'yanov & Andri-

evskii (2008). In our further consideration, only the basic hypothesis that the Przybylski star is a binary system containing a neutron star, will be retained. The observed properties of this unique star will be explained on the basis of this modified hypothesis.

2. The Przybylski Star is a Binary System

Following to Gopka, Ul'yanov & Andrievskii (2008), we assume that the Przybylski star is a component of the binary star, whose companion is a neutron star. The (many) lines in the spectrum of the Przybylski star are quite sharp, and we would be able to easily detect their periodic shifts with a time. Why cannot we detect the orbital motion (spectral line based) from the Przybylski's star spectrum? The simplest solution is that the orbits of the stars of this system lie in the plane of the sky (or very close to this plane). Thus, we see this star (and its companion) nearly polar-on, and this conclusion is also indirectly supported by the finding of Mkrtichian et al. (2008), who state that this star (in this sense) is a "slow rotator".

Nevertheless, such an assumption immedately raises another question: can we detect the proper motion anomaly of this star caused by a periodic change of its position in space? Przybylski star is located at the distance of about 100 pc from the Sun (*GR*3, *SIMBAD*). The most precise *GR*3 and *Hipparcos* astrometrical data from Kervella et al. (2019) do not show for this star the proper motion anomaly. These authors indicate the mass of this star of about 1.5 $M_\odot$ (see, also Mkrtichian et al. 2008). It is possible that both components have close masses, since a great majority of the neutron stars with well-defined masses have masses close to 1.5 $M_\odot$ (Stairs 2004). Despite the fact that the photocenter of the system can be offset to the Przybylski star ($L_{\rm NS}/L_{\rm PS}$ should be much less than 1), the comparable masses may hide the effect of changes in proper motion as a function of a time. It is also possible that the neutron star has a much smaller mass compared to the Przybylski star, therefore the proper motion of the Przybylski star appears to be undetectable (Valentim et al. 2011 show that the neutron star sample contains objects with masses less than 1 $M_\odot$).

A neutron star is a source of relativistic particles and radiation emitted from the certain parts of its surface. The topology of this radiation strongly depends on the the magnetic field configuration of the neutron star. In the literature, the following tradional pulsar high-energy emission models are discussed: the polar cap model, the slot gap and the outer gap model (see, e.g. Harding 2001, Harding 2009, Barnard 2021).

The first model assumes that high-energy electron-positron pairs and hard radiation are produced in the (magnetic) polar zones. Accelerated charge particles that move along magnetic lines emit electromagnetic quanta. In this model the radio-emission is genetically linked with the emission of the γ-quanta.

The model of the outer gap is based on the assumption that there is a vacuum gap in the outer magnetosphere of the neutron star, which arises due to the constant escape of charged particles through the light cylinder along the open magnetic field lines. In some particular cases, the direction of such escape may be roughly orthogonal to the rotation axis (see, for example, Hirotani 2013, Fig. 1, Brambilla et al. 2018, Figs. 14–15).

In contrast to the previously mentioned model, the outer gap model assumes that the γ-ray beam has a different spatial direction compared to the direction of the radio emission. Moreover, the outer gap γ-ray beam has a much larger solid angle compared to the radio-beam. The angle between the direction of the emitted photons and the open magnetic field lines could be quite large for not extremely high-energy particles (the angle is proportional to $(1-\beta^2)^{0.5}$, here $\beta = \frac{v}{c}$). If the rotation axes of the Przybylski star and the neutron star are close in direction (or even aligned), charged particles and hard radiation ejected in the approximately orthogonal direction at a large solid angle can enter the Przybylski's star atmosphere, causing there different physical processes.

The polar cap model with an angle between rotation and magnetic axes of about 90 degrees is not excepted either. Such an extreme case, when the magnetic dipole axis is orthogonal to the rotation axis in the neutron star was considered, for example, by Sturrock (1971). In this case, the Przybylski's star atmosphere may be exposed to radiation emitted in the polar cone.

Thus, in the cases considered above, the neutron star, in relation to the Przybylski star, is a γ-ray pulsar for it.

3. Free Neutron Source

To explain the high abundance of *s*-process elements in the atmosphere of this star, we must find a source of free termalized neutrons. Intuitively it is clear that such a source must be associated with the flux of high-energy particles and hard radiation emitted by the neutron star, which interact with the gas of the Przybylski's star atmosphere.

Here we propose as a possible source of the free neutrons the nuclear reactions between high-energy γ-quanta and nuclei of some atoms in the atmospheric gas. As a result, so-called *photoneutrons* can be generated. Large enough neutron flux can be produced in the reactions with quite abundant element. The best choice could be helium. Several years ago Tornow et al. (2012) considered photodisintegration cross-section of the reaction at the giants dipole resonance peak:

$$\gamma + {}^4\mathrm{He} = {}^3\mathrm{He} + n$$

Cross-section of this reaction has a maximum value for the γ-photons with energies of about 26 MeV. This energy is a boundary value between the energies characteristic of soft and hard γ-ray pulsars, and is regarded as the energy, which is typical for medium γ-ray pulsars (Kuiper & Hermsen 2015). Since the peak value of the cross-section of above reaction is about 2 Millibarn (Tornow et al. 2012), it is clear that γ-quanta have a quite large free path length in the star. Therefore they penetrate to a deep layers of the star (under the atmosphere), where the probability of reactions is much higher. (Short-scale) convection should then lift the reaction products into the atmosphere.

Other reactions with the rather abundant elements in the stellar atmosphere can also produce the free photoneutrons. For example, the following reaction has a giant dipole resonance at energy of about 20 MeV (Pywell et al. 1983):

$$\gamma + {}^{28}\mathrm{Si} = {}^{27}\mathrm{Si} + n$$

γ-quanta can be produced in the electron-positron interaction in the pulsar magnetosphere or in the Przybylski's star atmosphere in the interactions between positrons and local electrons. For this, the free positrons must reach the stellar surface.

The newly born free neutrons with energies of about MeV must be thermalized for reactions of *s*-process to occur. Neutron thermalisation can be quickly achieved by their collisions with atmospheric protons (hydrogen nuclei), since collisions with light nuclei take away a significant fraction of the energy of initially hot neutrons. For example, after one act of collision a neutron loses some part of its energy, which can be estimated by the following formula (Levin 1979; E_0 and E_1 are the initial energy and the final energy before and after one act of interaction, respectively):

$$E_1/E_0 = 1 - \epsilon/2,$$

$$\epsilon = \frac{4A}{(A+1)^2},$$

where A is the mass number of the nucleus. Numerical estimate gives a value of about 0.5 of the initial energy in one interaction. If the born photoneutrons have typical energies of 10–20 MeV, after about ten collisions with the nuclei of the most abundant element, they gain energies of the order of several KeV. For such resonant neutrons the absorption cross-sections of atomic seed nuclei, including nuclei of heavy elements, are high. Therefore, a large amount of *s*-process elements can be formed in the star. It is interesting to note, that the iron-peak elements, whose seed nuclei (iron, nickel, in particular), are also transformed into nuclei of heavier species in the *s*-process, do show a mild deficiency (about one order of magnitude) in the Przybylski's star atmosphere (Cowley et al. 1977, Cowley et al. 2000). It should be noted, that Shulyak et al. (2010) consider deficiency of Si, Ca, Fe, Ni, Ba as a result of the stratification in the stellar atmosphere.

Let us approximately estimate the flux of γ-quanta entering the Przybylski's star atmosphere. Since we do not know the specific characteristics of its hypothetical companion, it will be sufficient to use theoretical estimates of the target values. From the analytical outer gap solution, one can see that the typical pulsed γ-ray luminosities are in the range $10^{35} - 10^{36}$ erg s^{-1} (Hirotani 2013, Fig. 3). Another arbitrary value is the distance between components. For this value we will adopt 3×10^4 R$_\odot$, which is ten times larger than the distance between components of the close binary system (3×10^3 R$_\odot$, according to Tutukov & Yungelson 1993). In this case, the flux at the boundary of the Przybylski's star atmosphere should be about 10^4 γ-quanta per cm^2 s^{-1}. The ages of the soft-to-medium γ-ray pulsars does not exceed $10^5 - 10^6$ yrs (Kuiper & Hermsen 2015, Fig. 29). More than 10^{17} γ-quanta irradiating during this time each cm^2 of the stellar atmosphere perhaps may be able to produce a sufficient amount photoneutrons whose interaction with the seed nuclei is responsible for the Przybylski's star chemical peculiarity.

If the free electrons emitted by the pulsar magnetosphere manage to reach the stellar surface, an additional possible source of free neutrons can be activated:

$${}^N_Z A + e^- = {}^N_{Z-1} A + n + \nu$$

Another consequence of the high-energy material interaction with atmosphere gas is its inevitable local heating. As a result one can expect to detect the atoms in the ionization stages, which are not typical for the Przybylski's star effective temperature. Indeed, in several studies the detection of some ions in the second ionization stage was reported (like, Pr III, Nd III, Dy III, Er III, Th III, see, for example, Cowley et al. 2000).

The local atmosphere heating can also be responsible for the photometric variability of the Przybylski star with quite short period, which is not typical for the main-sequence star ($P \approx 12$ min, Kurtz 1978, Kurtz & Wegner 1979). A new period of oscillation (approximately 17 min) was discovered by Ofodum & Okeke (2016).

4. Time of Existence of Abundance Anomalies

Kuiper & Hermsen (2015) noted that soft γ-ray pulsars are all fast rotators and much younger than

high-energy γ-ray pulsars. How long can the abundance anomaly in the Przybylski star caused by the γ-ray pulsar persist? To estimate the time of the meridional circulation for mixing the surface and deep gas of the star, we use the formula from Sweet (1950):

$$t = 8 \times 10^{12} \frac{M^3}{LR^4} \frac{1}{\Omega^2} \quad \text{years}$$

Here all values are in solar units. The mass of the Przybylski star, as stated above, is 1.5 $M_\odot$, its radius and rotation velocity according to Kurtz (1980) are 1.3 $R_\odot$ and 17 km s^{-1}, respectively, and the luminosity of the star is about 6.3 $L_\odot$ (Mkrtichian et al. 2008). Thus, the characteristic time of the mixing process turns out to be high (comparable to the lifetime of the main sequence stage).

5. Concluding Remarks

Below I summarize the above discussion of the Przybylski's star chemical peculiarities. I emphasize that I propose only a hypothesis, which takes an additional step towards our understanding of this unique object.

1. The Przybylski star is a component of a binary star, the other component of which is a neutron stars. Both components have a similar mass of about 1.5 solar masses (it is also quite possible that the neutron star has a lower mass than the Przybylski star).

2. In this binary system, the orbits of its components lie in the plane of the sky (or quite close to it).

3. In relation to the Przybylski star, the neutron star is a *γ-ray pulsar* for it. The rotation axes of both components may be aligned or close to it. The γ-ray pulsar emits high-energy particles/photons toward the surface of the Przybylski star either approximately orthogonal to the rotation axis (magnetic axis is either aligned with ratational axis or tilted at some angle relative to it; outer gap model), or within the polar cone (magnetic axis is orthogonal to the rotation axis). Radiated high-energy particles and photons enter the atmosphere of the Przybylski star, causing various physical processes there.

4. The source of free neutrons is the nuclear reactions in the Przybylski star between the high-energy (MeV) γ-photons and nuclei of the abundant element helium. The photoneutrons produced in these reactions are rapidly thermalized and, as resonant neutrons, react with seed nuclei in the *s*-process.

5. Here we also note that together with *s*-process elements, the deuterium nuclei can be formed as a result of the interactions of the free thermalized neutrons with the hydrogen atoms. This issue will be discussed in the next paper.

Acknowledgements. SMA is grateful to the *Vector-Stiftung at Stuttgart, Germany*, for support within the program "2022–Immediate help for Ukrainian refugee scientists"under grants P2022-0063 and P2022-0064. Especial thanks to Prof. K. Werner and Dr. V. Suleimanov for their help with organizing his stay in the Institute of Astronomy and Astrophysics of the Tübingen University.

This research has made use of the *SIMBAD* database, operated at CDS, Strasbourg, France.

References

Barnard M.: 2021, *arXiv210310486*.
Brambilla G., Kalapotharakos C., Timokhin A.N., Harding A.K., Kazanas D.: 2018, *ApJ*, **858:81**, (14pp).
Cowley C.R., Cowley A.P., Aikman G.C.L., Crosswhite H.M.: 1977, *ApJ*, **216**, 37.
Cowley C.R., Mathys G.: 1998, *A&A*, **339**, 165.
Cowley C.R., Ryabchikova T., Kupka F., Bord D.J., Mathys G., Bidelman W.P.: 2000, *MNRAS*, **317**, 299.
Cowley C.R., Bidelman W.P., Hubrig S., Mathys G., Bord D.J.: 2004, *A&A.*, **419**, 1087.
Gopka V.F., Ul'yanov O.M., Andrievskii S.M.: 2008, *KPCB*, **24**, 36.
Goriely S.: 2007, *A&A*, **466**, 619.
Harding A.K.: 2001, *AIPCP*, **558**, 115.
Harding A.K.: 2009, *ASSL*, **357**, 521.
Kervella P., Arenou F., Migrand F., Thévevin F.: 2019, *A&A*, **623**, A72.
Kron G.E., Gordon K.C.: 1961, *PASP*, **73**, 267.
Kuiper L., Hermsen W.: 2015, *MNRAS*, **449**, 3827.
Kurtz, D.W.: 1978, *IBVS*, **No. 1436**.
Kurtz D.W.: 1980, *MNRAS*, **191**, 115.
Kurtz D., Wegner G.: 1979, *ApJ*, **232**, 510.
Levin V.E.: 1979, *Nuclear reactions and nuclear reactors, Moscow, Atomizdat (in Russian).*
Martinez P., Kurtz D.W.: 1990, *MNRAS*, **242**, 636.
Mkrtichian D., Hatzes A., Saio H., Shobbrook R.R.: 2008, *A&A*, **490**, 1109.
Ofodum C.N., Okeke P.N.: 2016, *NewA*, **43**, 42.
Przybylski A.: 1961, *Nature*, **No. 4766**, 739.
Pywell R.E., Berman B.L., Jyri J.W., Woodworth J.G., McNeill K.G., Thompson M.N.: 1983, *PhysRevC*, **27**, 960.
Shulyak D., Ryabchikova T., Kildiyarova R., Kochukhov O.: 2010, *A&A*, **520**, A88.
Stairs I.H.: 2004, *Sci*, **304**, 547.
Sturrock P.A.: 1971, *ApJ*, **164**, 529.
Sweet P.A.: 1950, *MNRAS*, **110**, 548.
Tornow W., Kelley J.H., Raut R., Rusev G., Tonchev A.P., Ahmed M.W, Crovell A.C., Stave S.C.: 2012, *PhysRew C85*, **061001 (R)**.
Tutukov A.V., Yungelson L.R.: 1993, *ARep*, **37**, 411.
Valentim R., Rangel E., Horvath J.E.: 2011, *MNRAS*, **414**, 1427.
Wegner G., Petford A.D.: 1974, *MNRAS*, **168**, 557.
Wegner G., Cummins D.J., Byrne P.B., Stickland D.J.: 1983, *ApJ*, **272**, 646.

DOI 10.18524/1810-4215.2022.35.268003

THE POSITRONE γ-SPECTROSCOPY OF SIMBIONIC SYSTEMS

D. N. Doikov

Odessa National Maritime University, Dep. of the Pre-Univ. Training and Dep. Mathematics, Physics and Astronomy, 34 Mechnikov str., Odessa, Ukraine
doikov@mail.bg

ABSTRACT. The γ-spectroscopy of rapid processes in space and Earth atmospheres we considered in this paper. One of considered object is AM Her types cataclysmic systems in soft γ-ray spectra. We calculated intensity of annihilation line who indicates the p-p thermonuclear explosions in a surface of the White Dwarfs (therefore WD). In the presented results we used, that the p-p detonation in degenerate plasma produce positrons. We confirmed that the formed annihilation γ-quants with energy 0.511 MeV is the suitable diagnostic possibility to study the effectiveness of thermonuclear reaction channels during such explosions. Presented application for registration of annihilation quanta shows that in case of AM Her stars system in detectors panel enter flows of the annihilation γ-quants with upper limit 177 $cm^{-1}sec^{-1}$. I noted, that times scale of detonation and γ-flyers are in intervals from 10^{-4} to 10^{-3}sec. These results show the reason for the lack of registration of γ-flares in other types of cataclysmic variables. For example, in this paper considered systems with classical accretion disks named how Periodical Novae. Because these explosion is rare and have specific in geometrical and physical conditions for him monitoring with other strategy of observation. In Earth atmosphere tame scale of formation of secondary positrons is same. We showed, that annihilation of positrons occurs in near Earth surface zone. In this case observatories based in height reaching 2000 and more meters are important, it is advisable to planning the placement of this kind of equipment. It is confirmed, that presented perovskite detectors have the necessary sensitivity and universal spectral sensitivity and the study and modeling of interaction processes allows you to set the operating modes of the interfaces in the monitoring modes of observations. In presented paper has been confirmed, that perovskite materials in form of binary detectors enables simultaneous observations of hard radiation and optical quanta. In this cases observation of CR, micro meteors and other rapid objects in Earth atmosphere greatly expands the possibilities of their study.

Keywords: γ-spectra, p-p explosions in degenerate plasma, rapid γ-flayers, positrons annihilation, White Dwarfs.

АНОТАЦІЯ. Гамма-спектроскопія швидких процесів в атмосферах Землі та Космосу є предметом запропонованої роботі. Розглянуто спектри катаклізмічних системи типу AM Her у м'яких γ-променях. Розраховано інтенсивність потоку квантів які формують анігіляційну лінію, яка вказує на p-p термоядерні вибухи на поверхні білих карликів. По представленим результатам було отримано що фізичні умови детонації у виродженій плазмі доводять до виробки позитронів. Ми підтвердили, що утворені анігіляційні γ-кванти з енергією 0,511 МеВ є придатною діагностичною можливістю для дослідження ефективності каналів термоядерної реакції під час таких вибухів. Вказано на можливість реєстрації анігіляційних γ-квантів від зірок типу AM Her, періодичних і класичних нових. У разі відмічених явищ на панель детекторів потрапляють монохроматичні потоки γ-квантів – продуктів від термоядерних ланцюгів P – P-циклу. Отримано, що верхньою межею потоку від катаклізмові системи AM Her є 177 квантів на $см^{-2}сек^{-1}$. Шкала часу детонації та γ-спалахів знаходиться в інтервалах від 10^{-4} до 10^{-3} сек. Ці результати показують чому зменшується імовірність реєстрації γ-спалахів в інших типах симбіотичних систем. Для поширення кількості об'єктів також розглядалися катаклізмічні системи з класичною дисковою акрецією, які викликають таке явище, як Періодичні Нові. Оскільки ці вибухи є рідкісними і мають специфічні геометричні та фізичні умови для їх моніторингу достатньо розглядати вже відоме сферичне наближення. Це спрощує стратегію спостереження і інтерпретацію отриманих γ-спектрів.

В земній атмосфері ручний масштаб руху космічних позитронів такий самий. У роботі показано, що на першому кроці доцільно спостерігати анігіляцію позитронів в приземній зоні. У цьому випадку в обсерваторіях, розташованих на висоті 2000 і більше метрів, доцільно планувати розміщення такого обладнання для реєстрації позитронів вторинного походження та їх анігіляцію. Підкреслено, що представлені пероксидові детектори мають необхідну універсальну спектральну чутливість на жорстке випромінювання, а дослідження та моделювання процесів взаємодії дозволяє задавати режими роботи інтерфейсів у моніторингових режимах спостережень. Ми отримали, що конструкція таких детекторів у вигляді бінарних девайсів дозволяє одночасно спостерігати жорстке випромінювання та оптичні кванти. У цьому випадку спостереження космічного випромінювання, мікрометеорів та інших швидких об'єктів в атмосфері Землі значно розширює можливості їх вивчення.

Ключові слова: γ-спектри, p-p-вибухи у виродженій плазмі, швидкі γ-спалахи, анігіляція позитронів, білі карлики.

1. Introduction

The registration of the γ-flayers in soft energetic region is actual interdisciplinary problem. For detection of this physical processes are having been developed new generation of the detector of hard radiation in base of perovskite crystal. One of them is CsPbBr3. Him mean atomic mass is 57.3 a.m. Under such conditions, it becomes possible to detect flares in a wide energy range. That is, a constructive possibility has arisen for the simultaneous detection of radiation from an object of interest to us practically from optics to the soft γ-range. In practice, the upper energy limit is limited by the physical thickness of the semiconductor crystal. The accuracy of registration of γ-quanta under such conditions makes it possible to construct profiles of γ-lines with an accuracy of 10 KeV. Progress in the growth of perovskite crystals (in our case CsPbBr3), in particular, an increase in the number of semiconductor layers, makes it possible to increase the accuracy of registration of γ-ray fluxes (Piro, 2012) and to build detailed spectral line profiles. The use of such detectors requires model measurements and model calculations of characteristic fluxes of the hard radiation. This is used as the basis for planning of monitoring of the observations of cosmic and atmospheric flyers of hard radiation. In this paper are presented calculations of possible γ-flares before registering of a sharp increasing of the intensity of optical radiation from cataclysmic variables. The main physical information about γ-ray spectra information from p-p detonation consisting in interval from 0.1 to 10 MeV. In X- and UV- emissions, we have the consequences of the movement of shock waves after near surface detonation in a magnetic column and an accretion disk. The registration of such spectra is more accessible, but it is also determined by a large number of parameters of the cataclysmic system. From γ-ray spectra we have possibility to more adequate investigation of the detonation structure because positrons generated only in one part of the thermonuclear p-p chain. This paper consists Abstract, Introduction, three section, Conclusion and Discussion. In first section we considered physical condition in surface of the WD in cataclysmic systems, bound conditions of the bottom part of the magnetic column in near surface layers. The second section is devoted to the calculation of hydrogen detonation and its consequences. In third section presented synthetic γ-ray spectra of the Cataclysmic systems in hard magnetic fields.

2. Physical conditions in near surface layers of the WD

The surface of the AM Her type WD in bottom part magnetic column consist a hot spot of dense degenerate plasma. The hydrogen-helium (therefore H-He) accretion flows from a star-companion in the bottom part accelerated by the gravitational field up to 10-20 km/sec. This ensures that the temperature of the near-surface layer rises to 10^8K and form hot spot. The H-He mass accumulation due within a few months. The mass loss from star-companion from optical observation has been estimated from ( ) and in bottom limit has $\dot{M} = 10^{-11} M_\odot$ or $M_{det} = 10^{18} - 10^{19}$ kg. Full number of the H and He atoms is N_{at} who took part in p-p chain reactions is $N_{at} \approx 10^{44} - 10^{45}$. From polarimetry of the AM Her the strength of magnetic field is $10^6 - 10^7 H$. The simplified model of the WD atmospheres presented in (). The given physical data allow us to conclude that at a certain moment of reaching the critical mass H - He of the mixture leads to its detonation. The radius of the magnetic column bottom $R_{bot} \approx 400\ km$. We have, that full pre exploding accreted mass in cylinder with R_{bot} and height $H_{cyl} \approx 20 - 30\ m$.

2.1. The detonation near surface of the WD

In next section we will consider two approaches of the detonation. This is point and cylindrical cases. For astrophysics application we can return to classical picture of the AM Her system. Relation between surfaces of the spot to full surface of the WD is $1.3 \cdot 10^{-2}$. In first approach this is point explosion on the surface of the WD. The velocity of the detonation fronts in degenerate zone is a relativistic. Than time scale of full detonation times is $t_{det} \approx 10^{-3}$ sec. Next step consists testing of Sedov approach with Zeldovich & Raiser correction. To do this, it is necessary to require that the distribution of the thermodynamic parameters of the atmosphere of a WD has a power law. In our case we have hydrostatic atmosphere, but in more deep layers' pressure depends from concentration in the relation $P \propto n^{2/3}$. During the accumulation of the heat from thermonuclear p-p reaction in the upper atmosphere, plasma degeneracy is removed faster than in more deep layers of WD. After this removing begins explosion in form of detonation. In inside part of the column removing of the degeneracy is very possibly relatively other type of symbiotic systems. The time interval between begining of the sharp ignition inside the column is very short. All this argument leads to the substantiation of the use of the Sedov approximation for a point explosion.

3. The point detonation inside magnetic column

In the lust paper (Doikov &Yuschenko, 2021) hase been used only the part of classical p-p reaction in the form important for γ-ray production:

$$p + p \rightarrow d + \boldsymbol{e}^+ + \nu_e \rightarrow d + p \rightarrow {}^3_2He + \gamma(5.49\ MeV)$$
$${}^3_2He + {}^3_2He \rightarrow {}^4_2He + 2p\ (12.86\ MeV) \rightarrow (25.7\ MeV) \quad (1)$$

The full number of positrons $N_{e^+}$and γ-quants from annihilation N_γ is: $N_{e^+} \approx N_\gamma \approx 10^{44} - 10^{45}$. Let D is velocity of the detonation front, than from [] depends from the specific internal and nuclear energy (J/kg)

$$D = \sqrt{2Q(\gamma^2 - 1)} \quad (2)$$

Where Q is the specific internal and nuclear energy (J/kg). The caloric content of such a chain is maximum for all possible reaction channels is near 26 MeV. Even such simple calculations show the relativistic nature of the propagation of detonation fronts. Next, based on the simplicity of the model, we calculate the radiation characteristics of the explosion in the γ-rays. The emissivity the γ-quants after annihilation between electrons and positrons depends from balance of the reaction rates of positron production

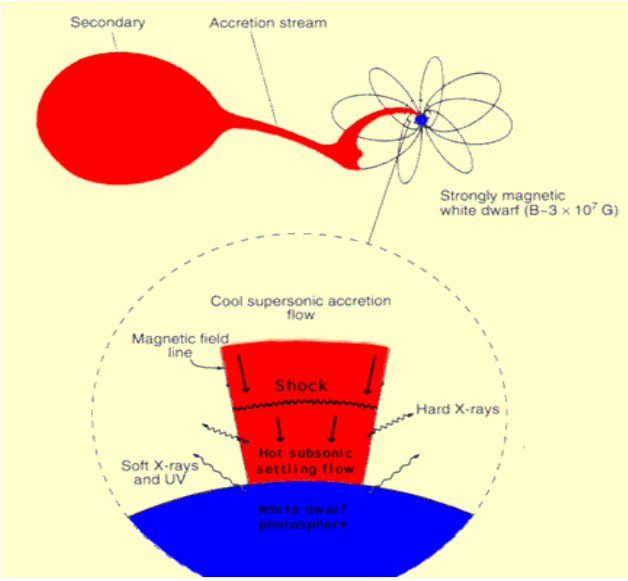

Figure 1: The classical picture of the AM Her polars type binary system (picture has been rewrites from popular internet resource).

and annihilation rates. Confirm that the correspondent γ-quants have energy $E_\gamma = 5.49 MeV$ and him relative intensity I(5.49 MeV) to intensity of annihilation quants I(0.511 MeV) is the foundation of the positron spectroscopy. From section 2.1 we have that the time of the point explosion in the bottom of the magnetic columns of the WD surface has maximum time $t_{det} \approx 10^{-3} sec$. Only in periods of the considered γ-flyers with $E_\gamma = 5.49 MeV$ we have possibility of independent diagnostics of the positron evolution in space and time. We begin from geometric of the point explosion in detonation H-He mixture. In contrast with other type Novae in bottom part of magnetic column the mixing with the lower layers adjacent to the helium zone cannot be expect. Then in combustion layers we expect only annihilation line 0.511 MeV and accompanied him γ-quant.

3.1. The geometric configuration

For the determine of the fronts in a relativistic shock waves after point explosion in WD it is necessary to specify the structure of the distribution of the gravitational potential with the height of the white dwarf atmosphere. In the first step we estimated boundary conditions for next solving of the transfer energy equation for γ-quanta who formed as a result of P-P reaction. It should be noted that the front of the shock wave, even at the initial moment of the explosion, exceeds at least 10% compared to the front of expansion of the substance. This phenomenon makes it possible to consider the transfer of γ-quanta in matter during its expansion into vacuum. In this case the gravity acceleration is $g \approx (10^7 - 10^8)\, m/s^2$ and maximum vertical height $H_{max} \approx 10^7$m. Initial velocity for unit mass fragments of the WD near surface atmospheres is $V_{atm} \approx (10^7 - 10^8) m/s$. The second cosmic velocity $V_{II} \approx 10^7$m/s and final density is $\rho \approx 10^{-4} kg/m^3$ or numerical density is $n \approx 10^{21} - 10^{22} m^{-3}$. For next calculation we can use this boundary conditions.

3.2. Radiation during explosion

The energy deposition of γ-rays, and the subsequent thermalization of the no thermal electrons are considered in (Cosma & Fransson, 1992) presented estimation for cross section:

$$\sigma_\gamma = A_i m_p k_\gamma \approx 2.3 \cdot 10^{-29} m^2 \quad (3)$$

For $A_i = 1.2$ the optical depth τ_γ for γ-rays allows to determine the thickness of the layer that is already transparent to the considered hard radiation. This depth H we can get from formula:

$$\tau_\gamma = n \sigma_\gamma H \quad (4)$$

For first approach $\tau_\gamma = 1$. Than

$$H = \frac{1}{n\sigma_\gamma} \approx 10^7\ m \quad (5)$$

The result obtained leads to the conclusion that 10^{-4} seconds after the explosion, the part of explosive shell is already transparent to γ-rays. It should be noted that the fraction of γ-quanta that exited the transparent part of the explosive shell is sensitive to the ratio of hydrogen and helium content. We think that with the noted set of physical parameters, the share of shells cut out reaches 20% of the total amount of γ-quanta with energies of 0.511 and 5.49 MeV. For the AM Her this flow is no more of 60-80 quantum for each energy in the time interval t_{det}.

4. P-P-detonation and reaction kinetics

The P-P reaction kinetics are investigated more 80-th years. In present time we have semi empirical formulae for P-P reaction rates links, presented in (1) in form (Leng 1978, pp107-118) and (formula 4.47 p.61), Table 42. p. 108 with coefficients $C_i, i = 1{,}5$). We used only nonzero coefficients. In this cases for the reactions speed we has:

$$N_A\langle\sigma v\rangle = C_1 T_9^{-2/3} exp\left[-C_2 T_9^{-1/3} - \left(\frac{T_*}{T_0}\right)^2\right] \text{ x}$$
$$\left(1 + C_3 T_9^{1/3} + C_4 T_9^{2/3} + C_5 T_9\right) \left(\frac{cm^3/sec}{g-mol}\right) \quad (6)$$

where $N_A = 6.022 \cdot 10^{23}$ atoms is the Avogadro number, $\langle\sigma v\rangle$ is reaction rate cross sections. This formula shows number of reacted atoms in unit volume who consists 1 gram-moll per 1 sec. T_0 is temperature, who formally correspondent to the Gamov resonance energy G. For considered thermonuclear reactions we received this energy from formula:

$$G = 2\pi^2 m_{ab} e_a^2 e_b^2 / h^2 \approx 3{,}96 \cdot 10^{-10} erg \quad (7)$$

then $T_0 \approx 2{,}48 \cdot 10^7 K$.The presented information in Fig. 2 shows that reaction rate cross sections $N_A\langle\sigma v\rangle$ depends from initial concentration of the plasma components in pre detonation time. In Bear & Soker (2016) considered possibilities the detonation of the He components, and after this indignation of the hydrogen layers. From this scenario it becomes clear that the energy of the explosion is limited not only

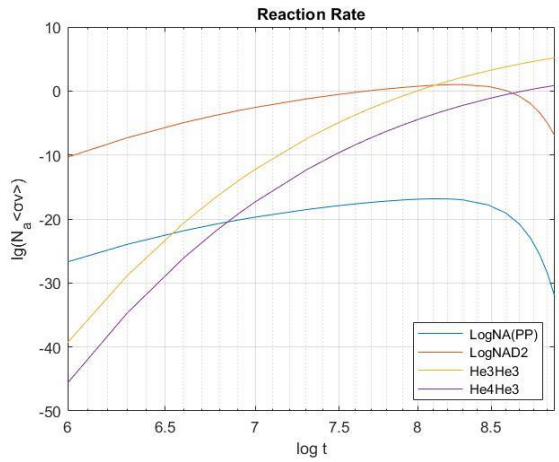

Figure 2: The reaction rates of the P-P reaction links.

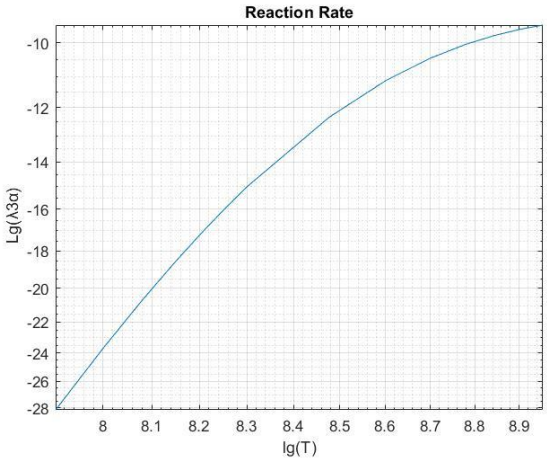

Figure 3: Time scale for 3 α reactions. The λ3α in years. T in Kelvin.

by the amount of hydrogen, but by the presence of conditions for removing plasma degeneracy. In case of AM Her type stars H-He plasma accelerated to (10-20) km/sec in fields of hard gravitation potential. In this case, the large mass of the H-He mixture are localized at the base of the magnetic column. The thermalization of the incident directed plasma flow leads to an increase in the temperature of the H-He layer. To answer of the question about detonation, it is necessary to take into account the results presented in Fig. 3 on the rate of thermonuclear reactions, taking into account helium and hydrogen isotopes and correspondent P-P and He links. We emphasize that helium plays the role of detonator, because the densities of the WD atmospheres and the temperatures of the bases of the magnetic columns lead to the considered explosive. The time of complete burnup $\lambda_{3\alpha}$ of helium in the H-He mixture as a result of the 3α-process (Leng, 1978) :

$$3He^4 \rightarrow C^{12} + \gamma + 7{,}274\ MeV \qquad (8)$$

is calculated by the semi-empirical formula:

$$\lambda_{3\alpha} = 9.36 \cdot 10^{-10}(\rho X_a)T_9^{-3}\exp(-\tfrac{4.411}{T_9}) \qquad (9)$$

This formula is valid in the temperature range who showed in Fig. 2. The diagnostic importance of positron for spectroscopy in astrophysics is considered of connection with reactions of thermonuclear transformations. His always based an unambiguous correlation between the appearance of a positron and the emission of a γ-quantum of a certain energy. The γ-detector register at the same time, quanta of annihilation origin with an energy of 0.511 MeV, but also precisely defined γ-quants of these reactions. In this case, the unambiguity of the discussed results is high.

5. Symbiotic system with accretion disk

Consistence of the accretion disk around WD with hydrogen leads to the fact that after the accumulation of a critical mass of hydrogen, the H-He mixture explodes in the all near surface zone. The spherical geometry of the explosion leads to lower event frequency. In this case full mass of the exploded H-He layer is much bigger. The positrons arise when available formation of the nonstable isotopes with proton exec ^{13}N, ^{18}F, ^{7}Be, ^{22}Na (Shing-Chi&, Thomas, 2022), (Wynn. Abigail at al 2002) In Table 1 is showed accompany γ-quants for considered elements.

Table 1: Synthesis of elements necessary for the production of positrons at energies not greater than 20 MeV.

N/N	Radioactive decay	E_γ KeV
1	$^{13}_{7}N \rightarrow {}^{13}_{6}\mathrm{C} + e^+ + \cdots$	1199
2	$^{15}_{8}O \rightarrow {}^{15}_{7}N + e^+ + \cdots$	1732
3	$^{17}_{9}F \rightarrow {}^{17}_{8}O + e^+ + \cdots$	475
4	$^{11}_{6}C \rightarrow {}^{11}_{5}B + e^+ \ldots$	

In the explosion of classical Novae, the high luminosity in the soft γ range is maintained solely by the decays of the proton-excess radioactive isotopes indicated. This means that in addition to the resulting positrons, an accompanying γ line also arises. The description of the explosion of the near-surface layer of the classical Novae fits into the spherically symmetric approximation similar to the explosion of the Super Nova (SN), but with different boundary conditions. In all the above models has been considered only that allow us to prove the high probability of expansion in outer circumstellar space of γ-quants accompanying the decay. This circumstance is important for the application of positron spectroscopy to this type of objects, highlighting the diagnostic criteria for γ-quanta accompanying the production of positrons during explosive thermonuclear combustion. The optical and γ-flayers are more power and sufficient long in time for observation in relation to AM Her type star systems. However, such events are quite rare in the vicinity of the solar system compared to flares at the polar. If we observe classical novae at a sufficient distance from the terrestrial observer, then its classification is noticeably simplified when γ-quanta emanating from it are detected.

5.1. Positron diagnostics of the accretion disc

In present time during in the AM Her, classic and recurrent Novae explosions no registries γ-flyers. The main reason for this is the time scale of detonation processes that cause explosions. All other intervals of the spectrum of the symbiotic system shine significantly at long times. In optics, the time of an optical flash is near week. The powerful shock waves create an ionization front and destroy accretion disk. The motion of positrons in a plasma differs from their interaction in a neutral gas in that. Positrons travel much longer distances in a strongly ionized gas due to the fact that the annihilation of a positron with an electron occurs only when it is thermalized. The motion of positrons with a plasma differs from their interaction with a neutral gas in that the positrons travel much longer distances in a strongly ionized gas. The reason for this phenomenon is the annihilation of a positron with an electron when both are thermalized. Deceleration and scattering of a positron in a cold accreting gas is more efficient. The probability of positrons transition into the space surrounding the WD is determined by the cross section of annihilation with an electron and ionization energy losses in the substance. In considered physical conditions the cross sections change from $10^{-27}cm^2$ detonation point to $10^{-16}cm^2$ in final points. The pass length for positrons and electrons is same in this condition and determine from:

$$\frac{dE}{dx} = -2{,}54 \cdot 10^{-19} Z^2 N(3ln\gamma + 20{,}2)\ (Ev/cm) \quad (10)$$

Substituting the characteristic parameters of the atmospheres of white dwarfs and their accretion disks, we can draw the following conclusion. Positrons can enter the accretion disk only from the uppermost layers. Getting into the accretion disk, positrons interact with plasma throughout the entire region of its localization. For the commonly accepted densities of the matter of the accretion disk, the ratio 10 shows that the ionization losses of positrons are such that if they leave the near-surface layers of the white dwarf, they will be detected from the presence along the entire accreting region.

6. The Earth atmosphere

The structure of the Earth atmosphere. The structure of the Earth's atmosphere in the first approximation can be given in the form of a barometric formula. In this case, the change in gas concentration with height is given by the following distribution:

$$N = N_0 \exp(-{}^{\mu g H}/_{RT}) \quad (11)$$

where N_0 – is number densities of molecules at sea level. H – atmospheric height relatively this level, μ – is a mean molar mass, T – is atmospheric level temperature, R-ideal gas constant. Substitution of this physical parameters lead to values of free pass length of γ-quants are varied between 1600 - 2000 m. The characteristic times of motion of charged particles through the considered layers are $10^{-6} - 10^{-5}$ sec. The real relaxation time of the heavy elements semiconductor have relaxation time near 10^{-6} sec. In this case we consider it acceptable to use them in the problems under consideration.

In contrast to astrophysical applications, the presence of different types of aerosols should be taken into account in the formation of annihilation lines in the earth's atmosphere. Aerosols often form clouds and other heterogeneous structures. All these circumstances affect the formation of the final annihilation line to a different extent. On the other hand, measurements of positron fluxes of solar and galactic origin show their excess in comparison with the expected calculations.

7. Discussion

The study of the thermonuclear processes in astrophysical and Tokamak plasma demands new generation of spectrometers of the hard radiation. In order for their diagnostics to be accurate with respect to the physical parameters of the system and to have a correct spatial distribution, it was necessary to develop new spectroscopy methods. Before the development of the corresponding equipment, it was necessary to understand in what time intervals and at what characteristic energy flows the terrestrial observer or satellite would receive the required information. Another important reason for the research disclosed in this paper was to determine the reason for the absence of γ-bursts for fast thermonuclear processes. The author came to the conclusion that calorimetric reassures of the explosions near WD surface can only be attributed to fast thermonuclear processes. For registration and further studies of possible γ-flares, binary or, even better, multichannel detectors in the γ- and optical ranges are needed. Such a choice of the observation technique makes it possible to record not only the fact of a γ-flare, but also the relationship of this event with the physical conditions both on the surface of the WD and in the magnetic column or the surrounding accretion disk. To register the described events, monitoring observations are required. The technical aspects of this monitoring are discussed in (Doikov M., 2022).

Technical requirements for monitoring equipment. Let's consider the list of physical parameters necessary for solving the problem of monitoring, registration and accumulation of spectroscopic information about γ-flares in cataclysmic systems These is flyers time τ_{fl}. In this paper we confirmed that $\tau_{fl} \approx \tau_{det} \approx 10^{-3} sec$, Upper level of the γ-flows is 170 quants per 1 cm^2 for each energy 0.511 and 5,672 MeV during in full flyers period for AM Her. Therefore, the relaxation times of the elementary pixel of the recording grating is no more 10^{-5} sec. In paper (Doikov M., 2022; Liu, Wu, Wei at all, 2022) discussed detectors, who consists heavy elements. These devices are relevant to the considered spectral properties during the thermonuclear explosions.

The many fast processes with a powerful energy emission are of nuclear origin. The main indicator of these processes is the presence of characteristic γ-lines. Many of these lines lie in the soft γ and hard X-ray ranges. Predict and prepare systematic observations of space and atmospheric objects considered in the article.

To achieve the set goals, it was necessary to develop and, in some cases, adapt the codes serving the new generation

detectors – peroxides. In our case this is semiconductor CsPbBa3. One of them crystal is many layer sandwich who work how spectrometer. In more deep layer we fix more energetic γ-quants. In combination with optic peroxide we have dual detector. In present work we calculated intervals of energies and times for using of this peroxide detector.

The nuclear processes in Earth atmosphere caused by cosmic rays (CR) who detects by peroxides consists γ-spectrum and ionizations traces together. Thus, the use of this type of crystals is one of the most promising areas of instrumental support for spectral studies.

Interaction between supersonic solar winds and meteors flows shows spectra only in optic- and middle IR-spectra from dusty plasma can be registered by a new generation of peroxide detectors.

8. Conclussions

The positron spectroscopy of γ-flayer in Symbiotic system is unique method of differentiation and determining the role of the corresponding reaction channels during transient explosions. Despite the transience and irregularity, the processes under consideration provide valuable information about the physical conditions in the atmospheres of white dwarfs that are part of Symbiotic system.

It has been shown that at the base of magnetic columns, based on the available data, there is a high probability of positron formation and the subsequent formation of annihilation lines. Together with the γ-quanta accompanying the formation of positrons.

The escape of positrons into the surrounding space makes it possible to expand the time frame for observing annihilation lines formed by the interaction of positrons with electrons of the substance of the accretion disk.

It has been found that the simultaneous measurement of γ-lines accompanying different chains of reactions leads to the selection of the most probable thermonuclear reactions.

References

Bear E., Soker N.: 2016, *RAA*, **16**, 114.

Doikov D.N.,Yuschenko A.V.: 2021, *Odessa Astron. Publ.*, **34**, 40.

Doikov M.D.: 2022, *Odessa Astron. Publ.*, **35**, in press.

Fangze L., Rong W., Jing W., Wanyi N. et al.: 2022, *ACS Energy Letters*, **7 (3)**, 1066-1085.

Kozma C., Fransson C.: 1992, *Ap.J.*, **390**, 602.

Lang K.R.: 1978, *Astrophysical Formulae*, Springer Verlag, **2**, 107 (in Russian).

Piro A.L.: 2012, *Ap. J.*, **759**, 83.

Shing-Chi L., Thomas S.: 2022, *Astro-ph ArXive*, 2112. 06893.

Wynn J.-G., Abigail V.P. et al.: 2020, *Ap.J.*, **896**, 165.

DOI 10.18524/1810-4215.2022.35.268000

DUAL HARD AND OPTICAL RADIATION DETECTORS FOR FAST NUCLEAR PROCESSES

Marko Doikov

Plovdiv University "Paisii Hilendarski", Faculty of Physics and Engineering Technology, Tzar Asen str., 4000 Plovdiv, Bulgaria, *marik.doikov@gmail.com*

ABSTRACT**.** The registration and monitoring of rapid nuclear processes in degenerate plasma is a field of our consideration. The flows of hard and optic radiation are considered from outlying astrophysical and atmospheric objects. For their detecting it was suggested to use dual semiconductor type detectors. Simultaneous flow measurements allow obtaining high-precision positions and spectral properties of the objects under study. Due to the high energies of hard radiation and the nature of the nuclear processes, it is shown that the probability of their detection is high. In this case, the detector does not enter in saturation mode. At the other part of this detector optical matrix and reflection mirror are located. It is determined that the characteristics of useful signals are considered for the same instrumental function.

Keywords: semiconductor detectors, hard and optic radiation detection, fast nuclear processes, γ-ray's registration.

АНОТАЦІЯ. Реєстрація та моніторинг швидких ядерних процесів у виродженій плазмі є предметом досліджень. Розглядається рівень та структура потоків жорсткого та оптичного випромінювання від віддалених астрофізичних та атмосферних об'єктів в яких відбуваються вибухи. Для детектування таких випромінювань було запропоновано використовувати здвоєні детектори напівпровідникового типу. Показано конструктивні переваги бінарних детекторів нового типу.

Запропоновано новий метод дослідження симбіотичних бінарних систем, в яких лунають термоядерні вибухи на поверхні білого карлика. Зроблено висновки про структуру інтерфейсу, необхідного для функціонування бінарного детектора та його калібрування. Одночасні вимірювання потоку дозволяють отримати високоточні положення та спектральні властивості досліджуваних об'єктів. Завдяки високим енергіям жорсткого випромінювання та характеру ядерних процесів показано, що ймовірність їх виявлення висока у разі виконання критеріїв моніторингу.

Отримано, що зазначені критерії моніторингу дозволяють відповідати фізичним умовам и динаміки явищ ядерних перетворень в космосі і в атмосфері Землі. У цьому випадку детектор не переходить в режим насичення і фізична інформація не втрачається. В іншій частині цього детектора розташована оптична матриця і відбивне дзеркало. Визначено, що характеристики корисних сигналів розглядаються для однієї інструментальної функції. Щоб уникнути перенавантаження інтерфейсу детектора зроблено не тільки підбір швидкодіючих мікропроцесорів, а і кодів для відсіву непотрібних фонових даних. Для формування потрібного сигналу необхідно, щоб на мікропроцесор входили сигнали з інтервалом часу 10^{-4} секунди. Отримано, що для системи АМ Her протягом року необхідна кількість вимірювань протягом року складає $4 \cdot 10^{13}$ для матриці 20x20 cells.

Ключові слова: напівпровідникові детектори, детектування жорсткого та оптичного випромінювань, швидкі ядерні процеси, реєстрація γ-променів.

1. Introduction

Simultaneous registration of fast processes in the energy range of hard radiation using semiconductor detectors I limited by energies of 0.1 – 10 MeV for γ-rays and 0.1 - 4 eV for optical ones. The current pulse generated by the quanta of these two energy ranges is formed due to the phenomenon of the internal photoelectric effect, which allows electrons to overcome the band gap of the semiconductor. The part of the detector that faces directly at the source of hard radiation consists of a grown semiconductor crystal containing atoms of heavy elements. Heavy atoms of the indicated semiconductor interact with the γ-quantum included in it according to the following most probable scheme. The γ-quants are interacting with the K-electron, less often with the L-electron the energy of the ejected K-(or L-, M-) electrons correspond on average to the energy of its binding to the nucleus. That is, the energy interval is limited to 8-14 KeV for elements heavier than iron. The formed chain of consecutive vacancies should be filled with superior 2p-electrons from the L-level or 3d-electrons of the M-level, with the transit passage of the p-electron vacation of the L-level. In the atoms of heavy elements, in addition to the removal of strong excitation in the form of marked radiative transitions. However, a transfer of part of the excitation energy to higher-standing electrons which freely leave the band gap is observed with a high probability. Such electrons are called Auger electrons. In ideal cases, one γ-quant generates $10^6 - 10^8$ conduction electrons (n-charge) and same positive dots on average. The second section is devoted to more accurate calculations of the energy distribution of current pulses. In the third section, we studied interactions between γ-quanta's and optic matrix and relaxation time of optics

quanta flows. In forth section we presented breadboard installation, where the binary detector is located. The conclusions are devoted to the studied physical objects in which fast processes occur. We carried out a modular experiment with the aim of the subsequent development and manufacture of a new generation of binary detectors that record rare events of a nuclear nature in Fig.1.

2. Physical aspects of hard radiation ilumination of the semiconducotrs

New material together with nanotechnology application is a modern effort in the higher precision γ-ray spectroscopy. This made it possible to create and model complex spatial images of radiating and absorbing biological and physical objects. Our attention will be focused on thermonuclear explosions during that simultaneously formed optical and γ-quanta in a partially degenerate dense plasma. In this case γ-quanta with energies of 0.1–10 MeV are illuminated. For detecting γ-radiation, detectors must meet several general requirements. First, they must have a high atomic number in order to provide a high cross section of γ-quanta; second, they must have high radiation and hardness. Third, γ-rays can undergo four different processes when they enter into the detector. However, because (Gould, 1980,1990) we do not consider Rayleigh (coherent), Compton scattering and pair formation in this energy range. Mainly, declared processes take place for photoionization. In next section, we will present numerical results from Auger effect electron production after formation of the K-L-dots.

3. Electron prodution in the semiconductor peroxite

The recent work dedicated to halide perovskites (Liu, Wu, Wei et al., 2022), confirmed that their crystals have superior advantages over other types of hard radiation detectors. The accurate calculation of the Auger electrons production for elements before Ni are presented in (Kaastra & Meve, 1973), (Doikov & Khrapatyi, 2020). In present paper, I used only common physical principals and experimental data for Auger electron production from for elements after Ni in periodic elements table. The subjects of investigation are halide perovskites crystals which are easy to grow and have important electro physical properties suitable for their advantageous use in the planning of our experiments. The technology of growing CsPbBr3, CsPbCl3, Cs2AgBiBr6, Cs3Bi2I9, Cs3Bi2I3 is presented in (Liu, Wu, Wei et al., 2022). For the monitoring rapidly changing glow of hard radiation, the most convenient are crystals CsPbBr3. In present paper, we considered the spectrum of Auger electrons produced by each of next elements: Cs, Pb, Br. After formation of the K-, L- or M-dot from incident on the atom γ-quantum a redistribution of the stored energy of a strongly ionized state has been observed. The main part of the Auger electrons in detectors crystals in a narrow energy range. Every Auger electron with energies, presented in the second column, forms secondary ionization for this semiconductor. In the third column the derivation dN/dE is the gradient coefficient for the distribution function N(E) of the Auger electrons. NF(E) are full number of the electrons – dot pairs. The

Table 1: Distribution of the Auger electrons in CsPbBr3

Atom	**Halide Perovskites Crystal CsPbBr3**		
	Energy of Auger electrons E (in eV) from single atoms	**dN/dE**	**NF(E)**
Cs (55)	47, 407, 420, 479 , 491, 583, 575, 620, 636, 650	0.57	10^6
Pb (82)	60, 90, 117, 130, 159, 181, 204, 249, 267, 389, 412, 458, 475, 693, 1160, 1286, 1407, 1431, 1488, 1617, 1637, 1717, 1910, 1987, 2048, 2186, 2283, 2319	0.71	10^7
Br (35)	56, 102, 108, 1172, 1210, 1270, 1285, 1318, 1396, 1442, 1479	0.71	10^5

presence of Auger spectra of the marked atoms makes it possible to obtain the distribution of secondary electrons, which actually cause the internal photoelectric effect of the semiconductor. I considered redistribution is after internal atomic photo effect due from γ-quants in halide perovskites crystal CsPbBr3 (Table 1).

No more than the half of ionization energy transforms in Auger kinetic energy for atomic numbers $4 < Z < 30$ (Kaastra & Meve, 1973). In other part of the periodic table Auger energy fraction increases drastically and kinetic energy of the Auger electrons is more and more gentle. The data presented in the table on the experimentally determined Auger resonant energies of electrons do not coincide with the energies of the bound electrons of individual atoms entering the crystal. This phenomenon can be explained by the fact that in crystals valence electrons can make a transition to a vacancy formed by ionization because they are already in orbitals for which the transition is already allowed by the selection rules. The themalisation of the Auger electrons in inner part of the CsPbBr3 crystal leads to the transition of valence electrons through the band gap to the conduction band. From (Liu, Wu, Wei et al., 2022), band gap energy equals 4.5 eV. The energy fraction of radiative transitions during K-L ionization reaches 30%. However, the crystal mainly absorbs such quanta after ionization of the L-M-N levels. Under the conditions of the task, this effect for heating the crystal is insignificant. In the energy range of γ-quants 0.1-10MeV, the average multichannel efficiency of creating electron-hole pairs is 30-40%. Finally, the excitation of the common bound electron N-O-levels in CsPbBr3 crystal produces electron-hole pairs. For mean part of γ-ray, Spectra Energy is 5 MeV. Including efficiency, every quant produces $10^5 – 10^6$ pairs. Time interval of rapid processes is a 10^{-3} sec. Number of γ-quants is 177. Finally, we have current $I=2.72*10^{-8}$ A. In binary detectors such a weak signal is recorded by a significant potential difference (before 800-900V).

4. The Gamma-ray signal structure and him treatment

The structure of the process under study is such that the dependence of the received energy on time has a delta-like character. This makes it easier to apply the formal base.

Based on which the signal processing is carried out and the errors of the measured values are estimated. In (Liu, Wu, Wei et al., 2022) authors presented methods of dealing with dark currents and semiconductors degradations. Here we dwell on the problems of separating emerging false γ-signals when monitoring fast γ-flares of cosmic origin. Calibration sources in this case can be isotopes that give γ-lines in the interval of interest to us. When observing cosmic rays from high-mountain stations, such isotopes may be located near the instrument.

However, X-ray pulsars are also good standards for the hard X-ray region. Among them, one can notice a small amount, which gives stable γ-radiation. The resulting current pulses are much smaller and this complicates the calibration.

The construction of the instrumental function (therefore IFUN) is an important step in the study of the rapid thermonuclear physical processes in Space. IFUN lies in the influence on the radiation and current impulse from detectors and other constructive elements. In our case, this is relaxation time T_{rel} after interaction of the single γ-quants with detectors. Due to the weak fluxes of γ-radiation, the saturation mode is not observed in the presented detectors. The resulting current pulse during one millisecond is made up of current pulses of 177 γ-quanta. The structure of the resulting impulse carries detailed information about the considered physical process and its characteristic time.

5. The hard ware realization of the monitoring detecting systems

In presented paper only a many layer halide perovskites crystal CsPbBr3 with mean layers' number 10^3 has been considered. This number is sufficient for my tasks. As noted previously, the characteristic time of information registration from the entire surface of the matrix is 10^{-4} sec. In other words, 10^7 current impulses in ideal cases should be processed in one second. Given that a useful signal is rarely formed for a short time, it is necessary to exclude the zero signal from the records.

The signal from the optical and gamma matrix goes to the microboard where it is further processed by the processor, which converts the voltage of the incoming pulses into digital form. The further digitized data is buffered where it is then sent to the computer. But in order for the PC to receive and process the data, it must first pass through the interface board. This in turn sends the data to the PC's RAM.

Since we are monitoring and analyzing gamma and optical radiation, we need to filter out the noise. To do this, you need to create a separate monitoring program written in C ++ and Assembler. Since our events will take place in a fraction of a second and with a large data flow, we need a powerful processor with characteristics like the ADSP-BF704. Below I presented layout modeling of the binary detector with emulating it in the LabWiev environment. This emulation consists of the shot noise of a semiconductor and a useful signal composed of the cumulative summation of impulses caused by γ-quanta characteristic of the fast process under study. In our case required method of signal processing that takes into account pulses signals from different detectors

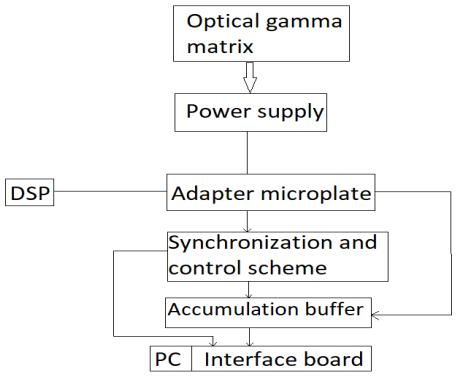

Figure 1: Block-diagram of binary detector

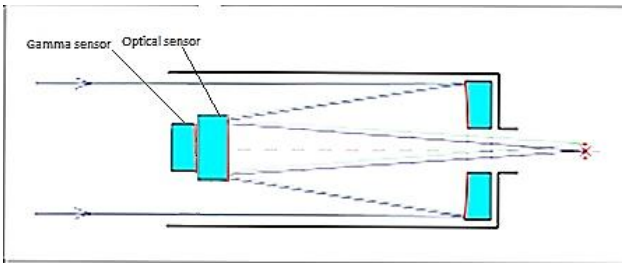

Figure 2: Structure of the binary detector

layers and him summed up. More energetic quants cover a larger number of layers, the length of the quantum path is determined by the total ionization losses of γ-radiation in the substance. Using the environment LabWiev we carried out a model calibration of the resulting signal from one or more quanta of a given energy. For solving the problems of constructing of the time and energy spectra from distant faint objects, I created an algorithm for separating quanta of different energies based on the coincidence method.

At the current 6 μJ flows described in this article, the temperature effect does not affect the sensor readings. The processes that occur during the passage of cosmic rays in the energy range under consideration cause the formation of secondary and so on particles called cosmic lines. In the structure of cosmic lines, there are both positrons and gamma quanta accompanying the processes of their formation and annihilation.

6. The optical detectors

The reverse side of the binary detector is facing the reflecting mirror and is an ordinary light-sensitive matrix with given transmission curve. A characteristic time of considered events is $10^{-3} - 10^{6}$ s for different types of Symbiotic system. Left part of this interval is important for rapid processes produced from cosmic rays (therefore CR) in Earth atmospheres. Accompanying information obtained in optics makes it possible to restore the physical structure of the object of study. The main advantage of a binary detector is the high accuracy of coordinate referencing to the object of study. The optical observations of cataclysmic stellar systems have been carried out for many decades and are important for considered effects. In many cases optical flash has been in much greater periods of time. But in several cases in periodical Novae the times of maximum

glow in gamma and optical rays are comparable during the day after detonation on the surface of a supermassive white dwarf. Unfortunately, this events are very rare. The time interval of optic flyers allows you to accumulate a useful signal with a high temporal resolution. The controller fixing and processing the activity of cataclysmic variables in time allows you to synchronize the flow of information from both parts of the binary detector.

Bogdan Pachinsky promoted this approach back in the 1990s for γ-busters. However, the technical capabilities of the detectors of interest to us did not allow us to solve such a problem. In space mission Fermi this event has only been registered for γ-rays with energies after 100 MeV. Therefore, perovskite detectors overlap the γ-radiation energies considered by us up to 26 MeV. In addition, these detectors produce good shielding of the optical part of considered devices and it can be noted, that cataclysmic systems in space are usable for many other objects that manifest themselves in a similar way.

7. The signal emulation and detection

The monitoring equipment consists of detectors of hard- and optic radiation. Every time after sequence of events associated with the input of γ- and optical quanta, an internal photoelectric effect is observed, current pulse is formed in the corresponding part of the semiconductors under consideration. Together with other semiconductor properties detector produces impulses that are described by an instrumental function. This means that the quantum that enters the corresponding perovskite layer corresponds to a pulse characterized by a width (signal dispersion) and its amplitude. In ideal cases in initial time the sniggle quant has the same amplitude and zero width. In the time required for the response of the detector and the operation of the entire electrical circuit, the considered amplitude of the output signal is formed. In the case of perovskites, such a response is formed, as previously mentioned, in 10^{-6} seconds. In this regard, perovskites have a much higher sensitivity and saturation of the detector occurs at much higher photon fluxes.

In this paper, I consider only multilayer perovskite detectors. This means that the signals are in the form of current pulses from each layer. In more deep layer we have more energetic quants. In special case when considered emits an annihilation and its accompanying quantum, who connect with corresponding decay reaction or synthesis of radioactive, proton-excess isotopes. From (Doikov, 2022) these are quants with energies 0.511 MeV and accompanying them γ-quants from specific nuclear reactions leading to the appearance of positrons in cataclysmic systems and events in Earth atmosphere. The free pass length of this γ-quants is much different and finalized in differ semiconductor layers.

At the other hand, more energetic γ-ray's photon can cause ionization losses in those layers of the detector that are responsible for the registration of γ-quanta of lower energies. The selecting of these events depends on the simultaneous operation of the controllers operating from the signals recorded in the corresponding perovskite layers on the ADC. The energy selection (resulting γ-spectra) of the incoming analog data depends on the information about signals from all layers.

7.1. Method of formation of the initial data

The Peroxide-based gamma sensors require multilayer partial honeycomb structures. In the problems of positron spectroscopy of flares occurring in various space objects that we are considering, we will restrict ourselves to the following gamma lines that arise under the following scenarios:

1) During proton-proton chain reactions e^γ=0.511 MeV.

2) Processes of thermonuclear combustion in periodic New (E_γ=0.511,5.65, … 10 MeV) .

Basically, gamma quanta formed by the decay of proton-rich light nuclei are limited to 10 MeV. Therefore, the thickness of the detector sufficient for registration (total absorption) reaches several centimeters, this is due to the fact that the CsPbBa3 semiconductor detector under consideration has a large average atomic mass (near 57.3 a.u.m.).

To construct a model detector sample, a model of a peroxide semiconductor with 10 layers is adopted, and the total thickness of the detector must correspond to the path length of a gamma quantum with E_γ=10 MeV. When the flow of gamma quanta enters the peroxide, gamma quanta with energies of 0.511 MeV should be absorbed by the upper layer (for example, layer No. 1). The current impulses coming from high-energy gamma rays form impulses in all lower layers. This means that the registration of gamma quanta with low energies will be the most problematic.

To solve this problem, I proposed a simulation model similar to the method of coincidence of events in nuclear physics. If the current pulse is formed in all layers simultaneously, then with a high probability we have a gamma quantum of the highest energy. If similar current pulses enter the signal analyzers at the same time, then these pulses are summed up and refer to the action from one photon.

The corresponding approach makes it possible to form the resulting pulse from gamma quanta of other energies. To obtain the spectrum of objects under study, the described events are sorted by their number and energy. The studied spectra have a pronounced emission character. The contour of each emission line characterizes the power of the process. One of them is the intensity of reactions leading to the formation of gamma quanta.

The width of such a contour is determined by both physical and instrumental parameters of the processes. To determine the instrumental function, when creating a layout, an "ideal" delta-shaped signal is formed and the resulting signal is studied after the interface has worked. To do this, I proposed a simulation model in which the real detector is replaced by a signal generator with the necessary pulses in shape and frequency, corresponding to a real physical process. Then, using the LabVIEW program (by National Instruments Corporation) virtual environment is formed in which the analog signal generator and the receiving interface device are located.

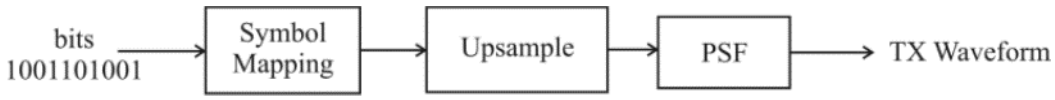

Figure 3: Block diagram of a modulating oscillator located in the LabVIEW environment

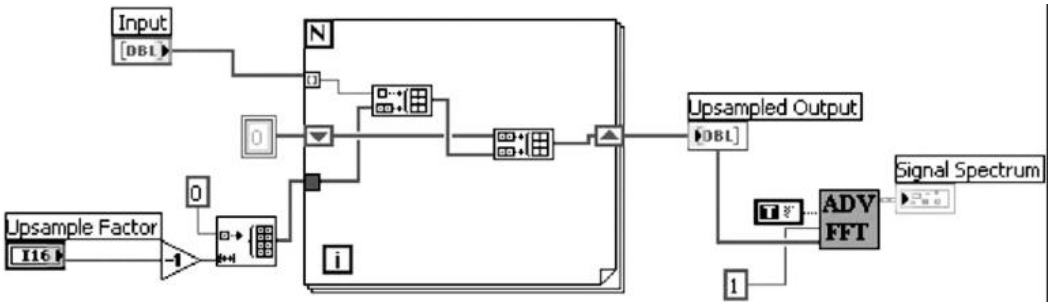

Figure 4: Block diagram of signal discrediting for shaping signals according to predicted physical effect

8. Conclusion

The morphology of the objects in Space is presented with binary system in which one of its components is WD. After sometime in WD hydrogen accumulates, causing surface thermonuclear detonation. For reliable identification, it is necessary to observe such a process in the gamma and optical ranges simultaneously. This circumstance led to the need to turn to the development of binary detectors operating simultaneously in the specified spectral ranges. Theoretical calculation of detonation in the WD surface are presented in (Doikov & Yuschenko 2021). The character time and hard radiation led to the fact that gamma-ray flashes have not yet been detected. At the other time so-called hydrogen-hydrogen (therefore P-P) detonation produced positrons and its annihilation quants with energies 0.511 and 1.022 MeV. In this cases halide perovskites crystal CsPbBr3 are suitable. Moreover, most importantly, we note that such detectors make it possible to solve the problem in the monitoring mode on short-focus instruments. In this case, we avoid the possibility of losing registration of such rare events.

To solve the problem of registration of the rare events in the gamma range, we take into account that the frequency of picking up a signal from a detector pixel should be 100 kHz. Taking into account the physical processes of an explosion in a degenerate plasma, the shape of such a pulse has the form of a delta function with a small signal dispersion.

The signal generator sends a pulse to the device in the form of an analog ADC converter. The second device must operate at that frequency. The third stage is to take advantage of this program. In the considered monitoring device inter drastically pulses number. But useful signals are rare, and the current pulses created by gamma quanta have a sufficiently large momentum in relation to noise and to simplify the solution of the problem. I decided to use a peroxide crystal detector that does not require cooling of the receiving device in which this crystal is placed.

In most of considered cases a proposed scheme to register each individual γ-quant operates in the monitoring mode. A significant potential difference, up to several kilovolts, is applied along each layer of the detector. To combat invariably occurring noises, the detector's own noise is studied in the background at the proposed characteristic times of the process. Noise has a shot thermal character and in most semiconductors the only way to remove it is to noticeably cool the receiving matrix. However, peroxides, as semiconductors, consist of heavy atoms whose average atomic weight can reach up to 50 -70 in atomic mass units. This leads to the fact that peroxide as a semiconductor has a large energy band gap, which is much larger than the energy of thermal motion at room temperature. That is, under normal conditions, the ratio between them is 187.91 times greater than the energy of thermal motion. Therefore, the energy of the electric field, which does not lead to a regular transition of electrons from the band gap to the conduction band, should not exceed 4.5 Ev. This means that the conduction electrons are mainly involved in the noise structure. At a difference of 1Kev, the contribution of the band gap electrons is 187.91 times smaller than the contribution of the conduction electrons. The impulse generated by the noise current must be much smaller than the amplitude of the useful signal. In the previous section, the amplitude of the current that occurs when 177 gamma quanta with energies 511Kev and 5460Kev hit is determined. Given the impulsive nature and short signal time, it becomes necessary to deal not only with noise, but also with random events leading to the formation of similar impulses. For example, the frequency of passage through 1 square cm of cosmic rays is 10 particles per second, each of these particles is able to cause the

corresponding current pulse, so peroxides effectively absorb the marked particles in the upper layers of the crystal, the particles do not reach deeper layers, thereby not causing false pulses.

9. Discussion

The selection and formatting of γ-color images of volumetric objects is an urgent problem. In this paper, we consider the interpreting weak rare γ-radiation signals from distant objects in space. When monitoring in γ-radiation, it is necessary to take into account the background values of the hard radiation of the environment in which the detector is located. Usually, during observations at sea level, this background is 10–20 CR particles per second. In the observed observation modes, this means that the error created by the background is much smaller than the instrumental noise over the observation interval. In the mountains, background measurements are also required for calibration, which is much higher. In this case, we plan to model the background with signals random in time and energy. Signal distortion by optical noise is the problem for future.

Acknowledgment. The author is grateful to professor V.Ya.Gotsulsky, professor B.Ya.Melech for critical remarks, discussions and interest to presented work.

References

Doikov D.N., Khrapatyi S.V.: 2020, *Physics of aerodisperse systems.*, **58,** 102.

Doikov D.N., Yushchenko A.V.: 2021, *Odessa Astron. Publ*., **34,** 40.

Doikov D.N.: 2022, *Odessa Astron. Publ.*, **35,** in press.

Fangze L., Rong W., Jing Wei et al.: 2022, *ACS Energy Letters*, **7 (3),** 1066.

Gould R.J.: 1980, *Astrophys. J.*, **235,** 650.

Gould R.J.: 1990, *Astrophys. J.*, **362,** 284.

Kaastra J.S., Mewe R.: 1993, *Astron. Astrophys. Suppl. Ser*., **97**, 443.

DOI 10.18524/1810-4215.2022.35.268006

PROTOPLANETARY DISKS AROUND CLASSICAL T TAURI STARS

N. Z. Ismailov[1], U. S. Valiev[2], N. S. Dzhalilov[1]

[1] Shamakhy Astrophysical Observatory named after N. Tusi of the National Academy of Sciences of Azerbaijan, Shamakhy, Azerbaijan, AZ 5626, *ismailovnshao@gmail.com*

[2] Batabat Astrophysical Observatory, Nakhichevan Branch of the National Academy of Sciences of Azerbaijan, Nakhichevan, Azerbaijan, *veliyev_ulvu@mail.ru*

ABSTRACT. We have studied the energy distribution curves for a statistically significant number of classical T Tauri stars. It is shown that out of 49 stars, only 7 (14%) has I type of spectrum distribution, the rest belong to type II. Fundamental parameters, including the mass and age of objects are determined. It is shown that the amount of excess radiation in the far IR range increases with age. The change in mass with age, in contrast to Herbig's AeBe stars, exhibits a complex character.

Keywords: Pre-Main sequence stars, circumstellar disks, energy distribution, evolution.

АНОТАЦІЯ. Зорі типу T Tau зазвичай можна виявити поруч із молекулярними хмарами та ідентифікувати за їх змінністю (дуже нерегулярною) в оптичному діапазоні та хромосферній активності. Більше половини зорь типу T Tau мають навколозоряний диск, який можна назвати протопланетним. Цей диск розсіюється за 10 млн років, частково випадаючи на зорю завдяки акреції, частково витрачаючись на формування планет і частково видуваючись зоряним вітром. Більшість зорь типу T Тельця є членами подвійних систем.

У цій роботі ми вивчили криві розподілу енергії для статистично значущої кількості класичних зір типу T Тельця. Показано, що з 49 зір лише 7 (14%) мають I тип розподілу спектра, інші відносяться до II типу. Визначено основні параметри, у тому числі масу та вік об'єктів. Показано, що з віком збільшується кількість надмірного випромінювання у далекому ІЧ-діапазоні. Зміна маси із віком, на відміну зір AeBe Хербіга, носить складний характер.

Ключові слова: попередні зорі головної послідовності, навколозоряні диски, розподіл енергії, еволюція.

1. Introduction

T Tauri type stars (TTS) are low mass ($M \leq 2\ M_\odot$) and have 1–15 Myr ages, have just emerged from their dust cocoon and they are in the Pre-Main Sequence (PMS) stage of evolution. TTSs are formally divided into two subclasses: the so-called classical T Tauri (CTTS) stars are surrounded by an optically thick circumstellar accretion disks. T Tauri stars with weak emission lines in the spectrum and with the partially dissipated residual circumstellar disks are named (WTTS) (Bouvier et al., 2007, Appenzeller & Mundt, 1989, Petrov, 2021). Historically, the strength of the equivalent width (EW) of the Hα emission line, equal to 10 Å, was proposed as the boundary between the CTTS and WTTS groups. However, since most WTTS show Hα emission also due to the chromospheric activity, it is problematic to establish a precise observational boundary between WTTS and CTTS. Later, it was shown that the width of the Hα emission line measured at the level of 10% of the peak intensity (hereinafter, Hα10%) and the Hα profile measured in high-resolution spectra are more sensitive diagnostics of accretion than the EW of the Hα line obtained from spectral data with low resolution (Mamajek et al., 2009). Non-accreting objects exibite narrow ($\Delta V \lesssim$ 230–270 km s^{-1}) and symmetric line profiles of chromospheric origin, while accreting objects has wide ($\Delta V \gtrsim$ 230–270 km s^{-1}) and asymmetric profiles (Ribas et al., 2014, Williams and Cieza, 2011).

It is known that planets are formed in gas- and dust-rich circumstellar disks of young stars. Therefore, the study of the physical properties and evolutionary mechanisms of protoplanetary disks in young stars is important for understanding of the planet formation processes. Various studies have shown that the typical dissipation time scale for protoplanetary disks is about 3 Myr (e.g., Mamajek et al., 2009; Ribas et al. 2014), and the oldest disks are typically up to 16 Myr old (Pollak et al. 1996). The evolution of circumstellar disks from the initial reservoir of the interstellar medium, the gas and dust mixture, towards planetary systems is occured by the growth of dust grains, viscous spreading and accretion onto the central star (or onto the forming protoplanets) and dissipation of the initial gas (Williams & Cieza, 2011). Although a large number of direct images and high-resolution spectroscopic data have been collected over the past decades, the various stages of disk evolution remains poorly distinguished for observations (Wyatt et al. 2015).

Our previous studies shows that the properties of disks apound individual stars of WTTS coincide with those of CTTS, and different populations with residual disks are distinguished, which can exhibit the stages of evolution between them (Ismailov & Valiyev, 2022a). It is assumed that when the primary disk is completely dissipated, the final stage of evolution will be characterized by residual disks, and/or will assemble into

planetesimals and planets. Collisions between planetary remnants or cometary evaporation can produce a second generation of the dust (Hughes et al. 2018). Studies of the dust mass distribution show their significant differences in various young clusters (see, for example, Villenave et al., 2021). These data show that there is a tendency for the dust to decrease in older clusters. According to Manara et al. (2020), even in clusters older than 5 Myr, the observed disk accretion rate is high, and the primary gas-to-dust ratio changes with time in a complex way.

The observed amount of excess radiation in the far-IR spectrum should be proportional to the mass of the dust in the disk. Therefore, the amount of excess radiation in the far-IR range can be an indicator of the amount of dust in the disk. In the present work, we studied the spectral energy distribution curves in the spectral range 0.36–100 μm (SEDs) of a statistically significant amount of CTTS.

2. Observational data

We have selected the program stars from the Herbig & Bell (1988) (HBC) catalogue. We tried to choose such stars for which the emission level in the spectral lines are different. Table 1 lists 49 program stars in ascending order of number in the HBC catalogue. The table 1 lists from left to right in columns: name of the object, the HBC number, the distance to the object, the interstellar extinction coefficient, the spectral types, the effective temperatures adopted to them according to Pecaut et al. (2013), and the main literature sources for each star. These references are given in a separate list in the footnote of the table. All source distances were rechecked and refined using the Gaia DR3 data archive (https://gea.esac.esa.int/archive/). For individual stars, the interstellar extinction coefficients, given in the literature by different authors differ significantly. In such cases, using the B–V color index for normal MS stars, we redefined the value of the parameter Av, assuming that the normal law of interstellar extinction is observed and the extinction coefficient is R=3.1.

Note that the photometric data of the optical and IR ranges collected from the catalogs were obtained non simultaneously; therefore, this can manifest itself as a weak excess IR radiation in the spectral energy distribution (SED) (Strom et al., 1989). In addition, the variability of individual stars can introduce some distortion on the SED curves. Typical brightness variations for TTS in the V band are of the order $\Delta V \approx 0.1$─0.5 mag (Grankin et al., 2007, Herbst&Shevchenko, 1999), so the expected maximum flux change in this band can be about 35%. The maximal variation in the K=2.2 μm band are about $\Delta K \approx 0.3$ mag (Kenyon &Hartmann, 1995), which can provide an error in the fluxes in this band of about 25%.

The procedure of constructing the SED curves for program stars and their approbation for standard stars, as well as the analysis of sources of measurement errors, are described in detail in our previous works (Ismailov, et al. 2021a, Ismailov 2021b, Ismailov & Valiyev 2022).

Table 1: Collected literature data for program stars

Target name	HBC	D, pc	Av	W(Hα) Å	Sp type	Teff K	Reference
LkHa 262	8	246	1.6	31	M0	3850	32, 17, 2
LkHα 271	13	279	4.6	186	K4	4620	2, 8
FM Tau	23	132	0.7	71	M0	3850	10, 9, 30
CW Tau	25	131	2.16	135	K3	4840	27, 10, 44
DD Tau	30	126	1.36	182	M3.5e	3300	10, 27
DG Tau	37	125	0.62	113	K7, K6ve	4050	9, 10,11
DK Tau	45	140	1.4	19	K7e, K8.5	4050	32, 27
XZ Tau	50	147	1.71	274	M2e	3550	27, 30
UZ Tau	52	140	1	80	M1/3Ve	3600	5,25 , 24
GH Tau	55	140	0.25	15	M0.6	3800	5, 26, 27
GK Tau	57	130	0.53	16	K 6.5	4200	1, 2,5
CI Tau	61	160	1.58	102	K7, K5.5	4050	10, 40, 27
DP Tau	70	140	1.22	85	M0.8	3700	30, 27, 9
GO Tau	71	142	2.44	81	M0, M2.3	3850	27, 10, 30
YZ Ori	120	388	0.218	70	K7e	4050	28, 29, 10
KP Ori	124	113	1.2	127	M0	3850	43, 44, 2
AB Ori	135	410	0.81	45	K7	4050	5, 31, 30
CE Ori	152	375	0.496	74	K5e	4450	44, 10
BC Ori	166	304	0.35	151	K7.5e	4000	41, 42
BE Ori	168	398	2.61	68	K0	5280	32, 18, 2

Haro 4-255	176	392	5.0	100	K7:	4780	17, 2, 52
LP Mon	214	830	0.7	58	K7	4050	19, 45, 33
NX Mon	216	706	-2.45	211	K7,M5	3550	50, 38,51
V591 Mon	235	717	0.25	106	K4	4620	33, 38, 39
V 432 MON	237	726	0.4	83	K5	4450	32, 33, 34
RU Lup	251	157	0.37	216	K7 e	4050	6, 21, 22
V 852 Oph	258	131	0.9	167	M0	3850	30, 3, 2
Haro 1-16	268	146	1.38	54	K3e	4840	2, 17
EM*AS209	270	121	1.2	71	K4ve	4620	2, 14, 15
S CrA	286	130	1.92	90	G0Ve	5900	32, 2, 12
FQ Tau	377	140	1	114	M3	3400	35, 32,36
IP Tau	385	129	0.2	11	M0.6	3800	30, 17, 2
FV Tau	386	136	4.73	23	K5	4450	9, 30, 37
Haro 6-13	396	128	2.81	88	M0	3850	9, 30, 17
FZ Tau	402	129	1.83	204	M0	3850	9, 53,
TW Cha	567	183	1	26	K8Ve,	3970	2, 47, 18
TW Hya	568	60	0.27	86	K6, M0	4100	14, 10, 46
Ass Cha T 1-15	574	190	1.55	94	K5Ve	4450	32, 47, 48
WW Cha	580	188	2.31	54	K2	5040	32, 2
Wy cha	583	174	1.65	52	K7-M0	4050	2, 16,17
VW cha	585	168	2.6	116	K8e, K7	3970	10, 20, 13
XX Cha	586	192	1	87	M3e	3500	2, 18,13
Ass cha T1-32	590	188	0.3	32	M0.5e	3800	2, 12, 13
THA 15-5	600	157	2.04	97	K7e	4050	2, 12, 49
HO Lup	612	200	1	220	M1	3680	32, 6,
SZ 102	617	422	0.32	20	K2, K0V	5040	2, 6, 7
SZ 111	622	158	0.5	145	M0	3850	11, 23, 12
AS 205	632	140	1.09	155	K0e, K5e	4500	1, 2, 3
V 1082 Cyg	728	646	0.13	11	K5, K6	4250	2, 4

List of References in the tabl.1:

(1) Zacharias N. et al., 2012yCat, 1322, 0; (2) Cutri R. M. et al., 2003yCat, 2246, 0; (3) Ducourant C. et al., 2005 A&A, 438, 769; (4) Alfonso-Garzón J. et al., 2012 A&A, 548A, 79; (5) Herbig G. H. 1977 ApJ, 214, 747; (6) Hughes J. et al., 1994 AJ, 108, 1071; (7) Merín B. et al., 2008 ApJS, 177, 551; (8) Winston E. et al., 2010 AJ, 140, 266; (9) Audard M. et al., 2007 A&A, 468, 379; (10) Ducati J.R. 2002 yCat.2237, 0; (11) Röser S. et al., 2008 A&A, 488, 401; (12) Cutri R. M. et al., 2014 yCat, 2328, 0 (13) Luhman K.L. 2004 ApJ, 602, 816; (14) Høg E. et al., 2000 A&A, 355L, 27;(15) Salyk C. et al., 2013 ApJ, 769, 21S; (16) Camargo J.I. et al., 2003 A&A, 409, 361; (17) Lasker B.M. et al., 2008 AJ, 136, 735; (18) Tonry J.L. et al., 2018 ApJ, 867, 105; (19) Chambers K.C. et al., 2016 arXiv 161205560; 20) Kirk H., Myers P.C. 2011 ApJ, 727, 64; (21) Bai Yu. et al., 2019 AJ, 158, 93; (22) Bourgés L. et al., 2014 ASPC, 485, 223; (23) Mowlavi N. et al., 2021 A&A, 648, 44; (24) Kraus A.L. Hillenbrand, Lynne A. 2009 ApJ, 704, 531; (25) Bianchi L. et al., 2017 ApJS, 230, 24; (26) Zacharias N. et al., 2009 yCat, 1315, 0; (27) Strom K.M. et al., 1989 AJ 97, 1451; (28) Cohen M., Kuhi L.V.,1979 ApJS, 41, 743; (29) Kounkel M. et al., 2016 ApJ, 821, 8; (30) Lawrence A. et al., 2007 MNRAS, 379, 1599; (31) Frasca A. et al., 2009 A&A, 508, 1313; (32) Sung H. et al., 1997 AJ, 114, 2644S (33) Rebull L.M. et al., 2002 AJ, 123, 1528; (34) Traven G. et al., 2015 A&A, 581, 52; (35) Lucas P.W. et al., 2008 MNRAS, 391, 136; (36) Zhang Z. et al., 2018 ApJ, 858, 41; (37) Luhman K.L. et al., 2010 ApJS, 186, 111; (38) Barentsen G. et al., 2014yCat, 2321, 0; (39) Broos P.S. et al., 2013 ApJS, 209, 32; (40) Torres C.A. et al., 2006 A&A, 460, 695; (41) Wiramihardja S.D. et al., 1991 PASJ, 43, 27; (42) Briceño C. et al., 2019 AJ, 157, 85B; (43) Da Rio, N. et al., 2009 ApJS, 183, 261; (44) Herczeg G.J. Hillenbrand L.A. 2014 ApJ, 786, 97; (45) Dahm S.E., Simon T. 2005 AJ, 129, 829D;(46) Wolf C. et al., 2018 PASA, 35, 10; (47) Frasca A. et al., 2015 A&A, 575A, 4; (48) Stelzer B. et al., 2004 A&A, 423, 1029; (49) Alcalá J.M. et al., 2014 A&A, 561A, 2; (50) Flaccomio E. et al., 2006 A&A, 455, 903; (51) Hsu Wen-Hsin. et al., 2012 ApJ, 752, 59;

3. Obtained results

3.1. SED curves

The constructed SED curves of program stars are shown in Fig. 1. The observational data were approximated by the Castelli & Kurucz (2004) standard stellar models. Since the R, I bands most free of excesses, for the SED curves of CTTS, when fitting with the theoretical curve for stars having the complex spectrum, we focused on these two bands. All SED curves are plotted on the log λ(mkm) ~ log (λF_λ) scale, where λ is the wavelength and F_λ is the absolute radiation flux at the given wavelength. The standard deviation level of points from the approximating curve for the parameter log λF_λ obtained from the SED curves of standard stars was determined as σ=±0.07.

As shown in Ismailov and Valiev (2022), two quantities were used as a measure of excess radiation. The first of them is the difference between the fluxes of the star and the standard in the K band (2.2 μm), i.e., the parameter ΔK. This parameter indicates the excess radiation in the near-IR range (Strom et al., 1989). The second parameter was used by us for the integral excess radiation, and it can be used to measuring both in the UV (denoted as S(UV)), and in the far IR range of the spectrum (signed as S(İR)) (Ismailov and Valiev (2022)). To calculate the integral excess radiation in the spectral region $\lambda_2 - \lambda_1$ (where $\lambda_2 > \lambda_1$), one can apply the expression

$$S = \int_{\lambda_1}^{\lambda_2} log \frac{F_*}{F_m} d\lambda \quad (1)$$

Here λ_1 and λ_2 are the initial and final wavelengths of the excess radiation region, F_* and F_m are the radiation fluxes of the star and the standard in this region of the spectrum. Obtained values of S(UV) and S(IR) characterise the integral value of excess radiation in the UV and IR ranges of the spectrum (see Fig. 4 in Ismailov and Valiev, 2022). All calculated parameters of excess radiation are given in Table 2.

One of the indicators of the existence of the disk accretion is the absolute luminosity in the Hα emission line. Following to Corcoran & Ray (1998), to calculate the luminosity of stars in the Hα (LHα) line the following relation was used:

$$L_{H\alpha} = 4\pi d^2 F_R W_{H\alpha} \quad (2)$$

where Table 1 d is the distance of the star, F_R is the absolute flux density in the photometric band R ($\lambda_{eff} \approx$ 7000 Å), WHα is the equivalent width of the Hα line, expressed in angstroms. Using expression (2) for program stars, the logarithm of the luminosity of radiation in the Hα line was calculated in units of the solar luminosity.

Figure 2 shows graphs, dependences of parameters ΔK ~ S(IR), S(UV) ~ S(IR), ΔK ~ log (LHα/$L_\odot$), and S(UV) ~ log (LHα/$L_\odot$). There is a correlation between the parameters ΔK ~ S(IR), in the order r = 52±2%. On the remaining graphs, there is no clear correlation between the corresponding parameters. The excess radiation index ΔK in the near-IR range is an indicator of the disk accretion. The lack of correlation between the parameters ΔK~ log (LHα/$L_\odot$) indicates that the luminosity in the Hα line is formed by various mechanisms, not only by accretion, but also, for example, by chromospheric activity.

To classify the SED curves of program stars, we used the value of the parameter α, obtained from expression:

$$\alpha = \frac{\log\lambda_2 F_2 - \log\lambda_1 F_1}{\log\lambda_2 - \log\lambda_1} \quad (3),$$

which was proposed by Lada (1987). Here λ_1 and λ_2 ($\lambda_2 > \lambda_1$) are the wavelengths of the corresponding to range on the SED curves, and F_1 and F_2 are the absolute radiation fluxes corresponding to these wavelengths. The parameter α determines the degree of slope of the given section on the SED curve. Our measurements for the region λ_1=2.2 μm and λ_2=12 μm showed that out of 49 stars, only 7 (about 14%) are corresponding to type I spectrum, and the rest have type II spectrum. The results of this classification are presented in Table 2.

3.2. Physical parameters of program stars

First of all, based on the V values cleared of the interstellar reddening, the distance to the star, and the bolometric corrections taken from Pecaut & Mamajek (2013), we have calculated the absolute bolometric stellar magnitudes Mv. Knowing the absolute luminosity of the Sun $Mv_\odot$=4.83 mag, we calculated the absolute luminosities of stars in units of solar luminosity $L/L_\odot$. Further, knowing the effective temperatures T_{eff} and luminosities, we calculated the radiuses of the stars in units of the solar radius $R/R_\odot$. The solar effective temperature $T_\odot$ was taken equal to 5800 K.

Using theoretical evolutionary tracks of Siess et al., (2000), the masses and ages of stars were also determined. The position of stars in the H–R diagram is shownig (Fig. 3) that the masses of program stars are within $0.3 \leq M/M_\odot \leq 2.5$. All calculated parameters are given in the corresponding columns of the Table 2.

To comparison of the masses of program stars obtained in this work with the literature data, on the left panel of the Fig.4 have shown the corresponding diagram. As can be seen, our data are consistent satisfactorily with the literature data. The second panel on the right shows the age-mass dependence in the scale log t ~ $M/M_\odot$ for program stars. As can be seen, no definite regularity is revealed in the distribution of stellar masses by age.

3.3. Spectral type – age relation

In the left panel of the Fig. 5, shown a diagram of the distribution of the parameter's value α with a step 0.25 for program stars. The ordinate shows the percentage ratio of the number of stars Ni to the total number of samples N for a given range of values of the parameter α. As can be seen from this, the largest number of stars (32.5%) have the parameter between $-1.0 \leq \alpha < -0.5$, and in general, the shape of the distribution is close to the normal distribution.

The second panel in Fig. 5 shows the dependence of the average value of the parameter α versus ages of stars. Each point is the result of averaging of the parameter α over a given range of values. The vertical bars indicate the value of the weighted average value of the log t age variance, and the horizontal bars indicate the variance α in the averaged group. The groups have a number of stars from 2 to 13.

As can be seen from this diagram, in the whole the coefficient α is increasing versus age. Although the reliability of this distribution is not very high (see, for example, Soderblom 2014), in general, there is a tendency for the values of the parameter α to increase, which is an indirect argument in favor of an increase in the value of the far excess IR radiation with age. This result shows that, apparently, the amount of dust in the protoplanetary disks of young stars should increase during evolution.

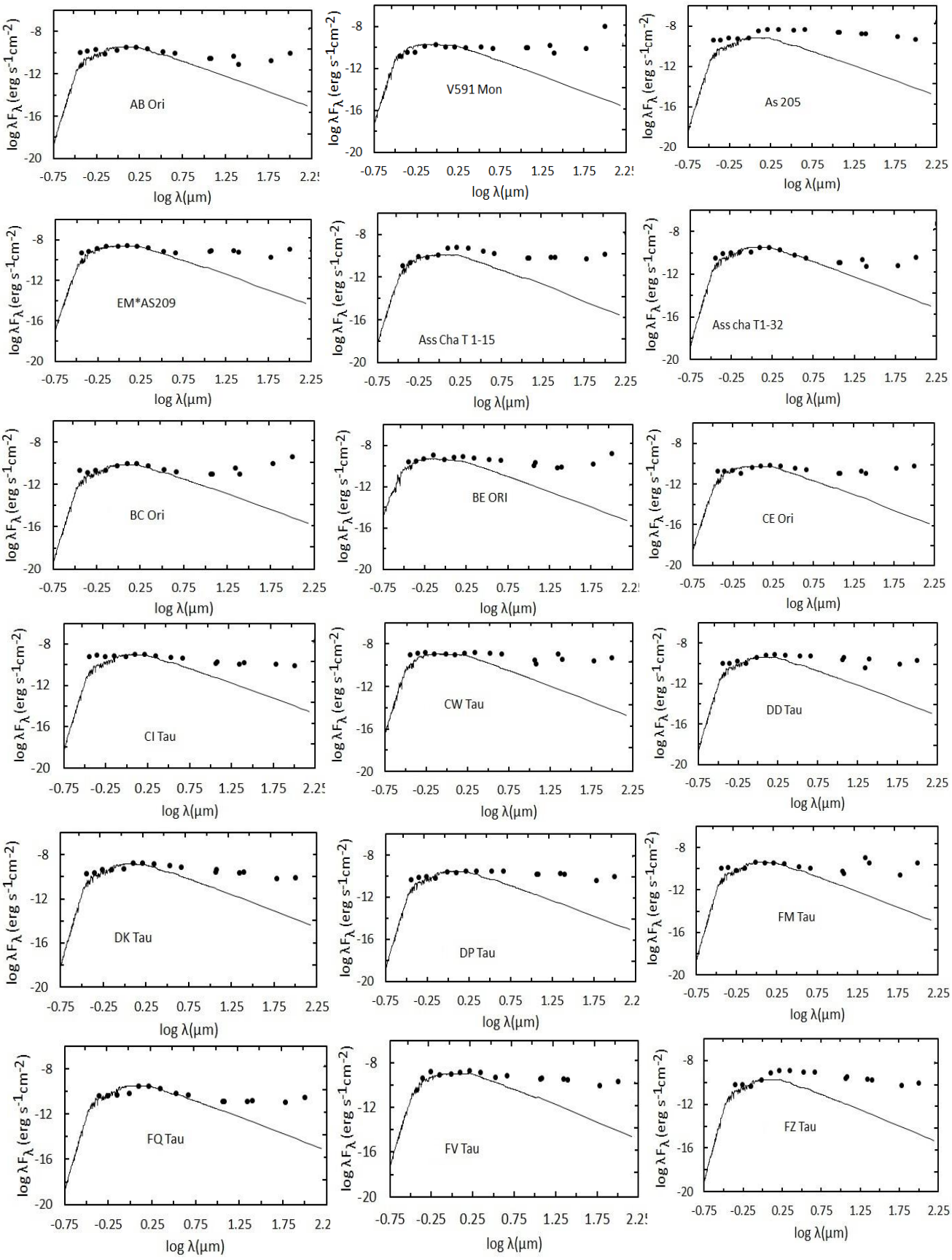

Figure 1: SED curves of program stars. Solid lines describe SEDs of standard star models by Castella and Kurucz (2004).

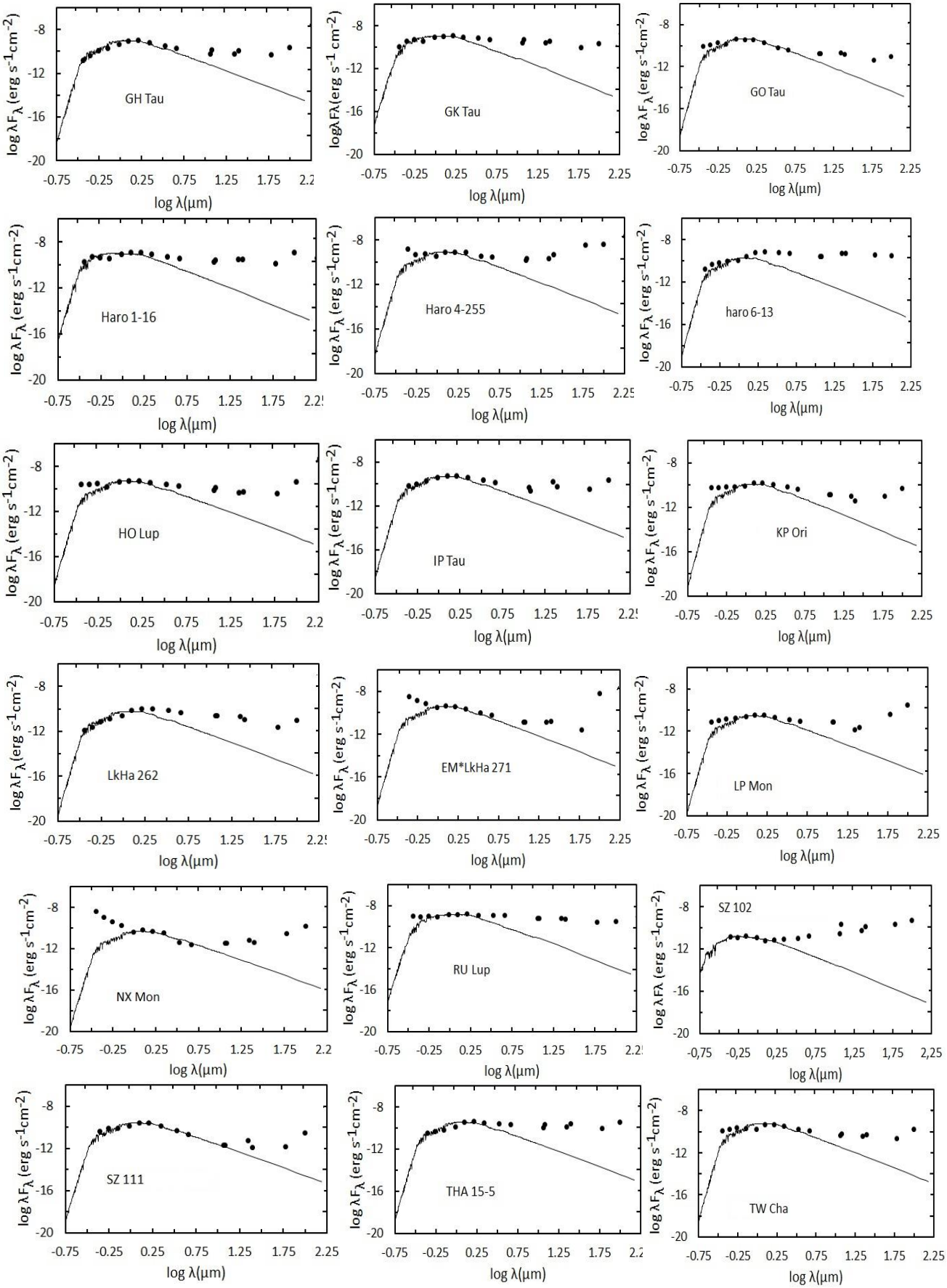

Figure 1 (Continued)

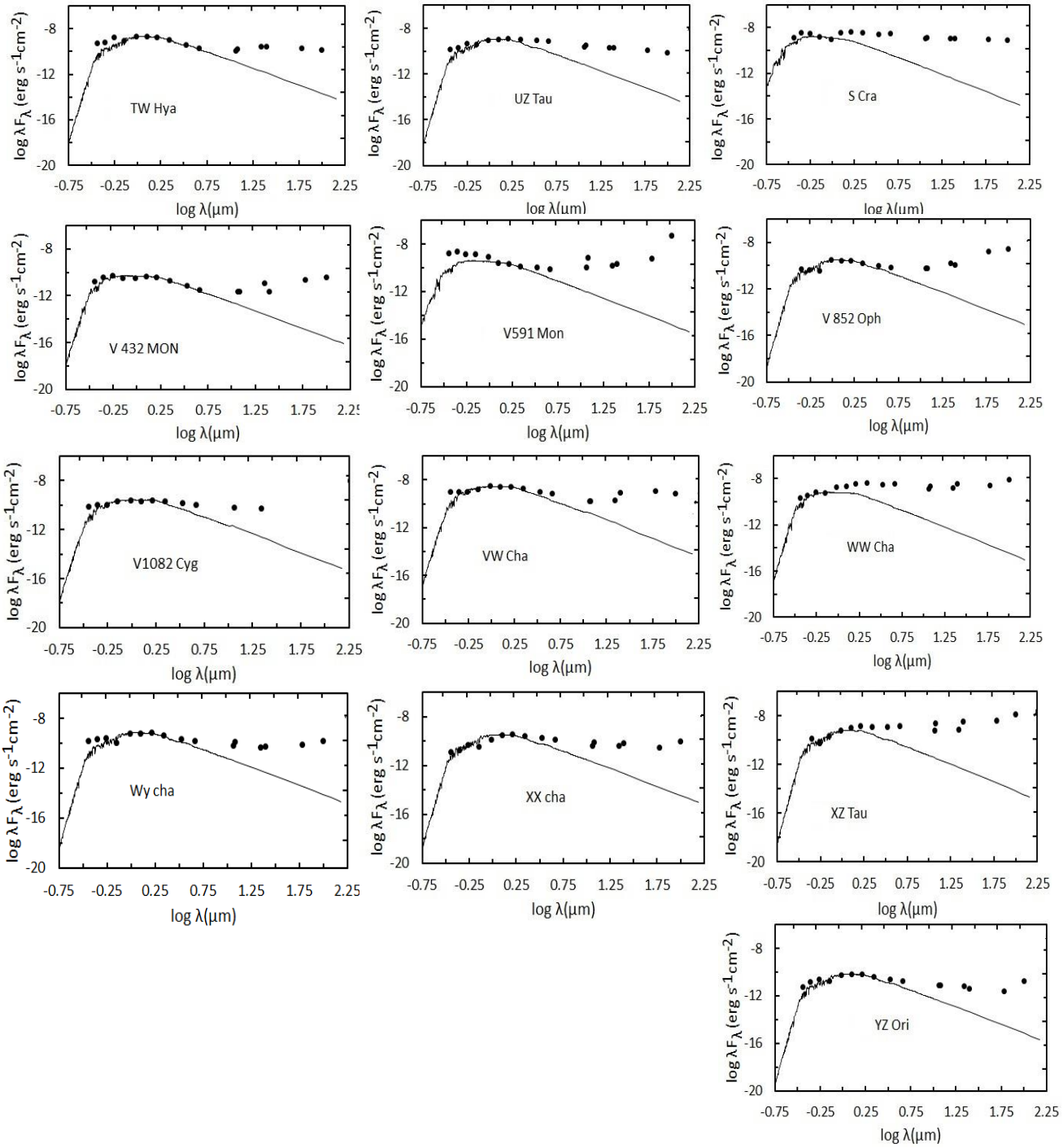

Figure 1 (Continued)

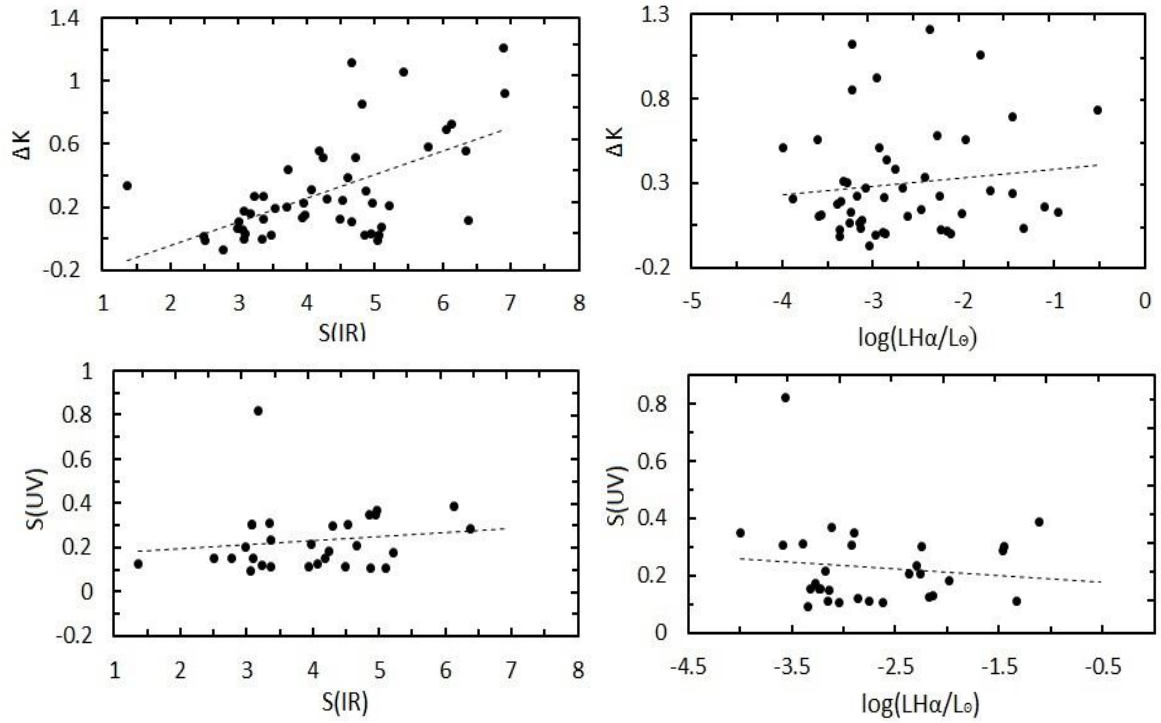

Figure 2: Diagrams of radiation excess parameters in the near (ΔK) ~ S(IR) far IR ranges, upper left panel, parameter ΔK and absolute luminosity in the Hα line, log (LHα) (top panel, right), between the parameters S(UV) ~ S(IR) bottom left, and S(UV) ~ log (LHα) – (bottom right panel). Dashed lines is linear regression.

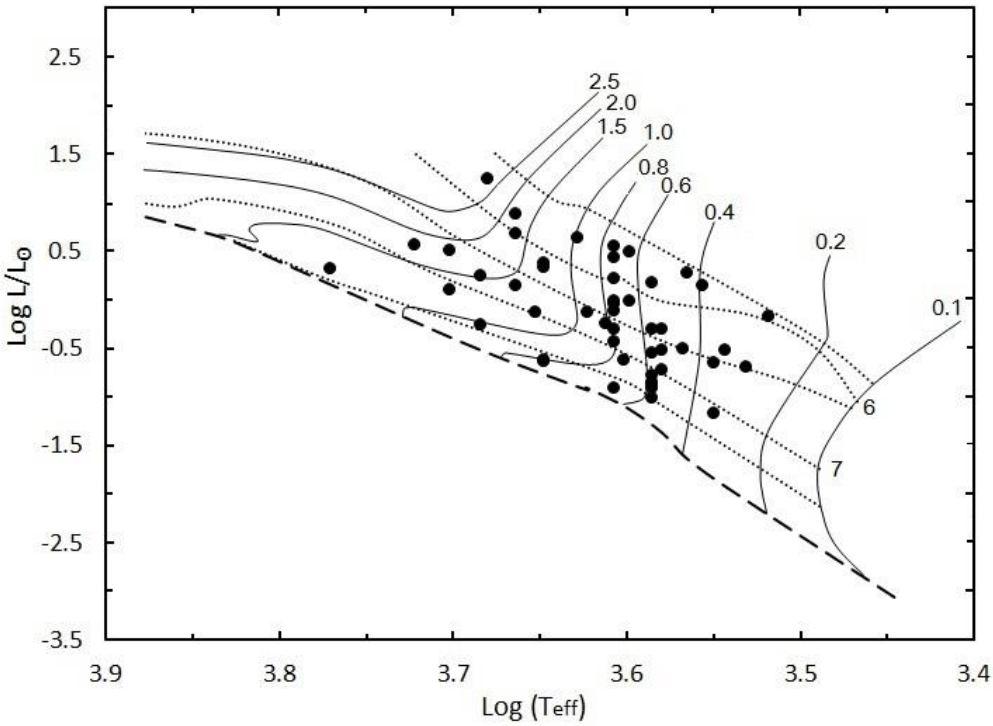

Figure 3: Location of program stars on the H-R diagram with evolutionary tracks according to Siess et al.(2000). The numbers on the solid lines indicate the masses, and near the dotted lines, the logarithms of the ages from 5.5 to 8 with a step of 0.5. The lower bold dotted line is the zero age line (ZAMS).

Table 2: The main parameters of program stars determined in this work

Target name	L*/L⊙	R/R⊙	M/M⊙	t, Myr	S(IR)	S(UV)	ΔK	type
LkHa 262	1.5	0.7	0.56	0.6	4.72		0.51	I
LkHα 271	7.9	3.0	1.8	0.6	4.94	0.35	0.03	II
FM Tau	0.2	0.5	0.6	15.8	3.94	0.11	0.13	II
CW Tau	1.8	0.7	1.5	5.6	4.19	0.15	0.55	II
DD Tau	0.7	0.8	0.3	0.3	4.24	0.18	0.51	II
DG Tau	0.5	1.2	0.75	5.0	3.08	0.31		II
DK Tau	0.9	2.9	0.73	5.0	3.24	0.12	0.27	II
XZ Tau	0.2	0.8	0.36	3.2	5.79		0.58	I
UZ Tau	1.4	3.1	0.4	0.5	3.36	0.23	0.27	II
VGH Tau	0.3	2.4	0.51	4.0	3.00		0.11	II
GK Tau	0.8	0.7	0.95	4.0	3.08	0.31	0.18	II
CI Tau	1.7	1.7	0.7	1.0	3.35	0.31		II
DP Tau	0.3	0.6	0.45	3.2	4.08	0.13	0.31	II
GO Tau	0.5	1.9	0.55	2.5	2.77	0.15		II
YZ Ori	0.4	2.7	0.8	7.9	5.10	0.11	0.08	II
KP Ori	0.1	0.8	0.6	25.1	4.97	0.37	0.23	II
AB Ori	3.6	1.0	0.7	0.5	4.67	0.21	0.11	II
CE Ori	0.2	1.4	0.8	39.8	4.87	0.10	0.31	II
BC Ori	0.2	1.7	0.75	35.5	5.22	0.17	0.21	II
BE Ori	3.7	0.4	1.75	6.3	6.06		0.69	II
Haro 4-255	15.4	4.7	2.7	0.32	4.53	0.30	0.24	II
LP Mon	1.0	0.8	0.72	5.6	6.37	0.29	0.11	II
NX Mon	0.1	1.3	0.36	15.8	3.18	0.82	0.16	II
V591 Mon	4.8	1.0	1.65	1.0	6.12	0.39	0.73	II
V 432 MON	2.2	2.2	1.25	1.8	5.07			II
RU Lup	2.7	2.9	0.7	0.6	4.29	0.30	0.26	II
V 852 Oph	0.1	1.3	0.59	31.6	5.05			II
Haro 1-16	0.6	0.7	1	25.1	4.60		0.39	II
AS209	1.4	1.0	1.4	4.0	3.36	0.11	0.12	II
S CrA	2.1	0.4	1.3	20.0	5.43		1.06	I
FQ Tau	0.2	0.7	0.3	3.2	3.47		0.02	II
IP Tau	0.2	4.3	0.52	10.0	3.71		0.20	II
FV Tau	2.4	2.5	1.25	1.6	3.72		0.44	II
Haro 6-13	0.1	1.6	0.95	25.1	4.81		0.85	I
FZ Tau	0.1	0.5	0.6	22.4	4.67		1.12	I
TW Cha	1.0	0.6	0.65	1.6	3.09	0.15		II
TW Hya	0.6	0.5	0.81	4.0	2.50	0.15		II
Ass Cha T1-15	0.2	0.9	0.75	63.1	6.91		0.92	II
WW Cha	1.3	2.1	1.3	12.6	6.90		1.21	II
Wy cha	0.8	2.6	0.72	2.5	2.99	0.20	0.07	II
VW cha	3.2	2.9	0.65	0.4	4.49	0.11	0.13	II
XX Cha	0.3	0.4	0.35	2.5	3.55		0.19	II
Ass cha T1-32	0.5	0.3	0.52	2.2	3.06	0.09		II
THA 15-5	0.1	0.8	0.7	50.1	3.96		0.23	II
HO Lup	1.9	0.8	0.45	0.4	3.98	0.21	0.15	II
SZ 102	0.1	0.4	1.8	5.0	6.34		0.56	I
SZ 111	0.3	0.5	0.59	5.0	2.49			II
AS 205	0.8	1.6	1.2	31.6	4.86	0.35		I
V 1082 Cyg	4.3	0.4	1	0.3	1.37	0.13	0.34	II

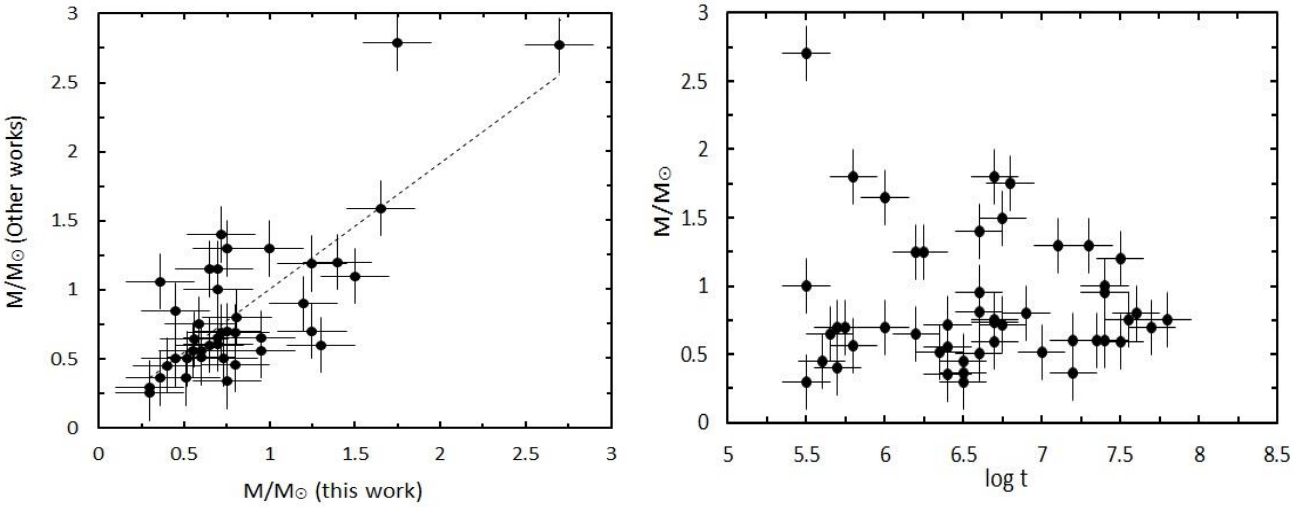

Figure 4: Comparison of the stellar masses obtained in this work with the data obtained in other works (left panel). The dotted line shows the linear approximation of the data. Vertical and horizontal bars shows the maximum error level. In the right panel, age-mass relation for program stars is presenting.

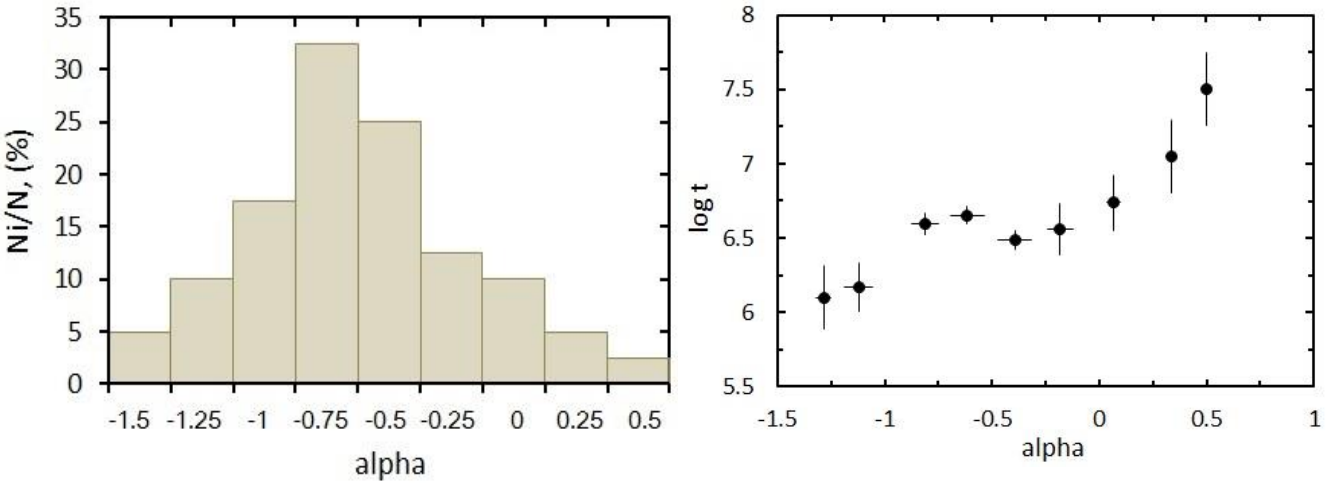

Figure 5: In the left panel, each step along the abscissa corresponds to the interval α for a given relative number of program stars Ni/N. The right panel shows the change in α with the age of the stars. Vertical and horizontal bars show the weighted average dispersion by parameters.

4. Conclusion

In this paper, we have studied the curves of the spectral energy distribution for 49 CTTS stars with variously developed emission lines in the spectrum. It is shown that in the set under consideration, all stars have a significant IR excess in the far IR range (10─100 μm). 30 of the selected program stars show a significant UV excess in the range of 0.36–0.70 μm. In addition, 39 stars exhibit excess emission in the near-IR range (2.2 μm) of the spectrum. As is known, the existence of UV excess radiation in CTTS is a consequence of the existence of disk accretion. It is obvious that in such disks the amount of gas is sufficient to support the accretion process. In addition to this, excess radiation in the near-IR range is also an argument in favor of the existence of gas accretion in the disk. Our data have shown that program stars often, but not always, have UV and ΔK excesses in their spectra simultaneously.

It was shown that only for 7 program stars the SED curve corresponds to type I, the remaining 42 objects have spectrum of type II. At the same time, no correlation is found between the UV and IR indicators of excess radiation. A correlation of about 52% between excess radiation in the near and far IR ranges was revealed. No correlation was found either with the luminosity in the Hα line and excesses in the UV and near IR ranges, which

indicates that different mechanisms are responsible for the emission of the Hα line.

We have determined the main parameters of the program stars. Comparison with literature data shows satisfactory agreement with the data obtained in other works. We have shown for the first time that the parameter α determined from relation (3) shows an increase with age. It is shown that with age, the amount of excess radiation in the far infrared range is increasing. Such a process is observed at least up the ages of 10 Myr.

The distribution diagram of the parameter α showed that the value of α is random, i.e. obeys the normal distribution law. At the same time, an increase in α (i.e., an increase in the excess in the far IR range) indicates an increase in dust in the disk with age.

References

Appenzeller I., Mundt R.: 1989, *Astron. & Astrophys. Rev.*, **1**, 291.

Bouvier J.P., Alencar S.H., Harries T.J., Johns-Krull M.C., Romanova M.M.: 2007, in *Protostars and Planets V*, ed. B. Reipurth, D. Jewitt, and K. Keil (Tucson, AZ: Univ. Arizona Press), 479.

Castelli F., Kurucz R.I.: 2004, ATLAS9, *https://www.user.oats.inaf.it/castelli/grids/*.

Corcoran M., Ray T.P.: 1998, *A&Ap*, **331**, 147.

Grankin K.N., Melnikov S.Yu., Bouvier J. et al.: 2007, *Astron. & Astrophys.*, **461**, 183.

Herbig G. H., Bell K. R.: 1988, *Lick Observ. Bull.*, **No 1111**.

Herbst W., She vchenko V.S.: 1999, *Astron. J.*, **118**, 1043.

Hughes A.M., Duchêne G., Matthews B.C.: 2018, *Ann. Rev. Astron. & Astrophys.*, **56**, 541.

Ismailov N.Z., Kholtygin A.F., Romanyuk I.I., Pogodin M.A.: 2021a, *Az. Astron. J.*, **16**, No 2, 5.

Ismailov N.Z., Kholtygin A.F., Romanyuk I.I., Pogodin M.A., Moiseeva A.V.: 2021b, *Astrophys. Bull.*, **76**, № 4, 415.

Ismailov N.Z., Valiyev U.S.: 2022a, *Astron. Rep.* (accepted for publication).

Jayawardhana R., Mohanty S., Basri G.: 2003, *Astrophys. J.*, **592**, 282.

Kenyon S.J., Hartmann L.: 1995, *Astrophys.J. Suppl. Ser*., **101**, 117.

Lada C.J.: 1987, *IAU Symposium*, **115**, 1.

Mamajek E.E.: 2009, in *AIP Conf. Ser. /*Eds. T.Usuda, M.Tamura, M.Ishii, **1158**, 3.

Manara C.F., Natta A., Rosotti G.P.: 2020, *A&Ap*, **639**, A58.

Pecaut M.J., Mamajek E.E.: 2013, *Astrophys.J.* Suppl.Ser. 208, 9.

Petrov P.P.: 2021, *Acta Astrophysica Taurica* 2, No 1, 1.

Pollack J. B., Hubickyj O., Bodenheimer P. et al.: 1996, *Icarus*, **124**, 62.

Ribas Á., Merín B., Bouy H., Maud L.T.: 2014, *A&Ap*, **561**, A54.

Siess L., Dufour E., Forestini M.: 2000, *A&Ap*, **358**, 593.

Soderblom D.R., Hillenbrand L.A., Jeries R.D., Mamajek E.E., Naylor T.: 2014, *Protostars Planets VI*, 219.

Strom K.M., Strom S.E., Edwards S. et al.: 1989, *Astron. J.*, **97**, 1451.

Villenave M., Ménard F., Dent W.R.F. et al.: 2021, *A&Ap*, **653**, A46.

Williams J.P., Cieza L.A.: 2011, *Ann. Rev. Astron. & Astrophys*., **49**, 67.

Wyatt M. C., Pani´c O., Kennedy G. M., Matrà L.: 2015, *Astrophys. & Spase Sci*., **357**, 103.

10.18524/1810-4215.2022.35.268674

RT VIR – A SEMIREGULAR STAR WITH MASER EMISSION: MATHEMATICAL MODELLING OF OPTICAL VARIABILITY

L.S.Kudashkina, I.L.Andronov

Department "Mathematics, Physics and Astronomy" Odessa National Maritime University, Odessa, Ukraine, *tt_ari@ukr.net*

ABSTRACT. The historical light curve of the semiregular pulsating star RT Vir (SRb, Sp M8III) with a maser emission is analyzed based on the AAVSO database. The star is extensively studied in the IR, radio and the optical ranges. The value of the period from the CCVS (155^d) conflicts with some observational data. Signs of a systematic variability were also detected in the radio frequency range with a period that was close to 200 days. Studies of the period showed that the period of this star varies with time and the latest value was found to be roughly 136 days. Period analysis result of the visual data from 1904 May to 2016 August provided by AAVSO for RT Vir. Published databases of "virtual observatories" - AAVSOnet, Hipparcos, ASAS-SN, KWS were used. Periodogram analysis revealed that the star still has several periods (320, 280, 169 and 153 days). In fact, the variations are not truly periodic, there are large shifts in time, changes in amplitude, and these smaller periods occur as smaller-amplitude peaks in-between the main ones with 320 period. Two-color diagrams of gloss in I and color index (V-I) from V were constructed. Approximation of "Running parabola" was carried out, average values <V>=8.457, <I>=3.658, <B-V>=+1.8 were determined.

Keywords: Stars: Pulsating: SR; Periodogram analysis

АНОТАЦІЯ. На основі бази даних AAVSO проаналізовано історичну криву блиску напіврегулярної пульсуючої зорі RT Vir (SRb, Sp M8III) з мазерним випромінюванням. Ця зоря широко досліджується в ІЧ-, радіо- та оптичному діапазонах. Значення періоду з GCVS (155^d) суперечить деяким даним спостережень. Ознаки систематичної змінності також були виявлені в радіочастотному діапазоні з періодом, який був близьким до 200 днів. Дослідження періоду показали, що період цієї зорі змінюється з часом, і було встановлено, що останнє значення становить приблизно 136 днів. Результат аналізу періоду візуальних даних з травня 1904 року по серпень 2016 року, наданий AAVSO для RT Vir. Використовувалися опубліковані бази даних «віртуальних обсерваторій» - AAVSOnet, Hipparcos, ASAS-SN, KWS. Аналіз періодограми показав, що зоря все ще має кілька періодів (320, 280, 169 і 153 дні). Фактично варіації не є справді періодичними, є великі зсуви в часі, зміни амплітуди, і ці менші періоди виникають як піки меншої амплітуди між основними з періодом 320. Були побудовані двоколірні діаграми блиску в I та показника кольору (V-I) від V. Проведено апроксимацію «Running parabola», визначено середні значення <V>=8,457, <I>=3,658, <B-V>=+1,8.

1. Introduction

The star RT Vir = BD+05º2708= HD113285= IRC+10262 = SAO119734 = ASASSN-V J130238.04+051108.2 = HIP 63642=RAFGL 1594 is known as a semi-regular variable (SRb) with brightness limits 7.41 – 9.0 V, spectral type is M8III (GCVS).

The Oxygen-Rich Asymptotic Giant-Branch (AGB) star RT Vir is surrounded by gas and dust as it loses its atmosphere to space. Several mass-loss estimates are given, lying between 1.1×10^{-7} $M_\odot$yr^{-1} and 5×10^{-7} $M_\odot$yr^{-1} (Paladini et al., 2017).

RT Vir is known as a maser source. The 22-GHz emission is located in approximately spherical, thick, unevenly filled shells. The outflow velocity increases two fold or more between the inner and outer shell limits. (Richards et al., 2012). The H_2O masers are located between 2.4 and 18.0 AU from RT Vir. Linear polarization was observed in 9 features around RT Vir. Circular polarization was found in 3 features around RT Vir. It is concluded that in the H2O maser region, the magnetic energy density dominates the thermal and kinematic energy density (Leal-Ferreira et al., 2013).

There are indications that the rate of mass loss correlates with pulsation period (McDonald et al., 2018). In connection with this, the question arises of the most accurate determination of the period (or periods, if the star is multiperiodic). The value of the period from the CCVS (155^d) conflicts with some observational data. For example, Wenzel (1977) obtained a value of about 200 days for the period from the light curve. Signs of a systematic variability were also detected in the radio frequency range with a period that was also close to 200 days. Studies of the period (Andronov et al., 1988) showed that the period of this star varies with time and the latest value was found on that moment to be roughly 136 days. Detailed information about the period values obtained by different authors for RT Vir is collected in the review by Kudashkina (2019).

2. Data and analysis

For periodogram analysis, the observations from the databases of AFOEV (ftp://cdsarc.u-strasbg.fr/pub/afoev), AAVSO (http://aavso.org), ASAS-SN (https://asas-sn.osu.edu/variables), ASAS-SN SKY PATROL (https://asas-sn.osu.edu/), KWS (Kamogata/Kiso/Kyoto Wide-field Survey http://kws.cetus-net.org/~maehara/VSdata.py) were used. A description of working with the data-bases can be found, for example, in the articles by Andronov and Marsakova (2006), Marsakova and Andronov (2006, 2007) and Vavilova et al. (2012). The methods for determination of the characteristics of individual extrema are reviewed by Andronov (2005), Andrych and Andronov (2019) and Andrych et al. (2020). The most recent review on various methods is presented by Andronov (2020), Andronov et al. (2020) and in this volume (Andronov and Chinarova 2020).

The least squares method is used for periodogram analysis. The method is described by Andronov (1994, 2003). The method allows the use of a trigonometric polynomial fit of the statistically optimal degree s:

$$m(t) = a_0 - \sum_{k=1}^{s} r_k \cos\left(2\pi k \cdot (t - T_{0k})/P\right)$$

where r_k are semi-amplitudes and T_{0k} are initial epochs for the brightness maximum (minimum magnitude) of the wave with a period $P_k=P/k$.

The preliminary value of the period (from the General Catalogue of Variable Stars, (Samus et al. 2007-2015) was corrected using the method of differential corrections for each order s of the trigonometric polynomial.

Figure 1 shows the periodogram obtained from AAVSO data. A pulsating period of 372 days is found for RT Vir. The periodogram shown on the fig. 2 has several peaks *V* and *Ic* filters (KWS data), there is no peak at 370^d. There are peaks corresponding to 320, 280, 169 and 153 days. Figure 3 shows 3-period approximation (320, 156, 169 days) of Japanese (KWS) *V* data.

The method of "running parabolae" for smoothing signals with both equidistantly and not equidistantly distributed in time signals was proposed by Andronov (1990, 1996) and was applied to light curves of stars of different types. Figure 4 shows dependence of the Running Parabola approximations with a statistically optimal ratio Signal/Noise (Δt=53 days) from the Japanese (KWS) database for the *B*, *V*, *Ic* filters and the color indexes *B-V* (too few) and *V-Ic*.

Mean values <*V*>=8.457, <*I*>=3.658, <*B-V*>=+1.8 were determined.

Figure 5 shows dependence of the brightness in I and the color (*V-I*) index on *V*, for the Running parabola approximations. If the filters were the same, the expected theoretical slope is 1 for the upper curve, and 0 for the lower one. Deviation of the slope shows a photometrical gradient of dI/dV=0.624±0.007.

3. Conclusions

An analysis of photometric observations of the semi-regular pulsating star RT Vir, whose envelope is the source of maser radiation, was carried out. Such objects are at active stages of evolution (Kudashkina and Rudnitskij, 1988, 1994; Kudashkina, 2003, 2019). Our previous study (Andronov and Kudashkina, 1987) was based on photovisual observations obtained at the Astronomical Observatory of Odesa National University. I.I. Mechnikova. The periodogram showed the presence of several peaks that satisfactorily describe the average light curve. In addition, it turned out that the period increases with time. Its last value at that time was equal to 136^d. Periodogram analysis revealed that the star still has several periods (320, 280, 169 and 153 days). In fact, the variations are not truly periodic, there are large shifts in time, changes in amplitude, and these smaller periods occur as smaller-amplitude peaks in-between the main ones with 320 period.

Two-color diagrams of gloss in *I* and color index (*V-I*) from *V* were constructed.

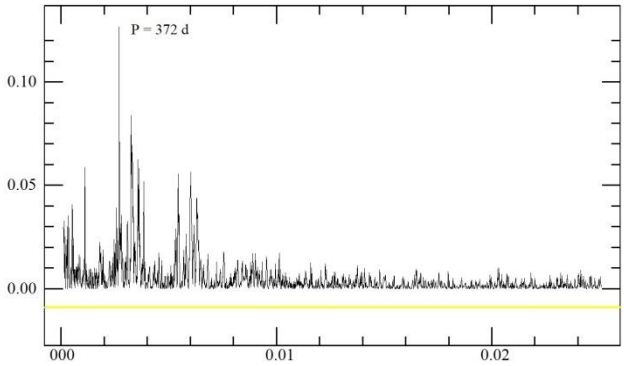

Figure 1: The periodogram obtained from AAVSO data. A pulsating period of 372 days is found.

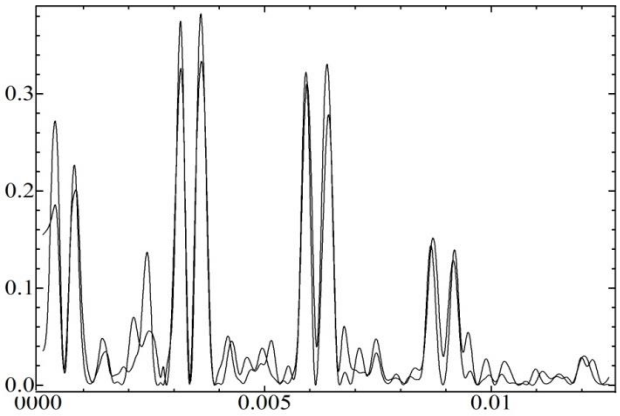

Figure 2: The periodogram has several peaks *V* and *Ic* filters, there is no peak at 370^d. There are peaks corresponding to 320, 280, 169 and 153 days. However, these are not strict periods, as the multi-period approximation shows. Large deviations, amplitude changes, phase shifts are present.

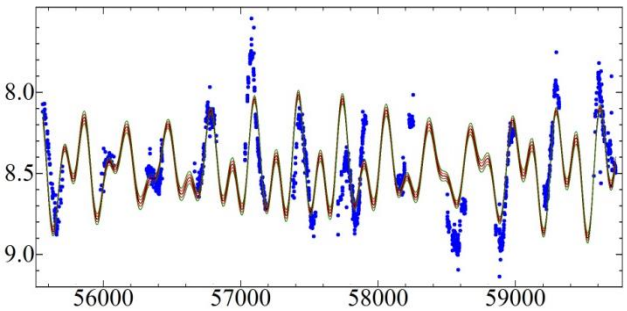

Figure 3: 3 shows 3-period approximation (320, 156, 169 days) of Japanese (KWS) V data.

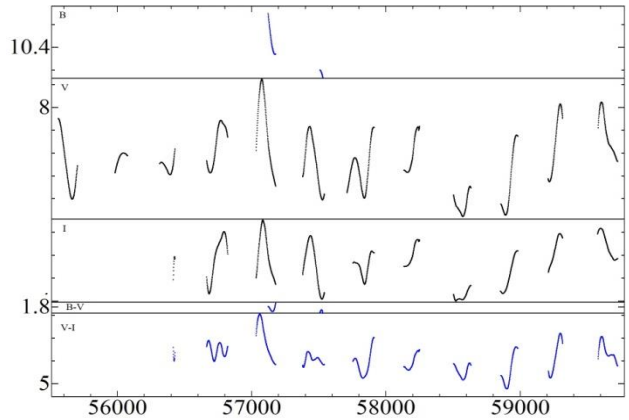

Figure 4: Dependence of the Running Parabola approximations with a statistically optimal ratio Signal/Noise (Δt=53 days) from the Japanese (KWS) database for the *B*, *V*, *Ic* filters and the color indexes *B-V* (too few) and *V-Ic*.

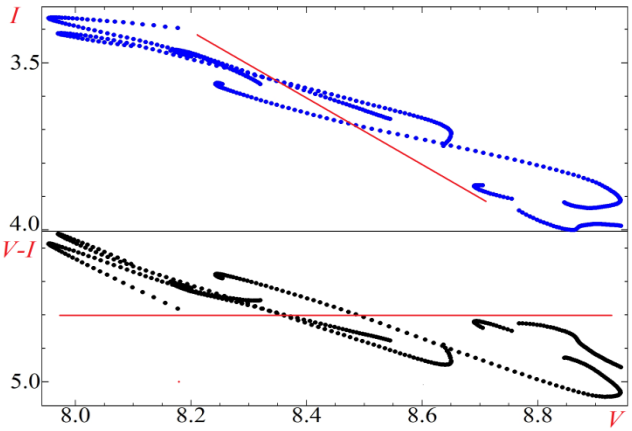

Figure 5: Dependence of the brightness in I and the color (*V-I*) index on *V*, for the Running parabola approximations.

References

Andronov I.L.: 1990, *KFNT*, 6, 6, 87 (1990KFNT....6...87A).

Andronov I.L.: 1994, *Odessa Astron. Publ.*, 7, 49. (1994OAP.....7...49A).

Andronov I.L.: 1996, The Proceedings of the 27th Conference on Variable Star Research. November 10-12, 1995. Brno, Czech Republic. editor M. Zejda. 107 pages, in English. ISBN 80-85882-05-1. Brno, 6 (1996vsr..conf....6A).

Andronov I.L.: 2003, *ASPC* 292, 391. (2003ASPC..292..391A).

Andronov I. L. (2005) *ASP Conf. Ser*. 335, 37

Andronov I. L. (2020) Knowledge Discovery in Big Data from Astronomy and Earth Observation: Astrogeoinformatics, ed. P. S˘koda et al., Elsevier, p. 191.

Andronov I. L. and Kudashkina L. S.: 1987, Arbeitskreis Veranderlichem Kulturbund der DDR, Information N. 121, 3.

Andronov I.L., Velichko E.V., Kudashkina L.S., Kukarin A.V., Shmagunov O.A.: 1988, *Peremennye zvezdy*, 22, 683.

Andronov, I.L.; Antoniuk, K.A.; Augusto, P.; Baklanov, A.V.; Chinarova, L.L.; Chochol, D.; Efimov, Yu.S.; Gazeas, K.; Halevin, A.V.; Kim, Y.; Kolesnikov, S.V.; Kudashkina, L.S.; Marsakova, V.I.; Mason, P.A.; Niarchos, P.G.; Nogami, D.; Ostrova, N.I.; Patkos, L.; Pavlenko, E.P.; Shakhovskoy, N.M.; Tremko, J.; Yushchenko, A.V.; Zola, S.: 2003, *A&AT*, 22, 4-5, 793. (2003A&AT...22..793A).

Andronov I.L., Baklanov A.V.: 2004, Astronomy School Reports, 5, 264. (2004AstSR...5..264A).

Andronov I.L., Kudashkina L.S.: 2008, *OEJV*, 84, 1. (2008OEJV...84....1A).

Andronov I.L., Marsakova V.I.: 2006, *Astrophysics*, 49, 370 (2006Ap.....49..370A).

Andronov I.L., Marsakova V.I., Chinarova L.L.: 2014, *AASP*, 4, 3. (2014AASP....4....3A).

Andronov I. L., Chinarova L. L. (2020) *AApTr* 31, 411.

Andronov I. L., Breus V. V., Kudashkina L. S. (2020) arXiv preprint arXiv:2007.14264.

Andrych K. D., Andronov I. L. (2019) *Open European Journal on Variable Stars* 197, 65.

Andrych K. D., Andronov I. L., Chinarova L. L. (2020) *Journal of Physical Studies*, 24, 1902.

Chinarova L.L., Andronov I.L.: 2000, *Odessa Astron. Publ.*, 13, 116. (2000OAP....13..116C).

Kudashkina L.S.: 2003, *KFNT*, 19, 3, 193. (2003KFNT...19..193K).

Kudashkina L.S.: 2015, http://arxiv.org/abs/1607.03722.

Kudashkina L.S.: 2019, *Astrophysics*, 62, no. 4, 556-572. https://doi.org/10.1007/s10511-019-09604-4.

Kudashkina L.S., Andronov I.L.: 1996, *Odessa Astron. Publ.*, 9, 108. (1996OAP.....9..108K).

Kudashkina L.S., Rudnitskij G.M.: 1988, *Peremennye Zvezdy*, 22, 925. (1988PZ.....22..925K).

Kudashkina L.S., Rudnitskij G.M.: 1994, *Odessa Astron. Publ.*, 7/1, 66-69.

Leal-Ferreira M. L., Vlemmings W. H. T., Kemball A., and Amiri N.: 2013, *Astron. Astrophys.*, 554, A134. DOI: 10.1051/0004-6361/201321218.

McDonald I., De Beck E., Zijlstra A. A. and Lagadec E.:2018, *MNRAS* 481, 4984. doi:10.1093/mnras/sty2607

Marsakova V.I., Andronov I.L.: 1998, *Odessa Astron. Publ.*, 11, 79 (1998OAP....11...79M).

Marsakova V.I., Andronov I.L.: 2006, *Astrophysics*, 49, 506 (2006Ap.....49..506M).

Marsakova V.I., Andronov I. L.: 2007, *Astrophysics*, 50, 76(2007Ap.....50..76M).

Paladini C., Klotz D., Sacuto S., Lagadec E., Wittkowski M., Richichi A., Hron J., Jorissen A., Groenewegen M. A. T., Kerschbaum F., Verhoelst T., Rau G., Olofsson H., Zhao-Geisler R., and Matter A.: 2017, *Astron. Astrophys.* 600, A136. DOI: 10.1051/0004-6361/201527210.

Richards A. M. S., Etoka S., Gray M. D., Lekht E. E., Mendoza-Torres J. E., Murakawa K., Rudnitskij G., and Yates J. A.: 2012, *Astron. Astrophys.*, 546, A16. DOI: 10.1051/0004-6361/201219514.

Samus N.N., Durlevich O.V., Goranskij V.P., Kazarovets E. V., Kireeva N.N., Pastukhova E.N., Zharova A.V.: 2007-2015, General Catalogue of Variable Stars, VizieR On-line Data Catalog: B/gcvs (2009yCat....102025S)

Vavilova I.B., Pakuliak L.K., Shlyapnikov A.A., Protsyuk Yu.I., Savanevich V.E., Andronov I.L., Andruk V.N., Kondrashova N.N., Baklanov A.V., Golovin, A.V., Fedorov P.N., Akhmetov V.S., Isak I.I., Mazhaev A.E., Golovnya V.V., Virun N.V., Zolotukhina A.V., Kazantseva L.V., Virnina N.A., Breus V.V., Kashuba S.G., Chinarova L.L., Kudashkina L.S., Epishev V.P.: 2012, *KPCB*, 28, 2, 85. (2012KPCB...28...85V).

Wenzel W.:1977, Mitt. Ver. Stern. 8, 18.

DOI 10.18524/1810-4215.2022.35.268007

COMPARATIVE ANALYSIS OF OBSERVATIONS OF THE SELECTED EXOPLANET TRANSITS OBTAINED AT THE KYIV COMET STATION WITH THE DATABASE OF THE ORBITAL TELESCOPES TESS AND KEPLER

M. Lobodenko[1], Ya. Pavlenko[2], I. Kulyk[2], A. Nahurna[1], M. Solomakha[1], O. Baransky[3]

[1] Taras Shevchenko National University of Kyiv, Kyiv, Ukraine
[2] Main Astronomical Observatory of the NAS of Ukraine, Kyiv, Ukraine
[3] Kyiv Comet station Lisnyky, Kyiv, Ukraine

ABSTRACT. We present a comparative analysis of observations of the selected exoplanet transits obtained at the Kyiv Comet station with the database of the TESS (Transiting Exoplanet Survey Satellite) and Kepler space telescopes. The light curves obtained by the TESS and Kepler orbital telescopes were processed using a program based on the Python package Lightcurve 2.3v which is freely available in the MUST archive (Barbara A. Mikulski Archive for Space Telescopes). The ground based observations were carried out with the 70-cm telescope AZT-8 (Lisnyky). Photometric processing of the ground based observation was performed by using the Muniwin program. The light curves and parameters of the observed transits as well as the exoplanet orbital parameters obtained from ground based observations were published in the ETD (Exoplanet Transit Database). Determined transit parameters were compared with the results of the TESS command, which are stored in the MUST archive. Here we presents a comparison of the parameters of transit phenomena (period, depth, transit duration) and some orbital parameters obtained from two independent sets of observations, terrestrial and orbital, performed in different epochs.

Keywords: transits, exoplanets, TESS, Kepler, exopanet parameters.

АНОТАЦІЯ. Ми презентуємо порівняльний аналіз спостережень транзитів вибраних екзопланет, отриманих на кометній станції Лісники, з кривими блиску їх батьківських зір, з бази даних космічних телескопів TESS (Transiting Exoplanet Survey Satellite) і Kepler. Криаві блиску, отримані орбітальними телескопами TESS і Kepler, були оброблені за допомогою програми, розробленої на основі Python пакету Lightcurve 2.3, який є у вільному доступі в архіві MUST (Barbara A. Mikulski Archive for Space Telescopes). Спостереження також проводились на 70-ти сантиметровому телескопі-рефлекторі АЗТ-8 (Лісники). Фотометрична обробка цих результатів проводилась за допомогою програми Munivin. Отримані нами з наземних спостережень криві блиску та оцінки параметрів спостережених транзитів та орбітальні параметри екзопланет опубліковані в базі даних ETD (Exoplanet Transit Database). Визначені нами параметри транзитів порівнювались з результатами команди TESS, які зберігаються в архіві MUST. В роботі представлено порівняння параметрів транзитних явищ (період, глибина, тривалість транзиту), а також орбітальних параметрів вибраних екзопланет, отриманих з двох незалежних наборів спостережень, наземних та орбітальних, виконаних в різні епохи.

Ключові слова: транзити, екзопланети, TESS, Кеплер, параметри екзопланети.

1. Introduction

There are a large number of methods for finding exoplanets. The transit method is one of the most effective. The planet covers part of the star when it passes over the disk of a star and the visible brightness falls. The time seria observed during a transit event allow us to see this fall. The magnitude of the fall in brightness depends on the relative size of the star and the planet. Therefore, the light curve provides information about the radius of the planet and some orbital parameters. But this method has several disadvantages. First, the plane of the planet's orbit should be located in such a way that we can observe the passage of the planet over the star's disk. Secondly, the planet must be large enough to be able to create a detectable drop in the star brightness. For this reason most of the planets are

found by the transit method and all the planets that we observe are hot Jupiters.

Hot Jupiters are planets with a mass of the order of the mass of Jupiter, which rotate close to their star and are always turned to it only by the one side. The period of the planet's rotation is small because they are very close to their stars. The small period allows us to observe transits regularly. Which makes hot Jupiters the most convenient targets for the observations.

The TESS and Kepler orbital telescopes conducted searches for exoplanets using the transit method. The quality of observations obtained from the orbital telescopes is definitely higher than the quality of observations obtained from ground-based telescopes. We are not hindered by various atmospheric phenomena we do not depend on the weather, time of day, phase of the Moon, etc. However, the ground based observations allow us to gather the data over large time span, which provide information about possible changes in transit parameters. The best result can be achieved by combining these two types of observations. To do this, it is necessary to determine how the results obtained from space and ground-based observations correspond to each other, and whether ground observations can be considered sufficiently accurate. The main goal of our research is to determine to what extent the parameters of exoplanets obtained from observations at the Lisnyky Comet Station coincide with the parameters obtained from observations from the TESS and Kepler orbital telescopes.

2. Observations obtained from the TESS and Kepler orbital telescopes

2.1. MAST

MAST (The Mikulski Archive for Space Telescopes) – it is an archive of data from the Webb, Hubble, TESS, Kepler space telescopes. The archive contains data from observations in the optical, ultraviolet and near-infrared ranges. The MAST archive also provides the calculated parameters (transit period, transit depth, the phase of transit event, and some orbital parameters) by the TESS and Kepler pipelines for all events surpassing some threshold. We used these published data in order to compare with the results of our ground based observations as well as with those transit parameters obtained from the Kepler and TESS light curves using our program.

2.2. TESS and Kepler missions

The TESS (Transiting Exoplanet Survey Satellite) space telescope was launched on April 19, 2018. The mission was planned for two years, during these years the telescope should examine the entire area of the sky. The celestial sphere was divided into 26 observation sectors, each sector being $24^\circ \times 96^\circ$ to detect transits of previously unknown exoplanets near the closest and brightest stars. TESS would focus on G, K, and M-type stars with apparent magnitudes brighter than magnitude 12, and 1000 nearest red dwarfs. The rotational period of the telescope is 13.7 days. Each sector is observed for 27.4 days. The sole instrument on TESS is formed of four wide-angle CCD cameras. Each camera has a 16.8-megapixel detector with a low energy consumption and low noise, which was developed in the Laboratory of Lincoln. Each camera has a $24^\circ \times 24^\circ$ field of view, a 100 mm effective pupil diameter, a lens assembly with seven optical elements, and a bandpass range of 600 to 1000 nm.

The Kepler Orbital Telescope is NASA's space telescope designed to search for exoplanets. The telescope was launched on March 7, 2009, from the spaceport at Cape Canaveral. Kepler repeats the path of the Earth, revolving around the Sun. This arrangement allows telescope to constantly monitor one part of the sky. Kepler's field of view covers 115 square degrees near the plane of the Milky Way. The telescope has a mass of 1,039 kilograms and contains a Schmidt camera with a 0.95-meter front corrector plate feeding a 1.4-meter primary mirror. The light reflected by the mirror is collected in the main focus, where there is a mosaic of 21 pairs of specially created astronomical CCD matrices, capable of recording almost every incident photon. The dimensions of the entire mosaic are approximately 30 × 30 cm and it consists of 95 megapixels. These stars are located in the Orion Arm of our Galaxy, at a distance of 600 to 3000 light years. In May 2013, the telescope's second flywheel engine failed. A year after the failure of the engine, the telescope began to transmit data to Earth again. The new mission has been named K2. The telescope began to observe a section of the sky along the ecliptic. Over 9 years of operation, the telescope has discovered more than 2,680 exoplanets, 550 of which may be rocky, and 21 potentially habitable.

2.3. The data processing

The program we used to process data from the TESS and Kepler orbital telescopes was developed based on the Python package Lightcurve 2.3v, which is freely available in the MUST archive (Barbara A. Mikulski Archive for Space Telescopes).

First, the program must find data for the object we are interested in catalogs. To do this, enter the object number in the catalog, indicate exactly which mission this object was observed. The next step is the program normalizes the light curve. For several sectors, the light curves are stitched and normalized. The program finds and subtracts long-period sinusoidal oscillations, which can be star's oscilations and some kind of artifacts. The Lomb-Scargle periodogram is used for this. To detect transit events we build a periodogram, using the Box Least Squares (BLS) method. This method is much more sensitive to periodic transits. Fig. 1 present the periodogrames of star TIC236887394 from the TESS data base constructed with Lomb-Scargle

and BLS methods.

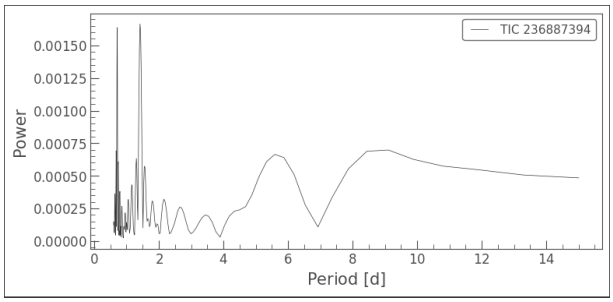

Figure 1: The Lomb-Scargle periodogram of star TIC 236887394 from the TESS data base

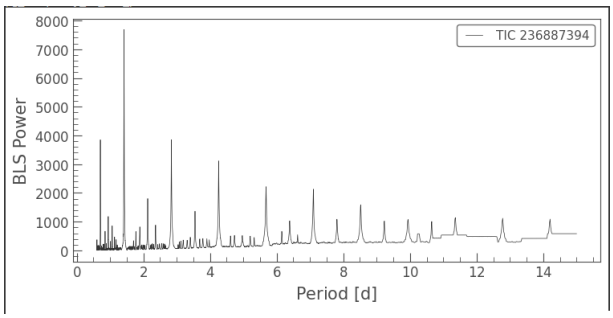

Figure 2: BLS periodogram of star TIC 236887394 from the TESS data base

The program outputs are period, duration, and first epoch of transit based on the periodogram built by the BLS method for the period at maximum power. Using these parameters we constract the folded light curve in the phase space, which helps to notice a shifts (if any) in the moments of the beginning and end of the transit. It helps to notice a shift in moments of the beginning and end of the transit. These displacements may indicate the presence of one or more planets in this system. Fig.3 demonsrates the folded phase curve for star TIC 236887394 from the TESS data bese. We can see decrease in the star brightness caused by the transit event.

In order to find other possible transits we cut out parts of the light curve where the first transit occurs and repeate the procedure again building periodogram using the BLS method.

3. Observations obtained at the Lisnyky Comet Station

3.1. Observations

Observations were also carried out from March 24, 2021, to February 14, 2022, at the Lisnyky Comet Station, on the 70-centimeter AZT-8 reflector telescope, using filter R.

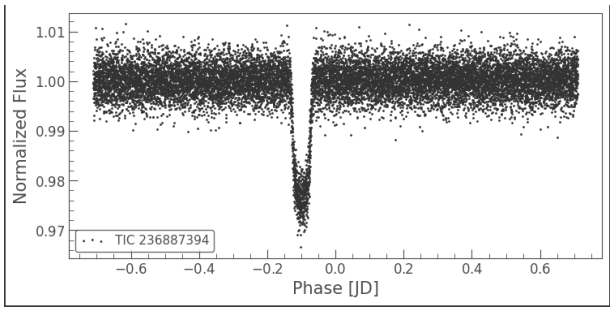

Figure 3: The folded phase curve of star TIC 236887394

The telescope is equipped with a FLI PL4710 back-illuminated CCD and UBV RI Bessel filters. For faint objects we use a mode with 2 × 2 binning, which gives a scale of 1.”96/pixel. The FoV of the instrument is 16’ × 16’ arcmin. The limiting magnitude of a 300 s exposure image is 20 mag under good sky conditions. It is possible to reach 21.5-22 mag with 1800 s exposures.For our observations, the exposure time varied from 10 to 30 seconds, depending on the brightness of the observed object.

We didn’t observe one particular object all the night. We chose the star and time span for expected transit event and conducted observations during the transit only. We began shooting half an hour before the intended start time of the event and completed half an hour after the intended completion to identify possible displacements in the moments of the beginning and end of the transit.

3.2. List of observed objects and their characteristics

	Spectral type	Fluxes	Distance [pc]	Constellation
TrES-3	G	12.4	231.34	Hercules
Kepler-17	G5V	14.14	720.75	Cygnus
Qatar-1	K	12.65	185.62	Draco
WASP-43	K7V	12.08	86.75	Sextans
WASP-3	F7V	10.52	231.16	Lyra
TrES-5	K	13.77	360.31	Cygnus
Qatar-2	K5V	13.45	181.37	Virgo
WASP-10	K5V	12.03	141	Pegasus

3.3. Processing observations with Muniwin

The processing of observations obtained in the Lisnyky Comet Station was carried out using the Muniwin program. This program uses differential photometry:

Table 1: Parameters of the selected transits obtained from the ground based and orbital telescopes

Kepler 17b

	Observation	MAST	obtained with Lightcurve 2.0
Period [day]	1.4857108*	1.4857108	1.4856924
Transit duration [hour]	2.41	2.29	2.40
Depth	0.0201 [mag]	1.7765[%]	
Planet radius [R_j]	1.34	1.31	
Inclination [°]	90.00	87.2	
Orbital radius [AU]	0.026*	0.026	

TrES-3b

	Observation	MAST	obtained with Lightcurve 2.0
Period [day]	1.3061861*	1.3061858	1.3061269
Transit duration [hour]	1.31	1.37	1.2
Depth	0.0279 [mag]	2.7361[%]	
Planet radius [R_j]	1.262	1.336	
Inclination [°]	81.76	81.93	
Orbital radius [AU]	0.023*	0.023	

Qatar-1b

	Observation	MAST	obtained with Lightcurve 2.0
Period [day]	1.4200246*	1.4200242	1.4202261
Transit duration [hour]	1.59	1.66	1.37
Depth	0.0203 [mag]	2.1557[%]	
Planet radius [R_j]	1.093	1.143	
Inclination [°]	83.43	84.48	
Orbital radius [AU]	0.023*	0.023	

WASP-43b

	Observation	MAST	obtained with Lightcurve 2.0
Period [day]	0.81347414*	0.813475	0.8134242
Transit duration [hour]	1.05	1.16	1.2
Depth	0.0280 [mag]	2.5371[%]	
Planet radius [R_j]	0.93	0.93	
Inclination [°]	81.18	82.15	
Orbital radius [AU]	0.014*	0.014	

WASP-3b

	Observation	MAST	obtained with Lightcurve 2.0
Period [day]	1.846835*	1.846830	1.846529
Transit duration [hour]	2.22	2.79	2.40
Depth	0.0124[mag]	1.0269[%]	
Planet radius [R_j]	1.36	1.42	
Inclination [°]	81.71	84.15	
Orbital radius [AU]	0.0317*	0.032	

TrES-5b

	Observation	MAST	obtained with Lightcurve 2.0
Period [day]	1.48224718*	1.48224690	1.48225292
Transit duration [hour]	1.852	1.846	1.200
Depth	0.0224 [mag]	2.192 [%]	
Planet radius [R_j]	1.208	1.256	
Inclination [°]	84.54	84.53	
Orbital radius [AU]	0.025*	0.025	

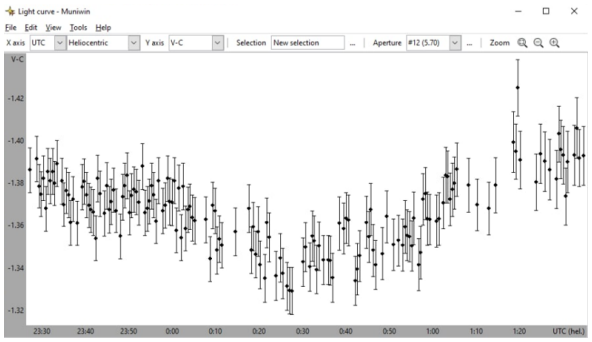

Figure 4: The light curve for the star TIC 36734222 obtained using the Muniwin program

we compare the brilliance of two or more stars. One star is one which brilliance must change due to the transit of the planet through its disk, and the other (others) are reference stars which brilliance should be unchanged. First, we calibrate the images using dark, bias, flatfield files. The next step is to set the parameters by which the program determines which object in the image is the star. The next step is to look for the corresponding stars on each image. After that, we select a star through the disk of which transit should take place and the stars which brilliance should be unchanged. Reference stars cannot be variable stars. We use the Simbad database to make sure that the selected star has constant brilliance. When the necessary stars are selected, we proceed to the light curve construction.

The resulting light curve was uploaded to the Czech Exoplanet Transit Database (ETD) for further processing.

3.4. Exoplanet Transit Database

The Exoplanet Transit Database is a Czech database. Observers can load light curves obtained from observations to this database. ETD has an algorithm for processing light curves, by which it determines the main transit parameters from these light curves: the moments of the beginning, end and middle of transit, the depth, duration and radius of the planet, and the inclination of the orbit. The period of the planet is determined from all observations published in the database.

All our observations were uploaded to this database and received data quality 2 and 3. The data quality in the ETD is estimated on a scale from 1 to 5, where 1 is the data with the highest quality.

4. Research results

The parameters of the exoplanet transits obtained from the ground-based observations and determined from the data base of the orbital telescopes are listed in Table 1. Some of parameters we could not extract from our own observations, therefore they were taken from ETD based on all observations published in this data base. Such parameters are indicated by symbol "*". The table also comprise period and transit duration calculated in this work from the Kepler and TESS light curves.

5. Conclusion

A comparison of parameters of transit phenomena determined from two different data sets, i.e., ground-based and space-based, indicates that:

1) The transit parameters (period and duration) obtained from ground-based observations with a small telescope agree well with those obtained from Kepler and TESS orbital telescopes, highlighting the high accuracy of the ground-based observations presented in this work.

2) It is shown that the average agreement of transit parameters is at the level of 0.00001 day (transit period) and 0.1 hour (transit duration)

3) Independent processing of the light curves from the Kepler and TESS databases indicates that the preliminary processing of the light curves (detrending, removing the long-periodic oscillations) can significantly affect the accuracy of determining the transit parameters.

References

Bunnell J.: 2018, Using Kepler Data to Plot a Light Curve, [online] Available at: (https://github.com/spacetelescope/notebooks/blob/master/notebooks/MAST/Kepler/Kepler_Lightcurve/kepler_lightcurve.ipynb)

Bunnell J.: 2018, Plotting Images from Kepler Target Pixel Files, [online] Available at: (https://github.com/spacetelescope/notebooks/blob/master/notebooks/MAST/Kepler/Kepler_TPF/kepler_tpf.ipynb)

Hall O., Barentsen G.: 2020, Using Kepler Light Curve Products with Lightcurve, [online] Available at: (https://github.com/spacetelescope/notebooks/blob/master/notebooks/MAST/Kepler/kepler_using_light_curve_products_with_lightcurve/kepler_using _light_curve_products_with_lightcurve.ipynb)

Hall O., Barentsen G.: 2020, Using Kepler Target Pixel File Products with Lightcurve, [online] Available at: (https://github.com/spacetelescope/notebooks/blob/master/notebooks/MAST/Kepler/kepler_using_ target_pixel_file_products_with_lightcurve/kepler_using_target_pixel_file_products_with_lightcurve .ipynb)

Hall O., Barentsen G.: 2020, Measuring and Removing a Rotation Period Signal from a Kepler Light Curve,[online] Available at: (https://github.com/spacetelescope/notebooks/blob/master/notebooks/MAST/Kepler/kepler_measuring _a_rotation_period/kepler_measuring_a_rotation _period.ipynb)

Hall O., Barentsen G.: 2020, Creating Periodograms and Identifying Significant Peaks, [online] Available at: (https://github.com/spacetelescope/notebooks/blob /master/notebooks/MAST/Kepler/kepler_creating _periodograms/kepler_creating_periodograms.ipynb)

Hall O., Barentsen G.: 2020, How to Understand and Manipulate the Periodogram of an Oscillating Star, [online] Available at: (https://github.com/spacetelescope/notebooks/blob/master/notebooks/MAST/Kepler/kepler_how_to_understand_and_manipulate_the_periodogram_of _an_oscillating_star/kepler_how_to_understand_ and_manipulate_the_periodogram_of_an_oscillating _star.ipynb)

Pavlenko Ya., Shubina O., Kulyk I., Kuznyetsova Y., Zakhozhay O., Korsun P., Borysenko S., Krushevska V., Andreev M.: 2021, Exocometary Activity Around Stars at Different Evolutionary Stages: Current Issues (Main Astronomical Observatory of the NAS of Ukraine, Kyiv, Ukraine)

Pavlenko Ya., Kulyk I., Shubina O., Vasylenko M., Dobrycheva D., Korsun P.: 2022 (arXiv:2202.13373)

Saunders N.: 2020, Identifying Transiting Planet Signals in a Kepler Light Curve, [online] Available at: (https://github.com/spacetelescope/notebooks/blob /master/notebooks/MAST/Kepler/kepler_identifying_transiting_planet_signals/kepler_identifying_transiting_planet_signals.ipynb)

Terebizh V.Yu.: 1992, Time series analysis in astrophysics, Moscow: Nauka, 394 pp - in Russian

DOI 10.18524/1810-4215.2022.35.268105

FROM SPECTROSCOPY TO THE CHEMICAL EVOLUTION OF THE GALAXY. PART 1.

T. Mishenina

Astronomical Observatory, Odesa National University, Odesa, 65014, Ukraine,
tmishenina@ukr.net

ABSTRACT. A brief review of the results obtained at Odesa Astronomical Observatory based on the stellar spectra analyses from 1892 to 2000 is presented. The review begins with the first observations of emission lines in solar prominences carried out in 1892 under the direction of Alexander Kononowitsch and includes an overview of spectrophotometric studies performed at the observatory using instruments and telescopes designed in-house; theoretical consideration of the issues of modelling physical conditions in stars and spectra simulation. It also describes the main results of the research of stars of various types, including cool giants K-, M spectral types, stars with various peculiarities of chemical composition, having enhanced lines of metals and CN bands, eclipsing binaries and binaries of different types, semi-regular and long-period variable stars, RR Lyraes, δ Scuti and λ Boötes stars, the diversity of Cepheids, blue stragglers in field and cluster populations, hot B Main-Sequence stars, etc., and finally, the enrichment with neutron-capture elements in the galactic stars.

Keywords: stars: abundances – stars: atmospheres – stars: different types – techniques: spectroscopic.

АНОТАЦІЯ. Подано короткий огляд результатів, отриманих в Одеській астрономічній обсерваторії за аналізом спектрів зірок з 1892 по 2000 рр. Огляд починається з перших спостережень емісійних ліній у сонячних протуберанцях, здійснених у 1892 році під керівництвом Олександра Кононовича, і включає огляд спектрофотометричних досліджень, проведених в обсерваторії за допомогою інструментів і телескопів, розроблених власними силами; теоретичний розгляд питань моделювання фізичних умов у зірках та моделювання спектрів починаючи з 60-х років 20-го століття. Також описані основні результати дослідження зірок різних типів, включаючи холодні гіганти K-, M спектральних класів, зірки з різними особливостями хімічного складу, який проявляється посиленими лініями металів і смуг молекули циану CN, подвійні системи різних типів та їх моделювання, напів-правильні та довгоперіодичні змінні зірки, зірки типів RR Ліри, δ Щита та λ Волопаса, різновиди цефеїд, блакитні страглери поля та скупчень, гарячі зірки B Головної Послідовності тощо, і, нарешті, збагачення галактичних зірок елементами захоплення нейтронів.

Ключові слова: зірки: хімічний склад – зірки: атмосфера – методи: спектроскопічний.

1. Introduction

The first spectral observations started in 1892 under the leadership of Alexander Konstantinovich Kononowitsch (1850-1910), the Director of Odesa Astronomical Observatory and Head of the Department of Astronomy of Odesa University, and they continued till 1895. Those were observations of solar prominences with a double-prism spectroscope for visual observation of the radiation spectrum (constructed in the workshop by Mr Toepfer, Potsdam) donated to Odesa observatory by the Academy of Sciences after Fedor A. Bredikhin, the Director of Pulkovo Observatory, arrived in Odesa in 1891. It was due to his direct involvement that systematic observations of the solar chromosphere with a prominence spectroscope began so early. The observations yielded drawings of solar prominences, marks of the width of the prominence base and height, as well as an indication of the presence of emission in the lines of hydrogen (Hα, Hβ and Hγ) and helium. Alexander Kononowitsch, Nicolas Zwetinowitsch, Artem Orbinsky and Aleksey Hansky participated in the observations. The observation results obtained over two years (1892-1893) were published in the Notes of Odesa University (Kononowitsch *et al.*, 1893). Later, there was a break in the spectral research until the 1960s, when throughout the globe an enormous interest in physics and space emerged, and young vigorous students and researchers joined the Department of Astronomy and Astronomical Observatory of Odesa University. Spectrophotometric and spectral studies of different types of stars, including variable stars, began to develop at the Astronomical Observatory, which traditionally dealt with astrometry, meteors and visual observations of variable stars.

2. Spectrophotometric investigations

Valentin Karetnikov and Yuri Medvedev started experimenting in this area of research as early as in 1964. They converted (adapted) an ordinary photoelectric photometer for spectroscopy (Karetnikov & Medvedev, 1966). Spectral energy distributions in the continuum of stars α And, β Ari and α Cyg were obtained, with α Lyr being observed as a reference standard, and then compared with those available in the literature. Noticeable chromatic aberrations in the red and especially blue regions due to the primary lens did not allow the researchers to obtain more accurate results or use the tool in their further research.

In the same years, Vladimir Pozigun and Nikolai Komarov created an electrospectrophotometer for observations in the near infrared region of the spectrum and, for the first time in the Soviet Union, they carried out observations and studies of stars by their energy distributions in the IR region of the spectrum (Komarov & Pozigun 1968). As a radiation receiver they used a photomultiplier, which had been semilegally brought back from a business trip to the USA (according to the legend, it was brought in a pocket) by Vladimir Platonovich Tsesevich, the Director of the observatory. The studies of energy distributions in the spectra of stars were performed at Odesa Astronomical Observatory (OAO) with a 17" telescope with an objective (4°) prism and an RCA7102 photomultiplier using evaporative cooling with carbon dioxide; the spectra were presented on a recorder. In September 1966, trial observations of Vega (α Lyr) and χ Cygnus were carried out. The IR electrospectrophotometer functioned at the observation station of the Astronomical Observatory in Mayaki village till 1970. The first observation station outside Odesa was arranged in the village Vannovsky (near Ashgabat, Turkmenistan) with a 17" telescope and an IR spectrometer transported and installed there; the station operated from 1970 to 1975.

In subsequent years, several telescopes were created at the Astronomical Observatory under supervision of its Chief Engineer, Leonid Paulin. Different equipment, spectrophotometers and photometers were also made by the Astro-Instrument Engineering Department and further employed in various observations at new observing stations and other observatories, where the new telescopes were installed or the existing ones were used. In particular, in the North Caucasus (Peak Terskol, during that period of time – at MAO of Academy of Sciences of Ukraine), they installed 80-cm AZT-7 telescopes (constructed at Odesa observatory) and spectrometers operating in the visible and infrared regions. Then, Seya-Namioka type spectrometers were installed on telescopes in Abastumani (Georgia, 1973-1974) and in the village of Mondy (Sayan mountains, Solar Observatory of the Siberian Branch of the USSR Academy of Sciences), at the stations of the MAO of the USSR Academy of Sciences (Bezymyanny (Nameless) Pass, Armenia and Murgab, Pamir, a 80-cm telescope); on the mount Dushak-Erekdag (Turkmenistan, a 80-cm telescope), etc.

3. Spectral investigations

After a brief report of the spectrophotometric studies conducted at the observatory, now let me focus our attention on the studies and analyses of both variable and non-variable stars, performed using spectra with low, medium and high dispersion (resolution), as well as on the studies related to the modelling of spectra, which have been carried out at OAO since the late 60s.

The first researcher who showed his interest in spectral research was Nikolay Komarov; his graduation research was devoted to the spectra of meteors and carried out under the guidance of Efim Naumovich Kramer, the graduation thesis was entitled *Spectra of Meteors*. In 1961, N. Komarov became a graduate student of Vladimir Platonovich Tsesevich with the research task to study variable stars. However, Sergei Rublev's actively developing theoretical studies of radiation transfer in stellar atmospheres and observations of stellar spectra appealed to Nikolay Komarov. Rublev directed Komarov to the Crimean Astrophysical Observatory in order to obtain spectra for his dissertation, and Nikolay Komarov conducted spectral observations with a 50(48)-inch reflector. Actually, the primary mirror of that refractor is 48 inches in diameter, but among astronomers it has been dubbed a "fifty inch" one. Ivan Kopylov, the Vice-Director of the Crimean Astrophysical Observatory and an outstanding scientist, suggested that N. Komarov deal with poorly studied so-called "metal" stars, the Main Sequence stars with enhanced metal lines. Among the stars belonging to the A2-F2 spectral types, there is a large group of stars with enhanced metal lines. These are the lines of such elements as Ca, Zr, Sc, Mg, Ti, V and H. The first PhD thesis that used stellar spectra and spectrum modelling and was successfully defended in Odesa was that one by N. Komarov entitled *Kinematic and Morphological Properties of Stars with Enhanced Metal Lines* (1969).

In his dissertation research, N. Komarov used spectrograms of 29 stars obtained with a spectrograph attached to the 122-cm (50") telescope of the Crimean Astronomical Observatory (CrAO). The following models of stellar atmospheres in the spectral interval of A0-F0 near the MS were constructed: LTE, plane-parallel, radiative and hydrodynamic equilibrium. The temperature distribution was found in the gray approximation and with the Chandrasekhar intensity averaging over direction. Metals were used to be a source of opacity. Subsequently, the temperature distribution was corrected for the non-gray atmosphere by the Swihart method assuming a constant flux of radiant energy at different optical depths. The grid of models was calculated on the Ural-2 computer at the Computing Centre of Odesa State University with different hydrogen content relative to metals for Teff = 9000, 8000, 7000 and 6000 K; log g = 4 and 3. The models with stellar envelopes were calculated (Golinko *et al.* 1969). A catalogue of 380 "metal" stars was compiled. It was the most advanced and up-to-date research performed at that time.

3.1 Analysing and modelling spectra

Analysing spectra provided new opportunities and gave a new tool in the examination of physical conditions in stellar atmospheres, thus enabling to determine the temperature and gravity on the surface of stars, the chemical composition, the relationship between various parameters and the physics of the different processes occurring in stars and manifesting themselves in the stellar spectra, etc. Stars of late spectral classes (cool stars) were of particular interest at the time. The interpretation of their spectra, streaked with molecular bands and lines, required new approaches both in determining parameters of such stars and in calculating the molecular spectra as such, as well as analysing their effects on the parameters and structure of atmospheres. A progress in that area of research could be made by in-depth studies of physical processes that enabled to model stellar atmospheres and

spectra. An important role in studies of cool stars was played by the *Stellar Atmospheres* Working Group founded by Nikolay Komarov, Nail Sakhibullin, Arved Sappar and Yanis Straume in the early 1970s.

The first study devoted to modelling atmospheres and envelopes of stars was the afore-mentioned research performed at OAO by N. Komarov in collaboration with V. Golinko and Zh. Krasnova (1969); it yielded model atmospheres and envelopes of A0-G5 stars. Theoretical modelling of processes in the atmospheres of cool stars was initiated by several investigations conducted by Vladimir Panchuk. He considered the propagation of a shock wave and convection in M-stars (Panchuk, 1970; 1972), and also calculated absorption spectra of titanium oxide molecules in the atmospheres of M-stars (Panchuk, 1974). Vladimir Panchuk constructed model atmospheres of stars of late spectral classes and deliberated *Equations of state. Part I* (Panchuk, 1974), *Sources of opacity. Part II* (Panchuk, 1975), and *The Possibility of Constructing Model Atmospheres of R CrB type Stars* (Panchuk, 1975). Blanketing effects in the radiation of cool M stars were studied by Alina Dragunova and Vladimir Panchuk using spectra with a dispersion of 37 A/mm (Dragunova & Panchuk, 1978).

Vadim Tsymbal, Vladimir Panchuk and Nikolay Komarov played a significant role in developing methods for analysing and modelling stellar spectra (computation of the synthetic spectrum). Vadim Tsymbal presented an important work entitled *Synthetic Spectra of Late-Type Stars* (Tsymbal, 1980). The programme code STARSP developed by Tsymbal to calculate the atomic and molecule synthetic spectrum with several subsequent modifications has been used by many scientists involved in studying chemical compositions of stars of different types up till now. Tsymbal calculated and reported *Column Densities of Opacity Particles in Cool Stars* (Tsymbal, 1980) and presented the tables of Franck-Condon factors with account for vibrational-rotational interaction for astrophysically important molecules ZrO, SiO, C2 and LAO (Tsymbal, 1980). Nikolay Komarov together with V. Tsymbal considered the thermochemical equilibrium of atoms, ions and molecules in the atmospheres of cold stars (Komarov & Tsymbal, 1980; 1987), calculated the effective depths of line formation and improved the growth curve method (Komarov *et al.,* 1979; Komarov & Mishenina, 1983). The effects of chemical composition in the atmospheres of M-, S- and C-stars were considered by Tsymbal & Panchuk (1980). To study those effects, the system of ionisation and dissociation equations was solved using an ES-1040 computer by the Newton-Raphson method; 94 chemical elements and 227 molecules were taken into account. The carbon content was a calculation parameter, O/C: 1.82, 1.2 and 1.02, which corresponded to M-, S- and C-stars, respectively. It was shown that the function of the number of M-, S- and C-stars should be monotonically decreasing over the whole range of spectral types and that one should expect a noticeable dispersion of the O/C ratio among M stars.

3.2. The equipment, telescopes and spectrographs

Since the 1960s, spectral studies have been carried out at OAO using spectra with high and low dispersion (to obtain parameters and chemical composition and to make spectral classification, respectively), obtained by the observatory staff using telescopes and spectrographs at other observatories in the Soviet Union and throughout the globe. High dispersion spectra have been obtained with the following telescopes: a 50 (48) inch or 122 cm reflector of the Crimean Astrophysical Observatory and an echelle spectrograph (Cassegrain focus, inverse dispersion (14 A/mm and 37 A/mm)); a 6-m Large Azimuthal Telescope (BTA) of the Special Astronomical Observatory of the Academy of Sciences of the USSR with the main stellar spectrograph (OZSP, inverse dispersion 5 A/mm) and NES (a high-resolution echelle spectrometer, R = 60 000), which are in the focus of Nasmyth-2; a 1-m telescope (Zeiss-1000) of the SAO RAS with a coudé-echelle spectrometer (R = 30 000); a 1.52-m telescope at the Observatoire de Haute Provence (France) with spectrograph AURELIE (R= 110 000); a 2.7-m telescope at McDonald Observatory, USA. In order to obtain low dispersion spectra, telescopes and prism spectrographs of Abastumani and Shamakhy observatories have been used.

4. Spectral studies (main results)

Now let me present the main results obtained by different groups of scientists at the observatory from the late 1960s to the year 2000.

4.1. Cool stars

Based on high-dispersion spectra (a dispersion of 5 A/mm), an analysis of the chemical composition of cool long-period and semi-regular variable stars was carried out by N. Komarov (Komarov *et al.,* 1973; Komarov *et al.,* 1977). The temperature was determined from the ratio of the intensities of the titanium oxide band heads. That made it possible to reliably determine elemental abundances from the lines of atoms and ions for cool variable stars. To analyse the chemical composition, a part of the spectrum in a narrow wavelength range free from strong absorption in molecular lines and the growth curve method were used. The studied stars were found to contain elements at levels close to the solar ones.

Applying the differential method of growth curves to the study of the chemical composition of stars (Komarov *et al.,* 1979; Komarov & Shcherbak, 1979) made it possible to determine the relative abundances of elements in atmospheres of stars with an accuracy of about ±0.1dex; to demonstrate by an example study of 12 galactic open clusters that the matter in the spiral arms of the Galaxy was distributed irregularly and might differ in the chemical composition (Komarov & Shcherbak 1980a) and to estimate the value of the radial metallicity gradient in the Galactic disc $d[Fe/H]/dR = -(0.07\pm0.03)$, which was close to the modern value (Komarov & Shcherbak, 1980b). Moreover, N. Komarov and A. Shcherbak investigated elemental abundances in the atmospheres of cool stars of different ages (Komarov & Shcherbak, 1980c), determined abundances of chemical elements in the atmospheres of cool giant stars (Komarov &

Shcherbak, 1980d) and in K-giants (Komarov & Shcherbak, 1980e).

In the 1980s, the research continued with studying the abundances of chemical elements in the atmospheres of K-giant of fields (Komarov *et al.,* 1985) and the Hyades cluster (Komarov *et al.,* 1986). An interpretation of spectra of K and M giants with low resolution was considered (Komarov & Motrich, 1987) and Catalogue of fundamental characteristics of stars of late spectral classes (Motrich, 1988) was created. Of particular note is to mention the study on the determination of the sodium abundance in the atmospheres of K-giants performed at OAO for the first time using the synthetic spectrum method developed by V. Tsymbal (Komarov *et al.,* 1985); the first works focused on studying neutron-capture elements, molybdenum and ruthenium in K-giants (Komarov & Mishenina, 1988), the abundances of barium and lanthanides in the Hyades giants (Gopka *et al.,* 1990) and abundances of heavy elements in Aldebaran (Gopka & Komarov, 1990). Moreover, the methods of research and modelling spectra were improved: a method for the simultaneous determination of atmospheric parameters was developed by Oleksandr Yushchenko, and the first study of the effects of deviations from Local Thermodynamic Equilibrium (LTE) on the sodium abundance was performed at OAO by Korotin & Komarov (1989).

In the 1990s, the advancement in the studies of possible sources of the origin of chemical elements, calculations of theories of nucleosynthesis, modelling the Type I and II supernovae and creating models of the chemical evolution of the Galaxy required the list of the studied elements to be expanded. To a large extent, that was due to the attention to the elements formed in neutron capture processes. The abundances of a number of elements formed in neutron capture processes (strontium, yttrium, zirconium, niobium, molybdenum, ruthenium, rhodium, barium, lanthanum, cerium, praseodymium, neodymium, samarium, europium, gadolinium, dysprosium, thorium, tellurium and erbium) were measured in K-giants, standard stars (Arcturus, Aldebaran and Procyon) and the Sun (Gopka *et al.,* 1991). Vera Gopka and Oleksandr Yushchenko carried out research on the identification of absorption lines of dysprosium in the solar spectrum (Yushchenko & Gopka, 1994a), determined and analysed the abundances of iron and light lanthanides in the atmospheres of Arcturus and Aldebaran (Gopka & Yushchenko, 1994), the thorium abundance in the atmosphere of Procyon (Yushchenko & Gopka, 1994b), the erbium content from the spectra of the Sun and Procyon (Gopka & Yushchenko, 1995), the abundances of rhenium and tellurium in Procyon (Yushchenko & Gopka, 1996a), the abundances of heavy elements in the atmosphere of Procyon (Yushchenko & Gopka, 1996b), as well as the abundances of thorium and uranium in the atmosphere of Arcturus that were determined in collaboration with A. Shavrina and A. Perekhod (Gopka *et al*., 1999). The abundances of magnesium isotopes – ^{24}Mg, ^{25} Mg and ^{26} Mg – in the atmospheres of G-K giants were studied by Kovtyukh *et al.* (1999).

The investigation of giant stars of late spectral types also continued. Fundamental characteristics of cool giant stars were determined from photometry in the Geneva and Gildenkern systems using a large number of standard stars for the calibration; the catalogues of T_{eff}, log g and Fe/H were obtained in the two afore-mentioned systems for 1,000 and 600 stars, respectively. The metallicity data of stars belonging to dynamical groups and open clusters did not confirm the presence of a linear metallicity-age relationship. A conclusion about the existence of two age groups among disc giants was drawn (Komarov & Korotina, 1992). Absolute apparent magnitudes, absolute bolometric magnitudes, luminosities, radii and masses were found for 1,370 giants in the vicinity of the Sun. The metallicities were determined for giants in 27 open clusters and moving groups of various ages. The velocity of mixing in the interstellar medium has been increasing in the course of evolution of the Galaxy. The age of cool giants, especially of metal-deficient ones, in the solar neighbourhood can be compared to the age of globular clusters (Komarov *et al.,* 1996). The chemical composition of two Praesepe stars was found via atmospherical modelling. The abundances of chemical elements in the atmospheres of K-giants were found to be close to those of the Sun (Komarov & Basak, 1993). The chemical composition of atmospheres of cool giant stars (Komarov, 1994), the effects of the diatomic molecules on the structure of the outer layers of cool giant stars (Komarov & Dulapchi 1994), the structure of the outer atmospheres of cool giant stars (Komarov & Shevchuk, 1995), the problems of determination of abundances in the atmospheres of K giant stars (Komarov *et al.,* 1997a), the chemical abundances in the atmospheres of K giant stars (Komarov *et al.,* 1997b) were investigated. The data on energy distributions in the spectra of 555 stars were reduced and used to compile the Spectrophotometric Star Catalogue in the wavelength range of 320-1080 nm for the B-M spectral types (Dragunova *et al.,* 1994); the mean stellar spectra of cool giant stars were obtained (Dragunova *et al.,* 1997) and mean energy distributions in stellar spectra were determined for 555 stars (Komarov *et al.,* 1998). The studies were aimed at the investigation of the low dispersion synthetic spectra of cool giant stars (Belik *et al.,* 1997), the energy distributions in the spectra of stars in the region of λλ320-750 nm (Komarov *et al.,* 1997c) and the determination of characteristics of F-, G- and K-type stars. The effective temperatures were determined (Komarov *et al.,* 1999), and the catalogue of fundamental characteristics of cool giant stars was compiled (Komarov *et al.,* 2000).

In the 1990s, the Galactic disc, open and globular clusters, as well as metal-poor stars, were included in the scope of research at OAO with active participation of Tamara Mishenina. Based on the studies of clusters and dynamical groups, it was shown that the chemical homogeneity of the Galactic disc was observed in the solar vicinity, within 1.5 kpc from the Sun (Klochkova *et al.,* 1989). The obtained oxygen abundance in the Hyades K-giants was close to the solar one; the determination was performed through the synthetic spectrum method in the LTE approximation (Komarov *et al.,* 1990). The behaviour of elemental abundances in metal-poor stars differed from that of the scaled solar abundance. It related, first of all, to various abundances of CNO elements, an

excess of α-elements and elements formed in the slow neutron capture processes (Mishenina *et al.,* 1995; Mishenina *et al.,* 1997). An evidence of mixing in giants of the M13 globular cluster was found based on the examination of five stars in the M13 globular cluster and two halo stars, using data taken from the literature (Mishenina & Kutsenko, 1994) and obtained in spectral research of some stars in the M13 globular cluster, including the II-90 giant (Klochkova *et al*., 1994), an RGB giant and an AGB giant (Klochkova & Mishenina, 1998). A comparison of elemental abundances in GC with those in halo stars showed a difference in the abundances of Na, Mg and elements of the rapid (r-) and slow (s-) neutron capture processes in the studied stars. The model atmospheric parameters and chemical abundance curve were derived for the infrared source IRAS 09276+4454 and identified with the peculiar supergiant HD 82040 (M6). The effective temperature was determined from the hand head intensity relations of the TiO α-system. The abundances of 11 chemical elements in the atmosphere of IRAS 09276+4454 were estimated. The chemical abundance pattern was found to be close to the solar one (Klochkova *et al*., 1997).

An important study performed by Mishenina *et al.* (2000) turned out to be a decisive argument in the astrophysicists' dispute about the oxygen enrichment of the Galaxy, in particular concerning the trend of oxygen and its abundance in low metallicity stars. In the study, oxygen abundances for 14 halo stars were derived from the O I 7774 A triplet using high-resolution spectra (R = 25 000; S/N > 100) obtained with the echelle spectrometer attached to the 6-m telescope of the SAO RAN. The effective temperature was determined from the wings of the Hα line using photometric indices. The oxygen content was analysed using both LTE and non-LTE approaches. To this end, a model of the oxygen atom was created by Sergei Korotin. The average value of [O/Fe] turned out to be 0.61 ±0.21 when determined in the non-LTE approximation. It was found that the oxygen abundance was increasing with decreasing iron abundance. The relationship between [O/Fe] and [Fe/H] was linear: [O/Fe] = -0.370 x [Fe/H] + 0.047. In addition to the sample of programme stars, 24 stars from the study by Cavallo *et al.* (1997) were also involved in the analysis after all necessary non-LTE corrections. The study may be called a reference one, because it was carried out by the authors representing an independent group of astrophysicists, using independent spectral observations, and received about 100 citations so far.

As a part of the study of the Galactic disc stars with specific features in the spectra, among the stars of late spectral types (giants and sub-giants), a special attention was drawn to those with enhanced metal lines, referred to as Super Metal Rich (SMR) stars, as well as to the stars with enhanced CN indices, which were characterised by enhanced CN molecular bands. Based on the high-dispersion coudé-echelle spectra obtained with the 1-m telescope at the SAO RAS, a number of parameters and chemical composition were determined for five stars with enhanced CN indices (Mishenina *et al.,* 1995), three stars with enhanced CN2 indices (Mishenina & Kutsenko, 1996) and 31 Aquilae (Mishenina, 1996). Four stars – namely, HD 176411, HD 181984, HD 190940 and HD 207130 – were found to be normal giants in the post first dredge-up phase; the star HD 222404 (γ Cep) was considered to be unmixed star. HD 181984 (τ Dra), being presumably a metal-rich star, exhibited a metallicity of [Fe/H] = +0.10 dex. It appeared to be deficient in C and O while overabundant in Na, Al and Mn. Three stars – HD 176411, HD 190940, and HD 207130 exhibited near-solar metallicity, they were deficient in C and O while overabundant in Na and Al. The derived abundances of O, Na (and Al) might be an evidence for anomalous mixing in those stars. The chemical composition of HD 222404 was close to that of the Sun. The programme stars had, on average, solar abundances of Y, Zr, Ba, La, Ce, Pr and Nd within the errors of determination. Three stars with enhanced CN2 indices turned out to be typical giants of the Galactic thin disc with an overabundance of Na and solar abundance of neutron-capture elements. The star HD 188056 (presumably, a SMR star) had [Fe/H] = 0.14 and was overabundant in C, Al and Mn.

31 Aquilae is the only evolved star for which the SMR status has been confirmed. This is why a new determination of the environmental parameters and chemical composition of 31 Aql was carried out (Mishenina, 1991). The new [Fe/H] value was +0.32±0.15 dex, which was close to the [Fe/H] limit for dwarf stars belonging to the thin disc of the Galaxy. The value of the Li abundance log A(Li) = 1.35. The value [C/H] obtained in the study was -0.05±0.11 dex. Within the errors, solar scaled values of [Element/Fe] were obtained for Na, Y, Zr, Ba, La, Ce, Pr and Nd. The age of 31 Aql and its location in the Galaxy were estimated, and a thorough analysis of the abundance determination errors was carried out. 31 Aql was found to be in the evolutionary stage when the convective envelope begins to extend. Two stars with the likely SMR status and an excess in metallicity – HD 121370 (8 Boo) and HD 218640 (89 Aqr) – were studied on the basis of spectra obtained with the echelle spectrometer of the 6-m telescope at the SAO RAS. Atomic and molecular spectra were used to determine abundances of 25 elements, including Li and elements of the CNO group. The metallicities [Fe/H] for the stars were +0.23±0.15 (8 Boo) and +0.19±0.19 (89 Aqr). Such values were close to the upper limit of [Fe/H] for dwarf stars in the Galactic disc (Mishenina, 1998).

To clarify the evolutionary status and spectral classification, the abundances of Li and CNO in the atmospheres of nine peculiar giants (eight CN-strong stars and the SMR star 31 Aql) were estimated through the method of model atmospheres (Mishenina & Tsymbal, 1997). The derived Li and CNO abundances were close to the mean values for the disc G-K giants; it suggested that the stars had gone through the mixing phase (were in the phase after the first dredge-up). For the CN-strong stars, the C/O ratios implied a slight carbon overabundance in their atmospheres, but it was insufficient to substantiate the hypothesis of Keenan & Heck (1994) that the CN-strong stars could be marginal R stars belonging to a special class of carbon stars. The sodium abundances in 12 peculiar disc stars with Na excesses were determined taking into account deviations from LTE. In some cases, the non-LTE corrections reached 0.2 dex; however, on

average, it did not exceed 0.1 dex, and the Na excesses for most of the stars were not eliminated by taking non-LTE corrections into account (Korotin & Mishenina, 1999).

4.2. Eclipsing binaries

The first spectrophotometric studies carried out by Valentin Karetnikov were focused on the Pleiades cluster stars (Karetnikov & Vykhrestyuk, 1973), the eclipsing star RZ Scuti on low-dispersion spectrograms (Karetnikov, 1967; 1972), the eclipsing binary V367 Cygni **(**Karetnikov & Perekresny, 1973) and the determining of the electron density in stellar atmospheres (Karetnikov *et al.,* 1973). Later, the results of a spectral study of Nova Cyg 1975 based on diffraction spectrograms obtained from August 30 to September 26, 1975 were presented (Karetnikov & Medvedev, 1977). The depths and intensities of the absorption and emission lines in the spectrum of Nova, as well as the velocity of the envelope of new absorption components based on the displacement and the half-widths of the emission lines were calculated (Karetnikov *et al.*, 1986), and spectroscopic observations of Nova Vul 1976 = NQ Vul were carried out (Karetnikov *et al.*, 1977).

Studying spectra of eclipsing stars, establishing spectral types of components, examining the behaviour of hydrogen and helium lines with the revolution period and phase, the presence of emission in the lines of metals and hydrogen, the "mass loss-envelope mass" relation, etc., made it possible to detect gas flows and envelopes in such systems and construct relevant models. The stars RY Per, V367 Cyg, V448, RY Gem, TX Uma and XZ Cep were studied. RY Per had a complex spectrum, and the spectral lines also changed in a complex way. The hydrogen lines showed a change in the equivalent width with the revolution period, while the helium line profiles changed markedly with the phase. The emission lines of metals were also found in the spectrum. The electron pressure was calculated from hydrogen lines, and the RY Per model was built from observational data (Karetnikov & Kutsenko, 1979). Based on diffraction spectrograms with a dispersion of 37 A/m in the wavelength range of 3700-4700 A, physical characteristics of the atmospheres of both stars in RY Per were determined by the method of growth curves. The results obtained were consistent with the spectral classes B5V and F61V for the two stars. It was suggested that gas streams and a common envelope were present in RY Per (Karetnikov *et al.*, 1979).

Spectral observations of the eclipsing binary star V367 Cyg reported that the structure of the spectrum was of the envelope type with emission in Hα and Hγ lines. The Mg II line at 4481 Å, as well as the wings of the hydrogen lines, was found exclusively in the main star. The structure and velocity of the gaseous medium in V367 Cyg were studied from the emission components in the Hγ line. A gas flow of the secondary component was observed passing through the Lagrange point L(1). The outflow of matter from V367 Cyg was estimated to be about 0.0000323 solar masses per year. A line showing the structure of the stellar envelope was presented (Karetnikov & Menchenkova, 1985). A spectroscopic study of the massive close binary system V448 Cyg was conducted. Based on spectrograms with dispersions of 9 and 28 Å/mm, the spectral types were determined as B1.2Ib+O8.9V. Hydrogen and helium line profiles had anomalies. The model of the eclipsing system V448 Cyg was discussed in detail (Glazunova *et al.,* 1986). The RY Gem binary system was also studied. The spectral type and luminosity, excitation temperature, turbulent velocity, electron pressure in the atmosphere and envelope, as well as concentrations of atoms of some chemical elements in the star were determined. It was noted that the concentrations of chemical elements were systematically lower than the "solar" concentrations (Karetnikov & Menchenkova, 1987).

Motions in circumstellar gaseous structures and rotations of the TX Uma stars were determined from the detected emission and absorption components of the profiles of the Hβ, Hγ, K Ca II and Mg II λ4481 Å lines. The value of the mass loss rate of the system was found (Karetnikov & Kovtyukh, 1987). For the RY Sct binary star system, the dependence "mass loss-envelope mass" was constructed on the basis of the data on the masses of the eclipsing binary star envelopes, derived using polarimetric and spectral methods, as well as on the mass losses calculated from the variations in the periods of those stars. The dependence was confirmed by the data on the RY Sct eclipsing star with an envelope (Karetnikov, 1987). The spectrum of the XZ Cep star turned out to be composite, with a complexly changing line profile, a phase change in the equivalent widths of hydrogen and helium lines, and a change in the electron concentration in the shell. The system consisted of the main star B1.5 II-III and the satellite B1.1 III-V, between which a gas flow was observed. Stars were surrounded by envelopes, the heavier of which surrounded the secondary component (Glazunova & Karetnikov, 1985). At that time, the studies aimed at modelling the flow of matter in the investigated close binary systems were carried out actively: for instance, the formation of a gaseous flow in the vicinity of the inner Lagrangian point for XZ Cep (V. Nazarenko 1992); the matter flow formation in W Serpentis-type binaries (Karetnikov *et al.,* 1995a), W Draconis binary stars (Karetnikov *et al.,* 1995b), semidetached AO Cassiopeiae-type eclipsing binaries (Karetnikov *et al.*, 1995c), W UMa contact close binaries (Karetnikov & Nazarenko, 1996a) and R CMa-type systems (Karetnikov & Nazarenko, 1996b).

4.3. Variable pulsating stars of the RR Lyr and δ Sct types and Cepheids

The RR Lyr and δ Sct type stars. Many magnetic stars are located within the instability band of short period δ Scuti type variable stars. Photometric periods of changes in the brightness of magnetic stars, obtained by different authors, often turn out to be close to the known periods of stars of the δ Scuti type. Therefore, it was of interest to study magnetic fields of pulsating stars. Magnetic fields in pulsating variable stars of the RR Lyr and δ Sct types were first studied at OAO. The magnetic field in variables of the RR Lyr type was first mentioned in the study by Romanov & Udovichenko (1981); later on, there were attempts to determine the magnetic field of the stars V474 Mon, α^2CVn and β CrB (Romanov, 1985; Romanov *et al.,*

1984; 1985), and variations in the depression in the 5200 Å region depending on the value of the magnetic field for α^2CVn and β CrB were presented (Udovichenko, 1987). The spectra obtained with the 6-m telescope at the SAO RAS were employed to study variations in the magnetic field strength and its polarity. It was found that the average value and polarity of the magnetic field changed with a period of 41 days (the Blazhko effect). It was suggested that long-period variations of the magnetic field with the Blazhko effect could be explained by the rotation of a star with the same period (Romanov *et al.*, 1987). A study of five stars – RR Lyr, V474 Mon, X Ari, TU Cas and VW Dra – as well as their rotational velocities and parameter ΔS was carried out on the basis of spectral research. The dependences of the decrease in the half-width of the Mg II λ448.1 nm and Fe I λ447.6 nm lines on the rotational velocities of the standard stars were found. Those relations were used to determine the rotational rates of the variable stars RR Lyr, V474 Mon, X Ari, TU Cas and VW Dra (Zaikova & Udovichenko, 1988). Based on the spectra with a dispersion of 37 Amm, the ΔS parameter of RR Lyrae stars was revised and rotational velocities of some pulsating SW And stars were determined (Zajkova & Romanov, 1988; Zajkova *et al.*, 1992). Based on the profiles of the hydrogen lines for 28 Be stars and Be stars with stellar envelopes, it was established that the origin of the envelopes in those stars was associated with the mass loss due to rotation, which corresponded to the presence of a rotating equatorial disc (Udovichenko & Konchagina, 1997). The radial velocities were determined for RZ Lyr (Romanov, 1977) and V474 Mon (Udovichenko, 1994).

Studying chemical composition of permanent and variable stars required knowledge of a certain reference chemical composition for stars - it related, first of all, to the chemical composition of the Sun, as well as chemical compositions of selected standard stars and the standard (unified) composition of stars of certain spectral classes. The standard chemical composition of the atmospheres of A1-G0 stars based on 14 chemical elements was determined for 12 stars of the A1-G0 spectral classes. The results obtained by the method of quantitative spectral classification were compared with the results obtained by the method of growth curves (Fenina & Romanov, 1980; 1982). Investigation of the spectral features of the variable stars RR Lyr and XZ Cyg showed a change in the spectral characteristics with the phase of the Blazhko effect (Romanov, Fenina and Vasilieva, 1981). A spectrophotometric study of the atmosphere of the yellow semiregular variable star VW Dra was carried out (Andrievsky *et al.*, 1985). The pulsating variable SW Andromedae and magnetic variable stars AF (73) Dra and β CrB were studied (Fenina & Romanov, 1985; Fenina & Zaikova, 1988). β CrB was analysed by the growth curve method (Zgonyaiko & Fenina, 1988). The system of equivalent widths of Fe I absorption lines was applied to determine regional (local) temperatures in physically variable stars and to analyse the two-component structure of the spectrum-forming metal layer in the Cepheid type star T Vul (Fenina *et al.*, 1990; 1991), as well as to study variations of parameters with phase in three Cepheids – RT Aur, T Vul and κ Pav (Fenina *et al.*, 1994). Based on several spectrograms of β CrB with opposite external characteristics, new independent determinations of the temperature of the spectrum-forming levels from the lines of neutral iron Fe I were carried out, and some physicochemical characteristics were determined by the methods of the growth curve and atmospheric models (Romanov *et al.*, 1998).

A series of studies focused on the δ Sct and RR Lyr type variable stars and Cepheids, based on the spectra obtained with the 50(48)" telescope at CrAO, were carried out by Gennady Garbuzov. An emission in the Hα line was deemed to be associated with the passing of a shock wave in the δ Sct type star VZ Cnc (Garbuzov & Mitskevich, 1984). Variations in the Hα line in the spectra of RR Lyrae stars - DH Peg and RZ Cep – were studied. Weak short-lived emission and splitting of the Hα absorption line into two components were found. The observed phenomena were compared for the RRab and RRc type stars, and it was concluded that the shock waves were formed in the atmospheres of RRc stars at higher layers than in the atmospheres of RRab stars (Garbuzov & Zaikova, 1986). A mechanism of excitation of chromospheric radiation from δ Sct stars was studied. It was suggested that such a mechanism could explain the occurrence and variability of chromospheric emission at the centre of the h and k Mg II lines in the spectra of pulsating δ Scuti stars. According to the model, the radiation was associated with the radiation of gas heated by a shock wave propagating in the outer layers of the star's atmosphere at phases close to the brightness maximum. Flux variability in the Mg II h and k lines was due to the motion of a shock wave in an inhomogeneous medium with decreasing density (Garbuzov & Andrievskii, 1986). The Hα line in the spectrum of the unique Cepheid V473 Lyr was studied. Variations in the Hα profile in the HR 7308 spectrum Cepheid were compared to those in beat Cepheids. It was concluded that the rapid Ha profile variations observed in HR 7308 were not characteristic of Cepheids. The qualitative similarity of those variations with the spectral manifestation of non-radial pulsations was emphasised (Andrievskij & Garbuzov, 1987). To search for and identify high-frequency radial oscillations in pulsating stars of the δ Scuti type, it was proposed to use information on variations in the equivalent widths and radial velocities on spectral lines formed in the outer layers of atmospheres (for example, Hα). The spectrograms revealed a fast variability of the Hα line in τ Peg, which was interpreted as a manifestation of radial vibrations in the 3rd and 5th overtones (Garbuzov *et al.*, 1987). Further studies focused on the Hα variability in τ Cyg (Andrievskii & Garbuzov, 1987) and a shock wave front in a continuum (Garbuzov & Paramonova, 1987).

Bimodal and multimodal Cepheids are stars that pulsate in two or more different modes. If the pulsation periods are close, then beats appear in the pulsations of Cepheids. Atmospheric parameters and abundances of a number of elements were determined in several studies of bimodal Cepheids. Deficiencies in iron and carbon, along with an excess of nitrogen, were obtained. Oxygen, α-elements and elements of the iron group, showed the solar ratios. The dependence of metallicity [Fe/H] on the period

ratio P_1/P_0 was obtained. The value [Fe/H] = -0.43 indicated that the TU Cas star was poorer in metals than other bimodal Cepheids (Andrievsky *et al.,* 1993). For three bimodal Cepheids – EW Sct, VX Pup and BQ Ser – the abundance analysis showed that a deficiency in carbon was accompanied by an excess of nitrogen and a normal (near solar) oxygen content. Alpha-elements and elements of the iron group, with few exceptions, showed the solar ratio [M/Fe]. Near solar iron abundance for EW Sct ([Fe/H] = -0.08) and metal deficiency for VX Pup ([Fe/H] = -0.39) and BQ Ser ([Fe/H] = - 0.36) strongly supported the existence of the P_1/P_0 to metallicity ratio (Andrievsky *et al.*, 1994). The abundances of helium and other chemical elements in the atmospheres of classical Cepheids were determined (Kovtyukh *et al.,* 1994).

The designation **s-Cepheid** is used for Cepheids with a short pulsation period and a small brightness amplitude with a sinusoidal light curve. It is reckoned that such objects pulsate in the first overtone. They are located near the red edge of the instability band. Studies of s-Cepheids with a short pulsation period show solar-like abundances of α- and iron-group elements, some Na overabundance; majority of these stars are deficient in carbon and overabundant in nitrogen which indicates that these s-Cepheids are not crossing the instability strip for the first time. But among them there are stars with different chemical composition, for instance, the unique Cepheid α UMi (Polaris), unique galactic Cepheid V473 Lyr and the s-Cepheid EV Sct binarity. An important factor in studying s-Cepheids is the idea to use barium lines as an indicator of luminosity. The s-Cepheids α UMi (Polaris) and HR 7308 (V 473 Lyr) were analysed. The unique Cepheid α-UMi exhibited a small overabundance of most elements relative to the Sun. A larger value of gravity as compared to the data of other authors could be due to a decrease in the Polaris pulsational amplitude. The analysis showed that light elements demonstrated a small overabundance while the Fe group elements were slightly deficient in the HR 7308 atmosphere (Andrievsky *et al.,* 1994).

Eight s-Cepheids and V1162 Aql (earlier classified as an s-Cepheid) were studied. All Cepheids (with the only exception of EU Tau) had solar-like abundances of α- and iron-group elements, and they all were overabundant in Na. The carbon deficiency found in EU Tau, DT Cyg and V440 Per and nitrogen overabundance (in DT Cyg) indicated that those s-Cepheids were not crossing the instability strip for the first time. The s-process elements were slightly enhanced in the programme stars. V1162 Aql did not show any changes in C and N abundances, the star known as a normal Cepheid (Cδ) was crossing the instability strip toward the giant branch for the first time. Such a conclusion was also confirmed by its position on the evolutionary diagram (Andrievsky *et al.,* 1996). A hypothesis about s-Cepheids' crossing the instability strip for the first time was verified by spectroscopic testing for seven s-Cepheids. V473 Lyr, IR Cep, UY Mon, BY Cas and V636 Cas had solar iron abundance whereas V526 Mon and V924 Cyg showed a moderate iron deficiency. The absolute carbon deficiency (relatively to the solar C/H value) found for all programme stars (with the exception of V636 Cas) and a nitrogen overabundance suggested that those s-Cepheids were not crossing the instability strip for the first time. V636 Cas also demonstrated a rather high abundance of carbon; perhaps, the star was crossing the instability strip for the first time. Na and Al were overabundant in all programme stars for which the two elements were estimated. The sodium overabundance was also observed in two Cepheids crossing the instability strip for the first time. Abundances of α-elements and iron-group elements were close to the solar ones, while those of s-process elements appeared to be slightly enhanced (Kovtyukh *et al.,* 1996).

The data for the unique galactic Cepheid V473 Lyr were revised. Results were obtained for 38 species of 32 chemical elements. The authors confirmed a slight underabundance of metals ([Fe/H] = -0.16). Carbon was deficient, and no significant overabundance was detected for sodium. Other elements with determined abundances did not show any marked anomalies (Andrievsky *et al.*, 1998). Spectroscopic manifestations of the s-Cepheid EV Sct binarity were reported. All lines in the spectrum of the Cepheid were noticeably asymmetric or even split, indicating that the system consisted of two components. Both components had similar effective temperatures; the difference in apparent values seemed to be small. Together with the preliminary results of the frequency analysis based on the published photometric data, such findings meant that the secondary was probably within the instability band as well, being a very short period Cepheid with P ~ 1.2 days (Kovtyukh & Andrievsky, 1999). The Ba II lines were proposed as indicators of the luminosity of yellow supergiants. In particular, it was shown that the equivalent width of the Ba II 5853.6 line correlated well with the luminosity for s-Cepheids (Andrievsky, 1998).

4.4. Blues stragglers, λ Boötes stars, B-stars and rapidly oscillating Ap stars (roAp)

Blue stragglers are Main Sequence stars in star clusters that are located above and to the left of the turnoff point on the Hertzsprung-Russell diagram. They have higher temperatures, luminosities and masses as compared to the other cluster stars. In several studies at OAO, the parameters and chemical composition of open-cluster and field blue stranglers were investigated. Blue stragglers in open clusters showed the same chemical peculiarities as ordinary cluster and Galactic field stars of the same spectral type. The modern view about the origin of blue stragglers states that they are the result of mergers of stars through mass transfers from an evolved star onto a main-sequence companion.

A spectral study of seven blue stragglers of the Galactic field was conducted. The iron abundance values for the studied stars varied from [Fe/H] = -0.9 dex to [Fe/H] = -0.3 dex. A preliminary interpretation of such findings was that the group of the field blue stragglers consisted of stars of different ages. Mg and Ca abundances (relative to iron) exceeded solar values (Andrievsky *et al.,* 1995). A spectroscopic investigation of 15 Galactic field blue stragglers and one normal F-dwarf showed that all stars were metal deficient. The mean value of [Fe/H] for 13 stars was -0.31±0.13 (two stars of the sample, namely HD54073 and HD88923, were likely to have a more pronounced iron deficiency); the estimated (C/H) and

(O/H) ratios were close to the solar values (i.e. those elements were slightly enhanced with respect to iron: [C/Fe] = ~[O/Fe] = ~0.3dex); sodium and α-elements in the field blue stragglers were slightly enhanced as well. Only magnesium showed practically the solar ratio: [Mg/Fe] was near solar one; as regards the iron group elements, Sc showed the solar ratio [Sc/Fe]. Cr and Ni were slightly overabundant; a rather great age of the investigated stars estimated from their metallicity was in contradiction to their locations in the evolutionary diagram. The problem could be eliminated by assuming that field stragglers were old objects with delayed evolution, similarly to blue stragglers in stellar clusters (Andrievsky *et al.*, 1996).

A spectroscopic study of four blue stragglers in old Galactic open cluster NGC 2632 (Praesepe) was carried out. The LTE analysis using Kurucz's atmospheric models and synthetic spectra technique showed that three stars, including the hottest star of the cluster HD73666, exhibited a uniform chemical composition: they showed a solar-like abundance (or a slight overabundance) of iron and an apparent deficiency in oxygen and silicon. Two stars exhibited a remarkable barium overabundance. The chemical composition of their atmospheres was typical for Am stars (metallic-line stars representing a type of chemically peculiar stars of spectral type A). One star of the studied sample did not share such a uniform elemental distribution, being generally deficient in metals (Andrievsky, 1998).

A spectroscopic study of blue straggler and Main Sequence B- and A-type stars in the open clusters NGC 3496, NGC 6475, NGC 6633 and IC 2602 was based on observations collected at the European Southern Observatory. A detailed analysis through Kurucz's atmosphere models showed that the MS stars rotated rather rapidly and exhibited abundances different from normal (solar) metallicity for only few light elements. The blue stragglers had significantly smaller projected rotational velocities. As a group, they showed the same chemical peculiarities as ordinary cluster and Galactic field stars of the same spectral type. Two blue stragglers and one MS star had a rather low content of helium. All investigated stars for which the C abundance could be measured showed a moderate-to-strong deficiency in carbon (Andrievsky *et al.*, 2000).

λ Boötes stars represent a rare type of peculiar stars. These stars are characterised by weak metal lines, indicating a lack of heavy elements, and extremely slow rotation. Most of them exhibit variability of the δ Sct type. The abundances of C, O, Na and S seem to be nearly solar ones for all investigated stars. There is a wide range of underabundances of all other elements in individual stars. Such results are consistent with the accretion/diffusion model adopted to explain the λ Boo phenomenon.

A new approach to the problem of the origin of λ Boo stars was discussed in the study by Andrievsky (1997). It was suggested that at least some of those stars might originate from contact binary systems of W UMa type. Simple estimations based on such hypothesis could account for the present-day number of λ Boo stars in the solar neighbourhood, their masses and spectral classes. What is also important is that the proposed scenario did not exclude circumstellar envelope formation, which was considered to be responsible for the chemical peculiarities of λ Boo stars. The atmosphere of VW Ari A (T_{eff} = 7200 K, log g = 3.7), the primary component of the visual binary system, was analysed. The synthetic spectrum technique applied in the analysis enabled to reveal that the atmosphere of the star was severely deficient in some metals whereas light elements were abundant at levels similar to the solar ones. Taking into account such results, VW Ari A could be assumed to be a lambda Boo type star. Another argument supporting such assumption could be found on the photometric diagrams. VW Ari A fell exactly in the region occupied by the λ Boo stars (Chernyshova *et al.*, 1998).

Seven well established λ Boo stars (a group of A to F type stars severely underabundant in Fe-peak elements while appearing to be solar abundant in C, N, O and S) – HD 31295, HD 125162, HD 142994, HD 149303, HD 192640, HD 204041 and HD 221756 – were studied. The abundances of C, O, Na and S seemed to be nearly solar ones for all investigated stars. There was a wide range of underabundances of all other elements within individual stars. No correlation between individual abundances and astrophysical parameters, such as T_{eff}, log g and vsini, was found. The results were consistent with the accretion/diffusion model adopted to explain the λ Boo phenomenon (Paunzen *et al*., 1999). Having analysed the accretion-based model of the dust-gas separation, which is regarded to be the most promising for the explanation of anomalous properties of λ Boo stars, we can conclude the following: (i) for any reasonable density profiles of the envelope, dust grains appear to be decoupled from the gaseous background within the region where the temperature drops below the condensation temperature of heavy elements, such as Mg, Ca, Fe, etc.; (ii) it is most likely that only small dust particles (of less than ~10-6cm in size) can be formed in the envelope of λ Boo-type stars; (iii) significant alteration of the initial atmospheric chemical composition can take place in the case when the density in the envelope changes as r^{-2} (Andrievsky & Paunzen, 2000). With regard to pulsation characteristics of λ Boötis-type stars for the star BD Phe (HD 11413): in-depth astroseismological studies have been carried out so far only for four members of this group of stars, and the number of identified frequencies for these stars varies from four to seven. In the relevant study, the authors presented a 30-hour UBVRI time-series photometry along with a 14-hour high signal-to-noise ratio high dispersion spectroscopy for the star BD Phe. At least seven frequencies were detected. Since they were all present in independent sets of observations, it was argued that the frequencies were fairly well defined despite the limited data. The results may be useful in the context of recently published models of δ Sct pulsations that take into account diffusion effects (Koen *et al.*, 2003).

B-stars hotter than the Sun are the MS stars located in a region close to the Cepheid region. A series of studies of B stars with the allowance for deviations from the Local Thermodynamic Equilibrium (NLTE) was carried out under the leadership of Sergei Korotin. To that end, he modified the complex programme MULTI (Carlsson, 1986), created models of the carbon and nitrogen atoms, and employed models of oxygen and sodium constructed

earlier. The carbon abundance in the atmosphere of the B star γ Peg indicated a slight deficit of [C/H] = -0.25 (Korotin *et al.*, 1998), so did the nitrogen content ([C/H] = -0.30) (Korotin *et al.*, 1999a), which did not substantiate the hypothesis of turbulent diffusion in massive MS stars. The abundances of C, N and O in the sample hot MS stars appeared to be sub-solar and probably unaltered by stellar evolution. A comparative analysis of elemental abundances in hot MS B stars, the Cepheid U Sgr and two cool supergiants belonging to young OC M 25 detected disagreement between abundances of carbon, oxygen and other elements in those stars; it might be due to the fact that chemical anomalies observed in B stars were caused by different mechanisms operated in those stars. It could indicate that turbulent diffusion in massive MS stars (discussed in Maeder, 1987) and the related appearance of the CN-processed material at the stellar surface could hardly be operating in γ Peg. Abundances of carbon and nitrogen in the sample hot MS stars were determined in the NLTE approximation and, in most cases, those abundances appeared to be sub-solar and probably unaltered by stellar evolution (Anrievsky *et al.,* 1999). The analysis was based on the spectra collected with a 1.52-m telescope at Haute Provence Observatoire (France). A non-LTE analysis of O II lines in a sample of hot MS B stars was performed. The derived oxygen abundances for the programme stars appeared to be sub-solar. A brief comparison between the oxygen abundance in B stars and those in stars of other related types was presented (Korotin *et al.,* 1999b). The chemical composition of B stars determined spectroscopically might not reflect correctly their true chemical composition or the chemical composition of the interstellar medium. On the other hand such abundance anomalies were not expected for F-G supergiants which had suffered the large scale mixing in the red giant phase (Luck *et al.,* 2000).

Investigation of non-radial pulsation of **Ap stars** was performed by David Mkrtichian. Rapidly oscillating Ap stars (roAp) belong to the class of non-radial pulsating stars oscillating in low-degree modes (l = 1–3) with a period of 4-15 minutes. A study of radial velocity (RV) and pulsation mode was carried out using a 2.7-meter telescope with an iodine cell at the McDonald Observatory (USA). For Θ Uma, variability was detected in radial velocities of the Hα hydrogen line with a period of 0.063 d. The variability had amplitude of 2K = 12.3 km/s and was reckoned to be caused by oscillations in the third radial overtone (Mkrtichian, 1990). Precise radial velocity (RV) measurements were carried out for five roAp stars (33 Lib, γ Equ, HR 1217, HD 134214 and HD 122970). Pulsational RV variations were detected in all five stars with amplitudes ranging from 50 to 400 m/s. For the roAp star HR 1217, the authors managed to detect 5 of the 6 known pulsation modes present in the star. A detailed line-by-line analysis of radial velocities revealed that the pulsational amplitude depended not only on atomic species, but on the line strength as well. It was deduced that the surface distribution of elements could act as a spatial filter thus enabling us to detect high degree modes, which was deemed to be not possible in stars with a more uniform distribution of elements due to cancellation effects. Precise RV measurements proved to be a powerful tool for probing both the vertical and horizontal structure of the pulsations in roAp stars (Hatzes, *et al.* 1998).

6. Conclusions

The first spectrophotometric observations in the near IR region of the spectrum were conducted at Odesa Astronomical Observatory in 1966. In the 70-80s, 28 telescopes with a primary mirror diameter from 30 cm to 1 m were constructed at the observatory under the general direction of Vladimir Platonovich Tsesevich and thanks to the developments of the Chief Engineer, Leonid Stepanovich Paulin. The mirrors were made and polished under the guidance of Nikolay Nikolayevich Fashchevsky. The Astro-Instrument Engineering Department, under the leadership of Vitaliy Nikonovich Ivanov, developed and constructed photometers and spectrophotometers for observations carried out in the Department of Astrospectroscopy under the leadership of Nikolay Sergeyevich Komarov. A large number of employees of the Department participated in spectrophotometric observation expeditions. In 1988, Valentin Karetnikov and in 1989, Nikolay Komarov successfully defended their doctoral theses entitled *Properties of Eclipsing Binary Stars at the Stage of the First Mass Exchange* and *Structure of the Atmospheres of Cool Giant Stars*, respectively.

Since the late 60s, the observatory has also been actively engaged in modelling spectra and radiation transfer in stellar atmospheres; the first calculations of atmospheric models were made by Nikolai Komarov and colleagues in 1969. The monograph *Cool Giant Stars* by N. Komarov summed up the results of work on modelling, as well as on spectrophotometric and photometric studies over the considered years (Komarov, 1999). The *Photometric and Spectral Catalogue of Bright Stars* was compiled in 1979 (Komarov *et al.,* 1979). Spectrophotometric observational data were partially included in the catalogue *Spectrophotometry of Stars in the Wavelength Range λλ 550 – 900 nm*" (Komarov *et al.,* 1983) and the spectrophotometric star catalogue (Komarov *et al.,* 1995), they were also presented in the final reports on 52 topics of the funded projects. A number of projects were carried out on spectral studies, modelling the structure of binary stars and the transport of matter in binary stars under the leadership of Valentin Karetnikov. Yuri Romanov and Sergei Udovichenko were practically the first to measure the magnetic field in RR Lyr type stars. A significant contribution to spectral research was made by Vladimir Pozigun, Vadim Karamysh, Alina Dragunova, Vadim Tsymbal, Zemfira Fenina, Tamara Mishenina, Svetlana Kutsenko, Stanislav Belik, Valery Motrich, Vera Gopka, Oleksandr Yushchenko, Elena Menchenkova, Lyudmila Glazunova, Tatiana Gorbaneva, Viktor Nazarenko, Sergey Korotin, Sergey Andrievsky, Valery Kovtyukh, Gennady Garbuzov, David Mkrtichyan and many others employees of the observatory. Successful research conducted at OAO in subsequent years proved that the scientific foundation laid in the 60-90s worked perfectly.

Acknowledgements. Author is grateful to the Laboratoire d'Astrophysique de l'Université de Bordeaux for their kind hospitality.

References

Andrievskii S.M., Garbuzov G.A.: 1987, *PAZh*, **10**, 223.
Andrievskij S.M., Garbuzov G.A.: 1987, *K FNT*, **3**, 94.
Andrievsky S.M., Makarenko E.N., Fenina Z.N.: 1985, *Prob Kosm Fiz.*, **20**, 60.
Andrievsky S.M., Chernyshova I.V., Ivashchenko O.V.: 1995, *A&A*, **297**, 356.
Andrievsky S.M., Korotin S.A., Luck R.E., Kostynchuk L.Yu.: 1999, *A&A*, **350**, 598.
Andrievsky S.M., Kovtyukh V.V., Usenko I.A.: 1996, *A&A*, **305,** 551.
Andrievsky S.M., Schönberner D., Drilling J.S.: 2000, *A&A*, **356,** 528.
Andrievsky S.M., Kovtyukh V.V., Bersier D. et al.: 1998, *A&A*, **329**, 599.
Andrievsky S.M.: 1998, *AN*, **319**, 239.
Andrievsky S.M., Chernyshova I.V., Kovtyukh V.V.: 1996, *A&A*, **310,** 285.
Andrievsky S.M., Chernyshova I.V., Usenko I.A. et al.: 1995, *PASP*, **107**, 219.
Andrievsky S.M., Gorlova N.I., Klochkova V.G. et al.: 1999, *AN*, **320,** 35.
Andrievsky S.M., Kovtjukh V.V., Makarenko E.N., Usenko I.A.: 1993, *M NRAS*, **265,** 257.
Andrievsky S.M., Kovtyukh V.V., Usenko I.A.: 1994, *A&A*, **281**, 470.
Andrievsky S.M., Kovtyukh V. V., Usenko I.A. et al.: 1994, *A&AS*, **108**, 433.
Andrievsky S.M.: 1997, *A&A*, **321,** 838.
Andrievsky S.M., Paunzen E.: 2000, *M NRAS*, **313**, 547.
Andrievsky S.M.: 1998, *A&A*, **334**, 139.
Belik S.I., Dragunova A.V., Komarov N.S.: 1997, *Odessa Astron. Publ.*, **10**, 50.
Chernyshova I.V., Andrievsky S.M., Kovtyukh V.V., Mkrtichian D.E.: 1998, *Contr. Astr. Skalnate Pleso*, **27,** 332.
Dragunova A.V., Panchuk V.E.: 1978, *Soob SAO*, **22**, 43.
Dragunova A.V., Belik S I., Komarov N.S.: 1997, *Odessa Astron. Publ.*, **10**, 52.
Dragunova A.V., Karamysh V.F., Komarov N.S.: 1994, *Odessa Astron. Publ.*, 7, 138.
Carlsson, M.: 1986, *Uppsala Astron. Obs. Rep*, **33**.
Cavallo R., Pilachovski K., Rebolo R.: 1997, *PASP*, **109**, 226.
Fenina Z.N.: 1985, *IBVS*, N 2790.
Fenina Z.N., Romanov Yu.S.: 1985, *Probl. Kosm. Fiz.*, **20**, 64.
Fenina Z.N., Zaikova L.P.: 1988, *PZ*, **22**, 902.
Fenina Z.N., Zgonyaiko N.S., Lemeshchenko N.D.: 1991, *IBVS*, No. 3595, 1.
Fenina Z.N., Zgonyaiko N.S., Lemeshchenko N.D.: 1990, *IBVS*, No. 3468, 1.
Fenina Z.N., Zgonyaiko N.S., Vasilyeva S.V.: 1994, *Odessa Astron. Publ.*, **7**, 62.
Fenina Z.N., Romanov Yu.S.: 1980, *ATsir*, **1144**, 1.
Fenina Z.N., Romanov Yu.S.: 1982, *Probl. Kosm. Fiz.*, no. 17, 93.
Garbuzov G.A., Andrievskii S.M., Malanushenko V.P.: 1987, *SvAL*, **13,** 131.
Garbuzov G.A., Andrievskii S.M.: 1986, *Astrofizika*, **25**, 251.
Garbuzov G.A., Mitskevich A.S.: 1984, *SvAL*, **10,** 92.
Garbuzov G.A., Paramonova O.P.: 1987, *Probl. astron. Ch. 2. Odes. univ. Odessa*, 123.
Garbuzov G.A., Zaikova L.P.: 1986, *KFNT*, **2,** 14.
Glazunova L.V., Karetnikov V.G.: 1985, *AZh*, **62**, 938.
Glazunova L.V., Karetnikov V.G., Kutsenko S.V.: 1986, *AZh*, **63**, 702.
Golinko V.I., Komarov N.S., Krasnova G.S.: 1969, *AAfz*, **8**, 35.
Gopka V.F., Komarov N.S.: 1990, *AZh*, **67**, 1211.
Gopka V.F., Komarov N.S., Mishenina T.V., Yuschenko A.V.: 1990, *AZh*, **67**, 1204.
Gopka V.F., Komarov N.S., Mishenina T.V., Yuschenko A.V.: 1991, *PAZh*, **17**, 368.
Gopka V.F., Panchuk V.E. Komarov N.S.: 1989, *AISAO*, **27,** 13.
Gopka V.F., Yuschenko A.V.: 1994a, *AstL*, **20,** 352.
Gopka V.F., Yuschenko A.V.: 1995, *AZh*, 7**2,** 743.
Gopka V.F., Yuschenko A.V.: 1996b, *AstL*, **22,** 460.
Gopka V.F., Yushchenko A.V., Shavrina A.V., Perekhod A.V.: 1999, *KFNT*, **15,** 447.
Hatzes A.P., Mkrtichian D.E., Kanaan A.: 1998, *BAAS*, **30**, 1338.
Hill V., Andrievsky S., Spite M.: 1995, *A&A*, **293**, 347.
Karetnikov V.G.: 1967, *AZh*, **44**, 22.
Karetnikov V.G.: 1972, *AZh*, **49**, 1188.
Karetnikov V.G.: 1987, *AZh*, **64**, 659.
Karetnikov V.G., Medvedev Yu.A.: 1966, *AZh*, **43**, 873.
Karetnikov V.G., Menchenkova E., Nazarenko V.: 1995a, *AN*, **316**, 163.
Karetnikov V.G., Menchenkova E., Nazarenko V.: 1995b, *AZh*, **72**, 519.
Karetnikov V.G., Menchenkova E., Nazarenko V.: 1995c, *ARep*, **39**, 619.
Karetnikov V.G., Kantsen L.E., Kutsenko S.V.: 1979, *AZh*, **56,** 1220.
Karetnikov V.G., Kovtyukh V.V.: 1987, *AZh*, **64**, 1256.
Karetnikov V.G., Korotikh T.N., Medvedev Iu.A.: 1973, *AZh*, **50**, 225.
Karetnikov V.G., Kutsenko S.V.: 1979, *SvA*, **23**, 570.
Karetnikov V.G., Medvedev Iu.A.: 1977, *ATsir*, **935**, 1.
Karetnikov V.G., Medvedev Iu.A.: 1977, *SvA*, **21**, 330.
Karetnikov V.G., Medvedev Yu.A., Yasinskaya M.P.: 1986, *PZ*, **22**, 401.
Karetnikov V.G., Menchenkova E.V.: 1985, *AZh*, **62**, 542.
Karetnikov V.G., Menchenkova E.V.: 1987, *AZh*, **64**, 367.
Karetnikov V.G., Nazarenko V.: 1996a, *KFNT*, **12**, 39.
Karetnikov V.G., Nazarenko V.: 1996b, *KFNT*, **12**, 48.
Karetnikov V.G., Perekresny S.M.: 1973, *Probl. Kosm. Fiz.*, **8**, 159.
Keenan P.C., Heck A.: 1994, *Rev Mex A&A*, **29**, 103.
Klochkova V.G., MisheninaT.V., Panchuk V.E.: 1989, *PAZh*, **15**, 315.
Klochkova V.G., Mishenina T.V., Panchuk V.E.: 1994, *A&A*, **287**, 881.
Klochkova V.G., Mishenina T.V., Panchuk V.E.: 1997, *Odessa Astron. Publ.*, **10**, 57.
Klochkova V.G., Mishenina T.V.: 1998, *ARep*, **42,** 307.
Koen C., Paunzen E., van Wyk, F. et al.: 2003, *MNRAS*, **338,** 931.
Komarov N.S.: 1967, *AZh*, **44**, 110.
Komarov N.S.: 1999, Cool Giant Stars, Odessa, Astroprint, 216 p.
Komarov N.S.: 1994, *Odessa Astron. Publ.*, **7**, 23.
Komarov N.S., Arkhipov M.G., Belik S.I. et al.: 1997c, *Odessa Astron. Publ.*, **10**, 59.
Komarov N.S., Basak N.Ju.: 1993, *AZh*, **70**, 111.
Komarov N.S., Basak N.Ju., Gorbaneva T.I. et al.: 1997a, *Odessa Astron. Publ.*, **10**, 61.
Komarov N.S., Basak N.Ju. , Gorbaneva T.I. , Kantzen L.E.: 1997b, *Odessa Astron. Publ.*, **10**, 64.
Komarov N.S., Belik S.I., Dragunova A.V.: 1999, *KFNT*, **15**, 215.
Komarov N.S., Dragunova A.V., Karamysh V.Ph. et al.: 1979, Photometric and spectral catalogue of bright stars. Kiev: Naukova dumka, 536 p.
Komarov N.S., Dragunova A.V., Belik S.I.: 1995, *Odessa Astron. Publ.*, **8**, 3.

Komarov N.S., Dragunova A.V., Belik S.I.: 1998, *KFNT*, **14**, 209.
Komarov N.S., Dragunova A.V., Korotina L.V., Shevchuk T.V.: 2000, *Odessa Astron. Publ.*, **13**, 65.
Komarov N.S., Dulapchi I.E.: 1994, IAU Colloquium 146: Molecular Opacities in the Stellar Environment. Eds. Peter Thejll and Uffe G. Jorgensen., p.59.
Komarov N.S., Gladushina N.A., Mishenina T.V.: 1977, *AZh*, **54**, 48.
Komarov N.S., Korotina L.V.: 1992, *AZh*, **69**, 1188.
Komarov N.S., Korotina L.V., Shevchuk T.V.: 1996, *KFNT*, **12**, 1.
Komarov N.S., Medvedev Yu.A., Mishenina T.V.: 1973, *AZh*, **50**, 1193.
Komarov N.S., Mishenina T.V.: 1988, *Afz*, **28,** 682.
Komarov N.S., Mishenina T.V., Panchuk V.E.: 1990, *Bull. SAO*, **26,** 33.
Komarov N.S., Mishenina T.V.: 1985, *KFNT*, **1**, 77.
Komarov N.S., Mishenina T.V.: 1983, *ATsir*, **1259**, 6.
Komarov N.S., Mishenina T.V., Motrich V.D.: 1985, *AZh*, **62**, 740.
Komarov N.S., Motrich V.D.: 1987, *Nablyud. i Interpretatsiya Zvezd. Spektrov. Vses. Soveshch. RG Astrosoveta Akad. Nauk SSSR*, Dushanbe, 1984. Dushanbe, 26.
Komarov N.S., Pozigun V.A.: 1968, *AZh*, **45**, 133.
Komarov N.S., Pozigun V.A., Belik S.I. et al.: 1983, Spectrophotometry of stars in the wavelength range λλ 550 – 900 nm, Kiev, Naukova dumka, 300 p.
Komarov N.S., Shcherbak A.N.: 1979, *ATsir*, **1074**, 6.
Komarov N.S., Shcherbak A.N.: 1980a, *ATsir*, **1104**, 6.
Komarov N.S., Shcherbak A.N.: 1980b, *SvAL*, **6**, 334.
Komarov N.S., Shcherbak A.N.: 1980c, *ATsir*, **1095**, 4.
Komarov N.S., Shcherbak A.N.: 1980d, *ATsir*, **1106,** 4.
Komarov N.S., Shcherbak A. N.: 1980e, *AZh*, **57,** 557.
Komarov N.S., Shevchuk T.V.: 1995, proceedings of IAU Sym 176, ed. Klaus G. Strassmeier, p.223.
Komarov N.S., Tsymbal V.V., Shcherbak A.N.: 1979, *ATsir*, **1081**, 4.
Komarov N.S., Tsymbal V.V.: 1980, *AZh*, **57**, 1010.
Komarov N.S., Tsymbal V.V.: 1987, *Conf. Stellar atmospheres*, 63.
Kononowitsch A., Zwietinowitsch N., Orbinsky A.: 1893, *Notes de l'Université d'Odessa*, **68**, 225.
Korotin S.A., Andrievsky S.M., Luck R.E.: 1999, *A&A*, 351, 168.
Korotin S.A., Andrievsky S.M., Kostynchuk L.Yu.: 1999a, *A&A*, **342,** 756.
Korotin S.A., Andrievsky S.M., Luck R.E.: 1999b, *A&A*, **351,** 168.
Korotin S.A., Andrievsky S.M., Kostynchuk L.Yu.: 1998, *A&SS*, **260,** 531.
Korotin S.A., Komarov N.S.: 1989, *AZh*, **66,** 866.
Korotin S.A., Mishenina T.V.: 1999, *ARep*, **43**, 533.
Kovtyukh V.V., Andrievsky S.M., Usenko I.A., Klochkova V.G.: 1996, *A&A*, **316**, 155.
Kovtyukh V.V., Andrievsky S.M.: 1999, *A&A*, **350,** L55.
Kovtyukh V.V., Komarov N.S., Andrievsky S.M., Dulapchi I.F.: 1999, *Odessa Astron. Publ.*, **12**, 195.
Kovtyukh V.V., Komarov N.S., Depenchuk E.A.: 1994, *AstL*, **20**, 215.
Luck R.E., Andrievsky S.M., Kovtyukh V.V. et al.: 2000, *A&A*, **361**, 189.
Mishenina T.V.: 1996, *A&AS*, **119**, 321.
Mishenina T.V.: 1998, *ARep*, **42**, 174.
Mishenina T.V., Klochkova V.G., Panchuk V.E.: 1997, *Bull. SAO*, **43**, 72.
Mishenina T.V., Klochkova V.G., Panchuk V.E.: 1995, *A&AS*, **109**, 471.
Mishenina T.V., Korotin S.A., Klochkova V.G., Panchuk, V.E.: 2000, *A&A*, **353**, 978.
Mishenina T.V., Kutsenko S.V.: 1994, *OAO*, **7**, 152.
Mishenina T.V., Kutsenko S.V.: 1996, *KFNT*, **12**, 12.
Mishenina T.V., Kutsenko S.V., Musaev F.: 1995, A&AS, **113,** 333.
Mishenina T.V., Panchuk V.E., Komarov N.S.: 1986, *AISAO*, **22**, 13.
Mishenina T.V., Tsymbal V.V.: 1997, *AstL*, **23,** 609.
Mkrtichian D.E.: 1990, *PAZh*, **16**, 1107.
Motrich V.D.: 1988, *Odes. Univ. Odessa*, 33 p.
Nazarenko V.V.: 1992, *AZh*, **69**, 1207.
Panchuk V.E.: 1975, *PZ*, **19,** 541.
Panchuk V.E.: 1974, *AAfz*, **22**, 37.
Panchuk V.E.: 1974, *ATsir*, **820,** 5.
Panchuk V.E. 1975, *AAfz*, **25**, 20.
Panchuk V.E.: 1972, *ATsir*, **742,** 6.
Paunzen E., Andrievsky S.M., Chernyshova I.V. et al.: 1999, *A&A*, **351**, 981.
Romanov Yu.S.: 1977, *PZ*, **20**, 299.
Romanov Yu.S.: 1985, SvAL, **11**, 157.
Romanov Yu.S., Fenina Z.N., Vasilieva S.V.: 1981, *Afz*, **43**, 43.
Romanov Yu.S., Fenina Z.N., Vasilieva S.V.: 1981, *PZ Prilozh.*, **4**, 35.
Romanov Yu.S., Fenina Z.N., Zgonyaiko N.S.: 1998, *Bull. CrAO*, **94**, 185.
Romanov Yu.S., Udovichenko S.N., Frolov M.: 1984, *IBVS*, No. 2645, 1.
Romanov Yu.S., Udovichenko S.N., Frolov M.: 1985, *SvAL*, **11**, 378.
Romanov Yu.S., Udovichenko S.N., Frolov M.: 1987, *PAZh*, **13**, 69.
Romanov Yu.S., Udovichenko S.N.: 1981, *Soob. SAO*, **32**, 13.
Tsymbal V.V., Panchuk V.E.: 1980, *Bull SAO*, **16**, 9.
Tsymbal V.V.: 1977, Tables of Franck-Condon factors with account for vibrational-rotational interaction for astrophysically important molecules. 2. N, ZrO, SiO. III. C2, IV LAO *Astron. obs. Odessk. univ. Odessa*, **47**. 38 p.
Tsymbal V.V., Panchuk V.E.: 1980, *AZh*, **57**, 881.
Tsymbal V.V.: 1980, *ATsir*, **1103**, 7.
Tsymbal V.V.: 1980, *ATsir*, **1103**, 5.
Udovichenko S.N., Konchagina E.I.: 1997, *Odessa Astron. Publ.*, **10**, 82.
Udovichenko S.N., Shtol' V.G., Valyavin G.G.: 1996, *Delta Scuti Star Newsletter*, Issue 10, 9.
Udovichenko S.N.: 1994, *KFNT*, **10**, 36.
Udovichenko S.N.: 1987, *Probl. astron. Ch. 2. Odes. univ. Odessa*, 117.
Vykhrestyuk T.P., Karetnikov V.G.: 1973, *AAfz*, **20**, 13.
Yushchenko A.V., Gopka V.F.: 1996a, *A&AT*, **10**, 307.
Yushchenko A.V., Gopka V.F.: 1996b, *AstL*, **22**, 412.
Yushchenko A.V., Gopka V.F.: 1994a, *Odessa Astron. Publ.*, **7**, 156.
Yushchenko A.V., Gopka V.F.: 1994b, *AstL*, **20**, 453.
Zaikova L.P., Udovichenko S.N.: 1988, *KFNT*, **4**, 43.
Zajkova L.P., Udovichenko S.N., Romanov Yu.S.: 1992, Proceedings of "Physics and evolution of stars". Eds Yu.V. Glagolevskij and I.I. Romanyuk. Sankt Petersburg: "NAUKA", 243.
Zajkova L.P., Udovichenko S.N.: 1988, *PZ*, **22**, 907.
Zajkova L.P., Romanov Yu. S.: 1988, *PZ*, **22,** 905.
Zgonyaiko N.S., Fenina Z.N.: 1988, *PZ*, **22**, 904.

DOI 10.18524/1810-4215.2022.35.268106

REFINED PHYSICAL PROPERTIES OF THE HD 327083 BINARY SYSTEM

A.S. Nodyarov[1], A.S. Miroshnichenko[2,3,4,1], S.A. Khokhlov[1], S.V. Zharikov[5,1], N. Manset[6], I.A. Usenko[7]

[1] Al-Farabi Kazakh National University. Al-Farabi Ave. 71, 050040, Almaty, Kazakhstan, *nodyarov.atilkhan@gmail.com*
[2] Department of Physics and Astronomy, University of North Carolina Greensboro, Greensboro, NC 27402, USA, *a_ mirosh@uncg.edu*
[3] Fesenkov Astrophysical Institute, Observatory 23, 050020 Almaty, Kazakhstan
[4] Central Astronomical Observatory of the Russian Academy of Sciences at Pulkovo Pulkovskoe shosse 65-1, Saint-Petersburg, 196140, Russia
[5] Universidad Nacional Autónoma de México, Instituto de Astronomía AP 106, Ensenada 22800, BC, México
[6] Canada-France-Hawaii Telescope Corporation, 65–1238 Mamalahoa Hwy, Kamuela, HI 96743, USA
[7] Astronomical Observatory, Odessa National University, 1B Marazlievska, Odessa 65014, Ukraine

ABSTRACT. HD 327083 is a member of a small group of supergiants exhibiting the B[e] phenomenon. It was found to be a binary system with an early-B and an early-F supergiant components. However the fundamental and orbital parameters of the system were not accurately known. We determined a new set of the system parameters that include the orbital period and the components' masses using a combination of photometric and spectroscopic data. A new orbital period of 107.7 days was found from both the spectral line positional variations and the visual light curve. Absorption lines of the cool component show a radial velocity semi-amplitude of 48.3 km s^{-1}, similar to that of emission lines that originate around the hot component. The system shows partial eclipses. We estimated the components' masses to be nearly equal and close to 6-8 $M_\odot$. The masses turned out to be smaller then the evolutionary masses that may be a consequence of a recent mass-transfer.

Keywords: circumstellar matter — stars: early-type — stars: emission-line, B[e] — stars, stars — individual: HD 327083.

АНОТАЦІЯ. HD 327083 є членом невеликої групи надгігантів, які демонструють явище B[e]. Було виявлено, що це подвійна система з компонентами надгіганта раннього B і раннього F. Однак фундаментальні та орбітальні параметри системи не були точно відомі. Ми визначили новий набір параметрів системи, які включають орбітальний період і маси компонентів, використовуючи комбінацію фотометричних і спектроскопічних даних. Новий орбітальний період 107.7 днів було знайдено як за змінами положення спектральних ліній, так і за кривою візуального блиску. Лінії поглинання холодного компонента демонструють напівамплітуду променевої швидкості 48.3 км с$^{-1}$, подібну до ліній випромінювання, які виникають навколо гарячого компонента. Система показує часткові затемнення. Ми оцінили маси компонентів як майже рівні та близькі до 6-8 $M_\odot$. Маси виявилися меншими за еволюційні маси, що може бути наслідком недавнього масопереносу.

Ключові слова: навколозоряна речовина, зорі раннього типу, зорі: емісійна лінія, B[e] зорі, зорі окремі: HD327083.

1. Introduction

The B[e] phenomenon is defined as the presence of permitted and forbidden low-excitation emission lines, such as H I, Fe II, [Fe II], N II and [O I], and a strong IR excess due to circumstellar dust in the spectra of B?type stars (Allen & Swings 1976) and first systematically analyzed Lamers et al. (1998), who suggested to call them objects with the B[e] phenomenon. These properties are observed in stars with a wide range of masses and evolutionary states. Despite a strong

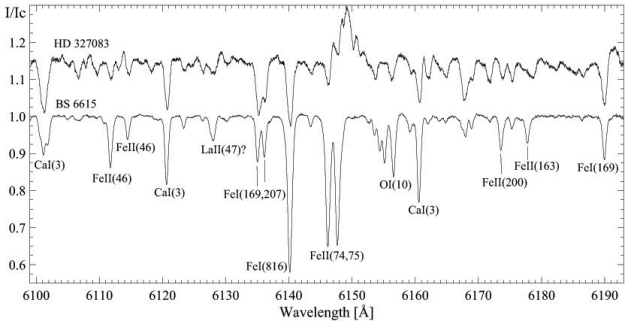

Figure 1: Absorption-line spectra of HD 327083 and BS 6615 (T_{eff}=7,000 K, log g = 1.5). The hot component (spectral type B1) and circumstellar matter contribute ∼10% to the continuum of HD 327083 in this wavelength region.

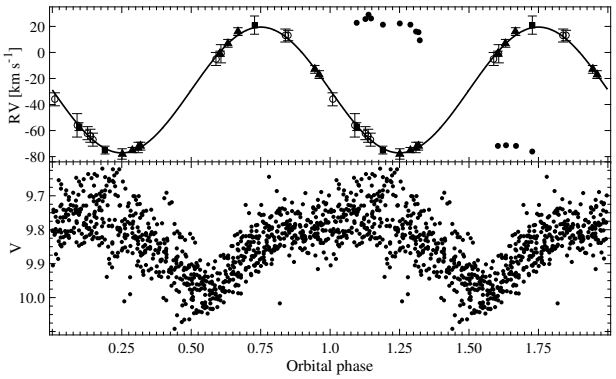

Figure 2: The RV curve (top panel) and the light curve (bottom panel) for HD 327083. RV of the photospheric lines are shown by open circles (data from Miroshnichenko et al. 2003), squares (CFHT), and triangles (ESO). The Fe II 6456Å emission line RVs are shown by filled circles with no error bars. The optical light curve was retrieved from the ASAS SN catalog and folded with the orbital period.

progress in understanding of these complex objects, nature of many of them was not revealed. This prompted Miroshnichenko (2007) to introduce a subgroup named FS CMa type objects that included nearly a half of the original list of 65 Galactic objects with the B[e] phenomenon, which were not associated with any known stellar group with a known evolutionary state, and suggest that they were binary systems with an ongoing or finished mass-exchange. B[e] supergiants and FS CMa objects need more observations to constrain their physical parameters and evolutionary status.

HD 327083 is a highly reddened object with optical color indices of a hot star. Miroshnichenko et al.(2003) concluded that it is a binary system with an early B-type and an early F-type supergiants and suggested two possible orbital periods of 55 and 180 days from only 8 spectra. Machado et al.(2003) studied optical high-resolution (R∼50,000) spectra and suggested that HD 327083 is a superluminous 60 $M_\odot$ single star with the following parameters: $\log(L/L_\odot)$=6.0, T_{eff}=11,500 K, and a mass loss rate of $8{\cdot}10^{-5}$ $M_\odot$ yr^{-1}. IR interferometry by Wheelwright et al.(2012) suggested that the system is surrounded by a circumbinary disk. Studying some emission-line profiles, Maravelias et al.(2018) suggested that the disk consists of several rings and reported 10 peaks in the Fourier power spectrum of the ASAS survey photometry with no further analysis.

All the mentioned studies did not determine the orbital period and fundamental parameters of the system with a reasonable accuracy. In this study we report new data and addressed these problems.

2. Observations

For this study we used 8 optical high-resolution spectra reported by Miroshnichenko et al. (2003) that were taken at the 2.1 m Otto Struve telescope of the McDonald Observatory (Texas, USA, R=60,000, 1 spectrum) in 2002 with the Sandiford spectrograph (McCarthy et al. 1993) and at the 2.1 m telescope of the Complejo Astronomico El Leoncito (Argentina, R∼15,000, 7 spectra) in 2000–2002 with the échelle-spectrograph REOSC, mounted in the Nasmyth-2 focus and equipped with a 2K × 2K CCD-chip.

This data set was enlarged by 3 spectra taken at the 3.6 m Canada-France-Hawaii Telescope (CFHT, Mauna Kea, HI, USA, R=65,000) in 2006–2008 with the ESPaDOnS spectropolarimeter (Manset & Donati 2003) and 9 spectra taken in 2009–2017 at the 2.2 m telescope of the European Southern Observatory (ESO, Chile, $R = 40,000 - 50,000$) with spectrographs FEROS and UVES retrieved from the ESO data archive. Observations obtained at CFHT were reduced with the Upena and Libre-ESpRIT software packages (Donati et al. 1997). Spectra from the other observatories were processed using the *echelle* package in IRAF.

Photometric observations in the V– and g–band that we analyse here were taken from the ASAS–3 (2003–2010, Wozniak et al. 2004) and ASAS SN (2014–2022, Kochanek et al. 2017) surveys.

3. Data analysis

The optical spectrum of HD 327083 exhibits absorption and emission lines, which were identified using a catalog by Coluzzi (1999). Their radial velocities (RVs) were determined by fitting the line profiles to a Gaussian, and the equivalent widths (EW) were measured by integration in the continuum normalized

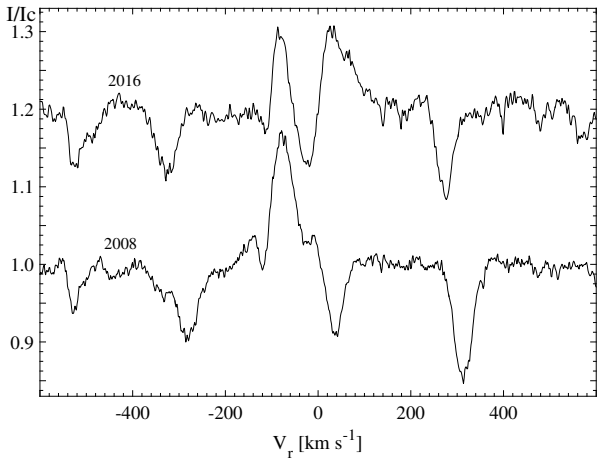

Figure 3: Comparison of high-resolution spectra taken at CFHT on 2008/07/19 (orbital phase 0.76) and at ESO on 2016/04/13 (phase 0.96). The cool component is located behind the hot one at the phase 0. The radial velocity (RV) scale is shown relative to that of the emission line Fe II (λ6456.38 Å). The intensity is normalized to the continuum.

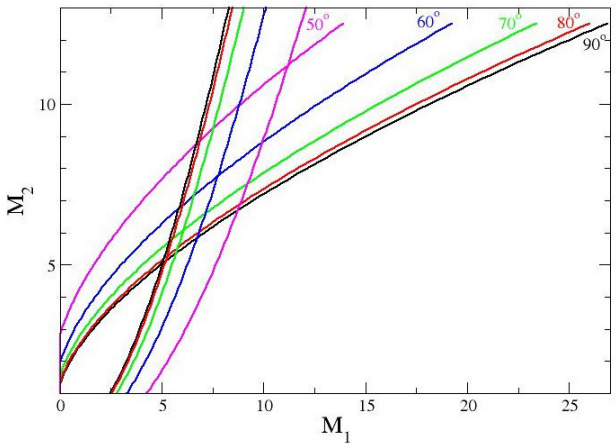

Figure 4: Mass function for the system components. Inclination angles of the system rotational axis are shown by different colors. Masses are shown in $M_\odot$.

spectra. The discovery of absorption lines of neutral metals in the spectrum of HD 327083 reported by Miroshnichenko et al. (2003) unambiguously indicates the presence of a secondary component, which is cooler than the primary component responsible for the emission-line spectrum. In Fig. 1 we compare a part of a high-resolution spectrum of HD 327083 with that of the yellow supergiant BS 6615. The absorption lines of BS 6615 are stronger than those of HD 327083 that suggests a noticeable contribution of the system's hot component.

The absorption lines of HD 327083 were also compared with model atmosphere spectra calculated with the code *SPECTRUM* by Gray & Corbally (1994). Parameters of the cool component ($T_{\rm eff}$ = 7000 K and $v\,sin\,i$ = 30 km s^{-1}, log g=2.0) were estimated from the detected absorption lines and their widths. The contributions of the hot and cool components to a wavelength range within the V-band were estimated by comparing the observed and calculated absorption-line strengths and found to be 40% and 60%, respectively.

Fourier analysis of the absorption lines RVs and subsequent fitting them with an orbital solution implies a circular orbit with a period of 107.68±0.02 days. The same period is detected in the photometric variations (see Fig. 2). Near the orbital phases 0.0 (the cool component is behind the hot one) and 0.5, some absorption lines are superimposed on emission lines that makes it impossible to measure the position of the latter (Fig. 3). Overall we confirm the result of Miroshnichenko et al. (2003) that the positions of the emission and absorption lines vary in anti-phase.

The interstellar absorption features in the spectrum of HD 327083 include diffuse interstellar bands (DIBs) as 5780, 5796, 6613, and 8620 Å as well as the lines of Na I at 5889 and 5895 Å. Using relationships between the EW of the DIB at 5780 Å and the color excess $E(B-V)$ found by Herbig (1993) and Kos & Zwitter (2013), we derived $E(B-V) \approx 1.8$ mag.

The optical light curve of HD 327083 shows a deep around the phase 0.5 (the cool component in front of the hot one). It may be due to a partial eclipse of the hot component or to a hot spot on the surface of the cool component created by the radiation from the hot one. Preliminary modeling of both processes suggest an inclination of the system's rotational axis to the line of sight of ∼55–60 degrees. This result along with the mass functions for the components (see Fig. 4) lead to their masses of ∼6–8 $M_\odot$. The scatter of data points on the photometric phase curve is related to the inhomogeneity of the circumstellar medium (Figure 2).

The spectral energy distribution (SED) data of HD 327083 were taken from different sources, which included both ground- and space-based photometric data. It was modeled with as a sum of a hot and a cool star model atmospheres taken from Kurucz (1994) with effective temperatures of $T_{\rm eff}$ = 20,000 K and $T_{\rm eff}$ = 7,000 K, respectively (see Fig. **??**). The best fit was found for the 60% contribution of the cool component and 40% contribution of the hot component. The theoretical SED of the sum of the two models is in good agreement with the observed one corrected for the interstellar extinction of $E(B-V)$ = 1.8 mag. Considering that in the direction of the object $A_V/E(B-V)$ = 2.95, we get A_V = 5.3 mag.

Using two alternative distances, D_1 = 1.5±0.5 kpc (Miroshnichenko et al. 2003) and D_2 = 2.26±0.15 kpc from (Gaia EDR3, Bailer-Jones et al. 2021), we calculated the luminosity of the system components

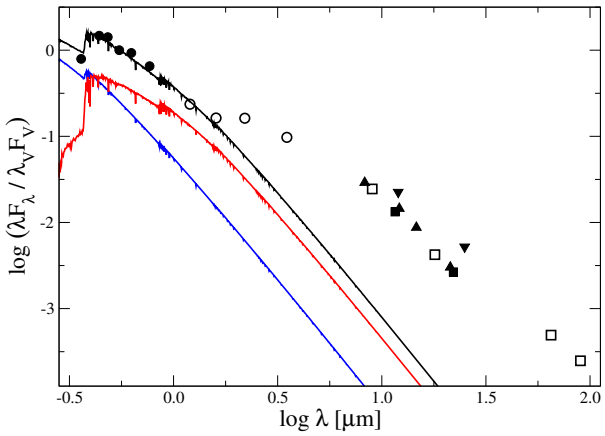

Figure 5: Spectral Energy Distribution of HD 327083 corrected for the interstellar reddening. Symbols: filled circles – optical photometry, open circles – near-IR photometry ($JHKL$), filled squares – WISE data, filled upward triangles – MSX data, open squares – AKARI data, and downward filled triangles – IRAS data. The model atmospheres from Kurucz (1994) for the system components are shown by the blue (hot component) and red (cool component) lines, while the sum of the models is shown by the black line.

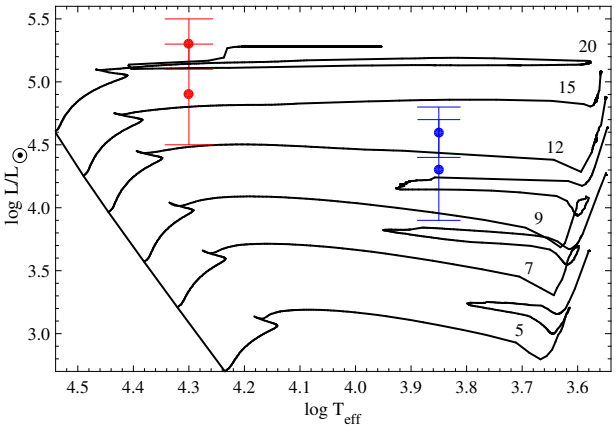

Figure 6: HR diagram with positions of the HD 327083 components for the distances D_1 (lower) and D_2 (upper). Evolutionary tracks for single rotating stars with indicated initial masses in $M_\odot$ (Ekström et al. 2012) are shown by solid lines.

and analyzed their positions in the HR diagram (Figure **??**). The hot component has $\log L/L_\odot = 4.9 \pm 0.4$ at D_1 and $\log L/L_\odot = 5.3 \pm 0.2$ at D_2, while the cool component has $\log L/L_\odot = 4.3 \pm 0.4$ at D_1 and $\log L/L_\odot = 4.6 \pm 0.2$ at D_2. The luminosity for both distances imply an evolutionary mass of $\sim$20 $M_\odot$ for the hot component and $\sim$12 $M_\odot$ for the cool component that is inconsistent with the masses derived from spectroscopy.

4. Conclusions

Our study of spectroscopic and photometric data of the southern emission-line object HD 327083 resulted in the following findings. We derived a new orbital period of the system 107.68±0.02 days and a semi-amplitude of the RV variations of 48.3±1.7 km s^{-1} for the cool component (nearly the same as that of the emission lines, which represent the motion of the hot component). We confirmed T_{eff} of the system components determined by Miroshnichenko et al. (2003): $\sim$7,000 K for the cool component and $\sim$20,000 K for the hot component. We found the components' masses from the mass function and the system inclination to be $M_{hot} \approx M_{cool} \approx$ 6–8 $M_\odot$ and 55–60°, respectively. This result still needs further refinement using a more accurate modeling of the object's light curve. The evolutionary masses are inconsistent with the spectroscopic ones. This discrepancy may be due to the ongoing interaction between the components.

Acknowledgements. This research has made use of the SIMBAD database, operated at CDS, Strasbourg, France, and was partly funded by the Science Committee of the Ministry of Education and Science of the Republic of Kazakhstan (Grant No. AP08856419). This paper is partly based on observations obtained with the Canada-France-Hawaii Telescope (CFHT) which is operated by the National Research Council of Canada, the Institut National des Sciences de l'Univers of the Centre National de la Recherche Scientifique de France, and the University of Hawaii as well as on observations obtained at the 2.1 m Otto Struve telescope of the McDonald Observatory (Texas, USA), 2.1 m telescope of the Observatorio Astronómico Nacional San Pedro Martir (Baja California, México), 2 m telescope of Complejo Astronomico El Leoncito (Argentina), and 2.2 m telescope of the European Southern Observatory (ESO). The observations at the Canada-France-Hawaii Telescope were performed with care and respect from the summit of Maunakea which is a significant cultural and historic site.

References

Allen D.A., & Swings J.P.: 1976, *A&A*, **47**, 293-302.
Bailer-Jones C.A.L., et al.: 2021, *AJ*, **161**, id. 147.
Coluzzi R.: 1999, *VizieR Online Data, Catalog*, VI-71A.
Donati J.-F. et al.: 1997, *MNRAS*, **291**, 658-682.
Ekström S., et al.: 2012, *A&A*, **537**, A146.
Gray R.O., & Corbally C.J.: 1994, *AJ*, **107**, 742-746.
Herbig G.H.: 1993, *ApJ*, **407**, 142-156.
Kochanek C.S., Shappee B.J., Stanek K.Z., et al.: 2017, *PASP*, **129**, 104502.

Kos J., & Zwitter T.: 2013, *ApJ*, **774**, id. 72.
Kurucz R.L.: 1994, *Kurucz CD ROM No. 19*, Smithsonian Astroph. Obs.
Lamers H.J.G.L.M., et al.: 1998, *A&A*, **340**, 117-128.
Machado M.A.D., & de Araújo F. X.: 2003, *A&A*, **409**, 665-675.
Manset N., & Donati J.-F.: 2003, *Proc. SPIE*, **4843**, 425-436.
Maravelias G., et al.: 2018, *MNRAS*, **480**, 320-344.
McCarthy J.K., Sandiford B.A., Boyd D., Booth J.: 1993, *PASP*, **105**, 881-893.
Miroshnichenko A.S.: 2007, *ApJ*, **667**, 497-504.
Miroshnichenko A.S., et al.: 2003, *A&A*, **406**, 673-683.
Wheelwright H.E., et al.: 2012, *A&A*, **538**, A6.
Woźniak P.R., Vestrand W.T., Akerlof C.W., et al.: 2004, *AJ*, **127**, 2436–2449.

DOI 10.18524/1810-4215.2022.35.268188

SPECTRAL OBSERVATIONS OF THE HERBIG Be STAR HD 53367

B.N. Rustamov[1,2], Kh.M. Mikailov[1], K.I. Alisheva[1], S.O. Mammadova[2], V.I. Aliyeva[2]

[1] Baku State University,
Baku, Azerbaijan

[2] Shamakhy Astrophysical Observatory named after N. Tusi Azerbaijan NAS,
Baku, Azerbaijan, *bayram_rustam@yahoo.com*

ABSTRACT. The unusual spectroscopic behavior of star Herbig Be HD53367 is described based on the spectra obtained on the Cassegrain focus of the 2-meter telescope at the Shamakhy Astrophysical Observatory, using the Fiber Echelle Spectrograph (ShAFES), with a spectral resolution of R=28000.The results of comparative behavior analysis of profiles of selected lines (Hα, Hβ, HeI λ5876 Å, NaID, H and K CaII) are presented with analogical data published in the literature.

Keywords: echelle spectrograph, radial velocities, line profiles, star HD53367.

АНОТАЦІЯ. На основі спектрів, отриманих у фокусі Кассегрена 2-м телескопа Шамахінської Астрофізичної Обсерваторії на волоконному ешеле спектрографі (ShAFES), з використанням CCD матриці STA4 150A з 4 x 4 елементів, проаналізовано поведінку незвичайної спектральної особливості зір типу Be Хербіга HD 53367. Розмір елемента матриці 15 мкм, спектральна роздільна здатність R=28000, охолодження – рідкий азот. Обробка ешеле-спектрів проводилася за стандартною методикою з використанням нової версії програми DECH30, розробленої Галазутдіновим.

З метою дослідження навколозоряного середовища, нами для аналізу були обрані наступні лінії у спектрі зорі HD53367: Hα, Hβ, HeIλ5876Å, NaID, H та K CaII, а також, для дослідження зір на предмет подвійності, включені для аналізу лінії фотосферного походження – HeIλ6878Å, HeIλ4471Å. Судячи з встановленої для цієї зорі ознаки (кореляція емісійного спектру з блиском), можна припускати, що спектральні спостереження проводилися близько до максимуму блиску зорі.

У період наших спектральних спостережень (січень 2019 – січень 2020 рр.) з Бальмерівських ліній водню тільки Hα повністю та Hβ частково спостерігаються в емісії, а лінії Hγ – Hε показують абсорбційний спектр. Лінії резонансних дублетів, нейтрального натрію (D1,2 NaI) та одноразово іонізованого кальцію (H & K CaII) представлені у наших спектрах міжзоряною складовою. Геліоцентричні променеві швидкості цих ліній (у середньому): 27,5 км/с (D2NaI); 28,4 км/с (D1NaI); 26,2 км/с (HCaII); 25,7 км/с (KCaII). Профіль лінії нейтрального гелію HeIλ5876Å являє собою центральну абсорбційну та емісійну компоненти на синьому крилі (25 січня 2019 р. та 17 січня 2020 р.) або на обох крилах (14.12 та 21.12.2019).

На основі літературних даних була побудована крива променевих швидкостей для фотосферних ліній: HeI 6878Å, HeI 5875Å, HeI 4471Å для зорі HD 53367, з періодом P = 183.34 дня, запропонованим М. Погодіним (2006). Виміряні нами променеві швидкості лінії HeIλ6878Å задовільно лягають на цю криву.

Ключові слова: ешелле-спектрограф, радіальні швидкості, профілі ліній, зоря HD53367.

1. Introduction

HD53367 (MWC166, V750 Mon, B0e – B1e III – V, V = $7^m.0$) is located in the vast star-forming region CMa R1 which contains more than a hundred young stellar objects of various masses and an association of reflection nebulae. This object is probably the most massive (15 – 25 $M_\odot$) (Tijn, Dije et al., 2001). HD53367 – a visual binary system (RST 3489) with Δm$\sim 1^m.3$ and component distance $\rho = 0''.6$ ($\sim$600 a.u. – assuming a distance of about one kpc proposed by Claria (1974)). Shows emission lines in the optical spectrum, and besides, Hα is the brightest, and its circumstellar environment shows evidence of cold, dusty matter as an excess in the far IR, at $\lambda \geq 10$ μm (Tijn , Dije et al., 2001). HD53367 is on Herbig's original list of young Ae/Be Herbig stars (Herbig, 1960). HD53367 has a long-term photometric variation with a period of 9 years. The brightness decrease of HD53367 is accompanied by the damping of emission in the lines. However, there is a significant difference in the time

scales of these processes. For example, the transition of HD53367 from a bright photometric state to a low one took more than one year (from August 1996 to October 1997), while emission in the Balmer lines was observed for another five years (until the end of 2002). HD53367 is also a spectroscopic binary star (Finkenzeller & Mundt, 1984). The main component shows ray velocity variations that may correspond to a period of 166 days and an amplitude of about 20 km/s at an average velocity of +48.2 km/s.

Two mechanisms were proposed to explain the photometric behavior of HD53367 (Tijn, Dije et al., 2001):

1. Magnetic activity in the star's photosphere stimulates the cyclic development of cold spots on its surface. As a result, it leads to a reduction in effective temperature, causing reddening of the star.

2. The second mechanism suggests the existence of a dense uniform perturbation slowly precessing in the CS disk around the Be star. The periodic eclipse of this region, along with amplified emission from the limb of the star, leads to the observed photometric and spectral variations. Another remarkable property of HD53367 is the significant ray velocity variations observed in several photospheric lines (Corporon & Lagrange, 1999).

As can be seen from the behavior of the profiles of the Balmer hydrogen lines (Hα and Hβ) borrowed from the data published in the literature, the types of profiles endure significant changes depending on the photometric state of the star. The emission and absorption profiles of hydrogen lines in different states of the photometric brightness of the star were recorded from observations, but there are no transition profiles between these states. Along with this, it is essential to carry out tight series of spectral observations of the star in the maximum state of brightness to investigate the behavior of the V/R ratios on periodicity. As mentioned above, significant ray velocity variations in selected photospheric lines are revealed on this star. Investigations of selected lines of cleanly photospheric origin would serve to refine the binary period of the star HD53367. The relevance of these researches is determined by the above experimental statements and, in general, by the role of binarity in the evolution of young Ae/Be Herbig-type stars.

2. Observations and data processing

Spectral observations of the star HD53367 were carried out at the Cassegrain focus of the 2-meter telescope of the Shamakhy Astrophysical Observatory named after N.Tusi, on fiber echelle spectrograph ShaFES (Shamakhy Fiber Echelle Spectrograph), by using CCD matrix STA4150A 4 ×4 K elements, cooled by liquid nitrogen, with an element size of 15 μm (Mikailov et al., 2020).

The quantum efficiency in the wavelength range $\lambda\lambda$ 3000-8000ÅÅexceeds 70 %, with a spectral resolution R = 28000, in the wavelength oblast $\lambda\lambda$ 3900–7500 ÅÅ. For the period January 2019 – January 2020, for 4 nights, we received two spectra of the star HD 53367 each night and a complete set of calibration frames: dark (or bias), flat-field, ThAr, and Sky. Processing of echelle spectra was carried out according to the standard method using the new version of the DECH30 program developed by Galazutdinov (http://www.gazinur.com/DECH software.htm).

3. Results of observations

The following peculiarities were chosen by us for analysis in the spectrum of the star HD53367:

Balmer series lines: 6562.817 Hα; 4861.332 Hβ; 4340.468 Hγ; 4101.737 Hδ; 3970.074 Hε.

Resonant sodium doublet: D1NaI (λ 5895.940 Å) and D2NaI (λ 5889.973Å).

Resonant calcium doublet: HCaII (λ 3968.492 Å) and KCaII (λ 3933.682Å).

Neutral helium: HeI λ 5876Å.

Lines of ionized iron FeII 42 ($\lambda\lambda$ 4923.921 Å, 5018.434 Å, 5169.03Å).

Photospheric lines: HeI λ 6678 Å, HeI λ 5876 Å, HeI λ 4471Å.

4. The discussion of the results

The picture of the spectral and photometric variability of the star HD53367 is quite complex. Therefore, studies of the circumstellar medium (from the profiles of the Hα and Hβ lines), as well as the gaseous component of this medium (from the profiles of the HeI l5876, NaID, H, and K CaII lines), in various states of the stellar photometric activity, are essential. Furthermore, observational data indicate the spectral binarity of the star HD53367.

Therefore, as indicators of binarity, absorption lines of photospheric origin were chosen by us for analysis Fig. 1 shows in our disposal the observed profiles of the Hα and Hβ, He λ5876Å, and NaID, H and KCaII lines in the spectrum of star HD 53367. As can be seen from Fig. 1 , from the Balmer hydrogen lines, only Hα is entire, Hβ is partially observed in the emission. The (Hγ – Hε) lines show the absorption spectrum. The Hα and Hβ line profile's form and intensities in spectrum of star HD53367, correlate with the star's optical brightness state (Pogodin et.al., 2006).

At the maximum brightness, the Hα line in the emission, while the brightness decreases, the emission intensity decreases, and after some threshold value of the brightness, the emission disappears, and the line becomes completely absorbing. Judging by this sign, from the shape of the profiles of the Hα and Hβ lines,

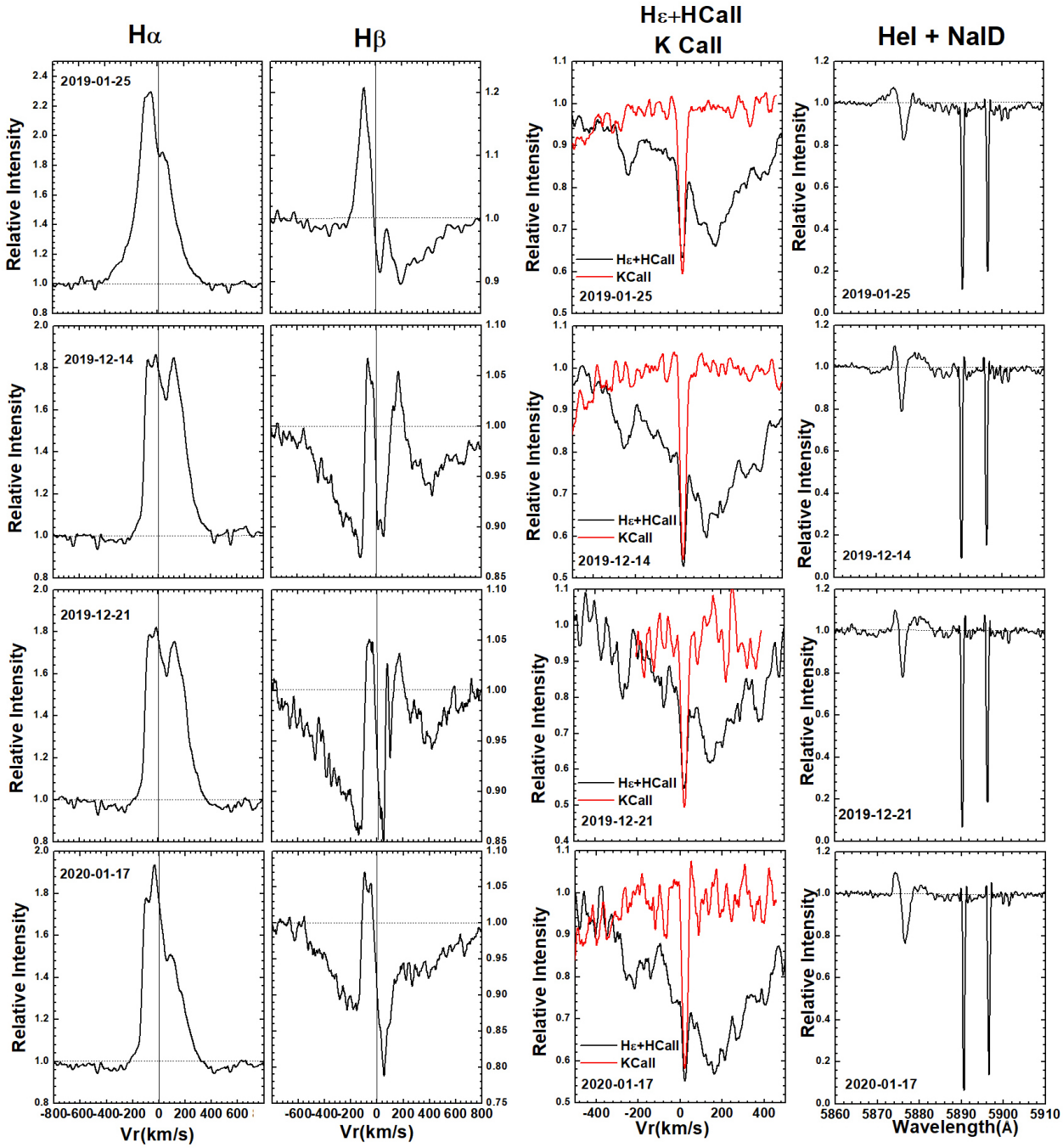

Figure 1: The observed profiles of the Hα and Hβ, H and KCaII, NaID and He λ5876Ålines in the spectrum of star HD 53367 (from left to right)

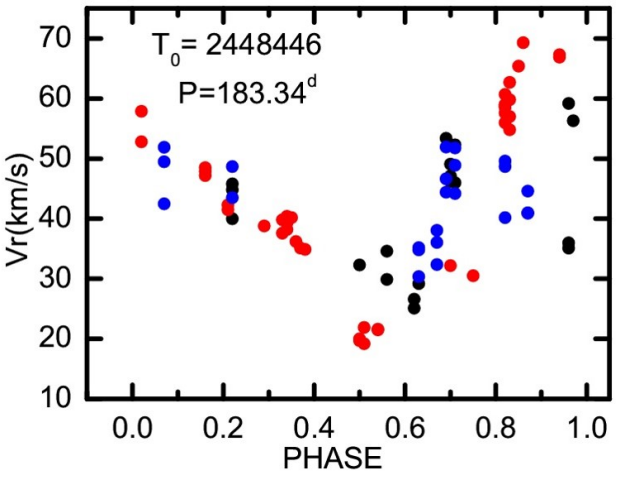

Figure 2: Radial velocities of the star HD53367 folded with the period of P = 183.34 days suggested by M. A. Pogodin et al. The following symbols are used measured for different authors: black circles – Corporon P., Lagrange A.M., 1999, A&AS, 136, 429; red circles – Pogodin M. A. et al., 2006, A&A, 452, 551; and blue circles measured at ShAO.

we can assume that our spectral observations were carried out near the maximum brightness of the star. The shape of the Hα line profiles in our spectra indicates the presence of an accretion disk around the star. During the formation of Hα lines, the dominant role on the dates [(12-14 and 12-21) 2019] belongs to the rotation (V/R≈1), and on the dates 01-25-2019 and 01-17-2020 – an accretion of matter to the surface of the star. During the transition from the emission mode to absorption, signs of accretion are observed in the profiles of the Hα and Hβ lines. In the spectra obtained in a time difference of 7 days [(12-14 and 12-21) 2019], the Hα; Hβ; HeI λ5876Åline profiles; are practically the same both in terms of the profile and ray velocities.

The lines of resonant doublets, neutral sodium (D1,2 NaI), and once ionized calcium (H, KCaII) are represented in our spectra by the interstellar component (IS); the circumstellar component (CS) is not visible. Heliocentric radial velocities of these lines (on average): 27.5 kms (D2NaI); 28.4 (D1NaI); 26.2 (HaII); 25.7 kms (KaII). The neutral helium line profile (HeI 5876Å) represents the central absorption and emission component on the blue wing (2019-01-25 and 2020-01-17) or both wings [(12-14 and 12-21) 2019].

Fig. 2 shows the radial velocity curve based on the measured radial velocities of the photospheric lines: HeI λ 6878Å, HeI λ5875Å, HeI λ4471Å. Radial velocities of the star HD53367 folded with the period of P = 183.34 days suggested by M. A. Pogodin et al. (see Fig.2). As can be seen from Fig. 2, our measurements fit satisfactorily on this curve.

5. Conclusions

1. The shape of the Hα line profiles in our spectra indicates the presence of an accretion disk around the star. During the formation of Hα lines, the dominant role on the dates [(12-14 and 12-21) 2019] belongs to the rotation (V/R≈1), and on the dates 01-25-2019 and 01-17-2020 – an accretion of matter to the surface of the star.

2. During the transition from the emission mode to absorption, signs of accretion are observed in the profiles of the Hα and Hβ lines.

3. The lines of resonant doublets, neutral sodium (D1,2 NaI), and once ionized calcium (H, KCaII) are represented in our spectra by the interstellar component (IS); the circumstellar component (CS) is not visible. Heliocentric ray velocities of these lines (on average): 27.5 km/s (D2NaI); 28.4 (D1NaI); 26.2 (HaII); 25.7 kms (KaII).

4. The neutral helium line profile (HeI 5876Å) represents the central absorption and emission component on the blue wing (2019-01-25 and 2020-01-17) or both wings [(12-14 and 12-21) 2019].

5. In the spectra obtained in a time difference of 7 days [(12-14 and 12-21) 2019], the Hα; Hβ; HeI 5876Åline profiles; are practically the same both in terms of the profile and ray velocities.

Acknowledgements. One of the coautors (S. Mammadova) acknowledges the support of the Innovation Horizon 2020 (2014-2020) under the Marie Sklodowska-Curie Grant Agreement No. 823734.

References

Claria J.J.: 1974, *AJ* , **79**, 1022.
Corporon P., Lagrange A.M.: 1999, *A&AS*, **136**, 429.
Finkenzeller, Mundt: 1984, *Astron. & Astrophys. Suppl. Ser.*, **55**, 109.
Galazutdinov G.: http://www.gazinur.com/DECH software.html.
Herbig, G.H.: 1960, *ApJS*, **4**, 337.
Mikailov Kh.M. et al.: 2020, *Kinem. and Physics of Celes. Bodies* , **36**, 22.
Pogodin M.A. et.al.: 2006, *A&A* **452**, 551.
Tjin A Djie et al.: 2001, *MNRAS*, **325**, 1441.

SOLAR SYSTEM AND SPACE ENVIRONMENT

DOI 10.18524/1810-4215.2022.35.268213

OBSERVATION OF AN OCCULTATION OF THE UCAC4 488-082551 STAR BY ASTEROID (76228) 2000 EH 75 ON 31 MAY 2022

Yu. M. Gorbanev[1], V. V. Kleshchonok[2] and S. R. Kimakovsky[1]

[1] Astronomical Observatory of Odesa I. I. Mechnykov National University, 1B Marazliivska St, Odesa, 65014, Ukraine

[2] Astronomical Observatory of Taras Shevchenko National University of Kyiv, 3 Observatorna St, Kyiv, 04053, Ukraine

skydust@ukr.net; klev@observ.univ.kiev.ua; keysunai@gmail.com

ABSTRACT. Observations of an occultation of the UCAC4 488-082551 star by asteroid (76228) 2000 EH 75 were carried out on 31 May 2022 at Kryzhanivka observation station of Odesa I. I. Mechnykov National University (the observatory code A85). A set of instruments, which included a Schmidt telescope (the primary mirror diameter D = 271.25 mm; the corrector plate diameter D_k = 223.9 mm; the focal length F = 440 mm), a GPS receiver and Videoscan-415-2001 CCD camera, was used to perform observations. The observing conditions were as follows: clear sky, the star's altitude 49^0 south, the Moon was below the local horizon. The target star from the UCAC4 catalogue (Zacharias *et al.* 2013) has the following photometric parameters: m_B = 14.008; m_V = 12.720; m_r = 12.284; m_i = 11.813. The diameter of the star has not been determined. Asteroid (76228) is a Main Belt asteroid with an orbital period of 4.17178 years. It has an absolute magnitude of 14.93, the visible geometric albedo of 0.123±0.013 and diameter of 5.00±0.23 km (Masiero *et al*. 2011). The time of occultation predicted using ephemerides was 23:52:44±4 sec. The maximum duration of the occultation was 0.4 sec, provided that the observing site was located at the centre of the occultation track (strip). A drop in the star's brightness observed during occultation was about 8^m.

The occultation event was recorded as a sequence of GIF images with the exposure time of 0.5 sec per frame. The system clock of the computer used for the occultation recording was controlled with a GPS receiver in a fashion similar to that described in the paper by Karbovsky *et al.* (2017).

The data processing yielded an estimate of the occultation duration of 0.46±0.04 sec. The uncertainty of the occultation start time within exposure results in the total estimate of accuracy in timing the maximum phase of occultation 23:52:44.06±0.10 sec. The chord length across the asteroid estimated by timing the occultation is L = 9.2±0.8. This chord length is close to the estimates of the asteroid diameter reported in the paper by Masiero *et al.* (2011).

Key words: asteroids, stellar occultation, photometry.

АНОТАЦІЯ. 31 травня 2022 р. були проведені спостереження покриття астероїдом (76228) 2000 EH 75 зорі UCAC4 488-082551 на спостережній станцій в с. Крижанівка (код A85) Одеського національного університету імені І.І.Мечникова. Для спостережень використовувався комплекс з телескопу системи Шмідта (Діаметр головного дзеркала D=271.25 мм, діаметр корекційної пластини Dk=223.9 мм, фокусна відстань F=440 мм),, GPS-приймача і камери «ВІДЕОСКАН-415-2001». Умови спостережень: ясно, висота зорі над горизонтом 49° в південному напрямку, місяць під горизонтом. Зоря з каталогу UCAC4 (Zacharias et.al, 2013), яка має наступні фотометричні параметри mB=14.008, mV=12.720, mr=12.284, mi=11.813. Діаметр зорі не визначався. Астероїд (76228) належить до Головного поясу астероїдів з періодом обертання 4.17178 років. Він має абсолютну зоряну величину 14.93, геометричне альбедо 0.123±0.013, діаметр 5.00±0.23 км (Masiero et. al, 2011). За ефемеридами момент покриття 23:52:44±4 сек. Максимальна тривалість покриття 0.4 сек при умові знаходження в центрі полоси видимості покриття. Падіння яскравості зорі під час покриття приблизно на 8^m.

Був отриманий запис покриття у вигляді послідовності gif файлів з тривалістю експозиції одного кадра 0.5 сек. Системний час комп'ютера, який використовувався для запису, контролювався за допомогою GPS-приймача, аналогічний тому, що описаний в роботі (Карбовський та ін., 2017).

Обробка показала, що оцінка тривалості покриття 0.46±0.04 с. Невизначеність початку покриття в межах експозиції дає сумарну оцінку точності моменту максимальної фази покриття 23:52:44.06±0.10 с. Оцінки хорди астероїда за тривалістю покриття L = 9.2±0.8. Ця оцінка близька до оцінок діаметру з роботи (Masiero et. al,, 2011).

Ключові слова: астероїди, покриття зір, фотометрія.

Table 1: Observations of occultations of stars by asteroids at the observing station of Odesa I. I. Mechnykov National University in Kryzhanivka village (the observatory code A85).

Date	Observation time, UTC	Object (asteroid)	Star	Exposure time, sec	Occultation status: recorded or not recorded
22.11.2021		(585) Bilkis	UCAC4 397-130023	0.5	not recorded
02.12.2021	21:27:00 - 21:30:57	(30512) 2001 HO8	UCAC4 426-009364	0.5	not recorded
31.01.2022	22:19:07 - 22:31:36	(44473) Randytatum	TYC 1366-02390-1	0.5	not recorded
28.03.2022	21:25:53 - 21:26:29	(9691) Zwaan	UCAC4 453-052057	2	not recorded
26.04.2022	02:19:57 - 02:22:56	(107) Camilla	UCAC4 394-075598	5	not recorded
27.04.2022	00:06:00 - 00:07:00	(26512) 2000 CL46	TYC 311-01134-1	0.5	not recorded
31.05.2022	23:52:10 - 23:53:00	(76228) 2000 EH75	UCAC4 488-082551	0.5	recorded
02.05.2022	20:48:14 - 20:50:00	(116228) 2003 YZ4	UCAC4 516-051041	0.5	not recorded
04.08.2022	22:36:48 - 22:50:01	(159342) 2006 JR	TYC 489-02574-1	0.2	not recorded

1. Introduction

Routine observations of asteroid occultations have been performed at the observing station of Odesa I. I. Mechnykov National University in Kryzhanivka village (the observatory code A85). A set of instruments, which includes a Schmidt telescope (the primary mirror diameter D = 271.25 mm; the focal length F = 440 mm), a GPS receiver and Videoscan-415-2001 CCD camera, is used to carry out such observations. An important component of the set of instruments employed to observe occultations is the timing system. For its operation, the computer system clock, which is continuously controlled with a GPS receiver in a fashion similar to that described in the paper by Karbovsky *et al*. (2017), is used.

2. Observations

Observational data are given in Table 1. The majority of observations did not prove that the occultation occurred. This information is still useful though because it can be leveraged to specify the sizes and ephemerides of asteroids more precisely.

Observations of an occultation of the UCAC4 488-082551 star by asteroid (76228) 2000 EH 75 were carried out on 31 May 2022 at the observation station of Odesa I. I. Mechnykov National University in Kryzhanivka village (the observatory code A85). The observing conditions were as follows: clear sky, the star's altitude 49^0 south, the Moon was below the local horizon. The target star from the UCAC4 catalogue (Zacharias *et al*. 2013) has the following photometric parameters: m_B = 14.008; m_V = 12.720; m_r = 12.284; m_i = 11.813. The diameter of the star has not been determined. Asteroid (76228) is a Main Belt asteroid with an orbital period of 4.17178 years. It has an absolute magnitude of 14.93, the visible geometric albedo of 0.123±0.013 and diameter of 5.00±0.23 km (Masiero *et al*. 2011). The time of occultation predicted using ephemerides was 23:52:44±4 sec. The maximum duration of the occultation was 0.4 sec, provided that the observing site was located at the centre of the occultation track (strip). A drop in the star's brightness observed during occultation was about 8^m. The observations resulted in the occultation event recorded as a sequence of GIF images with the exposure time of 0.5 sec per frame. The system clock of the computer used for the occultation recording was controlled with a GPS receiver in a fashion similar to that described in the paper by Karbovsky *et al*. (2017).

3. Processing

A program which enabled to automatically measure intensity of digital images of the target UCAC4 488-082551 star and comparison stars in each frame was employed to process observational data. Main image frames were processed using dark frame subtraction. Seven comparison stars were used as reference ones to improve reliability of photometric estimates for the observed occultation. When performing photometry of the occulted star, its position in each frame was determined by the relevant comparison star positions.

Photometric curves of some reference stars are shown in Figure 1. In order to factor in possible changes in the sensitivity of photometric measurements and in the atmospheric transparency, the resulting photometric curve of the occultation was divided by the weighted average photometric curve for a set of all comparison stars. First, all instantaneous intensities of individual stars were normalised to 1:

$$i_0(t) = i(t)/\overline{i(t)}$$

Then, the root-mean-square error (σ) of the normalised measurements of the comparison stars' intensities was determined. The inverse of this error was assigned as a weight to each k comparison star:

$$w_k = 1/\sigma(i_{ok})$$

The weighted average normalized photometric curve, $I_0(t)$, was determined by the expression:

$$I_0(t) = \sum_k w_k i_{ok}(t) \Big/ \sum_k w_k$$

Photometric estimates of the occulted star were normalized to 1 as well, and then they were divided by the weighted average photometric curve $I_0(t)$. The resulting curve, which is free from the effects of changing sensitivity of photometric measurements and transparency of the atmosphere, is presented in Figure 2.

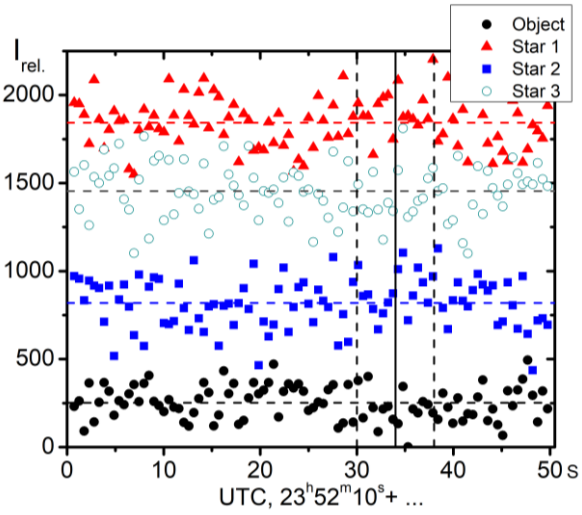

Figure 1: Photometric readings of the target star occulted by asteroid (76228) (denoted as "Object") and several reference stars in the field of view. Horizontal dashed lines depict the mean brightness of the stars. The vertical solid line marks the ephemeris time of the occultation. Vertical dashed lines represent the time range for the occultation start, taking into account prediction errors of ephemerides.

Vertical dashed lines show the limits of predictions of the occultation time using ephemerides. The horizontal dashed line depicts the lower limit of the 2σ range for the photometric curve of the target star. The only photometric reading at the predicted occultation time, which is outside the 2σ range, is marked with a downward arrow.

4. Conclusions

The instant of time which corresponds to the mid exposure time of the frame with captured occultation is 23:52:44.06±0.02 c. The star's brightness in this frame, taking into account statistical signal fluctuations, is 0.08±0.07 in relative units. Since the asteroid is too faint, then it can be assumed that the star disappears completely for the duration of occultation.

It yields an estimate of the occultation duration of 0.46±0.04 sec. The uncertainty of the occultation start time within exposure results in the total estimate of accuracy in timing the maximum phase of occultation of 23:52:44.06±0.10 sec. The chord length across the asteroid estimated by timing the occultation is L = 9.2±0.8. This chord length is close to the estimates of the asteroid diameter reported in the paper by Masiero *et al.* (2011).

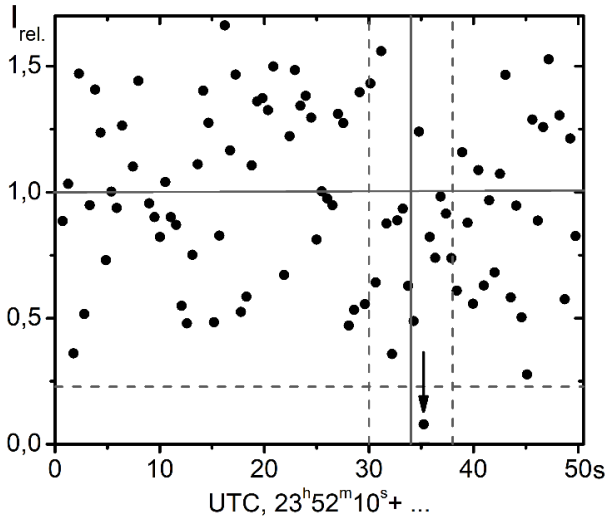

Figure 2: Photometric readings of the UCAC4 488-082551 star normalised to 1, taking into account statistical signal fluctuations, during its occultation by asteroid (76228) 2000 EH 75 on 31 May 2022. The vertical solid line marks the occultation time predicted using ephemerides. Vertical dashed lines represent the time range for the occultation start, taking into account prediction errors of ephemerides. The horizontal dashed line depicts two standard deviations 2σ from the mean intensity of the photometric readings. The downward arrow indicates the photometric reading that corresponds to the occultation.

References

Kleshchonok V.V., Karbovsky V.L., Buromsky M.I., Lashko M.V.: 2021, *Kinem. and Phys. of Cel. Bod.*, **37 (1)**, 41. https://doi.org/10.3103/s0884591321010025

Masiero J.R., Mainzer A.K., Grav T., Bauer J.M., Cutri R.M., Dailey J., Eisenhardt P.R.M., McMillan R.S., Spahr T.B., Skrutskie M.F., Tholen D., Walker R.G., Wright E.L., DeBaun E., Elsbury D., Gautier T., Gomillion S., Wilkins A.: 2011, *Astrophys. J.*, **741 (2)**. https://doi.org/10.1088/0004-637x/741/2/68

Zacharias N., Finch C.T., Girard T.M., Henden A., Bartlett J.L., Monet D.G., Zacharias M.I.: 2013, *Astron. J.*, **145 (2)**. https://doi.org/10.1088/0004-6256/145/2/44

10.18524/1810-4215.2022.35.268732

PHYSICAL PROPERTIES OF "HOT POPULATION" OBJECTS IN THE KUIPER BELT

H. Okhotko[1], V. Troianskyi[1,2,3], O. Bazyey[1,4]

[1]Department of Physics and Astronomy FMPIT of Odesa I.I. Mechnykov National University, Pastera Street 42, 65082 Odesa, Ukraine

[2] Astronomical Observatory Institute, Faculty of Physics, Adam Mickiewicz University, Słoneczna 36, 60- 286 Poznań, Poland

[3]Astronomical Observatory of Odesa I.I. Mechnykov National University, Marazlievskaya 1v, 65014 Odesa, Ukraine

[4] Department of Mathematics, Physics and Astronomy, Odesa National Maritime University, Mechnikov Street 34, 65029 Odesa, Ukraine

ABSTRACT. Most planetesimals formed at distances of 15 - 30 a.u. were gravitationally ejected from the Solar system as a result of the migration of the giant planets, but a small part remained, captured by Jupiter and the Kuiper belt. As a result, we can now observe such a variety, in terms of physical and dynamic characteristics, in the Trojan asteroids of Jupiter and in the Kuiper belt. Planetesimals captured by the Kuiper Belt are a "hot population" now. The term "hot" does not refer to the temperature of bodies, but characterizes the orbit of objects. ~120,000 objects larger than 100 km. in diameter are known in the "hot population". This population is characterized by an orbital inclination greater than 5 degrees and a large eccentricity. The main task of the work, based on physical and dynamic characteristics, is to search for the same properties Trojan asteroids of Jupiter and objects from the "hot population" of the Kuiper belt, which supposedly migrated earlier from the region of the original orbit of Neptune. The data from ground-based observations and space missions is used in the work.

Keywords: minor planets, TNO, asteroids.

АНОТАЦІЯ. Більшість планетезималей, що утворилися на відстанях 15-30 а.о., були гравітаційно викинуті з Сонячної системи в результаті міграції планет-гігантів, але невелика частина залишилася, захоплена Юпітером і поясом Койпера. У результаті ми зараз можемо спостерігати таку різноманітність, з точки зору фізичних і динамічних характеристик, у троянських астероїдів Юпітера і в поясі Койпера. Планетезималії, що захоплені поясом Койпера, зараз є «гарячою популяцією». Термін «гарячі» не стосується температури тіл, а характеризує орбіту об'єктів. Приблизно 120 000 об'єктів розміром понад 100 км в діаметрі відомі в «гарячому населенні». Ця популяція характеризується нахилом орбіти понад 5 градусів і великим ексцентриситетом. Основним завданням роботи, заснованої на фізико-динамічних характеристиках, є пошук однакових властивостей троянських астероїдів Юпітера та об'єктів із «гарячого населення» поясу Койпера, які, ймовірно, мігрували раніше з області первісної орбіти Нептуна. У роботі використані дані наземних спостережень і космічних місій.

Ключові слова: малі планети, ТНО, астероїди.

1. Introduction

During the evolution of the Solar system, planetesimals, originally located in the accretion disk, are dispersed due to gravitational interaction with the giant planets. Most of them are ejected from the Solar system, one small part is captured by Jupiter at the Lagrange points, and the other is scattered into the Kuiper belt and forms a "hot population" (Levison et al., 2021). The "hot population" is characterized by an inclination of more than 4 degrees and is located in the region of 39.4 - 55.8 au (Delsanti & Jewitt, 2006; Levison et al., 2008). Hot population objects are interesting in that most of them may be ancient or primary objects that have changed slightly since their formation.

2. Target selection

From 2000 known objects, we chose numbered objects that had a well-known orbit. These objects are shown in Fig.1, which demonstrates the dependence of the eccentricity on the semi-major axis and inclination on the semi-major axis. The dashed lines mark the resonances of Neptune with objects (3:2, 5:3, 7:4, 2:1, 5:2).

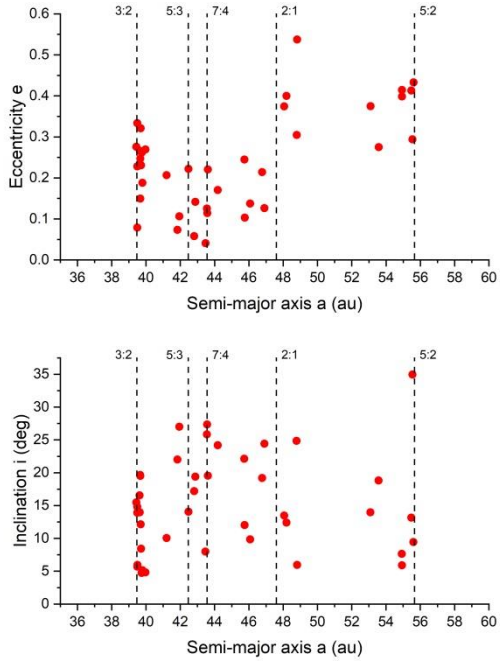

Figure 1: Orbital distribution of asteroids considered in this work.

3. Physical properties

Known periods of small bodies of the Solar system are presented in the diagram Fig. 2. On it, we marked in red the objects of the "hot population" with a known period. They fall into the region of trans-Neptunian objects (TNO), which are marked in yellow. The dotted line in the diagram marks the restriction on the rotation period, i.e. the spin barrier and the objects we have chosen do not exceed it.

$$H = -5lg\frac{D\sqrt{p}}{1329} \quad (1)$$

were H - absolute magnitude, D - diameter, p- geometric albedo.

Using the formula (1), we recalculated the values of diameter and absolute magnitude for objects 1993 SC, 1996 TO66, 1999 KR16, 2002 TX300 and obtained distribution Fig 3.

We also obtained the albedo and absolute magnitude values for the objects 1999 KR16, Quaoar, and Varuna. For the Quaoar object, we recalculated the values based on new diameter data (Morgado et al., 2022). As a result, we got the distribution in Fig. 4.

For the objects of the "hot population", we calculated the average albedo value $p = 0.104 \pm 0.054$.

From the database "IAU Minor Planet Center" we took the values of the phase function, which were obtained by ground-based observations and from the joint results of "Herschel and Spitzer observations" (Lellouch et al., 2013), and obtained a distribution on the absolute magnitude (Fig. 5).

We have averaged the phase function G = 0.137 ± 0.048 from ground-based observations and from Herschel and Spitzer observations.

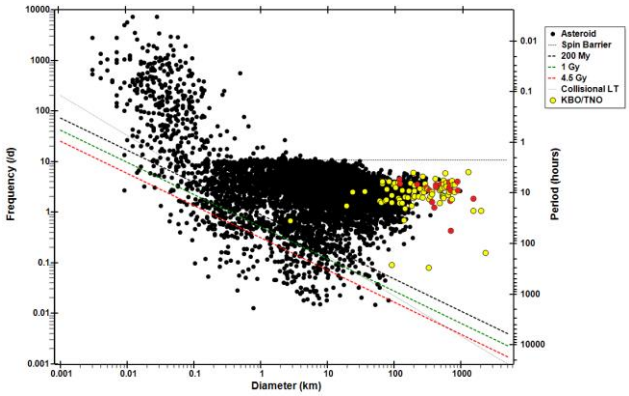

Figure 2: The distribution of asteroids based on rotation rate (frequency) versus diameter (Warner et al., 2009). Objects of the "hot population" from our list are marked in red.

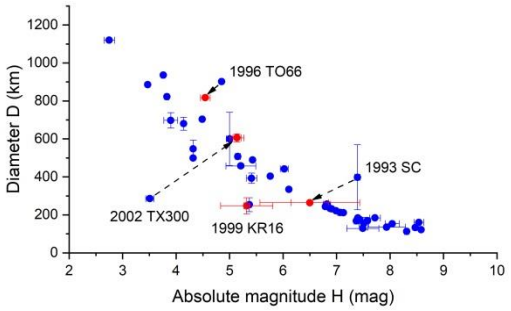

Figure 3: The distribution of asteroids based on diameter versus absolute magnitude. In the red marked recalculated values for 1993 SC, 1996 TO66, 1999 KR16, 2002 TX300.

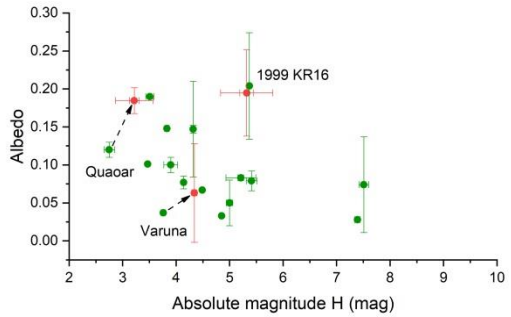

Figure 4: The distribution of asteroids based on albedo versus absolute magnitude. In the red marked recalculated values for 1999 KR16, Quaoar, Varuna.

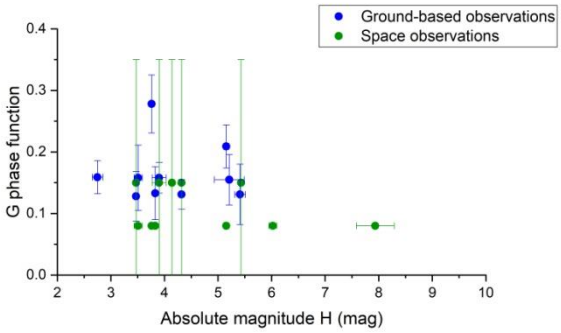

Figure 5: The distribution of asteroids based on phase function versus absolute magnitude.

4. Conclusion

As a result, we obtained the average albedo value for the objects of the "hot population" $p = 0.104 \pm 0.054$. It can be concluded that the objects are rather dark.

We also obtained the average value for the phase function based on ground-based observations and the results of the Herschel and Spitzer space missions ($G = 0.137 \pm 0.048$). Based on the obtained value, we can confirm the taxonomy of the object, using only photometric observations (Shevchenko et al., 2016; Oszkiewicz et al., 2021).

For asteroids 1993 SC, 1996 TO66, 1999 KR16, 2002 TX300, Varuna, Quaoar, we have received new values of diameter, absolute magnitude and albedo. The obtained refined physical parameters of our objects will be used in further work. Numerical simulation (Troianskyi & Bazyey, 2018; Oszkiewicz et al., 2019; Troianskyi et al., 2022) of orbits on − 4 Gy to must confirm the theory of "hot population" migration from the region of Neptune (Levison et al., 2021).

References

Delsanti A., Jewitt D.: 2006, Solar System Update, edited by P. Blondel and J. Mason. ISBN 3-540-26056-0. Library of Congress Catalog Card No. 2005936392. Published by Springer, Berlin, IX + 329 pp., 267.

Lellouch E., Santos-Sanz P., Lacerda P. et al.: 2013, *A&A*, **557A**, 60.

Levison H.F., Marchi S., Noll K. et al.: 2021, *IEEE Aerospace Conference (50100)*, 1-10, doi: 10.1109/AERO50100.2021.9438453.

Levison H.F., Morbidelli A., VanLaerhoven C.: 2008, *Icarus*, **196**, 258-273.

Morgado B.E., Bruno G., Gomes-Junior A. R. et al.: 2022, *A&A*, **664**, 15.

Oszkiewicz D., Kryszczynska A., Kankiewicz P. et al.: 2019, *A&A*, **632**, A170.

Oszkiewicz D., Wilawer E., Podlewska-Gaca E. et al.: 2021, *Icarus*, **357**, id. 114158.

Santos-Sanz P., Ortiz J. L., Sicardy B. et al.: 2022, *A&A*, **664**, A130.

Shevchenko V.G., Belskaya I.N., Muinonen K. et al.: 2016, *PSS*, **123**, 101-116.

Troianskyi V.V., Bazyey O.A.: 2018, *Contributions of the Astronomical Observatory Skalnate Pleso*, **48**, 356-380.

Troianskyi V., Kankiewicz P., Oszkiewicz D.: 2022, *16th Europlanet Science Congress 2022*, Spain, id.EPSC2022-888 doi: 10.5194/epsc2022-888.

Warner B.D., Harris A.W., Pravec P.: 2009, *Icarus*, **202**, 134-146.

DOI 10.18524/1810-4215.2022.35.268214

TIME AND GEOLOCATION UNCERTAINTIES AS COMPONENTS OF THE ACCURACY OF NEAS' GROUND-BASED OBSERVATIONS

A.V. Pomazan [1], N.V. Maigurova [2], O. M. Kozhuhov [3]

[1] Shanghai Astronomical Observatory, Shanghai, P.R. China, *antpomaz@shao.ac.cn*

[2] Research Institute "Mykolaiv Astronomical Observatory", Mykolaiv, Ukraine, *nadija@mao.nikolaev.ua*

[3] NSFCTC, SSAU, Kyiv, Ukraine, *a.m.kozhukhov@gmail.com*

ABSTRACT. The one of main tasks for solving the asteroid-cometary hazard problem is cataloging all objects that might come extremely close to Earth and pose a potential threat of collision. The reliability of their orbits significantly depends on the quality and the statistical treatment of astrometric observations, which are obtained by different observers and different techniques. Statistical analysis of the IAU MPC observational array of the small Solar system bodies and the development of a scheme for assigning weights to individual observation sets are important for performing asteroid orbit determination and refinement. Errors in the positions of asteroids associated with errors in the reference catalogs, observation epoch, observed brightness and rate of motion are considered in sufficient detail in investigations of Chesley et al. (2010), Farnocchia (2015), Vereš et al. (2017). Timing and geolocation uncertainties of the observer are less discussed in the literature. But in the case of observations of NEAs, especially at the moments of the close approaches to the Earth, timing errors and errors in the observatory's geolocation can significantly affect the accuracy of the obtained positions. Residual differences (O - C) in the equatorial coordinate system are usually used to search and identify functional errors dependencies. To detect errors caused by timing uncertainties, instead of residual differences (O - C) in equatorial coordinates, it is more convenient to use their along-track and cross-track representation. The cross-track differences are independent of timing errors and indicate only astrometric errors. On the other hand, timing errors are fully contained in the along-track component.

Here we present the simulation results of such errors and analysis using an array of observations from three observatories for the period 2017 - 2022. The array contains more than 18,000 positions of about 900 objects. Most of the objects belong to the group of NEAs, which include PHAs during close approaches to the Earth.

Keywords: astronomical databases, astrometry, positional errors, near-Earth asteroids.

АНОТАЦІЯ. Одним із головних завдань вирішення проблеми астероїдно-кометної небезпеки є каталогізація всіх об'єктів, які можуть наблизитися до Землі надзвичайно близько і становити потенційну загрозу зіткнення. Надійність їх орбіт суттєво залежить від якості та статистичної обробки астрометричних спостережень, які отримують різні спостерігачі з застосуванням різноманітних методів спостережень. Статистичний аналіз масиву спостережень малих тіл Сонячної системи МАС ЦМП та розробка схеми призначення вагових коефіцієнтів окремим серіям спостережень є важливими для визначення та уточнення орбіти астероїдів. Похибки в положеннях астероїдів, що пов'язані з похибками в опорних каталогах та залежать від епохи спостережень, яскравості і швидкості руху об'єкта досить докладно розглянуті в роботах Чеслі та ін. (2010), Фарночча (2015), Верес та ін. (2017) та ін. Менше обговорюється в літературі похибки, що пов'язані з невизначеністю часу та геолокацією спостерігача. Але у випадку спостережень навколоземних астероїдів (НЗА), особливо в моменти близьких наближень до Землі, похибки синхронізації часу та похибки геолокації обсерваторії можуть істотно вплинути на точність отриманих топоцентричних положень. Залишкові різниці (O - C) в екваторіальній системі координат зазвичай використовуються для пошуку та ідентифікації залежностей функціональних помилок. Для виявлення помилок, викликаних невизначеністю часу, замість залишкових різниць (O - C) в екваторіальних координатах зручніше використовувати різниці (O - C) вздовж та перпендикулярно напрямку руху об'єкта спостереження. Поперечні різниці не залежать від похибок синхронізації часу та визначаються позиційною похибкою спостережень. З іншої сторони, похибки синхронізації часу повністю містяться в компоненті уздовж траєкторії руху об'єкта.

Тут ми представляємо результати моделювання та аналіз таких похибок з використанням масиву спостережень трьох обсерваторій за період 2017–2022 рр. Масив містить понад 18 000 положень приблизно 900 об'єктів, більшість з яких є НЗА. включаючи потенційно-небезпечні астероїди (ПНА), протягом періодів близьких наближень до Землі.

Ключові слова: астрономічні бази даних, астрометрія, позиційні помилки, навколоземні астероїди.

1. Possible impact of geolocation and timing errors

The one of main tasks for solving the asteroid-cometary hazard problem is cataloging all objects that might come extremely close to Earth and pose a potential threat of collision. The reliability of their orbits significantly depends on

the quality and the statistical treatment of astrometric observations, which are obtained by different observers and different techniques. To improve the accuracy of the orbits, it is necessary to know the nature of the astrometric errors in NEAs observations. The main components of these errors usually include errors in the determination of the centroid and errors in the reference catalogue (both positions and proper motions). A number of investigations are devoted to the study and identification of such errors in the MPC database (Chesley et al., 2010; Farnocchia, 2015; Vereš et al.; 2017; etc.). The development of highly sensitive techniques (CCD and CMOS detectors) for object registration and creation of the accurate Gaia mission catalogs have led to a significant improvement in the positional accuracy of ground-based observations. However, in the case when we deal with objects that move at high apparent rates of motion, errors associated with the uncertainties of the time moment and the position of the observer can play a decisive role. The importance of taking them into account for obtaining homogeneous data arrays during large observational campaigns of individual objects, such as *2019 XS*, *2012 TC4*, and *Apophis (99942)* observations, was also discussed in the literature (Reddy et al., 2019; Farnocchia et al., 2015, 2022; Thuillot et al., 2015). Since these errors also become significant as asteroids approach the Earth, NEA observations during close approaches to the Earth are convenient observational material for searching for such errors.

1.1. Timing Errors

To identify possible errors associated with the synchronization of observation time, it is convenient to pass from residual differences (O - C) in equatorial coordinates to differences in along- (AT) and cross-track (CT) representation to the object's apparent trajectory motion. The CT residuals will depend only on the measuring procedure and indicate the internal accuracy of the observations. While the errors associated with the moment of time will be completely included in the AT component. Obviously, its value will depend on the rate of motion of the observed object:

$$(O-C)_{AT} \approx \Delta t \cdot V,$$

where $(O-C)_{AT}$ – along-track difference (O - C); Δt – timing error; V – asteroid's apparent full rate.

1.2. Geolocation Errors

When observed objects are at close distances to Earth, inaccurate or erroneous determination of the coordinates of the observation site can also be a source of important systematic errors in the topocentric positions of the asteroids. These errors can reach significant values for objects at extremely close distances to Earth.

As shown in Thuillot et al. (2015):

$$\theta \approx \frac{\Delta \cdot 206265}{x},$$

where θ – the difference in the astrometric position in arcsec; x – distance between observer and asteroid; Δ - distance between real and accepted geolocation.

In the report, based on the original observations of three observatories, we will show how timing and geolocation uncertainties could affect the accuracy of obtained topocentric positions.

2. Input Array: telescopes, statistics

2.1. Telescopes and observational technique

Observations from three observatories, which carry out regular observations of near-Earth asteroids, were chosen as an input array for simulations of time and geolocation uncertainties. Mykolaiv (MPC code 089) and Lishan (O85) observatories implemented a special technique (RDS CCD technique) for observing asteroids with high apparent rates of motion, which makes it possible to obtain observations of program objects at close distances from Earth with good positional accuracy. The main feature of the RDS CCD technique is the usage of a rotational platform and TDI mode of CCD to obtain separate CCD frames both for reference stars and objects which have a high apparent rate of motion (Tang et al., 2014; Pomazan et al., 2021) with different exposure time. Telescopes are equipped with GPS receivers. This allows us to assume that the moment of observation time for these observational arrays is determined with an accuracy of no worse than 0.1^s. Observations by Zalisci station (L18) are performed in the sidereal tracking mode, with the use of the "shift-and-stack" method for processing observations of relatively faint objects. The observations used in this paper were obtained with two telescopes: 0.3-m f/1.0 and 0.5-m f/3.8. Despite the fact that the first telescope began observations in 2017 (Maigurova et al., 2017) and the second one only in the middle of 2020, the bulk of the observations was carried out with the second telescope. The timing accuracy of L18 observations was also no worse than 0.1^s, except for a few cases with large errors caused by camera control software failure.

Instrumental characteristics of the telescopes used for observations are presented in Table 1.

2.2. Observations

The array of observations for the period 2017 -2022 (as of July 2022) was selected as the initial array for further simulation. The array contains over 18,000 positions of 885 asteroids. Most of the objects belong to the group of NEAs, which include PHAs, during close approaches to Earth. The observation array of 089 contains both fast-moving objects from the NEA group and asteroids from the Main belt. 22 (8%) NEAs from 089's array has full rate ≥ 40"/min during observations. The arrays of observations performed by L18 and O85 observatories include only NEAs. The part of fast-moving NEAs there is 12% and 18%, respectively for L18 and O85. Some objects were observed at very close distances from the Earth with extremely high apparent rates of motion, such as *2020 RZ6* (apparent rate in right ascension (RA) -95"/min, in declination (DE) -209"/min), *2020 DD0* (-508"/min and 15"/min), *2021 CO0* (-343"/min and -178"/min, correspondingly in RA and DE). Statistical characteristics of input arrays are presented in Table 2. Column **N1** in Table 2 represents the number of obtained positions, and **N2** – the number of asteroids.

Table 1: Technical specifications of the telescopes

Telescope	Lishan (O85)	Mykolaiv (089)	Zalisci (L18)
Diameter, m	0.5	0.5	0.3/0.5
Focal length, mm	3445	2975	300/1900
CCD	Alta U9000		ZWO ASI-174M Cool/ FLI ML16070*
Size, px	3056 x 3056		1936 x 1216 / 2432 x 1616*
Pixel size, μm	12 x 12		5.86 / 14.8*
Scale, ″/px	0.72	0.83	4.0/1.7*
FOV, ′	36.7 x 36.7	42.5 x 42.5	130 x 80 / 64.8 x 43
Filter	no	V*	no

* – Observations were carried out in the 2x2 binning mode.

Table 2: Statistical characteristics of the input array

Obs. Code	**N1**	**N2**	**O – C***	
			RA, mas	**Dec, mas**
089	9286	263	21±121	34±196
L18	6777	654	9±378	4±377
O85	2175	97	-2±157	-0±153
All	18238	885**	15±276	19±295

*residual differences (O – C) between observed data and HORIZONS online ephemeris service

**The actual number of objects may be less due to the observation of the same asteroids in different observatories

3. Simulation technique and results

To investigate how possible time and geolocation uncertainties can distort observational data, simulations of such errors were modeled on the input array of original observational data. The ephemerides for the true and shifted time moments were obtained using the HORIZONS online ephemeris service for timing errors simulation. Then the residual differences (O - C) were calculated in the expansion in equatorial coordinates and as AT and CT representation. To calculate the AT and CT differences, the equatorial coordinate system was rotated to alight the equator plane with the trajectory of an object's apparent motion trajectory. To eliminate possible curvation, the rotation angles were calculated based on consecutive ephemeris positions for the time moment of observations. Simulation data in the form of residual differences (O - C) in equatorial coordinates and AT/CT components are shown in Table 3. As can be seen from Table 3, with the usage of equatorial differences (O - C), timing errors of 0.5-1^s can be revealed only in the case of high-precision observations, when the part of objects with high apparent rates is sufficiently large, as in the case of O85's data. However, these errors become easily noticeable when passing from equatorial differences to differences in along-/cross-track projections to the object's motion trajectory. Figure 1 shows the mutual distribution of the equatorial differences (O - C) and differences for AT/CT representation for the initial array and for the case when the timing uncertainty is 1^s.

Another type of errors that can distort the accuracy of NEA positional observations is erroneous coordinates of the observation site. Since the uncertainty in the coordinates on the Earth's surface in most cases is much less than the distance to the celestial object, the significant influence of this error can only manifest itself when observing objects are at extremely close distances to Earth. In this case, even an error of several hundred meters will contribute a notable systematic component to the total observational error. To assess the influence of incorrect geolocation coordinates on the obtained topocentric positions, the residual differences with the ephemeris from HORIZONS online system, which were obtained for shifted site coordinates, were calculated. For simulation, the site coordinates for 089, L18 and O85 observatories were shifted in longitude and latitude by given values. For further calculations, only observations at a distance of less than 0.05 AU were selected (3019 positions of 294 asteroids). The simulation results are shown in Table 4, where Δ is the difference together in longitude and latitude between currently accepted and erroneous geographic coordinates. Of course, for modern ground-based observations, the 600" error seems unlikely, and the data in the last row are given only for a clearer visualization of the effect of geolocation uncertainties on topocentric positions of NEAs.

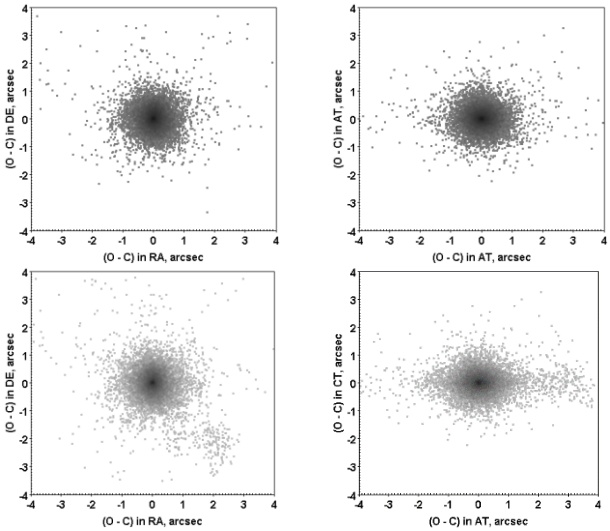

Figure 1: Mutual distribution of (O - C) differences in the equatorial coordinate system (left panels) and in AC/CT representation to object's trajectory (right panels) for original data array (top panels) and with 1^s timing uncertainty.

Table 3: The simulation results of timing errors for data arrays of considered observatories.

Observatory, MPC code	Δt, sec	(O - C), mas			
		Ra	Dec	AT	CT
089	Initial	21± 121	34 ±196	25± 172	22 ±155
	0.5	17± 157	33 ±225	20 ±228	22± 155
	1.0	13± 218	32 ±282	15 ±322	22 ±155
	2.0	5 ±350	30 ±418	7± 523	21± 155
	5.0	-17 ±803	25 ±921	-21 ±1213	22 ±155
	10.0	-55 ±1570	16±1790	-66 ±2377	22 ±155
L18	Initial	9± 377	4 ±377	20 ±423	5 ±312
	0.5	14± 516	3 ±465	23 ±616	7± 321
	1.0	15 ±624	-13± 576	22± 787	7 ±321
	2.0	19± 916	-43± 867	21 ±1221	8± 321
	5.0	29± 2053	138 ±1965	18± 2829	8 ±321
	10.0	48 ±4039	-297± 3868	12 ±5594	8± 321
O85	Initial	-3 ±155	2 ±151	-3 ±187	-5± 118
	0.5	21 ±394	5± 267	28 ±471	-5 ±118
	1.0	44± 726	13 ±449	59± 864	-5± 117
	2.0	88± 1356	27±809	116± 1607	-5 ±117
	5.0	227 ±3377	72± 1981	298 ±3995	-5 ±115
	10.0	88 1356	-	-	-

Table 4: The simulation results of geolocation uncertainties for observations, when the distance to Earth was less than 0.05AU.

Δ	(O - C), mas			
	RA	DE	AT	CT
0	7 ±597	60± 505	49 ±697	12 ±356
20"	52 ±598	100 ±506	73± 699	42 ±363
60"	144± 619	181 ±520	119 ±719	103± 406
600"	642 ±1378	591±1269	347 ±746	432± 929

As can be seen from Table 4, the incorrect observer coordinates will introduce a systematic error in the residual differences (O - C), which can appear even with relatively small inaccuracies in the position of the observer, for example, when several telescopes have the same MPC code. The dependencies of the residual differences vs distance of the object from Earth are shown in Figure 2.

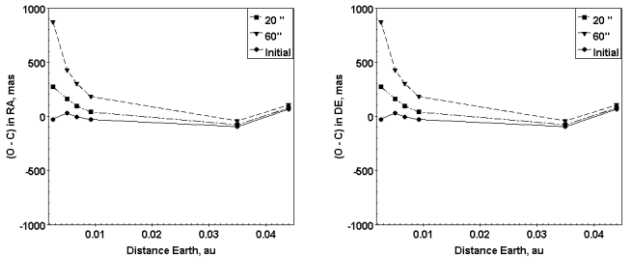

Figure 2: The dependency of positional accuracy of NEAs regarding to their distance from Earth for simulation of geolocation uncertainties based on observational data with objects' distances from the Earth less than 0.05 AU.

4. Conclusion

Timing errors can be easily detected by analyzing the residual differences (O - C) as along- and cross-track components. Simulation has shown that timing uncertainties of 0.5–2^s are not valuable when positional accuracy is worse than 0.2" for Main belt asteroids and slow-moving NEAs, but fast-moving objects (with rates of apparent motion more than 2"/min) needs time accuracy of at least 10^{-6} day (a large part of MPC observations has 10^{-5} day).

For the reveal of systematic timing errors, the analysis of the errors of individual sets of observations is required.

Geolocation uncertainties begin to affect the accuracy of observations of asteroids only at very small distances from Earth. To detect them, it is necessary to analyze the dependence of the total observation errors vs the distance between the observer and the asteroid.

In the future, it is planned to analyze close approach observations from the MPC array to detect such errors in observations from different locations.

References

Chesley S.R., et al.:2010, *Icarus*, **210**, 158.
Farnocchia D., et al.: 2015, *Icarus*, **245**, 94.
Farnocchia D., et al.: 2019, *Icarus*, **326**, 133.
Farnocchia D., et al.: 2022, PSJ, **3**, id. 156.
Maigurova N., et al.: 2017, *BKNUA*, **2** (56), 22.
Pomazan A., et al.: 2021, *RAA*, **21**, 175.
Reddy V., et al.: 2019, Icarus, **326**, 133.
Tang Z.-H., et al.: 2014, *Mem. Soc. Astron. Italiana*, **85**, 821.
Thuillot W., et al.: 2015, A&A, **583**, id. A59.
Vereš P.: 2017, Icarus, **296**, 139.
Vereš P., Payne M. J., Holman M. J., et al.: 2018, *AJ*, **156**, 5.

DOI 10.18524/1810-4215.2022.35.268215

DETERMINATION DEGRADATION OF SATELLITE SURFACE OPTICAL FEATURES BY PHOTOMETRIC METHOD

Peter. P. Sukhov [1,3], Vitaly P. Yepishev [2], Konstantin P. Sukhov [3], Alexei L. Pavlovskyi [3], Sergei A. Mamrai [3]

[1] Astronomical Observatory of the I.I. Mechnikov Odesa National University,1B Marazlyivska St, Odesa city, Ukraine, *psukhov@ukr.net*

[2] Laboratory of Space Researches, Uzhgorod National University, Ukraine, 2A Daleka St, Uzhgorod, Ukraine, *epishev1946@gmail.com*

[3] National Space Facilities Control and Testing Centre, Space Observation Centre, 40 Pushkinska St, Zhytomyr, Ukraine, *pal2978@bigmir.net; sergan1502@gmail.com*

ABSTRACT. A method is described for using photometric data to estimate the reflective properties of a satellite's surface material under conditions of its long stay in space. The technique of multicolour photometric B,V,R observations of several geostationary satellites built on different types of tires is shown, and the results obtained over a period of 3 to 9 years. These are geostationary satellites Astra 2E (on the Eurostar E3000 bus), Azerspace-2/Intelsat 38 (on the SSL-1300 bus), Sicral 2 (on the Spacebus-4000B2 platform) and Blagovest 11L (the Ekspress-2000 bus). It has been revealed that a pattern of change in the reflectivity of different geostationary satellites is dissimilar. Spacecraft materials used for the surfaces of geostationary satellites manufactured in the second decade of the 21st century are more resistant to the harsh space environment than those used for the satellites built in the late 20th century. We have proposed several ways of improving the method for identifying the spacecraft material type based on multicolour photometric observations. The presented results show that the proposed photometric method works and can be used for detecting spacecraft surface degradation.

Key words: spacecraftmaterial; reflectance index; multicolour photometry; satellite bus; degradation.

АНОТАЦІЯ. Описано метод використання фотометричних даних для оцінки відбивних властивостей матеріалу поверхні супутника в умовах його тривалого перебування в космосі. Показано методику багатоколірних фотометричних B,V,R спостережень кількох геостаціонарних супутників, побудованих на різних типах шин, і результати, отримані за період від 3 до 9 років. Це геостаціонарні супутники Astra 2E (на шині Eurostar E3000), Azerspace-2/Intelsat 38 (на шині SSL-1300), Sicral 2 (на платформі Spacebus-4000B2) і Благовіст 11L (на шині Експрес-2000). Було виявлено, що закономірність зміни відбивної здатності різних геостаціонарних супутників неоднакова. Матеріали космічних апаратів, які використовуються для поверхонь геостаціонарних супутників, виготовлених у другому десятилітті 21-го століття, є більш стійкими до суворих космічних умов, ніж ті, що використовуються для супутників, побудованих наприкінці 20-го століття. Ми запропонували декілька шляхів удосконалення методу ідентифікації типу матеріалу космічного корабля на основі багатоколірних фотометричних спостережень. Представлені результати показують, що запропонований фотометричний метод працює і може бути використаний для виявлення деградації поверхні космічного корабля.

Ключові слова: матеріал космічного корабля, показник відбиття, багатобарвна фотометрія, супутникова шина, деградація.

1. Introduction

One of the topical issues related to the development of durable thermal-control coatings for the spacecraft (SC) surface is exposure to solar radiation that includes electromagnetic radiation and charged particle fluxes. There are of other factors which also affect the satellite remaining in the space environment for a long time. These include high vacuum, zero gravity, space or meteoric dust, orbital man-made debris, solar flares, the current state of the near-Earth ionising radiation and thermal shocks which the satellite experiences when entering and exiting the Earth's shadow. Degradation of material in space changes mechanical, optical, spectral, electric and physical properties of coating materials used for the spacecraft hardware and also destroys fasteners used to mount solar panels (SP) and payload (PL) into the satellite bus. It results in breakdowns and failures that reduce the operational lifetime of the SC in orbit.

Studying and recording the interaction of different materials of the satellite surface with the near-satellite orbital environment has been mainly conducted experimentally under laboratory conditions or through simulation. However, simulations and laboratory experiments, despite their high cost, do not fully reflect actual space environmental effects on the SC surface. Such studies cannot factor in either a) the total effect of exposure to all space environmental factors on the geostationary satellite (GSS) surface; or b) ever-changing effects of the

Earth's atmosphere on the light falling onto or reflected off the satellite surface. Such "Relative complexity and high cost of tests in situ do not allow us to reckon them as a reliable tool for thorough investigation of the effects of the near-satellite environmental factors" [1].

More detailed information about changes in the reflectance properties of SC can be obtained from the analysis of colourimetric observations in particular spectral bands, as well as from the analysis of the reflectance spectrum produced from the SC materials.

The proposed method for studying the space environmental effects on the reflectance properties of the satellite surface materials is based on the analysis of ground-based multicolour photometric observations of the sunlight reflected off the satellite using known astrophysical methods. Although the method suggested here requires long-term studying GSS, in the authors' opinion, the results obtained will significantly improve our knowledge about the true state of the SC surface after its being in operation in space for a long time.

2. The main body

The only relevant publication known to the authors is the study by A. Didenko [2], which presents the results of observations of changes in the reflectance properties of GSS with time in several optical wavelength bands from the Earth's surface through the atmosphere.

In the above-referred study, three GSS were observed, namely those of the series Gorizont, Raduga and Intelsat, launched into orbit at the end of the 20th century and at the beginning of the 21st century over a time span of 4.5 years. A. Didenko [2] suggested examining the reflectance characteristics of GSS through changes in relative reflectance indices, $\Delta\gamma_{(B\text{-}V)}$ and $\Delta\gamma_{(V\text{-}R)}$, with time of the GSS operation in orbit. He made the following conclusions: a) the greatest changes in the reflectance properties of the SC surface occur during the first three years after launch; b) the pattern of change in $\gamma_{(B\text{-}V)}$ is dissimilar for different satellites. The computation of the relative reflectance index, $\Delta\gamma$, and spectral reflectance index γ_λ, as a fraction of incident solar radiation reflected from the SC surface was performed using a well-known formula for calculating the SC brightness [2]:

$$m_\lambda = m_\lambda^\Theta - 2{,}5\lg\left[\frac{S\gamma_\lambda F(\psi)}{d^2}\right]$$

Whence it follows that

$$\gamma_\lambda = d^2 \cdot 10^{\frac{m_\lambda^\Theta - m_\lambda}{2.512}} \;/\; S\cdot F(\psi),$$

where m_λ^Θ is the Sun's brightness (apparent magnitude) in the studied spectral band; S - is the apparent effective area of the SC surface illuminated by the Sun (estimated from the results of observations or adopted from the information sources); γ_λ is the spectral reflectance index in the B,V,R bands; F(ψ) is the phase function; d is the topocentric distance to the SC specified from the positional observations.

Publications by O. Murtazov *et al*. [3], H. Cowardin*et al*. [4] and G.A.McCue *etal*. [5] show high relevance of this line of research, as well as promising prospects for such studies, and present experimentally obtained B-V and V-R colour indices for some materials used in manufacturing surface hardware components of low-Earth-orbit SC. However, according to these data, it is quite difficult to determine the individual contribution from the SP and the satellite bus with external PL to the overall reflectance in a given spectral band. In the studies by V. Yepishev *et al*. [6, 7], the effectiveness of extending spectral bands in such observations was demonstrated using the results of observations of three GSS. Five colour filters, namely U, B, V, R, I, were employed in the experiment. An analysis of the obtained results showed that for the observed objects some characteristic features manifested themselves in the ultraviolet region, but not in other spectral regions. Besides, it was partly figured out which materials had been used in manufacturing particular surface hardware components of modern GSS. As can be deduced from the afore-mentioned publications, in order to conduct more thorough research, it would be desirable to know spectral reflectance indices γ_λ, at the time of observations or the tendency for these indices to change. In the latter case, it becomes possible to estimate degradation of the SC surface materials to a certain extent and to identify new spacecraft materials which have been developed to replace the outdated ones.

This paper presents the results of studying only four GSS with known satellite buses, namely Eurostar E3000 (manufactured by EADS Astrium), Spacebus-4000B2 (by Thales Alenia Space), SSL-1300 (by Space Systems/Loral) and Ekspress-2000 (by ISS named M.Reshetnev). The reflectance properties were monitored from the start of the GSS operation at the sub-satellite point through the year 2021. The duration of observations varied from 3 to 9 years. The GSS under study were launched in the second decade of the 21st century. This study has been aimed at checking whether it is possible to detect the SC surface degradation from multicolour photometric observations using known astrophysical algorithms for the information processing.

The observations were carried out using a 20-inch telescope based on the Cassegrain optical system. A high-speed photomultiplier FEU-79 was employed in the pulse counting mode. We used B, V, R colour filters with pass bands pretty close to the Johnson-Cousins broadband photometric system shown in Fig.1.

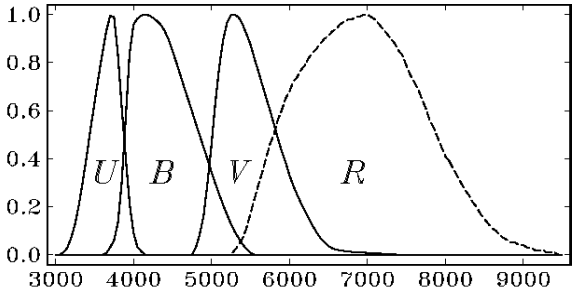

Figure 1: Schematic pass bands of the Johnson-Cousins multicolour system: the X axis represents the wavelength; the Y axis shows the spectral response of the photometric system expressed in relative units.

Table 1: The GSS under study

GSS name and year of observation	The satellite bus type	Application	Contractor
Astra 2E 2013-2021	Eurostar E3000	Communication	EADS Astrium (Europe)
Sicral 2 2015-2021	Spacebus-4000B2	Military communication	Thales Alenia Space (Franco-Italian)
Azerspace-2 2019-2021	SSL-1300	Communication	Space Systems/Loral (USA)
Blagovest 11L 2017-2021	Ekspress-2000	Military communication	ISS Reshetnev (Russia)

All GSS presented in Table 1 are three-axes stabilised objects deployed close to the observer's meridian of longitude; they did not change their positions throughout the observation period. The types of satellite buses (platforms) and dimensions of GSS were taken from electronic resources, such as Gunter Space Page [8] and Wikipedia [9], and also from the web-site of ICC M. Reshetnev [10].

Silicon was the most common element used in photovoltaic cells in SP for a long time. In the 21st century, new photovoltaic cells based on compound semiconductor materials, such as gallium arsenide (GaAs), indium gallium phosphide (InGaP), indium gallium arsenide (InGaAs), etc. appeared. The main function of SP is to absorb and convert solar radiation into electrical energy. This is why the reflectivity of modern SP is rather low. However, due to the fact that the SC solar arrays are quite large in area (covering up to several hundreds of square metres and beyond), sunlight reflection off the SP is observed predominantly in the B filter. The reflectivity of the satellite bus, which consists of a service module with all subsystems and a payload module, is very high. It is required for thermal control and normal operation of the onboard radio electronic equipment. The external payloads in the buses of many communication satellites, including feed arrays of radio antennas, are covered in a thin film of yellowish or, in some cases, gold colour, which has a high spectral reflectance index (γ_λ). In the V and R filters, one can observe the sunlight reflected off the satellite bus of a specific shape, such as cylinder, cone, cube, rectangular prism, etc., as well as off the external payload, including a service module and radio antennas of different shapes. Some portion of the reflected light observed in these filters is contributed from the SP based on GaAs, InGaP and other compound semiconductor materials.

In all the figures presented here below for each of the studied GSS the following data are depicted: changes in the averaged relative reflectance indices, $\Delta\gamma_{(B-V)}$ and $\Delta\gamma_{(V-R)}$, with time of the satellite staying in orbit and also changes in spectral reflectance indices $\gamma_B, \gamma_V, \gamma_R$. In all the figures, the values $\Delta\gamma_{(B-V)}$ and $\Delta\gamma_{(V-R)}$ correspond to the observed spectral region in the Johnson-Cousins system, which is 3000Å-5500Å and 5500Å-8200Å, respectively. The Y axis represents the values of relative reflectance indices, $\Delta\gamma_{(B-V)}$ and $\Delta\gamma_{(V-R)}$ (in figures - $\Delta\gamma$), the X axis shows the duration of the GSS staying in orbit in years.

The Eurostar E3000 satellite bus has been manufactured since 2004.As can be seen from the above-illustrated results for the Eurostar E3000 bus, the greatest changes in $\Delta\gamma_{(V-R)}$ are observed during the first 3 years after launch, when the averaged relative reflectance index, $\Delta\gamma$, is increasing from 0.050 to 0.065. Later on, this value is decreasing. For this satellite bus, the values $\Delta\gamma_{(B-V)}$ have barely changed over 7 years of observations, varying within the range 0.018-0.020.

Fig. 3 shows changes in spectral reflectance indices $\gamma_B, \gamma_V, \gamma_R$, of the GSS Astra 2E over the same time span of observations. As is seen from the plots, spacecraft materials which reflect light in the range from blue to yellow colours (at 3500Å-5500Å) are more susceptible to the deleterious effects of the space environment. Spacecraft materials reflecting red and near infrared colours (at 5500Å-8200Å) are less prone to change their reflectance properties.

Similar results of the studies obtained for the GSS Sicral-2 are illustrated in Figs. 4 and 5. The Spacebus-400B2 satellite bus has been produced since 1985. Over the first 3 years after launch, the relative reflectance index, $\Delta\gamma_{(V-R)}$, has decreased from 0.092 to 0.042; later on, this value starts increasing. As regards the relative reflectance index, $\Delta\gamma_{(B-V)}$, one can only observe a decrease from 0.038 to 0.09.

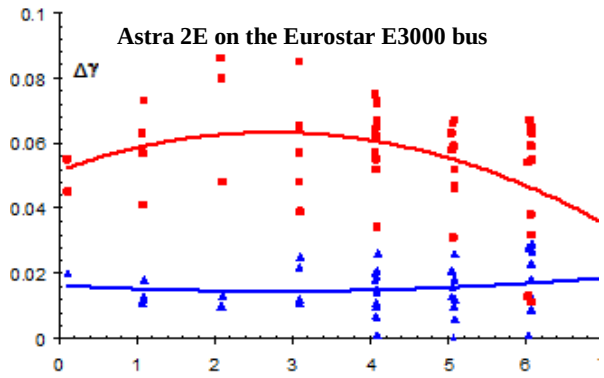

Figure 2: Changes in relative reflectance indices $\Delta\gamma_{(B-V)}$ – (blue colour) and $\Delta\gamma_{(V-R)}$ – (red colour), of the GSS Astra 2E observed during 2013-2021.

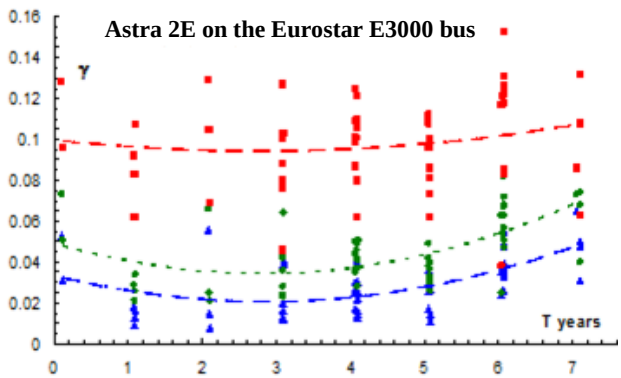

Figure 3: Changes in spectral reflectance indices, γ_B – (blue colour), γ_V – (green), γ_R – (red), of the GSS Astra 2E observed during 2013-2021.

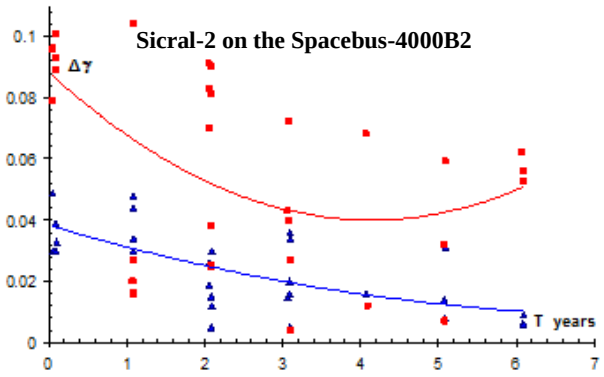

Figure 4: Changes inrelative reflectance indices, $\Delta\gamma_{(B-V)}$ – (blue colour), $\Delta\gamma_{(V-R)}$) – (red), of the GSS Sicral-2 observed during 2015-2021.

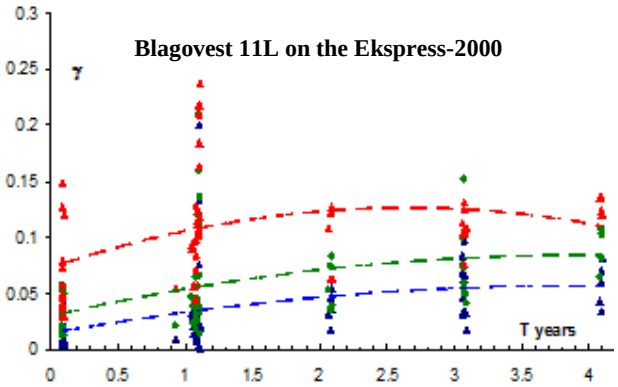

Figure 7: Changes in spectral reflectance indices, γ_B – (blue colour), γ_V – (green), γ_R – (red), of the GSS Blagovest 11L observed 2017-2021.

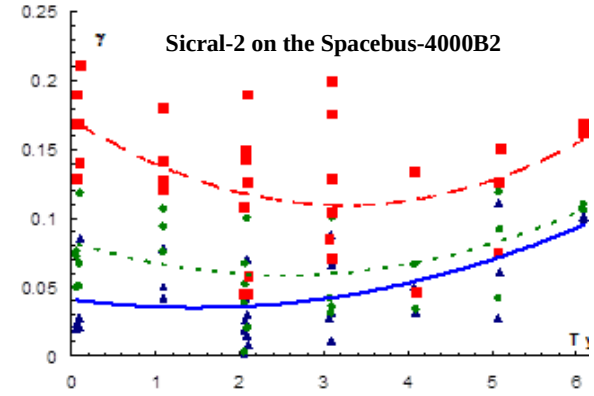

Figure 5: Changes in spectral reflectance indices,γ_B (blue colour), γ_V – (green), γ_R – (red), of the GSS Sicral 2 observed during 2015-2021.

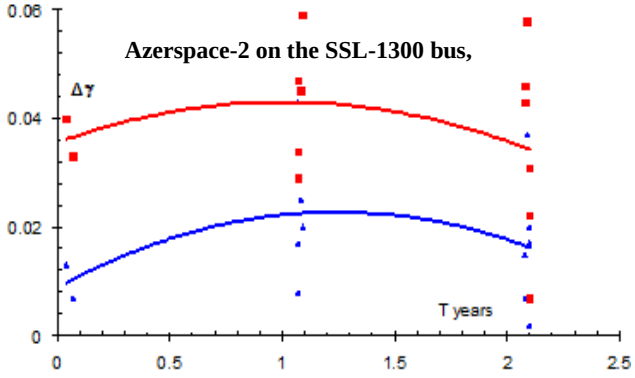

Figure 8: Changes in relative reflectance indices $\Delta\gamma_{(B-V)}$ – (blue colour), $\Delta\gamma_{(V-R)}$) – (red), of the GSS Azerspace-2 observed 2019-2021.

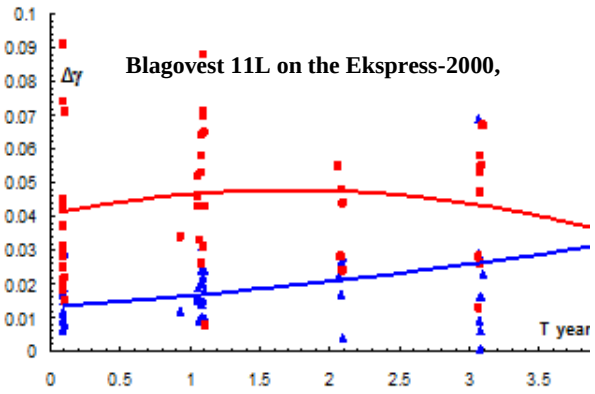

Figure 6: Changes in relative reflectance indices, $\Delta\gamma_{(B-V)}$ – (blue colour), $\Delta\gamma_{(V-R)}$) – (red colour), of the GSS Blagovest 11L observed 2017-2021.

A pattern of change in all three spectral reflectance indices, just like in relative reflectance indices, for this satellite bus is practically similar (see Fig. 5). These indices are decreasing over the first 3 year after launch, and then they all are increasing. The shape of the reflectance curves shown in Figs. 4 and 5 appears to be illogical!

The Express-2000 satellite bus employed in the GSS Blagovest 11L has been manufactured since 2014. As is seen from the data depicted in Fig. 6, there is a minor increase in the averaged relative reflectance indices. Over the first 1.5-2 years of the GSS staying in orbit, the index $\Delta\gamma_{(B-V)}$ has changed from 0.015 to 0.022, while $\Delta\gamma_{(V-R)}$ has varied within 0.037-0.048.

Spectral reflectance indices γ_R,γ_V and γ_R were increasing during the first 1.5-2 years, later on their growth rates slowed down (Fig.7).

The satellite bus SSL-1300 (Structure, Composite & Al honeycomb), used in the GSS Azerspace-2, has been produced since 1989. Minor changes in $\Delta\gamma_{(B-V)}$ and $\Delta\gamma_{(V-R)}$ can be traced during the first year of operation, when the averaged relative reflectance index $\Delta\gamma_{(B-V)}$ is increasing from 0.01 to 0.025 while $\Delta\gamma_{(V-R)}$ is increasing from 0.033 to 0.045.

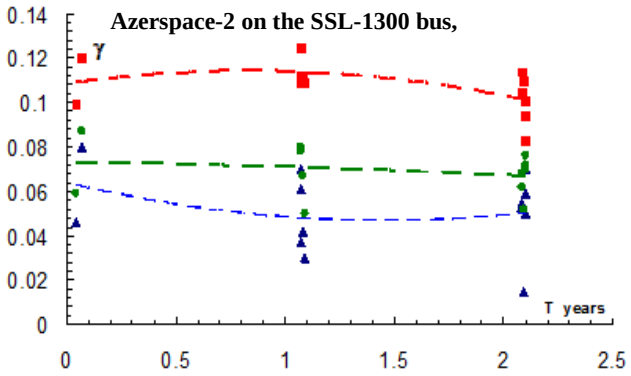

Figure 9: Changes in spectral reflectance indices, γ_B – (blue colour), γ_V – (green), γ_R – (red), of the GSS Azerspace-2 observed 2019-2021.

Likewise in Fig. 9, the curves for γ_B, γ_V and γ_R only show minor changes during the first year in operation; this may indicate that the SSL-1300 satellite bus is more resistant to the space environmental effects. However, it is possible that the period of observations is not long enough to make such a conclusion.

The data given in the Difference column of Table 2 enable us to predict the extent of degradation of the surfaces of the four studied satellite buses.

Table 2: The average range of the $\Delta\gamma_{(B-V)}$ and $\Delta\gamma_{(V-R)}$ values for the satellite buses over the first 3 years after GSS launch*.

GSS name and year of observation	**Bus type**	**Z** $\Delta\gamma_{(B-V)}$, $\Delta\gamma_{(V-R)}$	**Difference**
Astra 2E 2013-2021 EADS Astrium, (Europe)	Eurostar-3000	0.018 - 0.020 0.050 - 0.065	0.02 0.015
Sicral 2 2015-2021 Thales Alenia Space, (Franco-Italian)	Spacebus -4000B2	0.038 - 0.02 0.092 - 0.042	-0.018 -0.05
Blagovest 11L 2017-2021 ISS Reshetnev, (Russia)	Ekspress-2000	0.015 - 0.023 0,038 - 0,047	0.08 0.09
Azerspace-2 2019-2021 Space Systems/Loral, (USA)	SSL-1300	0.01 - 0.025 0.033 - 0.045	0.015 0.012

* Here, each cell in the Z column presents the range of changes in $\Delta\gamma_{(B-V)}$(the upper line) and $\Delta\gamma_{(V-R)}$(the bottom line). The Difference column shows the difference between the maximum and minimum $\Delta\gamma_{(B-V)}$ and $\Delta\gamma_{(V-R)}$ values, respectively.

3. Conclusions

The results presented in this paper show that the photometric method can be used to monitor and estimate the true degradation in optical properties of the SC surface with time of its stay in space.

It has been confirmed that a pattern of changes in the reflectivity of different GSS is dissimilar. It means that the leading manufacturers have been using different coating materials for the spacecraft SP and buses, which, in its turn, enables us to estimate the quality of these materials, as well as scientific and technological advances and innovations applied.

Spectral reflectance properties of the spacecraft materials used for the surfaces of GSS manufactured in the second decade of the 21st century make them more resistant to the harsh space environment as compared to those used for the GSS built in the late 20th century. It results from the technological progress. New materials are more resistant to the aggressive effects of the space environment.

On average, the reflectance properties of the studied GSS are similar; however, the GSS on the European satellite bus Eurostar E3000 (Astra 2E manufactured by EADS Astrium) and US satellite bus SSL-1300 (Azerspace-2/Intelsat 38 built by Space Systems/Loral) have some advantages.

It has been established that the spectral reflectance index γ_R is more prone to change while the spectral reflectance index γ_B changes just slightly, as expected.

A photometric method is cheaper than laboratory experiments; it reflects more precisely the effects of the space environment on the satellite surface materials as enables to record the total effect of exposure to all existing near-Earth space environmental factors affecting the satellite surface.

It has been corroborated that medium aperture telescopes can be successfully employed to study photometric and optical properties of GSS and to further collect and analyse information about near space (for instance, within the framework of the Space Situational Awareness (SSA) programme.

Successful estimating the extent of degradation of the SC surface material using a photometric method requires conducting routine long-term observations of GSS in narrowband filters, if feasible, with bandwidth less than 300Å. In the future, the proposed method can be further refined and improved.

References

1. Shuvalov V.A., Pys'movyy N.I., Kochubey H.S., Nosikov S.V.: 2011, *Kosmicheskaya nauka i tekhnologiya*, **17**, **№ 3**, 5. https://www.mao.kiev.ua/biblio/jscans/knit/2011-17/knit-2011-17-3-01.pdf
2. Didenko A.V.: 2005, *Vestnik KazNPU im. Abaya*, Ser. «Fiz–mat. nauki», **№ 1(12)**, 81. http://astronomer.ru/publications.php?act=view&id=168
3. Murtazov A.K.: 2000, *Okolozemnaya astronomiya i problemy izucheniya malykh tel Solnechnoy sistemy*, M.: Kosmosinform, 262.

4. Cowardin H., Seitzer P., Abercromby K., Barker E., Schildknecht T.: 2010, https://ntrs.nasa.gov/search.jsp?R=20110015517
5. McCue G.A., Williams J.G., Morford J.M.: 1971, *Planet. Space Sci.,* **19**, 851. https://doi.org/10.1016/0032-0633(71)90137-1
6. Yepishev V.P., Barna I.V., Kudak V.I., Perig V.M., Gabdeyev M.M.: 2017. *Nauchnyy vestnik Uzhgorodskogo vuza,* Seriya "Fizika", **41**, 132. https://physics.uz.ua/ru/journals/vipusk-41-2017/bagatokolirna-fotometriya-geostatsionarnikh-ob-rsquo-yektiv
7. Yepishev V.P., Kudak V.I., Pavlyuk M.M., Perig V.M.: 2017, *Nauchnyy vestnik Uzhgorodskogo universiteta*, Seriya "Fizika", **41**, 146. https://physics.uz.ua/ru/journals/vipusk-41-2017/doslidzhennya-poverkhnevikh-kharakteristik-geostatsionarnikh-suputnikiv-za-danimi-kolorimetriyi
8. https://space.skyrocket.de/cgi-bin/search.pl
9. https://ru.wikipedia.org/wiki/Астра_2E
10. https://www-russianspacewebcom.translate.goog/ekspress-2000.html?_x_tr_sch=http&_x_tr_sl=en&_x_tr_tl=ru&_x_tr_hl=ru&_x_tr_pto=sc

10.18524/1810-4215.2022.35.268799

DETERMINATION OF EXTERNAL GSS PAYLOAD FROM LIGHT CURVES

Peter Sukhov[1,3], Vitaly Yepishev[2], Konstantin Sukhov[3]

[1] Astronomical Observatory of the I.I. Mechnikov Odesa National University, *psukhov@ukr.net*

[2] Laboratory of Space Researches, Uzhgorod National University, *epishev1946@gmail.com*

[3] National Space Facilities Control and Testing Centre, Ukraine, *sppete@ukr.net*

ABSTRACT. They are offered reflective features to external surface geostationary satellites on which possible identify the separate external construction geostationary satellites. Such constructions can be; the type and forms radio antennas, solar panels, thermo film on surfaces of the platform. They are given to recommendations and specified moments of time, condition, under which possible find the external payload. The paper presents the results of colorimetric observations of 5 GSS of multi-purpose operation, on the platform of which an external payload in the form of several radio antennas was found, and in some cases the orientation and technical characteristics of the GSS were estimated.

Keywords: payload, radio antennas, multicolor photometry, light curve, GSS, color index, solar panels, thermo film, external payload.

АНОТАЦІЯ. Запропоновано світловідбивачі характеристики поверхні GSS, до яких можна визначити окремі зовнішні структури геостаціонарного супутника. Такі конструкції можуть бути; тип і форма радіо антеніни, сонячні батареї, термо-плівка на поверхні платформи. Дані рекомендації та моменти часу, умови, за яких можна знайти зовнішнє корисне навантаження. У роботі наведено результати колориметричних спостережень 5 ГСС багатоцільового призначення, на платформі яких виявлено зовнішнє корисне навантаження у вигляді кількох радіоантен, а в окремих випадках оцінено орієнтацію та технічні характеристики ГСС.

Ключові слова: Зовнішня корисна навантаження, радіо антени, багатоколірна фотометрія, світлова крива, GSS, кольоровий індекс, сонячні батареї, термо-плівка.

1. Introduction

Coordinate observations of geostationary satellites (GSS), carried out for the purposes of Space Surveillance Awareness (SSA), do not provide information about the shape of the satellite, its dynamics in orbit, the number and size of the external payload. The COSPAR Launch list also does not have such information about GSS. Under certain conditions of GSS visibility, such information can be obtained from multicolor photometric observations (non-resolved). Most modern GSS (communications, navigation, telecommunications, control over objects on the earth's surface and oceans) have triaxial stabilization, regardless of their operation in orbit. Their external payload (receiving and transmitting radio antennas, mirrors) basically does not change its orientation and direction to certain points on the planet or towards other geostationary objects. During each cloudless night, some of them, illuminated by the Sun, fall into the field of view of an earthly observer. Having special colorimetric equipment placed on telescopes, even of the middle class, it becomes possible not only to control the dynamics of the behavior of such satellites, but also to identify individual structures on their surface.

In this publication, we present the results of colorimetric observations of 5 GSS of multi-purpose functioning. On these GSS it was possible to detect external payload in the form of radio antennas, and in some cases to evaluate their orientation and technical characteristics.

2. Results

How to determine what “glare” is a radio antenna, a solar panel (SP) or a thermal film covering the GSS platform from overheating?

The answer – is according to the numerical value of the color index (B-V), (V-R). Specific values of the color index for many materials used on the surface of satellites were obtained earlier experimentally and published by A. Murtazov [1], V. Epishev [2,3], N. Cowardin [4]. But over time, materials change their reflective characteristics, or designers use new materials whose albedo is unknown to us. Therefore, when analyzing observational material, one must be careful not to make erroneous conclusions.

The GSS colorimetric is based on the transformation of the color indices of solar radiation after its reflection from the structural elements of the GSS surface. Color indices for the Sun [5]: (B-V) = 0.64, (V-R) = 0.52.

The satellite images below have been taken from online resources such as the Gunter Space Page [6] and Wikipedia [7].

1. "Intelsat 10-02". International telecommunications GSS. Figure 1 shows the phase light curve for 12.10. 2010. Near phase angles 27^0 - 30^0 in the V-filter, there are four small, but different amplitude, brightness rises. According to the calculated color indices (B-V) and (V-R), published in [1-4], it can be argued that they are caused by four pairwise different radio antennas, since smooth metal structures most intensively reflect sunlight in the spectral region V. This conclusion is also confirmed by the appearance of the GSS, shown in Fig. 2 showing four antennas.

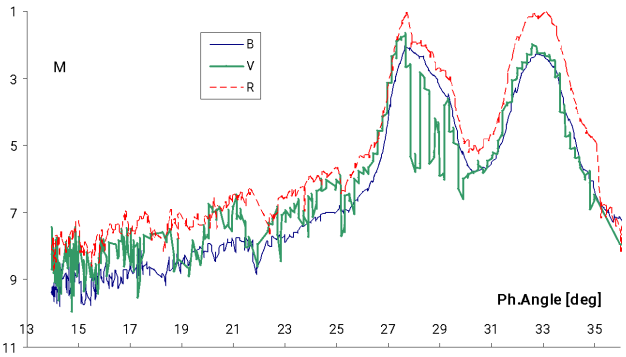

Figure 1: Phase light curve of GSS "Intelsat 10-02", B,V,R. 12.10.2004.

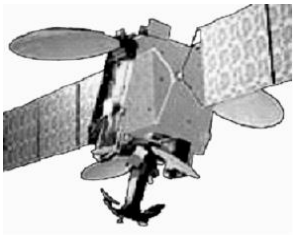

Figure 2: Appearance of the GSS "Intelsat 10-02"

2. "Cosmos-2397" (NPO of the S. Lavochkin). Russian early warning satellite. From the moment of launch in 2003, it was in an emergency condition and drifted to the east during the observations.

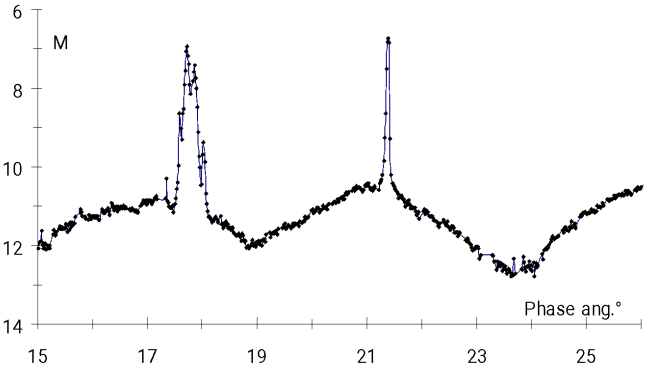

Figure 3: Phase light curve of GSS "Cosmos-2397". V-filter. 12.09.2004

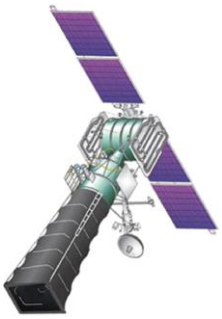

Figure 4: Appearance of the "Cosmos-2397"

Sharp almost mirror-like brightness rises are clearly generated by the solar panels of the satellite, which was rotating. Here, one filter V was enough to identify four SP. On Fig. 5 this is clearly seen when zooming in on the time interval of the first outburst on the light curve.

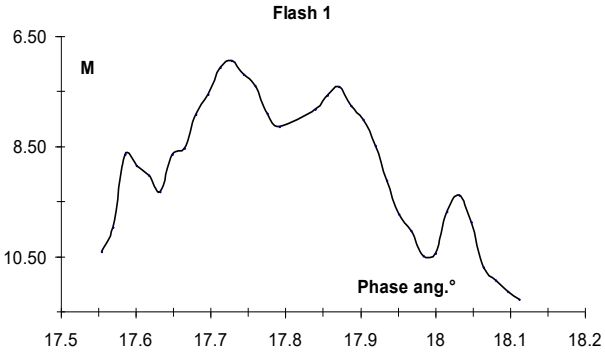

Figure 5: Zoom in on the first burst of the light curve "Cosmos 2397" 12.09.2004.

3. "SBIRS-GEO 2" (USA). GSS system for early detect of ballistic missile launches.

As a result of the studies, it was found that periodic specular flashes on the light curves (Fig. 6) were recorded from scanning mirrors, which, according to information from open sources, should be two on the GSS [8]. As can be seen from the light curves, they fluctuate with a period of P=15.66 sec. Periodic changes in the curves of the diffuse light component with P=62.64 sec. are caused, in our opinion, by oscillations of the GSS around an axis coinciding with the direction of its movement along the orbit. It is known that stabilized GSSs in the plane of the Earth's equator inspect the Earth's surface up to latitude of 83 deg. "SBIRS-GEO 2" examines it from North pole to South pole and, according to our results, it achieves this due to its oscillations with P = 62.64 sec. During this time, scanning mirrors scan the earth's surface twice in the northern hemisphere and twice in the southern hemisphere with P=15.66 sec. Thus, by estimating the directions of the mirrors, it was possible to simulate the rather complex dynamics of behavior in the orbit of this GSS as a whole.

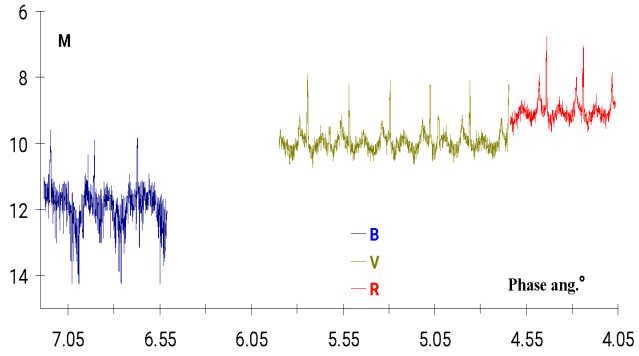

Figure 6: Phase light curve “SbirsGeo-2”. Filters B,V,R. 29.08.2014

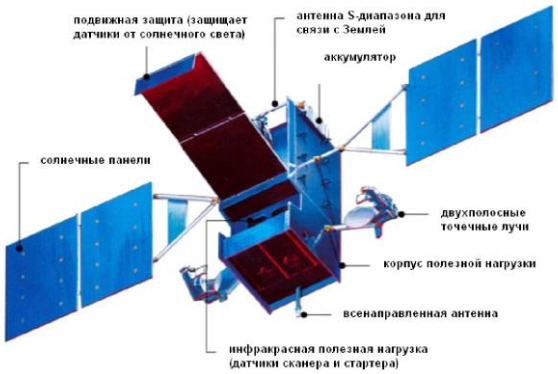

Figure 7: Appearance of the “SbirsGeo-2”

4. ГСС “Cosmos-2520”. A Russian military communications satellites of the heavy class "Blagovest".

The presented light curves show the results of observing the right side with respect to the observer of one of the “Cosmos 2520”. The large-amplitude periodic brightness changes on the curve are caused by the movement of the sun glare along the cruciform solar panels. In the last section of the curve, when the glare reached the body of the satellite, its slight changes are visible at the minimum brightness, caused precisely by the presence of radio antennas. At least three larger receiving radio antennas were recorded from this side. To estimate the number of radio antennas on the other side of the object, it was necessary to observe the satellite after it left the Earth's shadow.

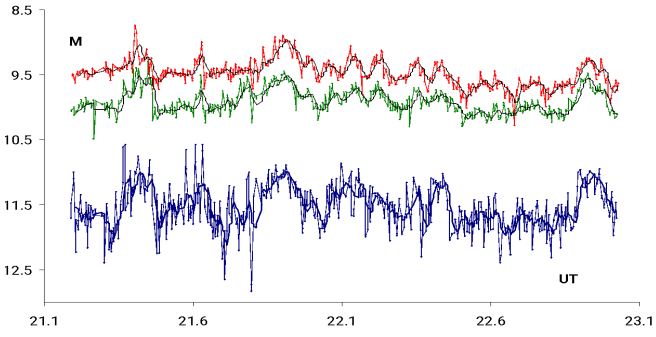

Figure 8: Phase light curve „Cosmos-2520”. B,V,R - filters. 12.08.2018

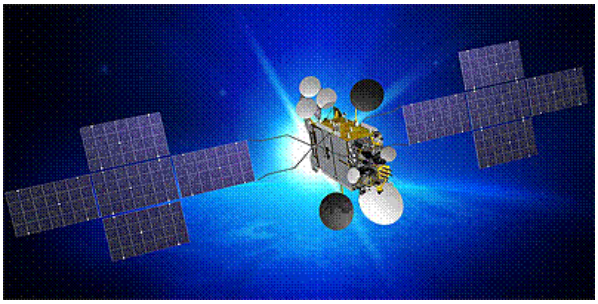

Figure 9: Appearance of the GSS “Cosmos 2520”

5. “Thuraya –2”, GSS mobile communication.

The brightness of this GSS is caused mainly by the reflection of sunlight from two large SP. The presence of a radio antenna is seen from small-amplitude brightness fluctuations along the curve. Such changes are typical for fine-structure antennas of the "fishing net" class. Similar low-amplitude brightness fluctuations from metal mesh radio antennas have been observed previously [9].

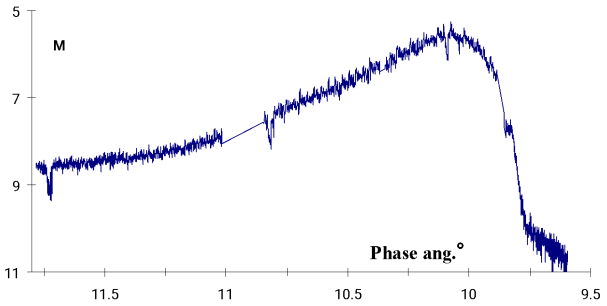

Figure 10: Phase light curve “Thuraya-2”. V-filter, 17.09.2014

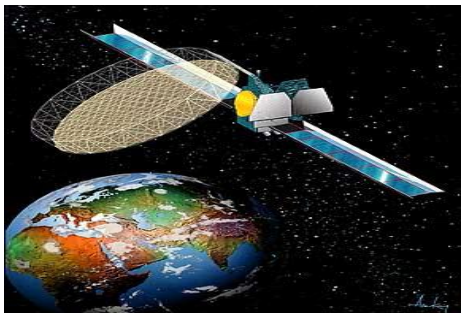

Figure 11: Appearance of the “Thuraya-2”

3. Conclusions

Estimating the number of radio antennas on the GSS is a rather difficult task. Not all of them are illuminated by the Sun during the observation session. Their visibility in most cases is possible closer to the epoch of the equinoxes and at small phase angles.

To increase the resolution of detecting small structures on the external GSS platform, it is necessary to reduce the accumulation time of a single measurement.

In the case of using large telescopes, this problem can be solved more qualitatively and quantitatively. Calorimetric allows this.

Reference

1. Murtazov A.K.: 2000, *Okolozemnaya astronomiya i problemy izucheniya malykh tel Solnechnoy sistemy*, M.: Kosmosinform, 262.
2. Yepishev V.P., Barna I.V., Kudak V.I., Perig V.M., Gabdeyev M.M.: 2017, *Nauchnyy vestnik Uzhgorodskogo vuza*, Seriya "Fizika", **41**, 132. https://physics.uz.ua/ru/journals/vipusk-41-2017/bagatokolirna-fotometriya-geostatsionarnikh-ob-rsquo-yektiv
3. Yepishev V.P., Kudak V.I., Pavlyuk M.M., Perig V.M.: 2017, *Nauchnyy vestnik Uzhgorodskogo universiteta*, Seriya "Fizika", **41**, 146. https://physics.uz.ua/ru/journals/vipusk-41-2017/doslidzhennya-poverkhnevikh-kharakteristik-geostatsionarnikh-suputnikiv-za-danimi-kolorimetriyi
4. Cowardin H., Seitzer P., Abercromby K., Barker E. et al.: 2010, https://ntrs.nasa.gov/search.jsp?R=20110015517
5. Allen K.V.: 1977, *Astrofizicheskiye velichiny*, M.: Mir, https://techlibrary.ru/b/2h1m1m1f1o_2s.3b._2h1s1t1r1p1v1j1i1j1y1f1s1l1j1f_1c1f1m1j1y1j1o2c._1977.pdf
6. https://space.skyrocket.de/cgi-bin/search.pl
7. https://ru.wikipedia.org/wiki/Астра_2E
8. https://mapgroup.com.ua/kosmicheskie-apparaty/26-kosmicheskie-apparaty-ssha/1808-sbirs-geo-1-2-3-4
9. Didenko A.V., Usol'tseva L.A.: 2011, *Izvestiya NAN Respubliki Kazakhstan*, **№ 4**, 7. http://lfvn.astronomer.ru/report/0000072/didenko_usoltzeva.pdf

RADIOASTRONOMY

DOI 10.18524/1810-4215.2022.35.268191

ANGULAR STRUCTURE OF THE RADIO GALAXY 3C239 IN THE DECAMETER RANGE

R.V. Vashchishyn[1], V.A. Shepelev[2], O.A. Litvinenko[3], G.S. Podgorny[2], V.G. Derevyagin[4], A.V. Lozonsky[4]

[1]Gravimetric Observatory of IGP NASU, Poltava, Ukraine, *vrv.uran2@gmail.com*

[2] Institute of Radio Astronomy of NASU, Kharkiv, Ukraine, *vshep258@gmail.com*

[3]URAN-4 Laboratory of IRA NASU, Odessa, Ukraine, *uran4@te.net.ua*

[4]Physical and Mechanical Institute of NASU, Lviv, Ukraine

ABSTRACT. We present the results of the observation of the radio galaxy 3C239 with the URAN interferometers at the decameter wavelengths. According to our study, the source in this range consists of two components that coincide in position and size with the lobes of the radio galaxy observed at the decimeter wavelengths, and a compact component corresponding to one of its hot spots. Another hot spot is not detected due to its low flux density at decameter wavelengths. In addition, an extended region of radiation with low surface brightness was detected, which surrounds the source lobes. The size of this halo is 28 arcsec, and its emission at the frequency of 25 MHz is about 20% of the total flux of the radio galaxy. A possible view of spectra of the radio source components and their variation in the range from decameter to decimeter wavelengths are determined. It is noted that in contrast to the high-frequency structure of 3C239, where radiation of the compact hot spots dominates, at decameter wavelengths about 90% of the radio galaxy flux is provided by more extended components — the source lobes and the halo.

Keywords: radio source, interferometer, decameter range, brightness distribution, decameter model.

АНОТАЦІЯ. Наведено результати спостереження радіогалактики 3C239 інтерферометрами УРАН на декаметрових довжинах хвиль. Згідно з дослідженням, джерело в цьому діапазоні складається з двох компонентів, які збігаються за положенням і розміром з пелюстками радіогалактики, що спостерігаються на дециметрових хвилях, та компактного компонента, що відповідає одній з її гарячих плям. Інша гаряча пляма не виявлена через низьку густину потоку. Крім того, була виявлена протягнена область випромінювання з низькою поверхневою яскравістю, яка охоплює пелюстки джерела. Розмір цього гало становить 28 кутових секунд, а його випромінювання на частоті 25 МГц становить близько 20% від загального потоку радіогалактики. Визначено можливий вигляд спектрів компонентів радіоджерела та їх змінювання в діапазоні від декаметрових до дециметрових хвиль. Відзначається, що на відміну від високочастотної структури 3C239, де домінує випромінювання компактних гарячих плям, на декаметрових хвилях близько 90% потоку радіогалактики забезпечується більш протягненими компонентами — пелюстками джерела і гало.

Ключові слова: радіоджерело, інтерферометр, декаметровий діапазон, розподіл яскравості, декаметрова модель.

1. Introduction

Studies of extragalactic radio sources with the URAN radio interferometers have shown that their structure in the decameter range differs markedly from images obtained at the decimeter and centimeter wavelength. The difference between the spectral indices of the emission of compact and extended source components, as well as the distortion of their "linear" spectra, caused, for example, by synchrotron self-absorption in hot spots at low frequencies and/or by synchrotron losses in extended lobes at high frequencies, leads to a significant change in the source brightness distribution at the decameter wavelengths compared to the shorter ones. An increase in the angular dimensions of components of the radio sources with frequency decreasing was also found.

The most intriguing feature found at decameter wavelengths is extended, low surface brightness halos with steep spectra that are larger than the full dimensions of the sources seen at shorter wavelengths (Megn et al., 2001, Megn et al., 2006). These components are found mainly in radio-loud quasars and rarely in radio galaxies, although the difference between these two types of extragalactic radio sources is only in the orientation of their axis relative to the line of sight to an observer. Because almost all radio galaxies that we observed with the URAN were extended sources with a small redshift, while the quasars were more compact and distant objects, it was interesting to study the compact radio galaxy 3C239, located in a distant cluster of galaxies with redshift $z = 1.781$.

This source was observed in a wide frequency range, from tens of megahertz to tens of gigahertz, but the maps have been obtained only at frequencies above 1.4 GHz using MERLIN radio interferometers and the VLA aperture synthesis system (Best et al., 1997, Liu et al., 1992).

At this frequencies, the radio galaxy is the FRII-type object with angular dimensions of about 15″. It consists of two elongated lobes (southwestern and northeastern) with hot spots in them. The total flux of the northeastern lobe and its hot spot exceeds the total radiation of the southwestern lobe with the hot spot located in it by more than 3 times.

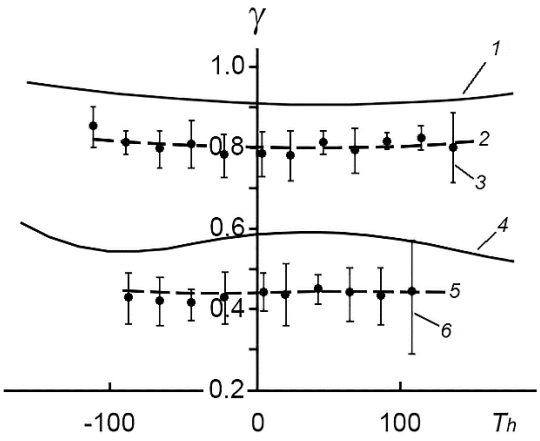

Figure 1: Normalized visibility modulus at the frequency of 25 MHz for the URAN-1*:* 1 – the high-frequency model, 2 – the decameter model, 3 – experimental data; the URAN-2: 4 – the high-frequency model, 5 – the decameter model, 6 – experimental data

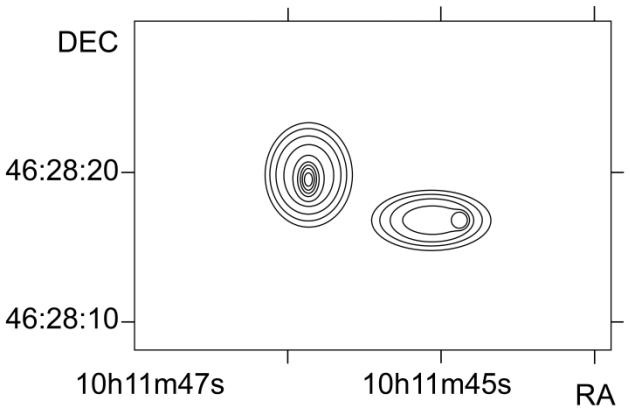

Figure 2: The model fitted to the 1.4 GHz map of 3C239

2. Observations and data reduction

Observations of the radio galaxy were carried out with the URAN interferometer network (Megn et al., 1997) at the frequencies of 20 and 25 MHz. The signals of the north-south antenna of the UTR-2 radio telescope were multiplied with the signals of four URAN antennas to form interferometer responses at different baselines. The observations of 3C239 were carried out at hour angles of ±120 minutes relative to the moment of crossing the meridian by the source with a scan duration of 20 minutes. The total amount of observations is about 20 days. The amplitudes of interferometer response obtained in the scans at a given hour angle were averaged over all observation days to find dependencies of the visibility function modulus versus the hour angle at four baselines and two frequencies.

An example of the experimental values of normalized visibility amplitudes and their errors measured with the URAN-1 and URAN-2 interferometers are shown in Fig. 1 by symbols *3* and *6*.

The dependences of the complex values of the visibility function, measured at different baselines, as is known, represent the Fourier transform of the source brightness distribution. If the coverage of the spatial frequency plane is sufficiently complete, the brightness distribution can be easily determined using the inverse Fourier transform. This approach is not acceptable with a small number of baselines and significant phase distortions typical for studies with the URAN at decameter wavelengths. So alternative method of model fitting with respect to the visibility function amplitudes is used to restore radio images of sources (Megn et al., 2001). According to this method, real source brightness distribution is represented by the model with a limited number of elliptical components with arbitrary orientated axes and a Gaussian radio brightness distribution. Then we calculate the model response for the URAN interferometers and change the parameters of the model (size, flux, and relative position of its components) attempting to minimize the difference between the calculated values and experimental dependences of the visibility modulus.

To achieve the best results of the fitting procedure, it is very important to select a good initial model. For this purpose, we choose a map of the studied radio source made in a range as close to the decameter as possible. This map should has a resolution no worse than that of the URAN's longest baseline and good reproduction of low spatial frequencies, to which the URAN-1 interferometer with the shortest baseline is sensitive. This map is transformed into the simplest model using the model fitting procedure described above. However, in this case, the calculated responses from the map are used instead of the experimental data. In this study, we used the digital map of 3C239 from the MERLIN archive, obtained at the frequency of 1420 MHz with the resolution of 0″.39×0″.34.

In the process of the map transformation into a model, individual structural elements – hot spots and lobes of the radio source were identified and their relative position, normalized flux, and angular size in the Gaussian approximation were determined. The general view of this model is shown in Fig. 2 and its parameters are in Table. 1.

The dependences of the visibility modulus on the hour angle calculated for this model are very close to the dependencies obtained for the map of the 3C239. Therefore, the resulting model describes well the real radio brightness distribution visible on the map. However, these dependencies, shown in Fig. 1 by lines *1* and *4* for the URAN-1 and URAN-2 interferometers, differ noticeably from the observational data at decameter wavelengths. It means that the angular structure of the source changes with frequency decreasing.

Table 1: High frequency model of 3C239

N	α,"	δ,"	S/S_0	θ,"	a/b	ψ,°
HS_{NE}	4,9	1,46	0,49	0,7	2	0
L_{NE}	4,9	1,7	0,28	2,8	1,2	0
HS_{SW}	-5,4	-1,4	0,08	0,46	1	0
L_{SW}	-3,3	-1,4	0,15	2,7	2	90

Note: *HS* – a hot spot; *L* – a lobe; α, δ – coordinates relative to the center of the source; S/S_0 – relative flux density; θ – angular size at half intensity; a/b – ratio of the axes of the elliptical component; ψ – position angle.

This "high frequency" model was extrapolated to low frequencies using all available information about the spectral characteristics of its components and taking into account the scattering in the interstellar medium that increases the dimensions of the most compact components of the source at decameters. The scattering angle calculated using formula (49) of (Shyshov, 2001) is equal to 0.86″ at 25 MHz and 1.4″ at 20 MHz The model with the parameters extrapolated in a such manner was used as the initial model in the fitting procedure with URAN's data to search for the brightness distribution of 3C239 at decameter wavelengths.

3. Results

An analysis of the spectra of the source components showed that the radiation of the southwestern hot spot is too weak to detect with the URAN interferometers, so the initial model becomes a three-component one. During the model fitting of the angular structure of the source, it was assumed that the position and orientation of the components of the initial model do not change at decameter waves, and their sizes in this range are increased due to scattering in the interstellar plasma. It was found that any change in the free parameters of this model cannot provide a satisfactory agreement between the calculated values and experimental visibilities. An acceptable result can only be achieved by adding an extended detail to the model, similar to those found in previously studied quasars. Thus, the most probable decameter source model consists of four components. In addition to the new region of extended radiation, it contains two lobes with the same shape and relative position as those at high frequencies and a compact hot spot in the northeast lobe. The dimensions of the last three components are slightly enlarged. The ratio of their fluxes has changed significantly. Whereas at high frequencies the northeastern hot spot provides about half of the radiation of the radio galaxy, in the decameter range its radiation is only 14% of the total source flux, and the main part of the flux is emitted by more extended source lobes. A new extended component with an angular diameter of about 30" supplies more than 20% of the source flux.

The parameters of the resulting decameter model at frequencies of 20 and 25 MHz are given in Table. 2.

The hour angle dependences calculated for the low-frequency model are shown in Fig. 1 by dashed lines *2* and *5* for the URAN-1 and URAN-2 interferometers. A general view of the model brightness distribution at decameter waves, together with MERLIN's map at a frequency of 1420 MHz, is shown in Fig. 3. Errors in determining the parameters of the model are estimated to be 15%.

The fluxes of the parts of the radio galaxy obtained during the fittings at high and low frequencies made it possible to determine component spectra in a wide frequency range.

Table 2: The model at frequencies of 20 and 25 MHz

N	α,"	δ,"	S/S_0	θ_{25},"	θ_{20},"	a/b	ψ,°
HS_{NE}	4,9	1,46	0,14	1,1	1,6	2	0
L_{NE}	4,9	1,7	0,48	2,9	3,1	1,2	0
L_{SW}	-3,3	-1,4	0,16	2,8	3	2	90
G	0	0	0.22	28	29	1	0

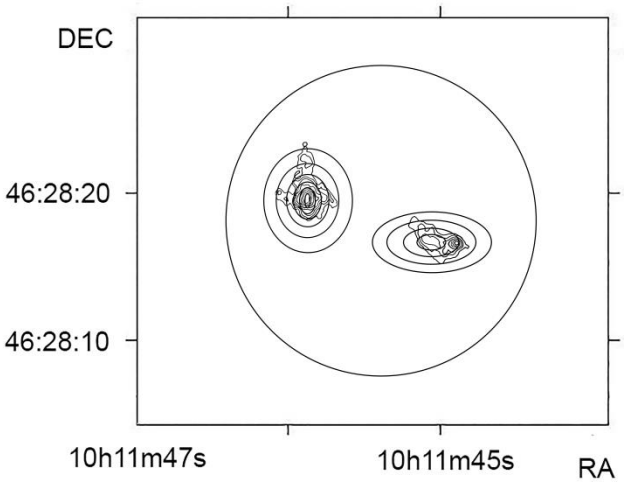

Figure 3: Model of 3C239 in the decameter range with the high-frequency map in the background

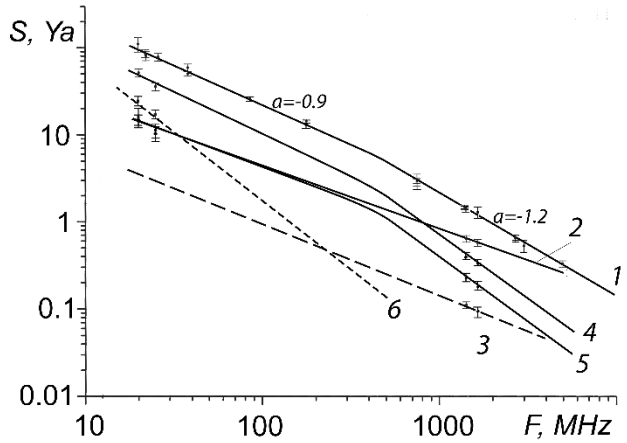

Figure 4: Spectral dependencies of 3C239

In Fig. 4. line *1* shows the total spectrum of 3C239, the spectrum of the northeastern hot spot is shown by lines *2*, the spectra of the lobes are shown by lines *4* and *5*, and the radiation of the extended halo is shown by *6*.

The decameter radiation of the southwestern hot spot is below the threshold of sensitivity of the URAN interferometers, and supposed spectrum of the component is shown by dashed line 3.

The values of the total flux density of the source at different frequencies are taken from NED (NASA/IPAC Extragalactic Database) with scale corrections according to (Baars et al., 1977). Data at the frequencies of 20 and 25 MHz were obtained in this work.

Linear approximations of the total spectrum are fitted by the least mean squares method separately at frequencies from 20 to 450 MHz and at frequencies above 450 MHz. Since the radiation of the southwestern hot spot is below the sensitivity threshold of URAN interferometers, its supposed spectrum is shown in Fig. 4 by dashed line 3.

Changes in the spectral index of the total radiation of a radio galaxy in the region of hundreds of megahertz arise from the peculiarity of the spectra of its lobes. Assuming that these features are associated with synchrotron radiation

losses in these components, one can determine the synchrotron age of radio sources using formula 2 from (Murgia et al. 1999). With a break frequency of 450 MHz and a magnetic field in the lobes given in (Liu et al., 1992), it is approximately 5 My.

4. Conclusion

The angular structure of the radio galaxy 3C239 in the decameter wavelength range has been studied, and the source brightness distribution model consisting of four components has been determined in this work. We determined that:

1. Two lobes and one of the hot spots visible in high-frequency maps of the radio galaxy are detected in the decameter range.

2. The dimensions and position of these components have not changed remarkably with decreasing frequency, but the ratio of their fluxes has changed significantly. At the decameter wavelengths, the radiation of the lobes predominates, while in the decimeter range hot spots are brighter.

3. An extended halo with a low surface brightness was found, which provides about 20% of the total radio source flux in the decameter range. This component was not observed at shorter wavelengths due to its steep spectrum.

4. A break in the spectrum of the source lobes caused by synchrotron losses was detected, which made it possible to determine the age of the radio galaxy.

References

Baars J.W.M., Genzel R., Pauliny-Toth I.I.K., et al.: 1977, *Astron. Astrophys*, **61**, 1, 99.

Best P.N., Longair M.S., Röttgering H.J.A.: 1997, *MNRAS*, **292**, 758.

Liu R., Pooley G., Riley J.M.:1992, *MNRAS*, **257**, 545.

Megn A.V., Braude S.Ya., Rashkovsky S.L., et al.: 1997, *AJ*, **2**, 4, 385.

Megn A.V., Braude S.Ya., Rashkovsky S.L., et al.: 2001, *Kinemat. Phys. Celest. Bodies*, **17**, 3, 195.

Megn A.V., Rashkovsky S.L., Shepelev V.A.: 2001, *RPRA*, **6**, 1, 9.

Megn A.V., Rashkovsky S.L., Shepelev V.A., et al.: 2006, *AJ*, **83**, 9, 776.

Murgia, M., Fanti, C., Fanti, R., et al.:1999, *A&A*, **345**, 769.

Shyshov V.I.: 2001, *AJ*, **78**, 3, 229.

SUN, SOLAR ACTIVITY AND ASTROBIOLOGY

DOI 10.18524/1810-4215.2022.35.268201

PREDICTION OF THE AMPLITUDE OF 25TH SOLAR CYCLE USING THE RATE OF INCREASE OF SOLAR ACTIVITY

V.M. Efimenko[1], V.G. Lozitsky[2]

Astronomical Observatory of the Taras Shevchenko National University of Kyiv, Kyiv, Ukraine
[1] *efim@knu.ua,* [2] *vsevolod.lozitsky@knu.ua*

ABSTRACT. A prediction of the amplitude of the 25th cycle of solar activity is proposed based on the analysis of data on 24 previous solar cycles, which relate to the statistical relationship between the rate of increase in the number of sunspots in the phase of the growth curve and the amplitude of the cycle. It turned out that the forecasting result depends on which section of the growth curve is taken as the basis for forecasting, as well as whether all 24 cycles are taken into account, or only the odd ones. The prediction result is also affected by the initial assumption about monotonicity or non-monotonicity of the growth phase. A comparison of the rates of sunspot growth in different parts of the growth phase of different cycles shows that the current cycle #25 does not show early signs of non-monotonic growth similar to those observed in the 24th cycle. It was concluded that, most likely, the maximum smoothed number of sunspots in the 25th cycle W_{max} (25) should be equal to 185 ± 18 units in the new system, which corresponds to the average power of the solar cycle, with the implementation of the Hnievyshev-Ohl rule. However, if cycle #25 will still have a non-monotonic curve of the growth phase, similar to such a curve in the previous cycle #24, then W_{max} (25) $\approx$ 130. With such parameters of this cycle, there are no signs of approaching the deep minimum of the age cycle in the middle 21st century. This does not exclude the fact that this deep age minimum can occur suddenly and sharply immediately after the 25th cycle, as was the case, for example, in the Dalton minimum.

Keywords: Sun, solar activity, number of sunspots, amplitude forecast of the 25th cycle, Gnievyshev-Ohl rule, minimum of the age cycle.

АНОТАЦІЯ. Запропоновано прогноз амплітуди 25-го циклу сонячної активності на основі аналізу даних про 24 попередні сонячні цикли, які стосуються статистичного зв'язку між швидкістю наростання числа сонячних плям на фазі кривої росту і амплітудою циклу. Виявилось, що результат прогнозування залежить від того, яку ділянку кривої росту взяти за основу для прогнозування, а також від того, приймати до уваги всі 24 цикли, чи лише непарні. На результат прогнозування впливає також вихідне припущення про монотонність чи немонотонність фази росту. Порівняння швидкостей наростання числа сонячних плям на різних ділянках фази росту різних циклів показує, що поточний цикл № 25 не виявляє ранніх ознак немонотонності росту, подібних до спостережених у 24-му циклі. Зроблено висновок, що, найімовірніше, максимальне згладжене число сонячних плям у 25-му циклу W_{max} (25) має дорівнювати 185 ± 18 одиниць у новій системі, що відповідає середньому по потужності сонячному циклу, з виконанням правила Гнєвишева-Оля. Однак, якщо все-таки цикл №25 буде з немонотонною кривою фази росту, подібною до такої кривої у попередньому циклі №24, то тоді W_{max} (25) $\approx$ 130. При таких параметрах цього циклу, немає ознак наближення глибокого мінімуму вікового циклу в середині XXI ст. Це не виключає того, що цей глибокий віковий мінімум може наступити раптово і різко одразу після 25-го циклу, як це було, наприклад, у мінімум Дальтона.

Ключові слова: Сонце, сонячна активність, число сонячних плям, прогноз амплітуди 25-го циклу, правило Гнєвишева-Оля, мінімум вікового циклу.

1. Introduction

Solar activity is a rather complex phenomenon in the Sun's atmosphere, which has a magnetic nature and cyclical changes over time. The most famous and visible is the 11-year cycle of solar activity, although there are also other cycles, including the 22-year, 44-year, and the age cycle with a duration of 70-100 years. Among specialists, the greatest attention is paid to forecasting the 11-year cycle, since it is this cycle that is associated with the most significant changes in the near-Earth space and geosphere. At present, reliable methods of forecasting solar activity have not yet been created, although there are quite a lot of scientific works on this topic. A comparison of the latest forecasts of solar activity in the new 25th cycle, which began in December 2019, is given in the work of Petrovay (2020). It follows from this comparison that even the most modern forecasting methods give significantly different results. For example, the neural network method gives the amplitude of the 25th cycle at the level of 57-91 units (Attia et al., 2013), and the attractor analysis - about 103 units. For comparison, it is worth recalling that in the previous 24th cycle, solar activity reached 116 units (in 2014). At the same time, the wavelet analysis predicts the height of the maximum of

the 25th cycle at the level of 132 units (Rigozo et al., 2011), and the method of internal precursors – 175 units (Li et al., 2015). Thus, in general, the situation with the maximum of this cycle, which is expected in 2024-2026, remains unclear. However, the situation was exactly the same before, when the previous 24th cycle of solar activity was predicted (see, e.g., Lozitsky & Efimenko, 2012, 2014; Attia et al., 2013; Pishkalo, 2014; Rigozo et al., 2011; Tsirulnik et al., 1997).

The current 25th cycle attracts attention because it can be used to conclude that the long-awaited minimum of the age cycle of solar activity is approaching, which falls around the middle of the 21st century. Zharkova and Shepherd (2022) note in the recently published paper that the major solar minimum should occur in cycles No. 25-27. The purpose of present work is to obtain a predictive estimate of the amplitude of the 25th cycle, based on the rate of increase in the number of sunspots during the growth phase of this cycle.

2. Observational data and their analysis

For our analysis, we used the data posted on the site http://www.solen.info/solar/. New, revised data on the number of sunspots are presented here based on the results of a revision made by International Data Center at the Royal Belgian Observatory (Clette et al., 2014). The main changes are that Alfred Wolfer's observational series, rather than Rudolf Wolff's, is used as a basis, which increases the earlier values by a factor of about 1.67, making them commensurate with modern estimates. In addition, the values were corrected after 1947, when M. Waldmayer, in determining the relative number of sunspots, introduced weighting factors according to the size of the spots. A variable trend was also found and eliminated in the observations of the Locarno observatory, which was a reference observatory after 1980.

Cycle No. 25 began in December 2019. From this month, the months of the 25th cycle were counted, and the rate of increase in the number of sunspots $\Delta W/\Delta T$ was compared with other cycles, as well as with the maximum smoothed number of sunspots W_{max} at the top of the cycle. Similar approach was applied by Lozitsky and Efimenko (2012) but for sunspot numbers of old system.

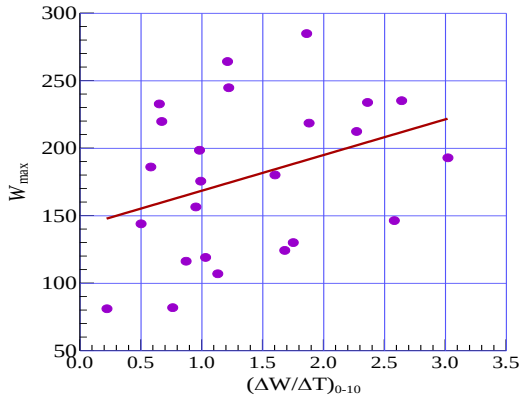

Figure 1: Empirical dependence between parameters W_{max} and $(\Delta W/\Delta T)_{0\text{-}10}$. It follows from this dependence that W_{max} (25) = 166.6 (see the text).

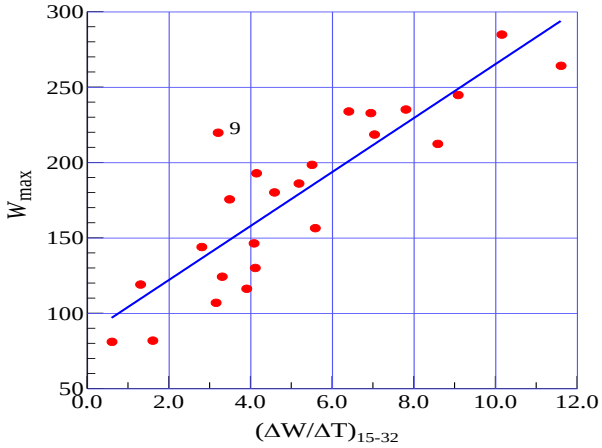

Figure 2: The same as on Fig. 1, but for averaging interval 15-32 months. From this Figure it follows that W_{max} (25) = 166.7 (see the text).

The following question is of interest: what minimum interval from the beginning of the cycle should be taken to reliably predict its maximum ? To find out this question, we considered test intervals of different lengths, starting from 10 months (Fig. 1). It can be seen from this Figure that the correlation dependence between the specified parameters is very scattered and can be approximated by a linear dependence

$$W_{max} = 26.44(\Delta W/\Delta T)_{0\text{-}10} + 141.91, \quad (1)$$

According to published data for 25th cycle, $(\Delta W/\Delta T)_{0\text{-}10}$ = 1.01, that correspnds to W_{max} (25) = 166.6. As it follows from Fig. 1, this is some middle value in range 100-250 units. Therefore, wider test intervals should be used to average out the random fluctuations of the parameters.

Fig. 2 represents the result at the averaging interval 15-32 months.

From Fig. 2 shows that the statistical relationship between the specified parameters is now closer and can be described by a linear relationship

$$W_{max} = 17.9(\Delta W/\Delta T)_{15\text{-}32} + 86.17, \quad (2)$$

According to observations for 25th cycle, $(\Delta W/\Delta T)_{15\text{-}32}$ = 4.5, which according to (2) gives the following value W_{max} = 166.7. As we can see, this value turned out to be very close to the previously obtained according to approximation (1). However, such a coincidence is obviously coincidental, given the large spread of points in Fig. 1.

Since the predicted cycle No. 25 is odd, it is interesting to consider similar correlation dependences only for odd cycles (Fig. 3). The corresponding approximating linear dependence is represented by the formula

$$W_{max} = 16.63(\Delta W/\Delta T)_{15\text{-}32} + 104.81, \quad (3)$$

Substituting the observed value for the 25th cycle $(\Delta W/\Delta T)_{15\text{-}32}$ = 4.5 into this formula, we have W_{max}(25) = 179.6. Thus, switching to considering only odd cycles increases the predicted value by 13 units.

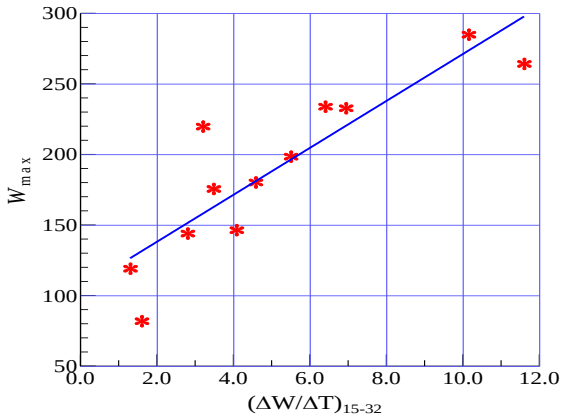

Figure 3: The same as in Fig. 2, but only for odd cycles. From the regression dependence (3), presented in this figure by a straight line, it follows that the predicted value of $W_{max}(25) = 179.6$.

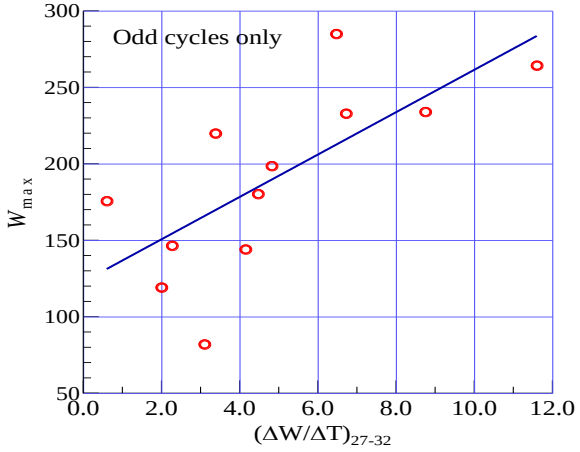

Figure 4: The same as in Fig. 3, but when averaging the $\Delta W/\Delta T$ parameter in the interval of 27-32 months. From these data it follows that $W_{max}(25) = 204.2$.

However, it turns out that the predicted value of $W_{max}(25)$ increases even more if we consider a narrower interval of 27-32 months of the cycle (Fig. 4). In this case, the regression equation has the form

$$W_{max} = 13.85(\Delta W/\Delta T)_{27\text{-}32} + 122.88, \qquad (4)$$

Substituting the observed value $(\Delta W/\Delta T)_{27\text{-}32} = 5.87$ into formula (4), we have $W_{max}(25) = 204.2$.

Thus, compared to approximations (1) and (2), the predicted value increases by almost 40 units. This growth means that in the interval of months 27-32 we have signs of "acceleration" (acceleration of growth) of the current cycle No. 25, that is, a situation opposite to the previous cycle No. 24.

It is worth recalling that in the first 20 months of the development of the 24th cycle, the activity did not exceed 20 units (in the old system), which promised a rather weak cycle. However, starting from the 24th month of the cycle, the general picture of the development of activity changed noticeably: the number of spots began to increase rapidly and this growth of activity continued until the 32nd month.

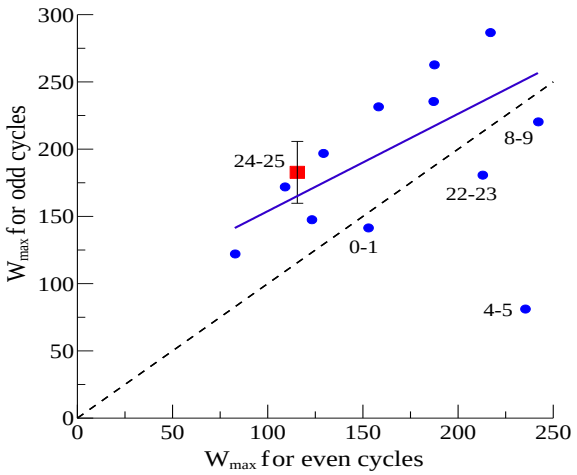

Figure 5: The ratio between the amplitudes of even and odd cycles (see the text).

After that, the activity grew more slowly and reached a maximum of about 67 units in the 38th month of the cycle (in March 2012). After that, the number of spots decreased slightly and remained almost unchanged during the 43-52 months of the cycle, being within 58-60 units. The actual amplitude of the 24th cycle turned out to be equal to $W_{max}(24) = 82$. Thus, the early forecast of Lozitsky & Efimenko (2012) based on the initial (monotonic) section of the growth phase was overestimated by ≈ 30%.

As for the above data for the 25th cycle, they correspond, in general, to the following most likely forecast $W_{max}(25) = 185 \pm 18$. If, after all, the current 25th cycle will continue to develop according to the scenario of the 24th cycle (which had a non-monotonic curve of the growth phase and an abnormally bifurcated peak – see Lozitsky & Efimenko, 2014), then one can expect $W_{max}(25) \approx 130$.

The above forecast $W_{max}(25) = 185 \pm 18$ corresponds well to the Gnevyshev-Ohl rule (Gnevyshev, 1977), according to which the amplitude of the odd cycle is, on average, 10-50% greater than the amplitude of the previous even cycle (Fig. 5). In this Figure, blue dots represent the actual data for 24 previous cycles, and a red square with vertical intervals represents the most probable forecast of the authors of the presented work. The solid straight line shows the linear approximation of the Gnievyshev-Ohl rule, performed on all cycles except for cycles 4 and 5. The dashed line shows the line of equal values of the amplitudes of even and odd cycles.

From Fig. 5, it can be seen that the Hnievyshev-Ohl rule was violated not only in a pair of cycles 4-5, but also in cycles 0-1, 8-9, and 22-23 (though, to a lesser extent). If this rule will be also violated in cycles 24-25, then it would be a double (that is, twice in a row) violation of this rule, which has not been observed until now. This is another argument in favor of the prediction of $W_{max}(25) = 185 \pm 18$ being more likely.

If this prediction is true, a possible Maunder or Dalton-type deep minimum of the age cycle could begin later, for example, from the 26th cycle of solar activity. More specifically, the nature of such changes can be traced to the relatively recent Dalton minimum (≈1800-1820).

Then, in the 4th cycle of solar activity, the amplitude of the smoothed number of sunspots reached $W_{max}(4)$ = 235.3, and in the next cycle it sharply dropped to $W_{max}(5)$ = 82.0 and remained practically the same in the next cycle: $W_{max}(6)$ = 81.2. Thus, the number of sunspots sharply decreased by a factor of 3, but in the next odd cycle No. 7 it increased to $W_{max}(7)$ = 119.2, i.e. almost by a factor of 1.5. Such sharp changes in established patterns of solar activity are called phase catastrophes by Tsirulnik et al (1997), i.e., this is a period when the amplitudes, periods and phases of oscillations that describe the observed changes in solar activity change dramatically. Periodic repetitions of phase catastrophes in the observed changes in solar activity indicate that the "memory" of solar activity can be relatively short - on the order of the duration of an 11-year cycle. In this regard, it can be expected that the method of internal predictors gives better forecasting results than the method of external predictors. The method proposed in the presented work is essentially a method of internal precursors, which uses a statistical relationship between current changes in solar activity (an increase in the number of sunspots in a certain area of the curve of the growth phase) and the amplitude of the cycle after a relatively short time (1-2 years) after the indicated changes in the number of spots.

Thus, the results presented in this study do not exclude the occurrence of a deep age minimum in solar activity in the next few cycles, for example, in only two cycles #26-27, as it was in the Dalton minimum. Given that solar activity has a complex deterministic-stochastic character, it is hardly possible to reliably predict this minimum by methods based on the patterns of many cycles of solar activity.

3. Conclusions

The main conclusion of this work is that the amplitude of the smoothed number of sunspots in the current 25th cycle will most likely be as follows: W_{max} (25) = 185 ± 18. It turned out that the forecasting result depends on which section of the growth curve is taken as the basis for forecasting, as well as whether all 24 cycles are taken into account, or only the odd ones. The prediction result is also affected by the initial assumption about monotonicity or non-monotonicity of the growth phase. A comparison of the rates of sunspot growth in different parts of the growth phase of different cycles shows that the current cycle #25 does not show early signs of non-monotonic growth similar to those observed in the 24th cycle. However, if cycle #25 will still have a non-monotonic curve of the growth phase, similar to such a curve in the previous cycle #24, then W_{max} (25) ≈ 130. Our forecast corresponds to the average power of the solar cycle, with the implementation of the Hnievyshev-Ohl rule. With such parameters of this cycle, there are no signs of approaching the deep minimum of the age cycle in the middle 21st century This does not exclude the fact that this deep age minimum can occur suddenly and sharply immediately after the 25th cycle, as was the case, for example, in the Dalton's minimum.

Acknowledgements. This study was funded by the Taras Shevchenko National University of Kyiv, project No. 22БФ023-03.

References

Attia A.F., Ismail H.A., Basurah H.M.: 2013, *Astrophys. and Space Science*, **344**, 5.

Clette F., Svalgaard L., Vaquero J.M., Cliver E.W.: 2014, *Space Sci. Rev.*, **186**, Iss. 1-4, 35.

Gnevyshev M.N.: 1977, *Solar Phys*., **51**, 175.

Li K.J., Feng W., Li F.Y.: 2015, *Journ. of Atmospheric and Solar-Terrestrial Physics*, **135**, 72.

Lozitsky V., Efimenko V.: 2012, *Visnyk Kyiv. Univ., Astronomija*, **49**, 47.

Lozitsky V.G., Efimenko V.M.: 2014, *Odessa Astron. Publ*., **27**, No.2, 90.

Petrovay K.: 2020, *Living Review Sol. Phys.*, **17**, art. No.2.

Pishkalo M.I.: 2014, *Solar Phys*., **289**, Iss. 5, 1815.

Rigozo N.R., Souza Echer M.P., Evangelista H., Nordemann D.J.R., Echer E.: 2011, *Journ. of Atmosph. and Solar-Terrestrial Physics*, **73(11–12)**, 1294.

Tsirulnik L.B., Kuznetsova T.V., Oraevsky V.N.: 1997, *Advances in Space Research*, **20**, 2369.

Zharkova V.V., Shepherd S.J.: 2022, *Monthly Not. of the Royal Astron. Soc*., **512**, Iss. 4, 5085.

Наукове видання

Одеські Астрономічні Публікації

том 35 (2022)

Англійською мовою

Технічний редактор *В. В. Ковтюх*
Комп'ютерна верстка *С. Л. Страхова*

Підписано до друку 15.12.22. Формат 60x84/8.
Ум. друк. арк. 12,5. Тираж 50 прим. Зам. № 2586.

Видавець і виготовлювач
Одеський національний університет імені І.І. Мечникова
Свідоцтво суб'єкта видавничої справи ДК № 4215 від 22.11.2011 р.
65082, м. Одеса, вул. Єлісаветинська, 12, Україна
Тел.: (048) 723 28 39
e-mail: druk@onu.edu.ua